



Fakultät für Medizin

Institut für Biologische und Medizinische Bildgebung

Augmented microscopy: Development and application of high-resolution optoacoustic and multimodal imaging techniques for label-free biological observation

Dominik Maximilian Soliman

Vollständiger Abdruck der von der Fakultät für Medizin der Technischen Universität München zur Erlangung des akademischen Grades eines

Doctor of Philosophy (Ph.D.)

genehmigten Dissertation.

Vorsitzender: Prof. Dr. Claus Zimmer

Betreuer: Prof. Vasilis Ntziachristos, Ph.D.

Prüfer der Dissertation:

1. Prof. Dr. Gil G. Westmeyer
2. Prof. Dr. Sibylle Ziegler

Die Dissertation wurde am 19.10.2016 bei der Fakultät für Medizin der Technischen Universität München eingereicht und durch die Fakultät für Medizin am 31.01.2017 angenommen.

For Leila, Karim & Robin

Zusammenfassung

Seit Jahrhunderten gewährt die optische Mikroskopie Einblicke in das strukturelle und funktionelle Gerüst, das dem Leben zugrunde liegt. Moderne Lasermikroskopie-Verfahren wie beispielsweise die konfokale oder Multiphotonen-Mikroskopie haben über die Jahre unser Verständnis von biologischen Prozessen und Strukturen revolutioniert, indem sie die Bildgebung von lebenden Organismen mit sub-zellulärer Auflösung mehrere hundert Mikrometer tief in Gewebe ermöglichen. Üblicherweise basiert der Kontrast bei konventionellen Lasermikroskopie-Methoden auf der Emission von Fluoreszenz und somit auf der Kennzeichnung spezifischer Strukturen mit Fluoreszenzmarkern oder der Expressierung fluoreszierender Proteine im untersuchten Gewebe. Bei der Bildgebung lebender Organismen können diese Marker jedoch zu toxischen Nebeneffekten oder einer zeitlichen Begrenzung der Observationszeit durch chemische Degradierung der Fluoreszenzmarker führen.

Ein neuartiges und vielversprechendes Lasermikroskopie-Verfahren für die Abbildung tiefliegender Strukturen stellt die hochauflösende optoakustische (photoakustische) Bildgebung dar. Diese Methode basiert auf der Erzeugung akustischer Wellen durch die Absorption von gepulster Laserstrahlung und der Detektion dieser akustischen Signale mittels Ultraschall-Transducern. Da die optoakustische Bildgebung optische Absorption mit großen Eindringtiefen abbildet, eignet sie sich hervorragend für die markierungsfreie Visualisierung von endogenen Gewebe-Chromophoren *in vivo*.

Diese Arbeit widmet sich dem Ziel, die hochauflösende optoakustische Bildgebung für die markierungsfreie Untersuchung biologischer Organismen voranzutreiben. Der Fokus liegt hierbei auf der Schnittstelle von Systementwicklung, Kombination mit anderen Mikroskopiemethoden und Forcierung simpler, kosteneffektiver Hardwarelösungen.

Im ersten Teil wird die Rasterscan optoakustische Mesoskopie (RSOM) eingeführt, eine Variante der hochauflösenden optoakustischen Bildgebung, die bezüglich der räumlichen Auflösung und Eindringtiefe einen Bereich zwischen mikroskopischen und makroskopischen Verfahren einnimmt. Eine Weiterentwicklung der bisherigen tomographischen Rekonstruktionsmethode unter Einbeziehung eines realistischen Modells des Detektions-Sensitivitätsfeldes wird vorgestellt. Zusätzlich wird eine verbesserte Visualisierung feiner Strukturen mittels eines Multi-Frequenz-Ansatzes in der Rekonstruktion erreicht. Darüber hinaus wird RSOM eingesetzt für die markierungsfreie dreidimensionale Darstellung der zellulären Dynamik von Melanophoren in lebenden Zebrafischen, zusammen mit einer neuartigen Analyseverfahren optoakustischer Frequenzen zur Registrierung von Zelldynamik-vermittelten Frequenzsignaturen.

Der zweite Teil präsentiert die Entwicklung eines optoakustischen Mikroskops (OM) im Durchlichtverfahren, welches die Abbildung feiner Strukturen in Modellorganismen mit einer räumlichen Auflösung im Mikrometer-Bereich ermöglicht. Das OM-System erlaubt zusätzlich die experimentelle Charakterisierung der elektrischen Impulsantwort des verwendeten Hochfrequenz-Transducers, welche anschließend für eine Korrektur des Verzerrungseffektes der begrenzten Eingangsbandbreite verwendet wird. Des Weiteren wird die Realisierung eines optoakustischen Mikroskops unter Verwendung eines π -phasenverschobenen Faser-Bragg-Gitter-Detektors demonstriert und die erstmalige Anwendung eines der-

artigen Sensors auf die Bildgebung biologischer Organismen *ex vivo* präsentiert. Im nächsten Schritt wird das OM-System mit RSOM, sowie drei Multiphotonen-Mikroskopie-Modalitäten kombiniert. Dieses hybride Mikroskop ermöglicht nicht nur die multimodale Visualisierung verschiedener anatomischer Strukturen basierend auf komplementärem, markierungsfreiem Kontrast, sondern eröffnet darüber hinaus die Möglichkeit, biologische Strukturen auf unterschiedlichen Skalen zu erfassen. Die Leistungsfähigkeit des hybriden Mikroskops wird anhand der Bildgebung von Modellorganismen und menschlichen Gewebeproben *ex vivo* demonstriert.

Im letzten Teil wird die Entwicklung eines Frequenzbereich-optoakustischen Mikroskops (FD-OM), basierend auf intensitätsmodulierten Dauerstrichlasern und der Erzeugung monofrequenter optoakustischer Signale, vorgestellt. FD-OM stellt eine vielversprechende Methode dar, da sie auf einfache und kosteneffektive Hardware zurückgreift und gleichzeitig hohe Bildraten mit Hilfe eines schnellen Laserscan-Verfahrens und simpler IQ-Demodulation erreicht. Im Unterschied zu bisherigen Implementierungen werden bei dem entwickelten FD-OM-System sequenziell Bilder bei verschiedenen Modulationsfrequenzen aufgenommen, was die Visualisierung unterschiedlich großer Strukturen und eine Extraktion begrenzter Tiefeninformation erlaubt. Durch die Kombination mit dem zuvor entwickelten Multiphotonen-Mikroskop wird eine hochauflösende markierungsfreie Bildgebung mit höheren multimodalen Bildraten erreicht, was die Aufnahme von größeren Regionen in lebenden biologischen Proben innerhalb der erlaubten Messzeiten begünstigt. Darüber hinaus ist es mit FD-OM möglich, Dopplerverschiebungen optoakustischer Frequenzen von sich bewegenden optischen Absorbern zu detektieren, was mit Hilfe mehrerer Phantome demonstriert wird. Diese besondere Eigenschaft wird im letzten Schritt ausgenutzt, um erstmalig den Blutfluss in Mikrogefäßen einer lebenden Maus mittels Frequenzbereich-Optoakustik zu messen und zweidimensional zu visualisieren. Die Möglichkeit der nicht-invasiven und markierungsfreien Messung von Mikrozirkulation mit FD-OM könnte neue Einblicke in krankheitsbezogene Veränderungen bestimmter funktionaler Parameter, wie beispielsweise Blutdruck oder Gewebemetabolismus, eröffnen.

Abstract

For centuries, optical microscopy has been 'shedding light' on structure and function of the underlying fabric of life. Contemporary laser microscopy approaches such as confocal fluorescence or multiphoton microscopy revolutionized our understanding of biological processes by allowing for the imaging of living organisms, achieving sub-cellular resolutions at tens or hundreds of micrometers deep inside non-transparent tissue. However, a severe impediment for the *in vivo* observation of biological organisms is the dependence of most optical microscopy techniques on fluorescent staining or labeling, which can potentially lead to toxic effects or limit the observation time through chemical degradation of the fluorophores.

A promising newcomer in the league of deep-tissue microscopy modalities is high-resolution optoacoustic (photoacoustic) imaging, which relies on the generation of acoustic waves through optical absorption of pulsed laser light by chromophores and a subsequent detection with ultrasound transducers. As optoacoustic imaging generally senses optical absorption, it enables the label-free visualization of endogenous chromophores at large imaging depths.

This work is dedicated to the advancement of high-resolution optoacoustic imaging for label-free biological examination at the intersection of system development, integration with other microscopy modalities and promotion of simple and cost-effective hardware implementations.

The first part introduces raster-scan optoacoustic mesoscopy (RSOM), a variant of high-resolution optoacoustic imaging that bridges the gap between microscopy and macroscopy in terms of resolution and imaging depth. A tomographic reconstruction method is presented, incorporating a realistic model of the detector sensitivity field and improving small-feature-visualization through the division of the reception bandwidth into multiple sub-bands. Furthermore, RSOM is applied to the label-free 3D monitoring of melanophore dynamics in living zebrafish, complemented by a novel method for picking up cell dynamics related signatures detected in the frequency spectra of optoacoustic signals.

The second part presents the development of a transmission-mode optoacoustic microscopy (OM) system that achieves sub-cellular resolution in model organisms such as zebrafish and mice. First, the OM system is used to characterize and correct for the electrical impulse response of the employed high-frequency transducer. Moreover, all-optical OM is demonstrated based on a π -phase-shifted fiber Bragg grating detector and the first successful application of such an optical sensor to *ex vivo* optoacoustic imaging of biological specimens is presented. Next, to enable the unique fusion of multicontrast and multiscale imaging capabilities in a single hybrid device, the optoacoustic microscope is combined with three label-free multiphoton microscopy modalities as well as RSOM. The performance of the developed hybrid microscope is demonstrated on the label-free imaging of model organisms and human tissue samples *ex vivo*, concurrently visualizing a broad range of anatomical features at different geometrical scales based on complementary contrast.

In the final part, the development of a frequency-domain optoacoustic microscope (FD-OM) based on intensity-modulated continuous wave (CW) laser excitation is presented.

The FD-OM system achieves high frame rates through fast laser-scanning and simple IQ-demodulation. It furthermore acquires images at different modulation frequencies - a unique feature that enables visualization over a wide range of absorber sizes and the retrieval of limited depth information, as compared to earlier single-frequency FD-OM approaches. FD-OM is a promising technique, since it relies on simple and cost-effective hardware, and is showcased through the label-free imaging of phantoms and biological specimens. The subsequent combination with multiphoton microscopy facilitates the fast hybrid imaging of extended fields-of-view in mouse ears *in vivo*. Moreover, FD-OM allows for the detection of optoacoustic Doppler shifts from moving absorbers. In the next step, this feature is built upon for the label-free imaging of microcirculatory blood flow in mouse ears *in vivo*, which is achieved for the first time in the frequency domain. This is an important ability as non-invasive imaging of microflow might offer novel insights into disease-related changes of certain functional parameters, such as blood pressure or tissue metabolism.

Contents

Zusammenfassung	iii
Abstract	v
List of abbreviations	xi
1 Introduction	1
1.1 Laser microscopy in biological research	1
1.2 The case for label-free imaging	2
1.3 High-resolution optoacoustic imaging	2
1.4 Goals and objectives	3
1.5 Structure of the thesis	4
2 Principles of laser microscopy	7
2.1 Interaction of light with matter	7
2.1.1 Absorption	9
2.1.2 Scattering	12
2.2 Basic optical concepts	13
2.2.1 Gaussian optics	13
2.2.2 Spatial resolution	15
2.2.3 Optical aberrations	18
2.2.4 Imaging depth	18
2.2.5 Field of view	19
2.3 Background on fluorescence microscopy	20
2.3.1 Fluorescent labels	20
2.3.2 Image formation and scanning	20
2.3.3 Objective lens and resolution	20
2.3.4 Optical filters	21
2.3.5 Detection and acquisition	21
2.3.6 Photobleaching	21
2.4 Optical laser microscopy techniques – an excerpt	22
2.4.1 Fluorescence confocal microscopy	22
2.4.2 Multiphoton microscopy	23
2.4.3 Light sheet fluorescence microscopy	28
2.5 The mesoscopic imaging regime	29
3 Raster-scan optoacoustic mesoscopy (RSOM)	31
3.1 Introduction	31
3.2 Theoretical foundation of optoacoustic imaging	32
3.2.1 Signal generation	33
3.2.2 Wave equation and forward solution	33
3.2.3 Frequency content of optoacoustic signals	36
3.2.4 Optoacoustic signals from solid absorbers	37

3.2.5	Acoustic attenuation	38
3.2.6	Focused ultrasound transducers and detection geometry	39
3.2.7	Spatial resolution in optoacoustic mesoscopy	43
3.2.8	The backprojection reconstruction method	44
3.3	Materials and methods	46
3.3.1	Experimental designs of RSOM	46
3.3.2	Scanning scheme and spatial resolution	47
3.3.3	Signal processing and reconstruction	48
3.4	Results	52
3.4.1	Phantom study	52
3.4.2	Imaging of mouse ear vasculature <i>ex vivo</i>	52
3.5	Conclusion	54
4	Volumetric monitoring of melanophore dynamics <i>in vivo</i> using RSOM	57
4.1	Introduction	57
4.2	Background on melanophore pigment translocation	58
4.3	Materials and methods	60
4.3.1	Setup, sample handling and image processing	60
4.3.2	Optoacoustic frequency analysis	60
4.4	Simulation of frequency shifts generated by absorber size changes	61
4.5	Results	62
4.5.1	Melanosome aggregation in frog melanophores <i>in vitro</i>	62
4.5.2	Frequency based optoacoustic monitoring of melanophore dynamics <i>in vivo</i>	63
4.5.3	Bioengineered pigment clustering sensors for dynamic optoacoustic imaging	67
4.6	Conclusion and outlook	69
5	Transmission-mode optoacoustic microscope	71
5.1	Introduction	71
5.2	Materials and methods	73
5.2.1	Experimental setup	73
5.2.2	Acquisition and image formation	74
5.2.3	Alignment of transducer and optical excitation	75
5.3	Characterization	76
5.3.1	Laser source	76
5.3.2	Transducer detection bandwidth and electrical impulse response	77
5.3.3	Spatial resolution	80
5.4	Results	81
5.4.1	Imaging of model organisms <i>ex vivo</i>	81
5.4.2	Electrical impulse response correction	82
5.5	All-optical optoacoustic microscope using an optical fiber detector	84
5.5.1	Motivation for optical sensors	84
5.5.2	Experimental setup	85
5.5.3	Characterization of the optical sensor	86
5.5.4	Imaging results	87
5.5.5	Summary and future plans	88
5.6	Conclusion and outlook	88

6	Integrated multiphoton and multiscale optoacoustic microscope (IMMSOM)	91
6.1	Introduction	91
6.2	Experimental setup	93
6.2.1	Optoacoustic microscope	93
6.2.2	RSOM modality	93
6.2.3	Multiphoton microscope	93
6.3	Characterization	95
6.3.1	Spatial resolution	95
6.3.2	Co-registration of the imaging volumes	96
6.4	Results	97
6.4.1	Multiscale optoacoustic zebrafish imaging	97
6.4.2	Hybrid mouse ear imaging	98
6.4.3	Hybrid zebrafish imaging	100
6.4.4	Hybrid human carotid atheroma imaging	101
6.5	Conclusion and outlook	103
7	Laser-scanning frequency-domain optoacoustic microscope (FD-OM)	105
7.1	Introduction	105
7.2	Theoretical background	107
7.2.1	Governing equations in the frequency-domain	107
7.2.2	SNR considerations	108
7.2.3	Principles of IQ-demodulation	110
7.3	Materials and methods	112
7.3.1	Experimental setup	112
7.3.2	Acquisition and image formation	112
7.3.3	Sample mounting and <i>in vivo</i> experiments	114
7.4	Characterization	115
7.4.1	Laser source	115
7.4.2	FOV and field distortion	116
7.4.3	Sensitivity field simulation for monofrequent excitation	116
7.5	Results	118
7.5.1	Suture phantom imaging and 3D reconstruction	118
7.5.2	SNR comparison to TD-OM	119
7.5.3	Zebrafish eye imaging <i>ex vivo</i>	119
7.5.4	Mouse ear vasculature imaging <i>in vivo</i>	120
7.5.5	Hybrid FD-OM and multiphoton mouse ear imaging <i>in vivo</i>	121
7.6	Conclusion and outlook	122
8	Visualization of microcirculatory blood flow <i>in vivo</i> with FD-OM	125
8.1	Motivation and status quo	125
8.2	Optoacoustic Doppler shift detection method	127
8.3	Characterization	128
8.3.1	Black varnish and moving transducer	128
8.3.2	Carbon particles flowing in a tube	129
8.3.3	Doppler shift calibration	130
8.4	Results	132
8.4.1	Blood flow monitoring during terminal experiment	132
8.4.2	Vessel flow profile and 2D blood flow map <i>in vivo</i>	133
8.5	Conclusion and outlook	135

9	Summary and conclusion	137
9.1	Conclusive summary	137
9.2	General outlook	140
A	MATLAB™ script for the simulation of optoacoustic signals	143
B	Numerical axial resolution simulation	147
C	Photographs of the optoacoustic microscopy systems	149
D	Published material and reprint permissions	151
	Acknowledgments	153
	List of publications	157
	Bibliography	159
	List of Figures	175
	List of Tables	179
	Index	181

List of abbreviations

α -MSH	α -Melanocyte-stimulating hormone
π -FBG	π -phase-shifted fiber Bragg grating
1D	1-dimensional
2D	2-dimensional
3D	3-dimensional
a. u.	Arbitrary units
ANSI	American national standard institute
APD	Avalanche photodiode
cAMP	Cyclic adenosine monophosphate
CCD	Charge-coupled device
CPS	Cumulative power spectrum
CRPI	Coherence-restored pulse interferometry
CT	Computed tomography
CW	Continuous wave
DAQ	Data acquisition
DC	Direct current
DNA	Deoxyribonucleic acid
DOCT	Doppler optical coherence tomography
dpf	Days post fertilization
DUS	Doppler ultrasound
EIR	Electrical impulse response
FD	Frequency-domain
FD-OM	Frequency-domain optoacoustic microscopy
FFT	Fast Fourier transform
FOV	Field of view
FPI	Fabry-Pérot interferometer

FWHM	Full width at half maximum
GPCR	G-protein-coupled receptor
GPU	Graphics processing unit
iFFT	Inverse fast Fourier transform
IMMSOM	Integrated multiphoton and multiscale optoacoustic microscope
LDI	Laser Doppler imaging
LED	Light-emitting diode
LO	Local oscillator
LSI	Laser speckle imaging
MAP	Maximum amplitude projection
MCH	Melanocyte-concentrating hormone
MFP	Mean free path
MIP	Maximum intensity projection
MORSOM	Multi-orientation raster-scan optoacoustic mesoscopy
NA	Numerical aperture
Norm.	Normalized
OM	Optoacoustic microscopy
OPS	Orthogonal polarization spectroscopy
PBS	Phosphate buffer saline
PC	Personal computer
PE	Pulse-echo
PMT	Photomultiplier tube
PSF	Point spread function
RBC	Red blood cell
rms	Root mean square
ROI	Region of interest
RSOM	Raster-scan optoacoustic mesoscopy
SEM	Standard error of the mean
SHG	Second-harmonic generation
SIR	Spatial impulse response

SNR	Signal-to-noise ratio
TD	Time-domain
TD-OM	Time-domain optoacoustic microscopy
TEM	Transverse electromagnetic
THG	Third-harmonic generation
TMFP	Transport mean free path
TOF	Time of flight
TPA	Two-photon absorption
TPEF	Two-photon excitation fluorescence
w.l.o.g.	Without loss of generality
WHSF	Weighted hyperbolic sensitivity field
WTF	Wildtype transplanted frog

1 Introduction

The answers to the big questions about the universe lie at the microscopic scale. It was not until the development of quantum mechanics that scientists could start to thoroughly explain many macroscopic observations, ranging from the interaction of light with matter to the large scale distribution of baryonic matter in the universe. Likewise, modern chemistry would not be possible without our current understanding of atomic and molecular structures and interactions.

In biology, the influence of the microscopic world is ubiquitous. The vast majority of living organisms, including bacteria and archaea, have sizes below 10 μm and thus elude direct observation [1]. Life in general is composed of micrometer-sized structural and functional units called cells and is governed by their structure, function and mutual interactions. Cells themselves contain an abundance of organelles and molecules that regulate many important biological processes, such as metabolism or signaling, and not least accommodate the blueprint of life: the DNA. It is in the end a distortion or malfunctioning of these cellular and sub-cellular processes that causes the majority of known diseases [2].

Driven by the desire to grasp the underlying principles of life, scientists have developed a vast collection of imaging techniques to uncover the microscopic biological world. This evolution started with the invention of the light microscope in the early 17th century, which allowed for the first time to observe microorganisms and cells, and culminated in the development of highly sophisticated modern methodologies, such as electron, atomic force or laser microscopy [1]. It is the latter that forms the general topical framework of the underlying thesis.

1.1 Laser microscopy in biological research

Laser microscopy is an implementation of optical microscopy that uses monochromatic laser sources for the illumination of the sample under investigation. In the majority of cases, a laser beam is tightly focused into the examined specimen and an image is created by raster-scanning of the focus within the sample, either mechanically or by using special scanning optics.

After the first experimental demonstration of a laser in 1960, it took almost three decades until these coherent light sources were successfully employed in optical microscopy [3]. In the following period, advances in laser and detector technologies, optical components and digital processing boosted the development of laser microscopy techniques. For the first time after centuries, microscopic examination was released from the requirement of micrometer-thick fixed tissue slices or transparent organisms including *C. elegans* or zebrafish (*Danio rerio*). Instead, modern approaches such as confocal or multiphoton microscopy allow for the imaging with micrometer or sub-micrometer resolutions hundreds of micrometers deep inside living tissue and revolutionized biological observation [4] (see section 2.4). Consequently, those modalities have become the tools of choice for a broad range of high-resolution *in vivo* studies including brain imaging [4], monitoring of morphogenesis [5], cancer research or ophthalmology [6].

1.2 The case for label-free imaging

The contrast in most of the commonly used laser microscopy techniques is based on fluorescence, which is generally imparted either through the use of exogenous agents or by employing genetically modified organisms that express certain fluorescent proteins (see section 2.3.1). After decades of discovery, fabrication and refinement of fluorescent labels, contemporary researchers can access an enormous pool of labels and stains to specifically target and visualize tissue components of interest. However, what undoubtedly poses one of the greatest assets of fluorescence based microscopy at the same time represents its weak point when it comes to *in vivo* imaging.

The reason for this is threefold. First, artificially added fluorescent molecules depend on several delivery related and microenvironmental parameters and can potentially interfere with physiological functions [7]. Second, the excitation light interacts strongly with both the tissue and the embedded fluorophores, a process that can result in altered molecules, such as reactive oxygen species or free radicals [8], which are known to be highly toxic for biological microenvironments (phototoxicity). Finally, such processes can lead to the chemical destruction of the fluorophores (photobleaching) [9], therefore setting limits on the total observation time (see section 2.3.6).

As a consequence, *in vivo* imaging schemes should ideally rely on label-free imaging. Whereas some multiphoton modalities such as second or third-harmonic generation microscopy (SHG and THG) visualize intrinsic contrast based on birefringence or optical inhomogeneity (see section 2.4.2), label-free imaging in fluorescence microscopy can generally be achieved by exploiting the naturally occurring autofluorescence ability of certain molecules. A recent technique to visualize endogenous optical absorption is optoacoustic (photoacoustic) imaging, which is increasingly applied in microscopy due to a number of unique features.

1.3 High-resolution optoacoustic imaging

Optoacoustic imaging is based on photoacoustic effect, i.e. the conversion of absorbed laser energy into heat, thereby generating acoustic waves that are commonly detected by ultrasound transducers [4] (see chapter 3). Because acoustic scattering in tissue is several orders of magnitude weaker than optical scattering, optoacoustic microscopy reaches penetration depths beyond the limits of traditional optical microscopy [10].

A key feature of high-resolution optoacoustic imaging is its scalability. In the case of focused laser illumination, the lateral resolution is defined by the optical focusing capabilities and is comparable to conventional microscopy. Consequently, this implementation is termed optical-resolution photoacoustic microscopy (OR-PAM) and is referred to as optoacoustic microscopy (OM) throughout this thesis. Even though the excitation photons are still prone to scattering, imaging depths of up to 1 mm are achieved due to the lower acoustic scattering [10]. On the other hand, if a broad illumination together with a focused ultrasound transducer is used, the lateral resolution is defined by the acoustic focusing abilities, which is typically in the order of a few tens of micrometers [11]. This implementation is also known as acoustic-resolution photoacoustic microscopy (AR-PAM) and referred to as optoacoustic mesoscopy in this work. The imaging depth of optoacoustic mesoscopy is mainly limited by optical absorption of the laser illumination and acoustic attenuation of the generated optoacoustic signals and can reach several millimeters in non-transparent tissue [12].

Because optoacoustic microscopy and mesoscopy visualize optical absorption with high sensitivity, they are ideally suited for the label-free imaging of endogenous tissue chromophores such as hemoglobin or melanin, but also other molecules depending on the excitation wavelength, including lipids or DNA¹ (see section 2.1.1) [13]. Furthermore, the use of several excitation wavelengths allows for the spectral differentiation of chromophores, which enables the extraction of metabolic parameters in *in vivo* experiments, such as the blood oxygen saturation based on the different absorption spectra of oxy- and deoxyhemoglobin [10].

Owing to the advantages of label-free visualization of absorption contrast, scalability and high penetration depth, high-resolution optoacoustic imaging has seen a tremendous evolution in terms of general performance, differentiation into specialized implementations and also the combination with other microscopy modalities (see section 6.1).

Recently, optoacoustic imaging has been also implemented in the frequency-domain, relying on intensity-modulated continuous wave (CW) lasers and the detection of monofrequent acoustic signals [14]. Frequency-domain optoacoustic microscopy (FD-OM) has the potential to employ cheap laser sources, thereby facilitating multi-wavelength illumination applications that can differentiate chromophores based on their spectral characteristics. Despite first successful applications [15, 16], FD-OM is still in its infancy and has so far not been demonstrated for label-free *in vivo* imaging or high-speed implementations.

1.4 Goals and objectives

The general ambition of this work is to push high-resolution optoacoustic imaging to a higher level. From a technological standpoint, the advancement of any existing imaging modality stands on three feet. First, the performance improvement of the modality itself, either by using better or different technology, or by establishing novel implementations. Second, the combination with other imaging techniques where the introduced modality enables new contrast or information to be visualized within traditional imaging frameworks. Third, the simplification of the existing approach leading to an improved handling or a reduction of costs. In this manner, the overall goal behind this thesis was fourfold:

- 1 Improvement and further development of existing high-resolution optoacoustic imaging techniques.
- 2 Combination of optoacoustic microscopy and mesoscopy with other optical microscopy techniques.
- 3 Development of novel optoacoustic microscopy implementations based on simple and cost-effective technologies.
- 4 Application of the high-resolution optoacoustic modalities to biological imaging.

Regarding the first three goals, the more specific objectives of this work involved:

- Improvement of the tomographic reconstruction used in raster-scan optoacoustic mesoscopy (RSOM) by incorporating a more realistic model of the detector geometry and by capitalizing on the broadband nature of optoacoustic signals.

¹ In principle, optoacoustic imaging can detect any molecule that exhibits sufficiently strong optical absorption, whereas fluorescence microscopy can only visualize molecules that relax the absorbed photon energy via fluorescence [10].

- Development of a method to measure the electrical impulse response (EIR) of high-frequency transducers and to correct optoacoustic measurements for the detector frequency response.
- Building of a transmission-mode optoacoustic microscope that enables biological imaging with micrometer resolution.
- Combination of the developed optoacoustic microscope with multiphoton microscopy to enable the concurrent visualization of complementary label-free contrast in biological specimens.
- Integration of RSOM into the developed hybrid microscope to allow for multimodal imaging at different geometrical scales.
- Development of a fast laser-scanning implementation of FD-OM that allows for *in vivo* imaging of mouse ear vasculature and combining it with the existing multiphoton microscope.
- Implementation of Doppler shift detection capabilities with FD-OM to enable flow measurements.

Concerning the fourth goal, the following questions regarding the application of the developed high-resolution optoacoustic modalities to biological imaging were addressed:

- Can RSOM monitor melanophore dynamics in living zebrafish and can such dynamic cellular responses be identified as signatures in the optoacoustic frequency spectra?
- Is RSOM capable of monitoring dynamic responses of externally stimulated xenotransplanted melanophores in juvenile or adult zebrafish *in vivo*?
- Can the detection of Doppler shifts from flowing particles with FD-OM be used to visualize microcirculatory blood flow *in vivo*?

1.5 Structure of the thesis

The different chapters of this thesis present and discuss several aspects of high-resolution optoacoustic imaging, such as development, improvement, characterization and application of mesoscopic and microscopic modalities in various implementations. For this reason, each chapter starts with an own introduction providing the overall motivation and state of the art for the specific project discussed, and finishes with an individual conclusion and outlook.

The overall theoretical background for the underlying mechanisms of laser microscopy that are relevant for this work is provided in chapter 2. Additionally, the most important concepts and hardware components used in laser microscopy are discussed, serving as a reference for the following chapters. Chapter 2 finishes with an introduction to confocal fluorescence, multiphoton and light sheet fluorescence microscopy, on the one hand to provide a reference frame for the covered optoacoustic techniques, and on the other hand to establish the foundation for the multiphoton microscopy modalities described in this work.

The theoretical foundation of optoacoustic imaging in general and optoacoustic mesoscopy in particular is given in chapter 3. In the second half of this chapter, the RSOM modality

is introduced and the developed reconstruction algorithm incorporating a more realistic detector model is described and compared to the original reconstruction method. Furthermore, the concept of multi-frequency reconstruction is introduced and the performance compared to the traditional full-bandwidth reconstruction scheme.

In chapter 4 the RSOM modality is applied to the *in vivo* monitoring of endogenous melanophore dynamics in zebrafish larvae and the readout of hormonal stimulation of xenotransplanted frog melanophores in juvenile zebrafish. A frequency analysis for the identification of cell dynamics related signatures is presented, applied to the *in vivo* data and compared to simulations of expanding and contracting optoacoustic absorbers.

After the previous two chapters were dedicated to optoacoustic mesoscopy, chapter 5 presents the development of a transmission-mode optoacoustic microscope. In the beginning, an introduction to optoacoustic microscopy is given. Subsequently, the OM system is described and the characterization of the laser source, ultrasound transducer as well as the spatial resolution is presented. Additionally, the system is used to measure the electrical impulse response (EIR) of the transducer, which is further utilized to correct the measured signals for the finite frequency response of the detector. Next, *ex vivo* imaging results of a mouse ear and a zebrafish larva are shown. In the final part of chapter 5, all-optical optoacoustic microscopy of model organisms *ex vivo* is demonstrated using an optical fiber detector.

In chapter 6, the combination of the developed OM system with transmission-mode RSOM as well as multiphoton microscopy incorporating two-photon excitation fluorescence (TPEF), second-harmonic generation (SHG) and third-harmonic generation (THG) microscopy is presented. After characterizing the resolution and the co-alignment of scanning volumes of the different modalities, the simultaneous mesoscopic and microscopic optoacoustic imaging of a zebrafish larva *ex vivo* is demonstrated. Afterwards, the full multiscale and multimodal visualization capabilities of the system are showcased on the label-free imaging of a mouse ear and a zebrafish larva *ex vivo*. Finally, the hybrid system is used to image a human carotid atheroma slice without any staining.

The last part of this thesis is concerned with the development and application of laser-scanning frequency-domain optoacoustic microscopy (FD-OM). Chapter 7 introduces the system, discusses the characterization and image formation principles and presents imaging results of a zebrafish eye *ex vivo* and mouse ear vasculature *in vivo*. Moreover, the combination of the FD-OM modality with the existing multiphoton microscopy system is demonstrated by the hybrid label-free imaging of a mouse ear *in vivo*.

In chapter 8, the FD-OM system is used for the detection of Doppler shifts from flowing absorbers. After discussing the relationship between optoacoustic Doppler shifts and flow, different Doppler shift detection schemes are introduced, demonstrated on phantoms and compared. The established approach is then used to measure microcirculatory blood flow in mouse ears *in vivo* and to create a 2D map of blood flow direction in the ear.

Finally, the thesis is summarized in chapter 9 based on the four main goals defined in the previous section and a general outlook of high-resolution optoacoustic imaging is given.

2 Principles of laser microscopy

This chapter provides the theoretical background of light matter interactions (section 2.1) and introduces the relevant concepts of optical laser microscopy (section 2.2). Furthermore, the most important components of laser microscopes as well as the basics of fluorescence microscopy are introduced (section 2.3). Many of these concepts will be taken up in later chapters during the discussion of the developed optoacoustic microscopy modalities. The final part gives an overview of the most commonly used laser microscopy techniques for deep tissue imaging that operate in a similar resolution and penetration depth regime as optoacoustic microscopy (section 2.4). The chapter is concluded with a brief discussion about mesoscopic imaging (section 2.5), leading over to the following chapter about optoacoustic mesoscopy.

2.1 Interaction of light with matter

All optical laser microscopy techniques are based on the interaction of light with the examined sample, involving specific optical processes and the subsequent readout of light or other forms of signals originating from the sample as a result of this interaction. Generally, when electromagnetic radiation enters a medium, its time-varying electromagnetic fields interact with the atoms of the constitutive matter¹. This interaction can affect the incident photons in essentially five different ways (see Figure 2.1). First, photons might get absorbed by depositing their energy in the medium. Second, light can undergo scattering by single particles, molecules or small structures, thereby changing its original direction. Scattering can be either elastic or inelastic, where the latter involves a partial transfer of the photon energy to the medium. Third, light gets bent around objects having a size in the order of the wavelength, a process called diffraction. Finally, whenever light encounters a change in refractive index, it is totally or partially reflected

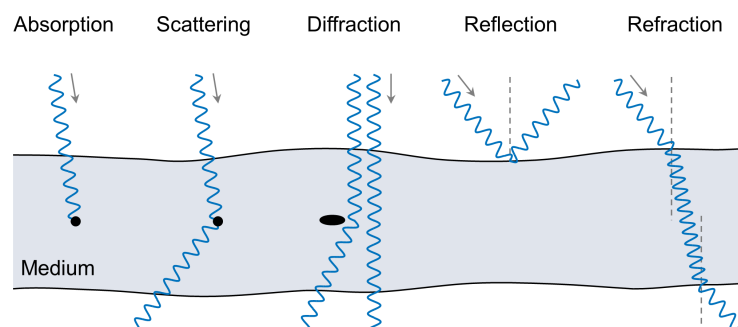


Figure 2.1: Basic interactions between light and matter.

¹ This section is based on [12, 14, 18–20].

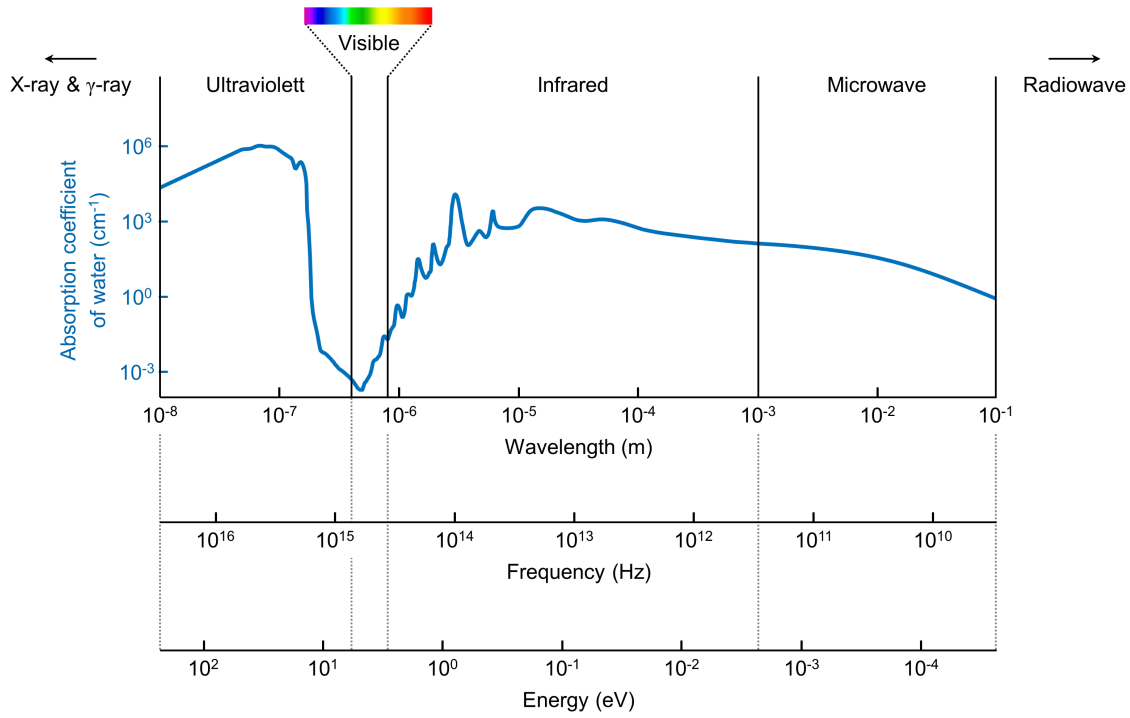


Figure 2.2: Absorption coefficient of water at different regions of the electromagnetic spectrum. (Data taken from [17].)

and, in case of an oblique incident angle, changes its direction through refraction². As opposed to charged particles that gradually lose energy when traversing matter, uncharged photons undergo abrupt absorption and scattering processes. Therefore, a beam of photons traveling through a medium does not change its energy spectrum but the intensity is exponentially attenuated as a function of the propagation distance x , as described by the Beer-Lambert law

$$I(x) = I_0 e^{-\mu_e x}. \quad (2.1)$$

Here, I_0 denotes the initial intensity at $x = 0$ and μ_e is the extinction coefficient (cm^{-1}). The inverse of μ_e is referred to as mean free path (MFP) and determines the average distance a photon can travel in a medium until it interacts with an object and is thereby removed from its original path. The extinction coefficient represents the sum of the absorption coefficient μ_a and scattering coefficient μ_s and is defined as

$$\mu_e = \mu_a + \mu_s = \sum_i n_i \sigma_i, \quad (2.2)$$

where σ_i represents the cross section (cm^2) of the interaction process i and n_i denotes the number density of the corresponding absorbers or scatterers (cm^{-3}).

² In fact, reflection, refraction and diffraction are closely related to scattering as those effects result from a superposition of incident and scattered electromagnetic waves from an ensemble of scatterers [21]. Consequently, the following discussion will be restricted to absorption and scattering in general.

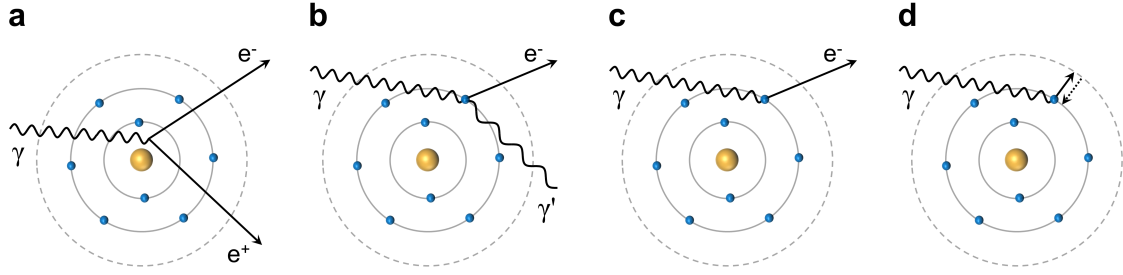


Figure 2.3: Light-matter interaction processes with atoms at high photon energies ($E_\gamma \gtrsim 1$ eV). (a) Pair production. (b) Compton scattering. (c) Photoelectric effect. (d) Electronic excitation and de-excitation. Yellow spheres: atomic nuclei. Blue spheres: bound electrons.

2.1.1 Absorption

Absorption of light can occur through a number of mechanisms, depending on the properties of the absorber material and the energy of the incident photons. Figure 2.2 shows the absorption spectrum of water at different regions of the electromagnetic spectrum. In the following, the different absorption processes in the respective spectral regimes will be discussed based on the example of the water absorption spectrum, since water represents the most abundant molecule in the majority of tissues.

Gamma and X-ray region

In the γ -ray region where the photon energies E_γ exceed twice the rest energy of the electron ($E_\gamma > 2m_e c^2 \approx 1022$ keV; m_e : electron rest mass, c : speed of light in vacuum), pair production can occur. In this process, a photon is converted into an electron-positron pair, which is emitted under 180° in the resting frame of the photon (see Figure 2.3(a)). Furthermore, pair production only takes place in the vicinity of nuclei because of momentum conservation. The cross section can be approximated by

$$\sigma_{pair} \propto Z^2 \ln(E_\gamma), \quad (2.3)$$

where Z denotes the atomic number, $E_\gamma = h\nu$ represents the photon energy, h denotes the Planck constant and ν refers to the frequency of the photon.

A second process, which is especially relevant at lower energies in the X-ray regime, is Compton scattering³. This process represents the inelastic scattering of photons by free or weakly bound charged particles, where the directions and wavelengths of the incident photons are altered (see Figure 2.3(b)). In the case of scattering by a bound electron, the atom gets ionized by the photon, which typically has a much higher energy than the binding energy of the electron. For energies above ~ 100 keV, the Compton scattering cross section is approximately given by

$$\sigma_{compt.} \propto \frac{1}{E_\gamma}. \quad (2.4)$$

³ Even though Compton scattering is not an absorption process, it is traditionally discussed together with pair production and the photoelectric effect and is therefore mentioned here.

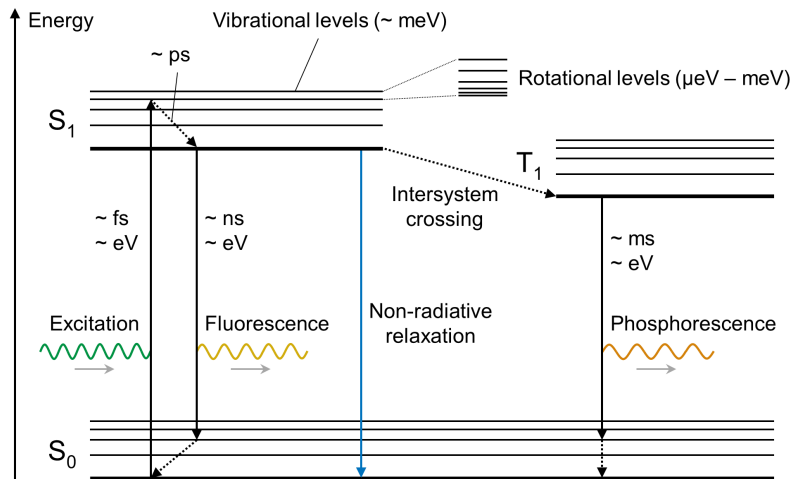


Figure 2.4: Jablonski diagram of electronic excitation and the most common de-excitation processes. S_0 : Ground state. S_1 : First excited singlet state. T_1 : First excited triplet state. Only the first excited states are shown, whereas typical values for the lifetimes and associated energies of the different processes are provided. The blue arrow indicates electronic de-excitation via non-radiative relaxation, which is the mechanism responsible for optoacoustic signal generation.

Ultraviolet region

At lower photon energies ranging from approximately 3 eV to 120 keV, the dominating absorption process in water is the photoelectric effect, i.e. the ejection of a bound electron from an atom by the absorbed photon (see Figure 2.3(c)). This process can only occur in bound electrons for momentum conservation reasons and requires a photon energy higher than the binding energy of the electron (typically a few eV). The cross section of the photoelectric effect can be written as

$$\sigma_{PE} \propto \frac{Z^2}{E_\gamma^3}, \quad (2.5)$$

showing a strong dependency on Z . Thus, the range where the photoelectric effect dominates absorption varies with the material properties, as opposed to Compton scattering.

Visible region

In the visible region of the electromagnetic spectrum, absorption in water is significantly lower, which is the reason for its high visible transparency. The relevant photon absorption mechanism in this regime is the elevation of an electron (usually a valence electron) to an excited state, followed by a transition back to the original energy level (see Figure 2.3(d)). The electrons bound in atoms or molecules can only take on discrete energy levels (quantization) and the photon energy therefore has to exactly match the energy difference between two states to elevate an electron. In the case of molecules, the principal energy levels are further subdivided into vibrational energy levels and, if the molecules exhibit a net electric dipole moment, rotational states. According to the Franck–Condon principle, electronic transitions are instantaneous compared to nuclear displacements because of the huge mass difference. Therefore, the excitation and de-excitation processes in molecules will take place into vibrational levels with the highest overlap of the corresponding

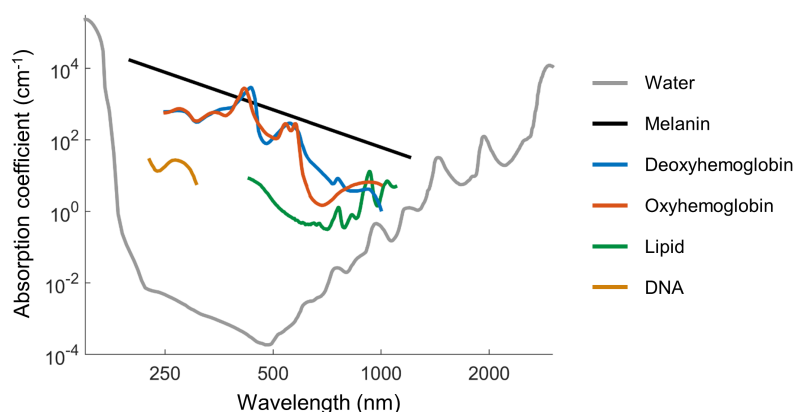


Figure 2.5: Absorption spectra of the most abundant tissue chromophores. Gray: Water [17]. Black: Melanin [22]. Blue: Deoxyhemoglobin. Red: Oxyhemoglobin [23]. Green: Lipid [24]. Orange: DNA [25].

waveforms, which normally do not coincide with the lowest or highest levels in the vibrational bands [26].

Following the elevation of an electron from the ground state S_0 to an excited state (e.g. the first excited singlet state S_1) through light absorption, the de-excitation can occur via different mechanisms. The most relevant de-excitation processes are summarized by the Jablonski diagram shown in Figure 2.4. The electronic excitation occurs on a timescale of femtoseconds and typically lifts an electron to one of the higher vibrational levels of an excited state. Subsequently, the electron relaxes within picoseconds to the lowest vibrational level of the excited state via non-radiative vibrational relaxation (and internal conversion if a non-radiative transition between different energy states is involved, e.g. from S_2 to S_1) and heat dissipation. Generally, the de-excitation through the emission of a photon is called photoluminescence. In its most common form, the transition occurs between two singlet states (e.g. from S_1 to S_0). This incoherent process is called fluorescence and has a lifetime in the order of nanoseconds. Due to the vibrational relaxation processes before and after the transition, the emitted photon has a lower energy than the absorbed photon (Stokes shift). An important quantity in fluorescence is the quantum yield, which represents the ratio of the number of photons emitted to the number of photons absorbed.

It can happen that the excited molecule undergoes a transition from a singlet to a triplet state T_1 (intersystem crossing), which is characterized by a total spin of 1 and a lower energy. Consequently, the relaxation into the singlet ground state S_0 involves a change in spin, which is classically forbidden by quantum mechanical selection rules. Because of the spin-orbit coupling of the excited electron, the transition from T_1 to S_0 will occur eventually, albeit with a relatively long lifetime in the range of milliseconds to seconds [26]. The corresponding radiative de-excitation process is called phosphorescence and yields, similarly to fluorescence, an emitted photon with lower energy than the absorbed photon. Alternatively, the excited molecule can transform back to the ground state via non-radiative relaxation. This process does not yield the emission of a photon but takes place through heat dissipation, which is the relevant mechanism for optoacoustic signal generation (see chapter 3).

Even though the absorption coefficient of water is relatively low in the visible range (see Figure 2.2), many tissue constituents exhibit strong optical absorption in this regime. Figure 2.5 compiles the absorption spectra of the most prominent tissue chromophores in

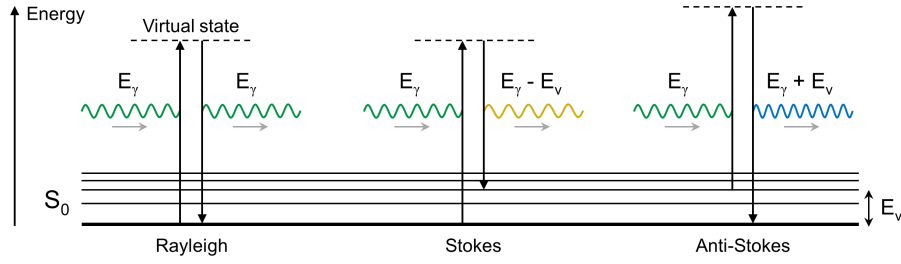


Figure 2.6: Jablonski diagram of molecular scattering processes.

the visible range. As can be seen from the spectra, melanin and hemoglobin represent the strongest optical absorbers. At the same time, both melanin and hemoglobin have a fluorescence quantum yield of less than 1% [27, 28], rendering them strong endogenous contrast agents for optoacoustic imaging.

In the spectral region between $\sim 600\text{--}1300\text{ nm}$, optical absorption in tissue is relatively low compared to shorter and longer wavelengths where hemoglobin and water limit the penetration of light due to absorption, respectively. This region is referred to as optical window and is used by many imaging techniques to visualize deeper structures in tissue.

Infrared region

As already mentioned previously, molecules exhibit vibrational energy levels corresponding to distinct modes of vibrational movements, such as stretching or bending of the different molecular bonds. The associated energies are in the range of meV and can thus be excited by infrared radiation. The vibration spectrum typically features a series of distinct peaks that are characteristic for the molecular structure of the absorbing medium. More specifically, a molecule with n atoms has $3n$ degrees of freedom, 6 of which correspond to rotations and translations, and thus features $3n-6$ vibrational modes ($3n-5$ in the case of linear molecules). The exact frequency and strength of the individual vibrational modes depends on the molecular structure, environment and quantum mechanical selection rules. In the water spectrum, the vibrational peaks are located mainly in the range of $1\text{--}10\ \mu\text{m}$.

Microwave region

Finally, at sufficiently low photon energies in the μeV to meV microwave range, rotational movements of polar molecules are excited. The absorbed energy is dissipated as heat through frictional motion, which represents the working principle of microwave ovens.

2.1.2 Scattering

Photon scattering refers to the deflection of light from its original path and can be either elastic (i.e. the energy of the scattered photon does not change) or inelastic (energy is lost or gained by the scattered photon). Figure 2.6 illustrates the most relevant processes of optical scattering by molecules. The elastic scattering of light by structures much smaller than the wavelength (e.g. atoms, molecules or nanoscale structures) is generally referred to as Rayleigh scattering and is characterized by a strong dependence of the scattering cross section on the photon wavelength λ :

$$\sigma_{Rayleigh} \propto \frac{1}{\lambda^4}. \quad (2.6)$$

Photons undergoing Rayleigh scattering are emitted in all directions with equal probability. The scattering process can be described by an excitation of an electron to a virtual state⁴ followed by a transition back to the ground state via the re-emission of a photon with the same energy. Alternatively, the relaxation from the virtual state can potentially end up at a higher vibrational energy level (Stokes scattering). The emitted photon carries therefore a lower energy than the original photon, which is reduced by the energy of the higher vibrational level. Conversely, if the excitation to the virtual state occurs from a higher vibrational level and the relaxation ends up at a lower level or the ground state, the emitted photon will have a higher energy than the incident photon (anti-Stokes scattering). The latter two inelastic scattering processes are referred to as Raman scattering and have a cross section that is several orders of magnitude weaker than the one for elastic scattering [30].

Finally, light scattering from objects of any size is described by the Mie theory, which simplifies to the previously introduced Rayleigh scattering in the limit of small scatterers. In contrast to Rayleigh scattering, Mie scattering (i.e. the scattering from objects comparable to or larger than the photon wavelength) is relatively independent of the wavelength but dominates in the forward direction. Generally, the scattering of light in biological tissue originates from various structures with different sizes, depending on the tissue type. In soft tissue, the main contribution arises from Mie scattering by larger constituents in the μm range, such as cells, nuclei, mitochondria or organelles. Nanometer scale structures including collagen fibrils or cell membranes on the other hand contribute to Rayleigh scattering and can dominate light scattering in fibrous tissue such as skin [31].

2.2 Basic optical concepts

The following sections establish and discuss the fundamental concepts of optical imaging that are relevant to the imaging systems developed in this work and are based on [21, 26, 30, 32].

2.2.1 Gaussian optics

The beams of most laser sources used in optical microscopy have an approximate Gaussian intensity profile, as depicted in Figure 2.7(a). Such laser beams are called Gaussian and represent the fundamental (TEM_{00}) mode of the laser resonators. Unlike in geometrical optics, Gaussian beams cannot be perfectly collimated but will eventually diverge, which is a fundamental result of light diffraction. However, in practical applications with finite beam paths, the divergence can often be neglected and the beam treated as being collimated. Another fundamental diffractive property is that Gaussian beams cannot be focused to an infinitely small spot⁵ but rather feature a finite radius at the focal spot referred to as the beam waist ω_0 . Figure 2.7(b) illustrates the geometry of a focused Gaussian beam, where the blue lines represent the beam diameter as defined by the $1/e^2$ level of the intensity profile. For a given laser wavelength λ , the beam waist fully

⁴ It should be mentioned that virtual states occur from time-dependent perturbation theory and are not real states that correspond to stationary solutions of the time-independent Schrödinger equation. Thus, virtual states do not possess a well-defined energy eigenvalue and their lifetime is determined by the uncertainty principle [29].

⁵ Compared to other beam profiles, Gaussian beams are characterized by minimum divergence and minimum focal spot size.

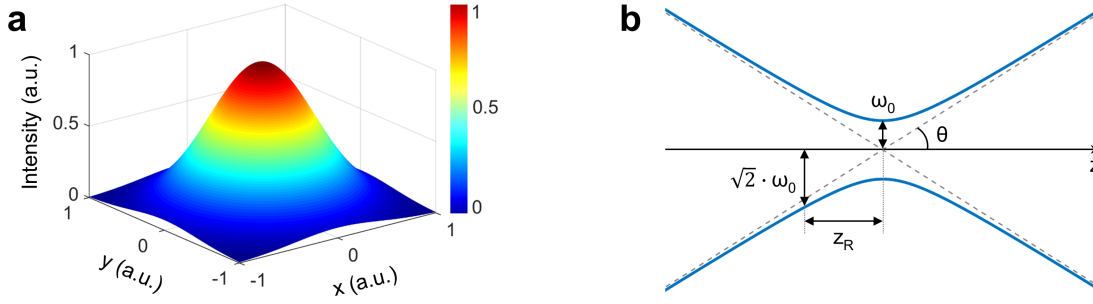


Figure 2.7: Shape and geometry of Gaussian beams. (a) Transverse cross sectional intensity profile. (b) Geometry of a focused Gaussian beam.

determines the far-field divergence angle

$$\theta \approx \frac{\lambda}{\pi \omega_0} \quad (2.7)$$

and the depth of focus (or confocal parameter)

$$b = 2 z_R = \frac{2 \pi \omega_0^2}{\lambda} \quad (2.8)$$

of a perfect Gaussian beam⁶. Here, z_R denotes the Rayleigh length, which is defined as the axial distance from the focus for which the beam radius becomes $\sqrt{2} \cdot \omega_0$.

For the transition of Gaussian beams through optical elements such as lenses, the relationships from geometrical optics can still be used in many cases. However, due to the finite diameter of the beams, diffraction effects have to be considered. For example, Gaussian beams cannot be focused to infinitely small points. Instead, the waist of a beam focused by a lens can be expressed as

$$\omega_0 \approx \frac{2 f \lambda}{\pi d}, \quad (2.9)$$

where f denotes the focal distance of the lens and d represents the diameter of the beam incident on the lens. As can be seen from this relationship, the waist of a focused beam can be reduced either by using a lens with shorter focal distance f or by increasing the initial beam diameter d . The latter can be achieved by an arrangement of lenses that form a so-called beam expander.

Beam expansion

The most commonly used beam expander in optical microscopy is the Keplerian telescope⁷. As schematically depicted in Figure 2.8, such a beam expander consists of a set of collimation lenses with coinciding focal planes at the distances f_1 and f_2 . According to

⁶ For real laser sources, the divergence as well as the beam waist is increased by a factor $M^2 > 1$, which is referred to as the beam quality of a laser.

⁷ An alternative design is the Galilean telescope, which uses a diverging lens as the first lens. This implementation is shorter than the Keplerian design and avoids the focusing of the beam between the two lenses, which can be problematic in high-intensity laser applications.

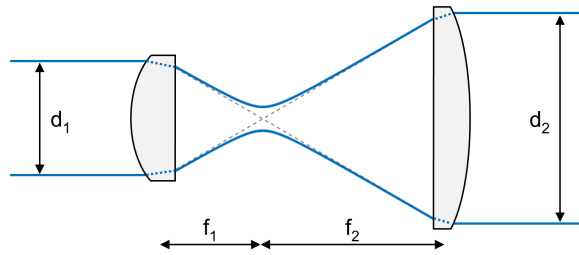


Figure 2.8: Optical path of a Keplerian beam expander. The gray shapes represent plano-convex collimation lenses.

the rules of geometrical optics, the ratio of the beam diameters d_1 and d_2 is equal to the ratio of the focal distances:

$$\frac{d_1}{d_2} = \frac{f_1}{f_2}. \quad (2.10)$$

Hence, the diameter of Gaussian laser beams can be reduced or increased by choosing an appropriate combination of collimation lenses. Additionally, the divergence of an expanded beam is reduced by the expansion factor, as can be seen from Eq. (2.7).

Spatial filtering

An advantage of Keplerian beam expanders is the occurrence of a beam focus between the lenses. This feature can be utilized to spatially filter the laser beam by means of a pinhole, as depicted in Figure 2.9. Usually, the intensity profiles of laser beams are not perfectly Gaussian but deviate from the TEM_{00} profile due to resonator imperfections or because of dust particles and scratches on the optical elements in the beam path. Such distortions introduce interference patterns on top of the Gaussian beam profile. However, the focusing quality of a microscope depends on how much the beam deviates from a perfect Gaussian profile.

Generally, the beam intensity profile at the focal plane of a lens represents the Fraunhofer diffraction pattern for a circular aperture and corresponds to the spatial Fourier transform of the incident beam profile. Because the interference patterns of an imperfect beam usually exhibit higher spatial frequencies than the underlying Gaussian profile, the imperfections will produce intensity patterns outside of the central lobe. On the other hand, the spatial Fourier transform of a Gaussian is again a Gaussian and thus the TEM_{00} mode will stay in the center of the beam focus. If the diameter of the pinhole is chosen appropriately, the Gaussian peak is allowed to be transmitted, whereas the higher spatial frequencies originating from the imperfections are blocked. Consequently, little energy is lost while a smooth Gaussian profile is restored through the spatial filtering.

2.2.2 Spatial resolution

In optical imaging systems, spatial resolution describes the ability to discern structures that are located at a close distance to each other as separate objects. In this context, the spatial resolution corresponds to the minimum distance that two similar point sources can be separated to still be resolvable as being distinct. Besides the blurring effects of optical imperfections, aberrations or misalignment, the spatial resolution in optical microscopy is fundamentally limited by diffraction. For this reason, light cannot be focused to an infinitely small point and perfect point sources cannot be imaged as infinitely small points.

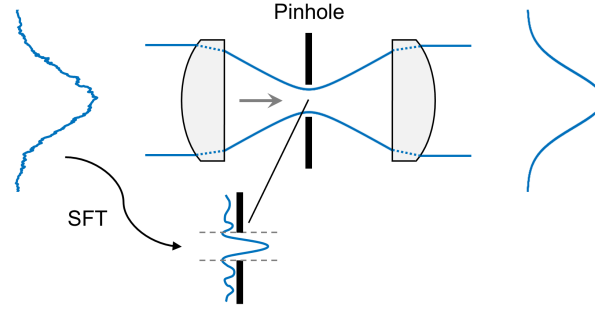


Figure 2.9: Spatial filtering of a Gaussian beam with a pinhole. SFT: Spatial Fourier transform.

The point spread function (PSF) is the response of an imaging system to a point source and fully characterizes the spatial resolution of the system by the extent of blurring of the imaged source. In the case of an imaging system with focused illumination, detection or both, the transverse PSF has the shape of a round spot surrounded by concentric rings and is called Airy pattern. Figure 2.10(a) illustrates the Airy disk (central lobe) and the first ring of a 2D transverse PSF. The intensity of the Airy pattern as a function of the radial distance r to the center is given by

$$I_{lat}(r) = I_0 \left| \frac{2 J_1(\zeta)}{\zeta} \right|^2, \quad (2.11)$$

where I_0 denotes the peak intensity of the central lobe, J_1 represents the Bessel function of first order and $\zeta = NA \cdot 2\pi r/\lambda$. The numerical aperture

$$NA = n \sin(\theta) \quad (2.12)$$

determines the ability of an optical component such as a lens or a microscopy objective lens to focus and collect light. Here, θ denotes the half opening angle of the light cone transmitted or collected through the lens and n denotes the refractive index of the immersion medium. A cross sectional profile through the center of the Airy pattern is shown by the blue curve in Figure 2.10(b). According to the Rayleigh criterion, two point sources are just resolvable if the maximum of the first PSF coincides with the first minimum of the second PSF. Thus, the radial location of the first minimum defines the lateral resolution according to the Rayleigh criterion as

$$R_{lat, Rayleigh} = 0.61 \frac{\lambda}{NA}. \quad (2.13)$$

Figure 2.10(c) depicts the summed intensity profile (blue curve) of two point sources (dotted gray curves) resolved by the Rayleigh criterion. The central dip has an intensity value of $\sim 74\%$ of the maximum.

However, because the first ring of the Airy pattern is difficult to measure due to its low intensity, the PSF is typically approximated as a Gaussian function with a standard deviation of $\sigma \approx 0.21 \lambda/NA$. The dotted red curve in Figure 2.10(b) shows the Gaussian approximation matching the central lobe of the Airy disk. In the case of Gaussian PSFs, the resolution criterion is usually chosen according to the full width at half maximum

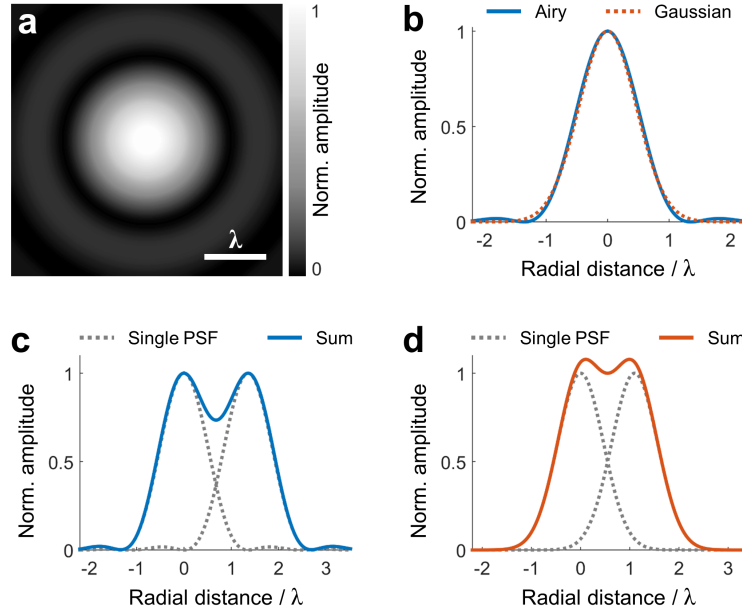


Figure 2.10: Point spread function and resolution. (a) Airy pattern representing the 2D transverse point spread function (PSF) of a focused imaging system. (b) Cross sectional profile of the Airy disk (blue curve) and Gaussian approximation of the central lobe (red dotted curve). (c) Summed intensity profile (blue curve) of two point sources (gray dotted curves) with a distance according the Rayleigh criterion. (d) Summed intensity profile (red curve) of two point sources (gray dotted curves) with a distance corresponding to the full width at half maximum (FWHM) of their Gaussian PSFs.

(FWHM) of the Gaussians. Consequently, two point sources are considered just resolvable if their radial distance corresponds to the FWHM of the PSF, which can be expressed as

$$R_{lat,FWHM} = 0.51 \frac{\lambda}{NA}. \quad (2.14)$$

The summed intensity profile (red curve) of two Gaussian PSFs with a distance of one FWHM is shown in Figure 2.10(d). Compared to the Rayleigh criterion, the central dip that defines the discernability of the point sources is shallower and has an intensity of $\sim 93\%$ of the maximum. This latter definition will be used for lateral resolution estimations throughout this work.

Finally, the intensity function of the axial PSF as a function of the axial distance z to the center is given by

$$I_{ax}(z) = I_0 \operatorname{sinc}^2\left(\frac{\xi}{4\pi}\right), \quad (2.15)$$

where $\operatorname{sinc}(x) \equiv \sin(\pi x)/\pi x$ and $\xi = 2\pi NA^2 z/n\lambda$ [33]. From Eq. (2.15), the axial resolution according to the Rayleigh criterion for the special case of two axially separated identical point sources can be defined as

$$R_{ax,Rayleigh} = \frac{2n\lambda}{NA^2}, \quad (2.16)$$

which is in the order of the confocal parameter b as defined by Eq. (2.8).

2.2.3 Optical aberrations

In laser microscopes, a combination of several optical components, such as lenses, mirrors, filters and objective lenses, are used to guide and focus the illumination into the examined object and to retrieve the optical signals from the sample for detection. These optical components inevitably introduce imperfections and aberrations to the system, which can be partially but not completely eliminated by proper alignment and the use of specialized components. Optical aberrations fall into two main categories: geometrical and chromatic aberrations.

In the first category, the most relevant aberrations include spherical aberrations, curvature of the imaging field and image distortions. Spherical aberrations occur in lenses because light rays passing at the periphery experience stronger refraction than rays passing through the center. Hence, peripheral and central light rays do not coincide at the same focal plane. Most microscope objectives are corrected for spherical aberrations by the use of additional correction lenses. In Keplerian beam expanders, spherical aberrations are reduced by orienting the plano-convex collimation lenses in such a way that the flat surfaces point towards the intermediate beam focus.

Field curvature distortions describe the effect that the focal distance of a lens decreases with an increased incident angle of passing light. Therefore, the focal plane is not flat but bent and, thus, flat extended objects cannot be brought into focus. Again, this aberration is compensated for in most microscope objectives (commonly denoted by the label 'plan'). Finally, image distortions become noticeable as rotationally symmetric changes in the shape of images, i.e. straight lines that do not cross the center are bent inwards (pincushion distortion) or outwards (barrel distortion). This effect is especially relevant for laser-scanning applications, where the distance between the scan unit and the imaging plane depends on the scan angles [34].

In imaging applications where several wavelengths are detected or used for illumination, chromatic aberrations have to be considered. The origin of chromatic aberrations is the dependency of the refractive index of optical elements on the light wavelength (dispersion). Typically, shorter wavelengths experience stronger refraction than longer ones, resulting in a shorter focal distance. The simplest way to correct for chromatic aberrations is the combination of a convex and a concave lens with different refractive indices. Such a doublet is called 'achromat' and corrects chromatic aberrations for two wavelengths. Microscopy objectives where chromatic aberrations are corrected for three to five wavelengths are referred to as 'fluorite' or 'apochromat' and are normally used for multiwavelength applications [35].

2.2.4 Imaging depth

The spatial resolution of most of the commonly used laser microscopy techniques relies on the ability to tightly focus laser light into the examined sample. However, the strong scattering of visible light in tissue rapidly degrades the focusing capability with increasing penetration depth. According to the way that light is scattered at different depths in tissue, three regimes can be defined.

Within the ballistic regime, most photons travel unscattered along straight lines or undergo only one scattering event and can be focused to nearly diffraction limited spots. The range of the ballistic regime is defined by the mean free path (MFP) of the imaged tissue, which represents the average photon traveling distance between two interaction events [4]. Since scattering in most tissues is much stronger than absorption, the total

MFP is approximately equal to the scattering MFP, which is defined as the inverse of the scattering coefficient:

$$MFP \approx \frac{1}{\mu_s}. \quad (2.17)$$

The MFP marks the boundary of the ballistic regime and is in the order of 100 μm in most tissues.

In the quasi-ballistic regime beyond one MFP, photons increasingly experience multiple scattering events and start to get randomized with depth. However, since forward-directed Mie scattering by micrometer sized organelles such as nuclei or mitochondria dominates in most tissues, quasi-ballistic photons are still directive. The mean propagation distance before photons on average lose their initial directivity is referred to as transport mean free path (TMFP), which is defined as

$$TMFP \approx \frac{1}{\mu_s(1-g)}, \quad (2.18)$$

where g denotes the anisotropy factor accounting for the degree of forward scattering [4]. In tissue, typical values of g range between 0.8 and 0.99 [36] and the TMFP is in the order of 1 mm.

After one TMFP, light propagation becomes diffusive and completely randomized. This regime is called diffusive regime and the TMFP is also known as the optical diffusion limit.

Conventional microscopy techniques such as brightfield and widefield fluorescence microscopy are limited to a depth of a few tens of micrometers within the ballistic regime. Certain microscopy approaches achieve penetration depths within the quasi-ballistic regime of several hundreds of micrometers by performing optical sectioning (e.g. confocal, multiphoton and selective plane illumination microscopy). However, microscopic imaging beyond the optical diffusion limit is typically not feasible with pure optical modalities. On the other hand, optoacoustic microscopy relies on the detection of ultrasound, which experiences orders of magnitude less scattering than light and can thereby achieve penetration depths in the order of one TMFP (see chapter 5).

2.2.5 Field of view

The field of view (FOV) of a microscopy modality depends first and foremost on the scanning method. In approaches that use a mechanical scanning of the sample or the detection unit, the FOV can be in principle arbitrarily large (within the range of the scanning stages). However, in order to properly visualize the sample with the maximum resolution, the Nyquist–Shannon sampling theorem requires a spatial sampling step size smaller than half of the achieved spatial resolution [30]. Therefore, a bigger FOV comes at the cost of longer acquisition times in mechanical scanning. In widefield microscopy modalities as well as in approaches using scanning mirrors or other beam deflection devices, the maximum FOV is determined by the magnification of the objective lens (and the applicable scanning angles). A higher magnification results in a smaller FOV and vice versa. Such modalities usually achieve FOVs in the order of tens to hundreds of micrometers but enable much faster imaging than mechanical scanning methodologies. In order to achieve bigger FOVs while at the same time limiting the acquisition time, hybrid scanning schemes can be employed.

2.3 Background on fluorescence microscopy

This section discusses the basic principles of fluorescence microscopy with a focus on laser excitation and is based on [37,38]. Furthermore, the most important components of fluorescence microscopes are introduced, which will be again taken up later in the descriptions of the developed optoacoustic systems.

2.3.1 Fluorescent labels

Fluorescence microscopy is based on the detection of fluorescence light emitted from the examined specimen after excitation with a white-light source (typically xenon arc or mercury-vapor lamps) or a laser. The structures of interest within the sample are usually labeled with fluorescent markers, either through direct binding (e.g. DAPI or Hoechst stains binding to DNA) or via specialized antibodies that tag biomolecules of interest. Additionally, biological specimens can be genetically modified to express fluorescent proteins (e.g. green fluorescent protein (GFP)) at specific sites. A key feature of fluorescence microscopy is its high specificity, as the detected fluorescence originates mainly from the fluorescent markers, whereas the background is efficiently suppressed [26]. Alternatively, some biological structures such as mitochondria, lysosomes and the extracellular matrix exhibit strong intrinsic fluorescence (autofluorescence) arising from molecules including elastin, nicotinamide adenine dinucleotide phosphate (NADP) or flavins [39] and can be imaged in a label-free manner, i.e. without the need for external labeling.

2.3.2 Image formation and scanning

In widefield fluorescence microscopy, the entire sample is illuminated by the excitation light and the emission is detected with a camera. Alternatively, laser excitation light can be focused into the sample to a point, which is laterally scanned to form an image. The scanning is typically performed by a set of galvanometric (galvo) mirrors, which rotate around two orthogonal axes and deflect the beam accordingly. For proper scanning, the angular deflection of the laser beam by the mirrors has to be transformed to an angular movement at the back aperture of the microscope objective, which results in a transverse movement of the focus inside the sample. Such a transformation can be achieved by a pair of collimation lenses that are arranged in a 4f configuration, where the back-focal plane of the objective, the four focal planes of the lenses and the mirror rotation axis coincide⁸.

2.3.3 Objective lens and resolution

As discussed in section 2.2.2, the spatial resolution of a microscope is, among others, determined by the numerical aperture of the employed objective lens. Recalling that $NA = n \sin(\theta)$, the numerical aperture can be increased by using an immersion medium with a higher refractive index n or by increasing the half-opening angle θ of the objective. The latter is limited to below 90° , in which case the objective would touch the sample.

⁸ In the case of two scanning mirrors, it is usually sufficient to place the focal plane of the first lens at the center between the two rotation axes. Alternatively, a second 4f lens pair can be placed between the two scanning mirrors to yield a perfect angular movement in both directions at the back aperture of the objective.

Thus, air-immersion objectives ($n = 1.0$) generally have an NA below 1. To increase the NA beyond 1, water-immersion ($n = 1.33$) or oil-immersion ($n = 1.51$) objectives can be used, which practically achieve numerical apertures of up to 1.2 and 1.4, respectively [40]. An increase of the NA in turn results in a reduction of the working distance, which represents the distance between the front lens of an objective to the closest surface of the cover slip.

2.3.4 Optical filters

In order to separate the excitation from the emission light, a dichroic mirror can be used, which is either reflective below and transmissive above a certain cutoff wavelength (longpass) or vice versa (shortpass). Such a separation is possible because the fluorescence emission light has a longer wavelength than the excitation light due to the Stokes shift (see section 2.1.1). Additionally, optical filters are commonly used to pick the desired excitation wavelength in case of white-light illumination (excitation filter) and to specifically select the emission wavelength band corresponding to the imaged fluorophores (emission filter). These optical filters are typically realized using colored glass or an alternating layer of dielectric materials (interference filter) and either transmit only a certain band of wavelengths (bandpass filter) or act as shortpass or longpass filters.

2.3.5 Detection and acquisition

Whereas the fluorescence in widefield applications is detected with a camera, the detectors in laser-scanning approaches do not have to be position sensitive, as the respective pixel coordinate is determined by the location of the optical focus and thus by the angular position of the scanning mirrors. Most commonly, photomultiplier tubes (PMT) are used for the detection of fluorescence signals. PMTs are highly sensitive detectors of light between the ultraviolet and the near-infrared range and are based on the photoelectric effect. Primary electrons created in the entrance window form a current, which is accelerated between successive electrodes and thereby multiplied by a factor of $\sim 10^6$, forming detectable signals even at very low photon intensities [41]. As the output of PMTs are current signals, a current-to-voltage converter has to be used to generate voltage signals that can be recorded by a data acquisition (DAQ) device, which digitizes the analog signals and transfers them to a PC for further processing.

Even higher sensitivities of up to single photons can be attained by avalanche photodiodes (APD), which are the semiconductor-based equivalent of PMTs.

2.3.6 Photobleaching

After absorbing a certain number of photons, fluorophores generally lose the ability to emit fluorescence. This effect of photoinduced chemical destruction is called photobleaching and sets limits on the observation time of all fluorescence microscopy techniques. In many cases, permanent structural changes of fluorescent molecules happen in excited states by reactions with surrounding molecules such as oxygen or other fluorophores [9]. Especially excited triplet states are thought to play a key role, as their longer lifetime increases the chances of molecular interactions [26]. The average number of absorption processes before photobleaching occurs varies among different fluorescent molecules and depends on the local molecular environment. For a given fluorophore, the number of excitation and emission cycles is approximately constant and proportional to the product of laser

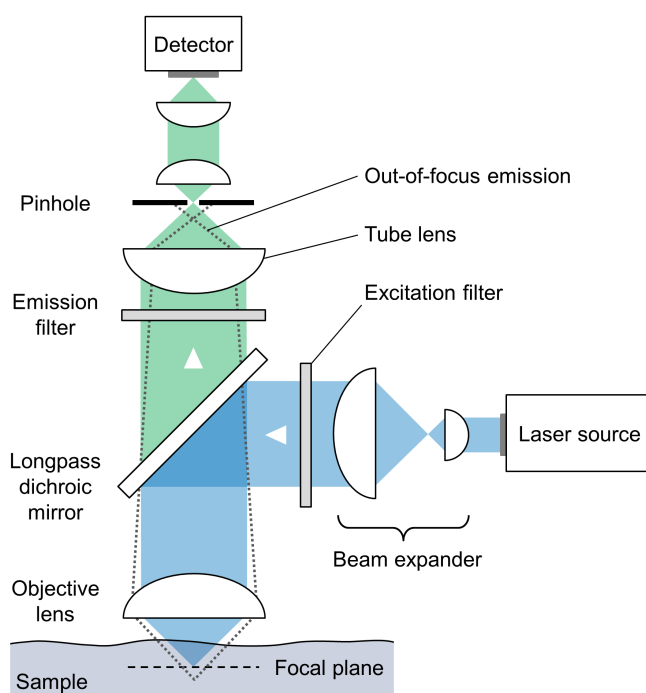


Figure 2.11: Schematic depiction of a typical confocal microscope.

intensity and irradiation time [42]. Thus, high laser powers generally reduce the maximum observation time in fluorescence microscopy.

2.4 Optical laser microscopy techniques – an excerpt

The following section provides an overview of the most commonly used laser microscopy techniques that achieve sub-cellular spatial resolutions at imaging depths ranging into the quasi-ballistic regime and is mostly based on [29, 38, 43–45]. The selection of microscopy approaches is not comprehensive or complete. However, the modalities discussed below operate in the same resolution and imaging depth regime as optoacoustic microscopy, which achieves imaging depths of up to 1 mm.

2.4.1 Fluorescence confocal microscopy

A major problem in traditional fluorescence microscopy is the emission of out-of-focus fluorescence from essentially the entire thickness of the examined specimen, which leads to a substantial blurring of the acquired images. Furthermore, the penetration depth of a traditional fluorescence microscope is limited to the ballistic regime due to the strong scattering of both, excitation and emission light in the specimen. These obstacles can be overcome by optical sectioning approaches, i.e. the confinement of the recorded emission to a thin slice within the sample. By stacking several successively acquired slices along the depth dimension, a 3D volume can be generated.

In a confocal microscope, optical sectioning is achieved through the blocking of out-of-focus emission light by a pinhole, which is placed at a conjugate focal plane in the detection path. Figure 2.11 illustrates the configuration of a typical fluorescence epi-illumination confocal microscope. In many implementations, the excitation source is a continuous wave (CW) laser, which emits at a single wavelength and has a constant intensity. The laser beam is

expanded to completely fill the back aperture of the objective lens, which is required for achieving a diffraction limited spatial resolution. Fluorescence light from the sample is collected back through the objective lens and transmitted through a longpass dichroic mirror, which is reflective for the shorter wavelength excitation beam. The emission light is subsequently focused by a tube lens and detected by a PMT or avalanche photodiode. The focal plane of the tube lens represents a conjugate plane to the focal plane in the sample and thus forms an image of the focal spot. A pinhole placed at this plane permits the transmission of light from the focal spot but prevents light from above or below the focal plane to pass the pinhole (see dashed gray lines in Figure 2.11). Additionally to the out-of-focus background reduction, the pinhole can lead to an improvement of the achieved lateral resolution by a factor of $\sqrt{2}$ if the pinhole size is in the order of the Airy disk, as the total PSF is the product of the objective PSF and the pinhole PSF. However, the drawback of such a small pinhole size is a considerable intensity reduction of emission light reaching the detector. Thus, the pinhole diameter can often be changed depending on the requirements in resolution and sensitivity. Alternatively, the lower sensitivity can be compensated for by increasing the laser power, which, however, in turn results in increased photobleaching. Finally, the out-of-focus rejection in confocal microscopy facilitates imaging at depths of several hundreds of micrometers, because scattered light compromising the resolution is blocked by the pinhole.

Naturally, the laser focus has to be scanned in confocal microscopy, which is usually achieved via scanning mirrors⁹. Since the pinhole is stationary, the raster-scanned laser beam has to be descanned, i.e. the emitted fluorescence light is guided back over the scanning mirrors before being separated from the excitation beam and consequently becomes stationary.

2.4.2 Multiphoton microscopy

In multiphoton microscopy, optical sectioning is achieved by confining the excitation volume itself instead of blocking out-of-focus signals. The restriction of the excitation volume is based on non-linear optical processes involving two or three photons (see Figure 2.12).

In the case of low-intensity light propagating through a dielectric medium, the polarization P (i.e. the dipole moment per unit volume) is linearly proportional to the electric field E of the electromagnetic waves:

$$P = \varepsilon_0 \chi E. \quad (2.19)$$

Here, the constant ε_0 denotes the vacuum permittivity and the proportionality constant χ represents the electrical susceptibility¹⁰. In the case of monochromatic laser light with

⁹ The point-scanning approach based on scanning mirrors typically achieves imaging speeds in the order of seconds. While such an acquisition speed is sufficient for most fixed samples, higher frame rates are necessary in order to capture fast dynamic processes in living organisms, which occur in the order of milliseconds. Recently, millisecond image frame rates have been achieved by using fast rotating disks accommodating microlenses and pinholes, which rapidly scan several focal spots simultaneously across the specimen. The emission light is separated between the two disks by a dichroic mirror and detected with a camera. A detailed introduction to spinning disk confocal microscopy can be found in [46].

¹⁰ χ is generally a tensor and reduces to a scalar in the case of an isotropic dielectric medium. Moreover, the polarization and electric field are vectors in the general case.

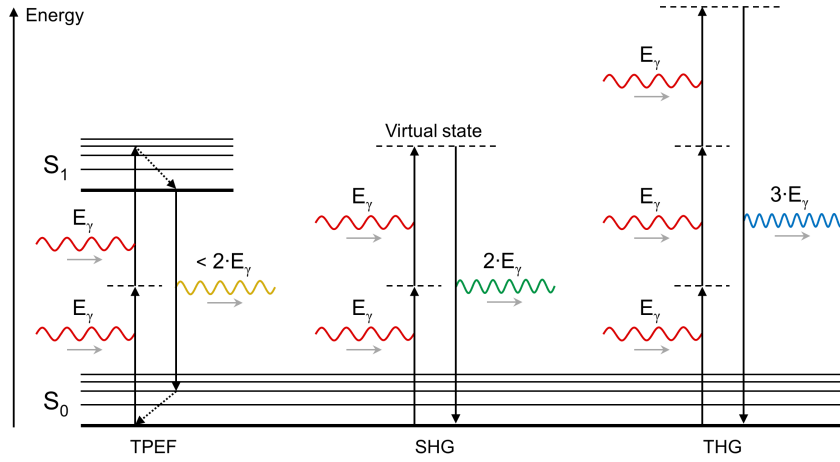


Figure 2.12: Jablonski diagram of the most common non-linear optical processes used in multiphoton microscopy. TPEF: Two-photon excitation fluorescence. SHG: Second-harmonic generation. THG: Third-harmonic generation.

an angular frequency of $\omega = 2\pi c/\lambda$, the time-varying electric field can be represented by

$$E = E_0 \sin(\omega t), \quad (2.20)$$

where E_0 denotes the magnitude of the oscillating field. For very high light intensities with corresponding electric fields in the order of atomic field strengths, the linear relationship in Eq. (2.19) does not hold anymore as the polarization becomes saturated [43]. Instead, the non-linear polarization response has to be described by an expansion of P as a power series in the electric field strength E . By using Eq. (2.20), the non-linear polarization can be written as

$$P = \chi^{(1)} \varepsilon_0 E_0 \sin(\omega t) \quad (2.21)$$

$$+ \chi^{(2)} \frac{\varepsilon_0 E_0^2}{2} [1 - \cos(2\omega t)] \quad (2.22)$$

$$+ \chi^{(3)} \frac{\varepsilon_0 E_0^3}{4} [3 \sin(\omega t) - \sin(3\omega t)]$$

$$+ \dots,$$

where $\chi^{(1)}$, $\chi^{(2)}$ and $\chi^{(3)}$ represent the first-order, second-order and third-order susceptibilities, respectively. The first term in Eq. (2.21) corresponds to the linear polarization response as defined in Eq. (2.19) and is responsible for common optical phenomena such as reflection or refraction. The absence of non-linear optical processes at normal light intensities originates from the small values of the higher-order susceptibilities. Whereas $\chi^{(1)}$ is close to 1, the values of $\chi^{(2)}$ and $\chi^{(3)}$ are in the order of 10^{-12} and 10^{-22} , respectively [43].

Two-photon excitation fluorescence (TPEF)

The non-linear effect most commonly exploited in multiphoton microscopy is two-photon excitation fluorescence (TPEF). Unlike ordinary one-photon excitation fluorescence, TPEF is based on two-photon absorption (TPA), which represents a third-order non-linear optical process. As illustrated in the Jablonski diagram in Figure 2.12, TPEF can be described

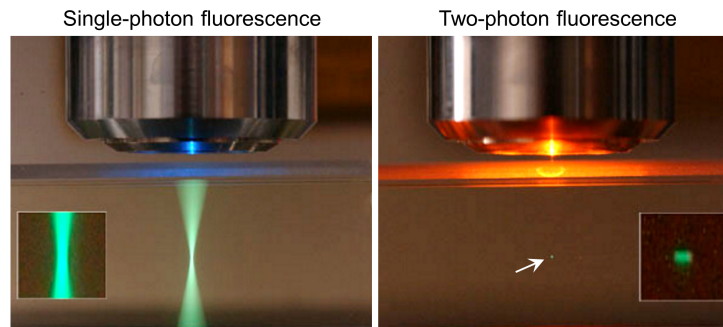


Figure 2.13: Comparison of the excitation volumes in single-photon (left) and two-photon excitation (right) fluorescence. The insets represent close-ups of the respective focal volumes. (Source: [47], © S. Ruzin and H. Aaron, UC Berkely.)

as the excitation of a molecule by the simultaneous absorption of two photons with energy E_γ (usually in the infrared range) and a subsequent fluorescent relaxation via the emission of a photon with higher energy in the visible range. The TPA process involves an intermediate virtual state with a lifetime in the order of femtoseconds as governed by the uncertainty principle, which constitutes the timescale for what is referred to as a 'simultaneous' absorption of two photons. The TPA intensity (i.e. the intensity loss within a distance dx due to TPA) is proportional to the imaginary part of $\chi^{(3)}$ and the square of the incident light intensity I , as can be seen by the relation

$$\left(\frac{dI(x)}{dx}\right)_{TPA} \propto -\Im m\left(\chi^{(3)}\right) I^2(x), \quad (2.23)$$

where $\Im m$ refers to the imaginary part [48].

The intrinsic optical sectioning of TPEF arises from the dependency of the TPA process on the square of the light intensity and the small value of $\chi^{(3)}$. Compared to single-photon absorption where fluorescence is emitted from a large double-conical volume above and below the optical focus, the required intensity for TPEF is only reached directly around the focal spot, whereas the probability for TPA quickly drops with the distance to the focus. The strong optical sectioning effect in multiphoton microscopy is showcased by Figure 2.13, which compares the fluorescence excitation volumes (green color) for single-photon (left panel) and two-photon absorption (right panel) in a liquid dye solution. As can be seen from the insets, the TPEF is confined to a small volume around the focal spot. Since no stationary pinhole is used in the detection path, the emission light does not have to be descanned but is usually separated from the excitation path between scanning mirrors and objective lens. Furthermore, a spatial resolution improvement of $\sqrt{2}$ compared to conventional fluorescence microscopy is the same as in confocal microscopy, as the total PSF corresponds to the square of the single-photon absorption PSF.

The high light intensities required for TPA are achieved by a tight spatial and temporal confinement of the excitation photons. Spatial confinement is ensured by focusing through high NA objectives. On the other hand, temporal confinement is enabled by mode-locked lasers that emit ultra-short pulses in the order of hundreds of femtoseconds with a fixed repetition rate of 80–100 MHz. Commonly employed laser sources for multiphoton microscopy are solid state lasers based on TI:Sapphire or Nd:YLF.

Multiphoton microscopy features several advantages compared to confocal microscopy. First, the use of longer wavelength photons for excitation (typically in the infrared range)

enables deeper penetration than visible excitation light. The reason is mostly the reduced optical absorption in the near-infrared range (optical window, see section 2.1.1) but also lower Rayleigh scattering, which is proportional to ω^4 . Second, multiphoton microscopy is less affected by light scattering. Even in strong scattering tissue, the intensity of scattered emission light is usually not sufficient to generate noticeable non-linear optical signals outside the focal volume [44]. Conversely, because TPEF is known to originate from the focal volume, scattered fluorescence light reaching the detector still contributes to the signal, whereas it is mainly blocked by the pinhole in confocal microscopy. Overall, the penetration depth achieved with conventional multiphoton microscopes can reach 500 μm and more, depending on the sample. Finally, photobleaching and phototoxicity are reduced compared to single-photon absorption based imaging as only the small focal volume is excited at a time.

Disadvantages of multiphoton microscopy are the high costs of mode-locked laser sources and the necessity for point-scanning, whereas confocal microscopy relies on cheaper CW lasers and offers high frame rates through advanced approaches such as spinning disks confocal microscopy [46]. Moreover, the longer excitation wavelength in the order of 1 μm results in a lower spatial resolution compared to the visible excitation used in confocal microscopy.

Second-harmonic generation (SHG)

The second term in Eq. (2.21) contains a component that is proportional to $\cos(2\omega t)$, describing a polarization response and thus a re-emission of light at twice the frequency of the incident electric field. The corresponding non-linear optical process is called second-harmonic generation (SHG) and is illustrated in Figure 2.12. SHG represents a coherent scattering process where two incident photons of energy E_γ are converted into one photon of exactly twice the energy $2E_\gamma$. Similarly to TPEF, the SHG intensity I_2 is proportional to the square of the incident intensity I_1 and is given by

$$I_2(\Delta k) \propto [\chi^{(2)}]^2 \text{sinc}^2(\Delta k x') I_1^2. \quad (2.24)$$

Here, x' denotes the half light propagation distance in the medium and Δk represents the wave number difference of the incident photons k_1 and the emitted photon k_2 . Eq. (2.24) is valid for both, planar and focused Gaussian beam excitation. From the sinc function, it can be inferred that the SHG intensity is maximized in the case of perfect phase matching, which reads as

$$\Delta k = 2k_1 - k_2 = 0. \quad (2.25)$$

As the wave number is defined as $k_N = n_N \omega_N / c$ with N denoting the harmonic order, Eq. (2.25) simplifies to the following statement for phase matching:

$$n_1 = n_2. \quad (2.26)$$

Thus, the refractive index for the incident light has to be equal to the refractive index for the double frequency radiation, which cannot be fulfilled in normal dispersive materials, where n increases with the light frequency. Consequently, SHG can only occur in birefringent materials, which are characterized by a polarization direction dependent refractive index. In this manner, phase matching can be fulfilled if the incident light is

polarized along the direction with higher refractive index to compensate for the dispersion of the emitted light that is polarized along the other direction. The phase matching requirement can also be understood from a phenomenological standpoint. In order to exhibit birefringence, the atomic dipoles in a material have to possess a net degree of orientation. The SHG radiation emitted from well orientated structures in turn interferes constructively and coherently with itself and with the incident electric field and yields a strong detectable signal. Additionally, SHG can only occur in non-centrosymmetric materials, i.e. in structures that lack an inversion center. This requirement results from the fact that the even-order components of susceptibility tensors vanish in centrosymmetric media [30].

Overall, SHG imaging follows the same characteristics as TPEF and can be readily implemented in a multiphoton microscope by using a narrow optical filter to specifically select the emission wavelength at half the fundamental wavelength. The SHG signals can be detected either in forward or backward direction. Furthermore, SHG signal generation is maximized if the direction of light polarization is parallel to the orientation axis of the imaged structures [49].

Because of the requirements for birefringence and non-centrosymmetry, SHG microscopy can specifically visualize oriented structures such as collagen, myosin or starch without the necessity of labeling.

Third-harmonic generation (THG)

The third-order term of Eq. (2.21) contains a component proportional to $\sin(3\omega t)$, which corresponds to a re-emission of light at three times the incident frequency. Analogously to SHG, this process describes the conversion of three photons of energy E_γ into a photon of exactly three times the incident energy $3E_\gamma$ (see Figure 2.12) and is referred to as third-harmonic generation (THG). The THG intensity I_3 is proportional to the cube of the fundamental intensity I_1 :

$$I_3 \propto [\chi^{(3)}]^2 I_1^3. \quad (2.27)$$

As opposed to SHG, the sinc function behavior of the wave number difference Δk in THG is only valid for plane wave excitation. In the case of focused Gaussian beam excitation used in microscopy applications, THG signal generation is found to be suppressed for negative and perfect phase matching¹¹ and maximized for a positive wave number mismatch, which reads as

$$\Delta k = 3k_1 - k_3 > 0. \quad (2.28)$$

This relation can be fulfilled because of the angular spread of the wave vectors within the focused beam [50]. Eq. (2.28) can be simplified to

$$n_1 > n_3. \quad (2.29)$$

Consequently, THG cannot be generated in normal dispersive materials. In fact, Eq. (2.29) can only be fulfilled if the laser beam is focused on an interface between two materials that

¹¹ The destructive interference of THG signals in the case of phase matching is a result of the Gouy phase shift of π radians at the center of focused Gaussian beams and the dependence of the THG polarization response on E^3 [30, 43].

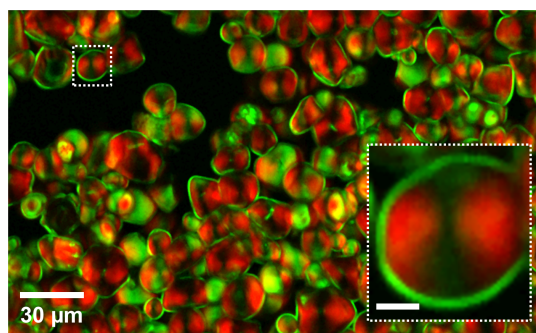


Figure 2.14: SHG and THG microscopy of starch granules. Red color: SHG signals from the radially orientated amylopectin fibrils inside the granules. Green color: THG signals from the granule walls. The imaging was performed with the multiphoton system introduced in chapter 6. Scale bar in the inset: 5 μm .

exhibit different refractive indices (or third-order susceptibilities [51]) for the fundamental and THG frequencies [43].

Unlike SHG, THG can be generated in non-centrosymmetric, as well as in centrosymmetric media, due to the dependence on $\chi^{(3)}$. It is hence the requirement of optical inhomogeneities that prevents aqueous environments surrounding the structures of interest to generate a strong THG background. As a result, THG microscopy can visualize optical interfaces presented by cell membranes or lipid droplets with a high signal-to-noise ratio (SNR) and in a label-free manner.

A shortcoming of THG imaging is the fact that the non-linear radiation is mainly emitted in the forward direction, which makes this modality impractical for applications in epi-illumination mode [52]. On the other hand, the dependence on the cube of the incident intensity leads to a further improvement of the achieved spatial resolution in THG microscopy [30].

Figure 2.14 illustrates the label-free imaging capabilities of SHG and THG microscopy on a sample consisting of starch granules suspended in water, which was performed with the multiphoton microscope introduced in chapter 6. In the overlay image, the green color shows the THG signals originating from the boundaries of the starch granules to the surrounding water. The SHG signals are represented by the red color, visualizing amylopectin fibrils contained in the granules, which are known to be strong SHG sources [53]. Since the amylopectin fibrils are radially orientated in the granules and because of the polarization direction dependence of SHG, the inner parts of the granules are not detected homogeneously. Instead, only the regions corresponding to a fibril orientation parallel to the excitation light polarization are effectively visualized by SHG.

2.4.3 Light sheet fluorescence microscopy

A third method to achieve optical sectioning is light sheet fluorescence microscopy (LSFM). In LSFM, the sample is illuminated by a thin sheet of laser light, whereas the emitted fluorescence is detected in the perpendicular direction. The light sheet is either created by a cylindrical lens or by rapidly scanning back and forth a focused Gaussian beam in one dimension via a scanning mirror. Usually, the sheet is centered around the focal plane of the detection objective and has a diffraction limited thickness between 1 and 10 μm . Consequently, fluorescence emission is confined to a thin slice defined by the light sheet thickness, thus leading to an improved axial resolution of LSFM. 3D volumes

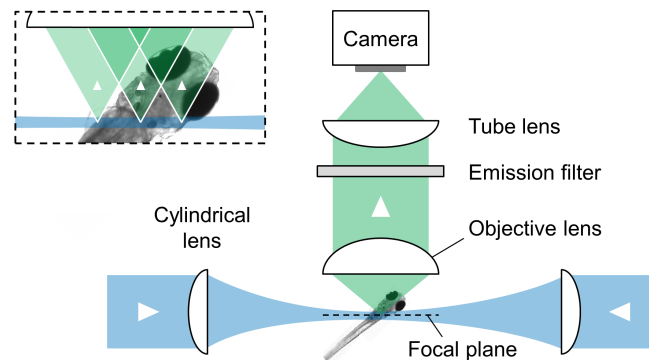


Figure 2.15: Schematic depiction of a typical LSFM implementation.

can be generated by mechanically translating or rotating the specimen through the focal plane or by moving the light sheet itself. The FOV is determined by the confocal parameter of the focused light sheet, which is proportional to the beam waist and thus to the thickness of the sheet (see section 2.2.1). Regarding the imaging depth of LSFM, scattering inside the sample degrades the light sheet focusing and at the same time affects emitted fluorescence light. Nevertheless, light sheet microscopy achieves penetration depths comparable to confocal microscopy at lateral resolutions determined by the NA of the detection objective [4].

Besides optical sectioning, the light sheet illumination reduces photobleaching in the sample, as only a plane instead of the whole volume is illuminated at a time. Furthermore, sheet illumination enables the widefield detection of fluorescence originating from the entire FOV by means of a camera, which facilitates high frame rates in the order of 10–100 Hz as opposed to slower point-scanning approaches such as confocal or multiphoton microscopy [54].

Figure 2.15 schematically depicts a typical LSFM configuration where the light sheet is created by splitting the excitation beam and focusing it from opposite sides of the sample via cylindrical lenses. This implementation increases the FOV for a given sheet thickness and leads to a more homogeneous illumination within the sample compared to an irradiation from one side only. As illustrated by the inset, fluorescence is collected simultaneously from the entire illuminated plane.

A drawback of LSFM is its hindered applicability to larger specimens such as mice due to space restrictions of the orthogonal illumination and detection geometry. Typical samples imaged with LSFM are therefore zebrafish or *Drosophila melanogaster* embryos and larvae, which are usually mounted inside thin columns of transparent gel hanging inside a sample chamber.

2.5 The mesoscopic imaging regime

Even though deep tissue optical microscopy techniques such as confocal or multiphoton microscopy reach penetration depths of several hundred micrometers, high resolution imaging beyond one TMFP poses a great challenge due to overwhelming scattering in non-transparent tissue. Thus, these modalities fail to visualize many tissue structures and organs, as well as entire specimens at advanced stages and bigger animals.

At the macroscopic level, several well-established non-invasive techniques aim at the 3D morphological imaging of entire animals or even humans, including ultrasound imaging,

magnetic resonance imaging (MRI) and X-ray computed tomography (X-ray CT). However, these imaging approaches are not suitable for using the rich collection of optical labels to specifically target certain tissue components [55]. On the other hand, optical macroscopic imaging of tissue biomarkers has recently been enabled by modeling the diffusive propagation of photons at depths corresponding to several TMFPs [4] in combination with advanced tomographic illumination and detection schemes [56]. While each of these tomographic imaging modalities comes with specific contrast mechanisms, advantages and drawbacks, they are generally limited in spatial resolution to several hundreds of micrometers.

The imaging of organisms with a resolution and penetration depth ranging in the gap between microscopic and macroscopic imaging techniques is referred to as mesoscopy. As many developing organisms fall into this range, there is a steady demand for appropriate methodologies operating at this intermediate scale. The mesoscopic equivalent of fluorescence based optical tomography for the imaging at several millimeters in tissue is mesoscopic fluorescence tomography (MFT) [57]. Another approach called optical projection tomography (OPT) visualizes morphology and labeled structures in organs and embryonic specimens based on the transmission of light - the optical equivalent of X-ray CT [55]. However, high-resolution OPT requires the chemical treatment of the imaged specimens to render them transparent, which limits its applications to *ex vivo* samples. Recently, optoacoustic imaging has enabled the imaging of endogenous tissue chromophores and exogenous contrast agents in depths beyond the optical diffusion limit at resolutions of a few tens of micrometers [4]. Based on the detection of ultrasound, optoacoustic mesoscopy achieves superior resolution compared to pure optical techniques, while at the same time relying on optical absorption contrast.

3 Raster-scan optoacoustic mesoscopy (RSOM)

This chapter discusses the theoretical foundation of optoacoustic imaging (section 3.2) and the backprojection reconstruction algorithm (section 3.2.8). Furthermore, the raster-scan optoacoustic mesoscopy (RSOM) modality is introduced (section 3.3) based on [11, 58, 59]¹. In the results part (section 3.4), an improved weighted backprojection algorithm as well as the concept of multi-frequency reconstruction is presented.

3.1 Introduction

Optoacoustic (photoacoustic) imaging is a relatively new modality that has been kicked off in the mid 1990's [60–62] by technological advances in the fields of laser sources and ultrasound detection [63]². The optoacoustic imaging technique is based on the photoacoustic effect and is schematically illustrated in Figure 3.1. Typically, the sample is illuminated by a pulsed laser using short nanosecond pulses in the visible or near-infrared range. The laser pulses propagating through the tissue establish a time-varying electromagnetic field, which is partially absorbed by certain chromophores (see section 2.1.1). Part of the absorbed energy is radiationless converted into heat, leading to a transient local temperature rise (usually $< 0.1^\circ\text{C}$ [13]) and generating an initial build-up of pressure through thermoelastic expansion [4]. This generated pressure propagates through the sample in form of a broadband acoustic wave, which is captured by an ultrasound detector such as a transducer. Since acoustic waves are reflected by differences in acoustic impedance $Z_a = c \cdot \rho$, where c is the speed of sound and ρ the mass density of the medium, an acoustic coupling medium (usually water or ultrasound gel) has to be inserted between the sample and the detector to avoid losses and reflections. The recorded temporal optoacoustic signals (so-called A-scans) represent one-dimensional depth profiles of light energy deposition in the sample. If the transducer is mechanically scanned or if a detector array is used, cross-sectional slices (so-called B-scans) can be obtained from neighboring A-scans along a line. Finally, by measuring the time of flight (TOF) of the optoacoustic signals, together with the knowledge about the speed of sound in the medium, an image can be formed similar to the pulse-echo ultrasound technique [13]. Depending on the implementation, the A-scans are directly used to form images or tomographic reconstruction methods are employed (see section 3.2.8).

The rise of the optoacoustic technique to a widely noticed and successfully applied imaging modality in the biomedical field is owed to the unique combination of the advantages of optical and ultrasound imaging. On the one hand, it relies on absorption based contrast, giving rise to a much richer differentiation of tissue chromophores (e.g. hemoglobin or melanin, see section 2.1.1) than pure ultrasound imaging. On the other hand, optoacoustic imaging achieves large penetration depths of up to several centimeters at high

¹ The experimental development of RSOM was initiated and lead by Dr. Murad Omar.

² Detailed overviews of the historical development of optoacoustic imaging starting with the discovery of the photoacoustic effect by Alexander Graham Bell in 1880 can be found in [63] and [64].

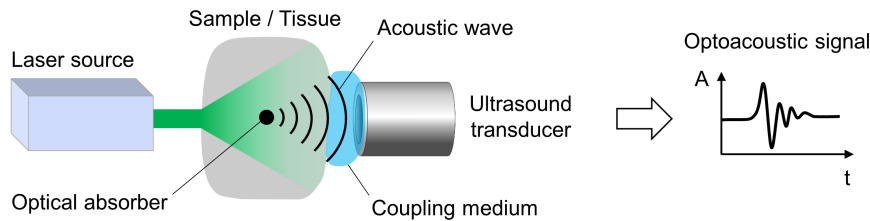


Figure 3.1: Principle of optoacoustic imaging.

spatial resolutions defined by the frequency content of the generated acoustic waves. The reason is that acoustic scattering in tissue is several orders of magnitude weaker than optical scattering, which limits the imaging depth and spatial resolution of pure optical techniques [65]. In this manner, optoacoustic imaging decouples the mechanisms of contrast and spatial resolution [59].

An important feature of the optoacoustic modality is the continuous scalability of resolution and imaging depth achieved. The detection of higher optoacoustic frequencies (> 100 MHz) by using short laser pulses and broadband detectors enables high resolutions (< 30 μm) but limits the penetration depth to a few millimeters through acoustic attenuation (see section 3.2.5). Conversely, macroscopic optoacoustic implementations operate at lower acoustic frequencies (typically < 20 MHz), corresponding to resolutions of hundreds of micrometers, while achieving centimeters of imaging depth. Within such a classification scheme, optoacoustic mesoscopy³ bridges the gap between microscopic and macroscopic approaches, allowing for the high-resolution examination of non-transparent samples at depths beyond the optical diffusion limit. Successful mesoscopic imaging applications include *Drosophila melanogaster* pupae, mouse organs and microvasculature in animals and humans [66–68].

Recently, raster-scan optoacoustic mesoscopy (RSOM) has been introduced in transmission [11] as well as in epi-illumination mode [58, 69]. The technique is based on raster-scanning a single-element spherically focused transducer above the sample within a 2D plane. 3D volumes representing optical absorption in the sample are generated using a filtered backprojection reconstruction algorithm (see section 3.2.8). In order to improve the reconstruction method of the RSOM modality, a weighted backprojection algorithm was developed, incorporating a realistic model of the transducer sensitivity field. To further capitalize on the broadband nature of the optoacoustic signals detected in RSOM, a multi-frequency reconstruction scheme was developed in order to enhance the visibility of fine structures otherwise masked by low-frequency components of the signals.

3.2 Theoretical foundation of optoacoustic imaging

This section provides a theoretical basis for optoacoustic imaging and is mainly based on [12, 70–72]. The main focus will be on the concepts relevant for the high-resolution optoacoustic modalities developed and described in this work. Omitted topics such as diffusive light propagation, spatial impulse response (SIR), model-based reconstruction, spectral imaging and unmixing, as well as sensitivity and artifacts in optoacoustic imaging are comprehensively discussed in [73–75].

³ Also referred to as acoustic-resolution photoacoustic microscopy (AR-PAM).

3.2.1 Signal generation

A laser pulse heating a certain tissue region through the optical absorption of chromophores leads to a fractional volume expansion, which can be defined as

$$\frac{dV}{V} = -\kappa p(\vec{r}) + \beta T(\vec{r}), \quad (3.1)$$

with κ denoting the isothermal compressibility, $p(\vec{r})$ representing the pressure change, β being the thermal volume expansion coefficient and $T(\vec{r})$ denoting the temperature change. If the laser pulse is sufficiently short, the fractional volume change is negligible and the initial pressure rise $p_0(\vec{r})$ directly after the excitation can be written as

$$p_0(\vec{r}) = \frac{\beta T(\vec{r})}{\kappa} = \Gamma \eta_h \mu_a(\vec{r}) \phi(\vec{r}). \quad (3.2)$$

Here, the temperature rise $T(\vec{r})$ was expressed as a function of the optical fluence $\phi(\vec{r})$ (J/cm^2), the optical absorption coefficient $\mu_a(\vec{r})$ (cm^{-1}) and the heat conversion efficiency η_h ⁴. Additionally, the dimensionless Grüneisen coefficient $\Gamma = \beta/\kappa \rho C_V$ was introduced, where ρ denotes the mass density and C_V the specific heat capacity at constant volume. Generally, Γ and η_h are considered to be constant, though tissue dependent [77].

The approximation of a negligible fractional volume expansion and, thus, Eq. 3.2 is only valid if the following two conditions are fulfilled. First, for the heat conduction during the excitation to be negligible, the laser pulse has to be shorter than the thermal relaxation time

$$\tau_{th} = \frac{d_h^2}{\alpha_{th}}, \quad (3.3)$$

where d_h represents the characteristic dimension of the heated volume and α_{th} denotes the thermal diffusivity (m^2/s). Second, the laser pulse must be shorter than the stress relaxation time

$$\tau_{st} = \frac{d_h}{c}, \quad (3.4)$$

so that the propagation of built-up stress can be neglected during the excitation. Here, c is the speed of sound in the heated medium. Typically, τ_{st} is much smaller than τ_{th} and in the order of 7 ns for an absorber diameter of 10 μm .

3.2.2 Wave equation and forward solution

Upon the generation of an initial pressure rise, a bipolar (i.e. having both positive and negative amplitudes) acoustic wave propagates through the medium, which can be detected by an ultrasound transducer. Under the condition of thermal confinement, the wave equation for the pressure $p(\vec{r}, t)$ propagating in an acoustically homogeneous medium

⁴ Since optoacoustic signal generation depends on transient heat generation through non-radiative relaxation (see blue arrow in Figure 2.4), the heat conversion efficiency η_h and hence the initial optoacoustic pressure amplitude is increased for non-fluorescent or low-quantum-yield fluorescent chromophores [76].

is given by

$$\left(\nabla^2 - \frac{1}{c^2} \frac{\partial^2}{\partial t^2}\right) p(\vec{r}, t) = -\frac{\Gamma}{c^2} \frac{\partial}{\partial t} H(\vec{r}, t). \quad (3.5)$$

The right side of the wave equation represents the source term, where $H(\vec{r}, t)$ denotes the heating function (W/cm^3) being defined as the thermal energy converted from optical absorption per unit volume and per unit time. It is linearly proportional to the time derivative of the optical fluence $\phi(\vec{r}, t)$, which is equal to the light intensity $I(\vec{r}, t)$ (W/cm^2):⁵

$$H(\vec{r}, t) = \eta_h \mu_a(\vec{r}) \frac{\partial}{\partial t} \phi(\vec{r}, t) = \eta_h \mu_a(\vec{r}) I(\vec{r}, t). \quad (3.6)$$

Since the source term is proportional to the time derivative of $H(\vec{r}, t)$, optoacoustic pressure waves cannot be generated by time-invariant heating. Thus, appropriate laser sources have to be either pulsed or modulated.

The forward solution to the wave equation (3.5) is obtained by finding the corresponding Green's function $G(\vec{r}, t)$, which is the response to a spatial and temporal delta source⁶ of the differential equation

$$\left(\nabla^2 - \frac{1}{c^2} \frac{\partial^2}{\partial t^2}\right) G(\vec{r}, t) = \delta^3(\vec{r}) \delta(t). \quad (3.8)$$

With the Green's function, the forward solution can be expressed as

$$p(\vec{r}, t) = - \iiint_V \int_t G(\vec{r} - \vec{r}', t - t') \frac{\Gamma}{c^2} \frac{\partial}{\partial t'} H(\vec{r}', t') d^3\vec{r}' dt'. \quad (3.9)$$

The free-space Green's function has the following form [81]:

$$G(\vec{r} - \vec{r}', t - t') = -\frac{1}{4\pi} \frac{\delta\left((t - t') - \frac{|\vec{r} - \vec{r}'|}{c}\right)}{|\vec{r} - \vec{r}'|}. \quad (3.10)$$

It can be interpreted as a spherical wave emanating from a position \vec{r}' and generated at time t' propagating with the speed of sound c . Furthermore, the amplitude of the spherical wave decreases linearly with the distance $|\vec{r} - \vec{r}'|$ from the origin.

5 Often, the heating function is written as a function of the optical fluence rate $\Phi(\vec{r}, t)$ (W/cm^2): $H(\vec{r}, t) = \eta_h \mu_a(\vec{r}) \Phi(\vec{r}, t)$, which is not to be confused with the optical fluence $\phi(\vec{r}, t)$ (J/cm^2). The optical fluence rate corresponds to a local ensemble-averaged value of the optical intensity, which is used to model light propagation in diffusive biological tissue [78, 79].

6 The delta function $\delta(x)$ is defined as being zero for all real numbers except at $x = 0$ and satisfies the identity [80]

$$\int_{-\infty}^{\infty} \delta(x) dx = 1. \quad (3.7)$$

In this context, the term 'delta pulse' will be used throughout this work to indicate an infinitely short laser pulse.

By inserting this expression into Eq. (3.9), the forward solution can be written as

$$\begin{aligned}
 p(\vec{r}, t) &= \frac{\Gamma}{4\pi c^2} \iiint_V \int_t \frac{\delta\left((t-t') - \frac{|\vec{r}-\vec{r}'|}{c}\right)}{|\vec{r}-\vec{r}'|} \frac{\partial}{\partial t'} H(\vec{r}', t') d^3\vec{r}' dt' \\
 &= \frac{\Gamma}{4\pi c^2} \frac{\partial}{\partial t} \iiint_V \frac{d^3\vec{r}'}{|\vec{r}-\vec{r}'|} H(\vec{r}', t') \Big|_{t'=t-|\vec{r}-\vec{r}'|/c}.
 \end{aligned} \tag{3.11}$$

Eq. (3.11) is the optoacoustic equivalent of Huygens' principle, stating that the total pressure that is measured at position \vec{r} and time t is the time derivative of the sum of point-source driven spherical waves weighted with the heating function.

Because of the essentially instantaneous light propagation within the limited sample dimensions, the heating function can be decomposed into a position and time dependent term $H(\vec{r}, t) = H_r(\vec{r}) \cdot H_t(t)$. For very short laser pulses, the temporal term can be approximated as a delta function $H_t(t) = \delta(t)$. Under this condition, Eq. (3.11) simplifies to

$$p_{\delta t}(\vec{r}, t) = \frac{\Gamma}{4\pi c^3} \frac{\partial}{\partial t} \left[\frac{1}{t} \iint_S H_r(\vec{r}') dS \right]_{|\vec{r}-\vec{r}'|=ct} = \frac{\partial}{\partial t} \left[\frac{t}{c} \iint_S p_0(\vec{r}') d\Omega \right]_{|\vec{r}-\vec{r}'|=ct}, \tag{3.12}$$

because $p_0(\vec{r}')$ can be written as $p_0(\vec{r}') = \Gamma \eta_h \mu_a(\vec{r}') H_r(\vec{r}')$. Accordingly, the total pressure at position \vec{r} and time t for delta pulse excitation originates from spherical shells with radius $c \cdot t$ centered at \vec{r} (spherical Radon transform). The time derivative encodes the bipolarity of the pressure signal, which has an N-shape in case of a uniform spherical absorber (see section 3.2.3). The physical explanation for the bipolarity is the fact that the emanating pressure wave is composed of a diverging and a converging compression wave. As the latter travels through the center of the spherical absorber, it is transformed into a diverging rarefaction wave responsible for the subsequent negative peak of the measured signal. For the special case of such a spherical absorber with the same properties as the surrounding medium and excited by a delta pulse, an analytical forward solution yielding an N-shaped signal can be found as

$$p_{\delta t, sph}(\vec{r}, t) = p_0 \frac{R-ct}{2R} \Theta\left(\frac{d_a}{2} - |R-ct|\right), \tag{3.13}$$

where d_a is the absorber diameter, $R = |\vec{r} - \vec{r}_a|$, \vec{r}_a is the center position of the absorber and Θ is the Heavyside function defined as $\Theta(x) = 0$ if $x < 0$ and $\Theta(x) = 1$ if $x \geq 0$ [80]. For a finite pulse duration, the forward solution $p_{\delta t}(\vec{r}, t)$ given by Eq. (3.12) has to be convolved with the temporal pulse profile $H_t(t)$:

$$p(\vec{r}, t) = \int_{-\infty}^{\infty} H_t(t-\tau) p_{\delta t}(\vec{r}, \tau) d\tau. \tag{3.14}$$

On the other hand, if the absorber can be approximated as a point source that is w.l.o.g.

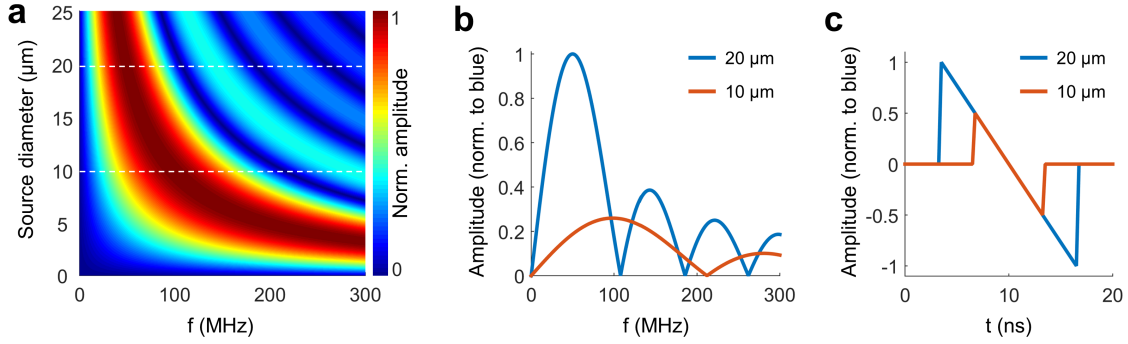


Figure 3.2: Simulation of optoacoustic signals for different source diameters. The signals were calculated for fluid absorbers using Eq. (3.13). (a) Normalized frequency spectra for different source diameters. (b) Frequency spectra for 10 and 20 μm absorbers (see dashed white lines in (a)) normalized to the 20 μm spectrum (blue). (c) Corresponding time signals.

located at the origin: $H_r(\vec{r}) = \delta(\vec{r})$, Eq. (3.11) can be simplified to

$$p_{\delta r}(r, t) = \frac{\Gamma}{4\pi c^2 r} \frac{\partial}{\partial t} H_t \left(t - \frac{r}{c} \right). \quad (3.15)$$

Finally, for a delta pulse excitation of a point absorber, i.e. $H_t(t) = \delta(t)$ and $H_r(\vec{r}) = \delta(\vec{r})$, the forward solution to Eq. (3.5) is simply given by

$$p_{\delta t, \delta r}(r, t) = \frac{\Gamma}{4\pi c^2 r} \frac{\partial}{\partial t} \delta \left(t - \frac{r}{c} \right). \quad (3.16)$$

3.2.3 Frequency content of optoacoustic signals

Optoacoustic signals are composed of a broad distribution of frequencies in the MHz range. Since the time duration of optoacoustic pulses is proportional to the diameter of the source under stress confinement, the frequency bandwidth scales inversely with the size of the absorber. Figure 3.2(a) shows a simulation of generated optoacoustic frequencies as a function of the source diameter d_a using the analytical expression for fluid spherical absorbers given by Eq. (3.13). The time signals were convolved with a Gaussian function yielding a FWHM of 1.5 ns to mimic the effect of a finite laser pulse duration (see Eq. (3.14)). For the simulation, a range of source diameters corresponding to typical structures imaged with RSOM was chosen. As can be observed from (a), the frequency bandwidth increases with decreasing absorber size, extending into the range beyond 200 MHz for diameters smaller than 10 μm . The peak frequency of the spectra is given by

$$f_{peak} \approx 0.66 \frac{c_a}{d_a}, \quad (3.17)$$

where c_a is the speed of sound in the absorber [82]. Figure 3.2(b) illustrates two frequency spectra for source diameters of 20 μm (blue) and 10 μm (red). Both spectra were normalized to the 20 μm curve. The frequency distributions show several side lobes, whereas the amplitude of the spectra increases with the absorber size. The corresponding time courses are depicted in (c), yielding the characteristic bipolar N-shape of optoacoustic signals. As predicted by Eq. (3.13), the duration as well as the amplitude of the signals

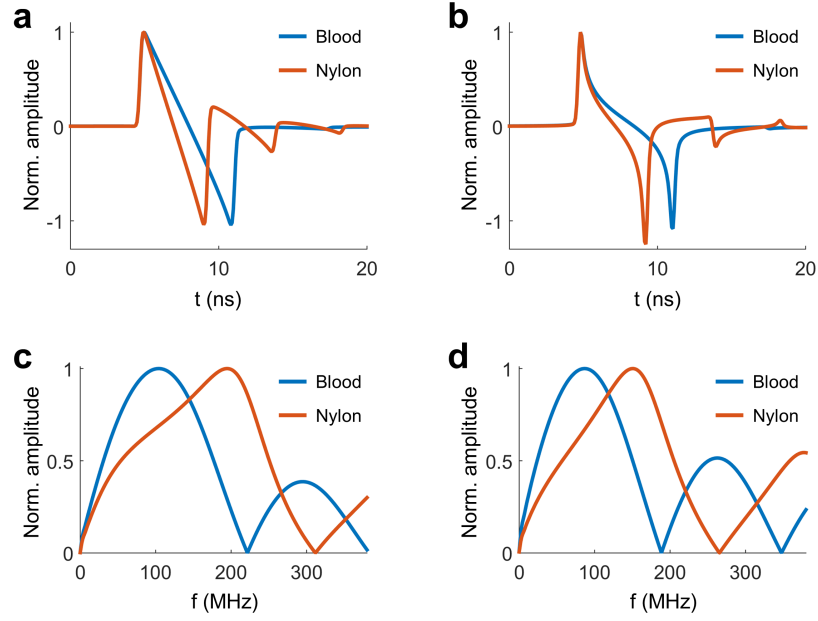


Figure 3.3: Simulation of optoacoustic signals from solid absorbers made of different materials. (a-b) Time signals for a spherical (a) and cylindrical (b) absorber geometry using the material properties of blood (blue) and nylon (red). The corresponding frequency spectra are shown for the spherical (c) and cylindrical (d) shape.

are directly proportional to the source diameter under stress confinement.

3.2.4 Optoacoustic signals from solid absorbers

In the special case of a fluid absorber with the same speed of sound and density as the surrounding medium, the detected optoacoustic pressure can be described by the analytical expression given by Eq. (3.13). The resulting N-shaped signals are a valid approximation of the real signals for most of the tissue chromophores such as hemoglobin and melanin. However, solid absorbers including sutures, microspheres or nanoparticles, which are commonly used in phantoms or as contrast agents, usually have a larger density and speed of sound than the surrounding medium. Thus, the signals are narrowed in time compared to fluid absorbers of the same diameter and consequently the frequency responses are shifted to higher values. Furthermore, the acoustic impedance mismatch at the absorber-medium interface leads to multiple reflections depending on the properties of the absorber.

The frequency domain solution of the wave equation (3.5) for a solid spherical absorber with diameter d_a using the continuity equation for stress at an interface is given by

$$\hat{p}_s(\vec{r}, \omega) = iC \frac{d_a^2}{4q^2 R \rho_a c_l} \cdot \frac{\sin(q) - q \cos(q)}{\left(1 - \tilde{\rho} + \tilde{\rho} \frac{\tilde{c}^2}{q^2}\right) \frac{\sin(q)}{q} - \left(1 + \tilde{\rho} \frac{\tilde{c}^2}{q^2}\right) \cos(q) + i\tilde{\rho} \hat{c} \left[\left(1 - \frac{\tilde{c}^2}{q^2}\right) \sin(q) + \frac{\tilde{c}^2}{q} \cos(q)\right]}, \quad (3.18)$$

with the dimensionless quantities $q = \omega d_a / c_l$, $\tilde{c} = 2c_t / c_l$, $\hat{c} = c_l / c_m$ and $\tilde{\rho} = \rho_a / \rho_m$ [83]. Here, ω denotes the angular frequency, $R = |\vec{r} - \vec{r}_a|$, \vec{r}_a is the center position of the absorber, c_m denotes the speed of sound in the medium, c_l and c_t are the longitudinal

and the transverse speeds of sound in the absorber, respectively, ρ_a is the density of the absorber, ρ_m denotes the density of the medium and C represents a tissue dependent constant. By Fourier transforming Eq. (3.18), the time domain solution is obtained. The latter simplifies to Eq. (3.13) for a transverse speed of sound of zero and if the longitudinal speed of sound and the density of the absorber are set to be equal to the values of the surrounding medium. Figure 3.3(a) shows the optoacoustic signals from two spherical absorbers with 10 μm diameter and the material properties of blood (blue, $c_l = 1570$ m/s, $c_t = 0$, $\rho_a = 1060$ kg/m³) and nylon⁷ (red, $c_l = 2200$ m/s, $\rho_a = 1140$ kg/m³). For the nylon absorber, the transverse speed of sound was set to zero, which is valid under the assumption of homogeneous illumination. In contrast to the N-shaped signals in Figure 3.2(c), the reflections from the absorber medium boundary can clearly be observed. The corresponding frequency spectra are shown in Figure 3.3(c). Due to the larger speed of sound in nylon, the time signal is shorter, leading to higher frequencies in the Fourier spectrum.

For a cylindrically shaped solid absorber with diameter d_a , the frequency domain solution of the wave equation (3.5) can be written as

$$\hat{p}_c(r, \omega) = iC \frac{d_a^2}{4q \rho_a c_l} \frac{J_1(q) H_0(\hat{c} \hat{r} q)}{J_1(q) H_0(\hat{c} q) - \tilde{\rho} \hat{c} H_1(\hat{c} q) \left[J_0(q) - \frac{c^2}{2q} J_1(q) \right]}, \quad (3.19)$$

where J_n and H_n denote the n-th order Bessel and Hankel functions of the first kind, $\hat{r} = 2r/d_a$ and r is the radial distance to the cylinder axis [84]. Again, the respective time domain solution is obtained by the Fourier transform of Eq. (3.19). Figure 3.3(b) shows the optoacoustic signals from cylindrical absorbers with 10 μm diameter made of blood (blue) and nylon (red). The corresponding frequency spectra are depicted in Figure 3.2(d). For the simulation, the signals were convolved with a 1.5 ns pulse. The simulation of optoacoustic signals in this work was performed with a MATLABTM script, which can be found in appendix A.

3.2.5 Acoustic attenuation

As pressure waves propagate through a medium, part of their acoustic energy is lost leading to an attenuation of optoacoustic signals. The acoustic attenuation effect is caused by internal frictional losses and by heat diffusion between regions of different temperature due to non-adiabatic and non-isothermal pressure changes [85]. The acoustic attenuation process can be described by a frequency dependent attenuation coefficient $\alpha(f)$, which has been empirically shown to satisfy a power law dependence of the form

$$p(r, f) = p_0 \cdot e^{-\alpha(f)r} = p_0 \cdot e^{-\alpha_0 |f|^n r}, \quad (3.20)$$

where p_0 is the initial pressure amplitude, α_0 denotes the attenuation constant in units of *neper*, r is the propagation distance, f represents the optoacoustic frequency and n is a medium dependent exponent [86]. For water, the attenuation constant in units of *decibels* has a value of $\alpha_{0, dB} = 0.00217$ dB/MHz² cm and an exponent of $n \approx 2$. On the other hand, soft tissue has an average attenuation constant in the order of $\alpha_{0, dB} = 0.5$ dB/MHz cm,

⁷ Nylon was chosen because the sutures that were used in this work as reference samples in phantoms were made of this material.

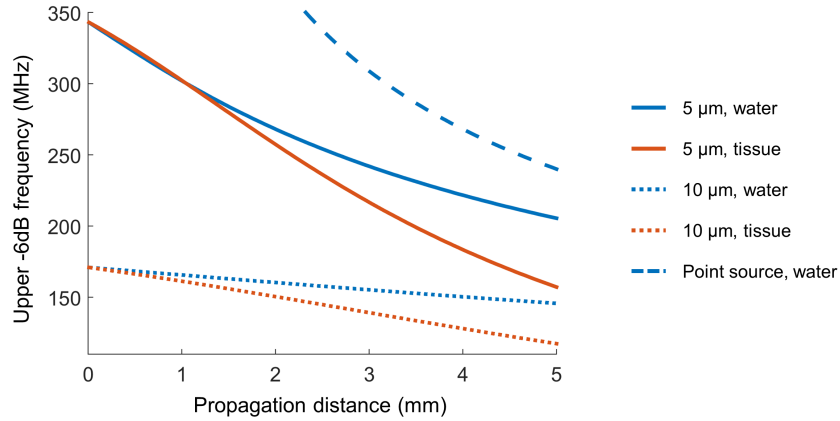


Figure 3.4: Simulation of optoacoustic signal attenuation in water (blue) and tissue (red). The solid and dotted lines denote spherical absorbers with $5\ \mu\text{m}$ and $10\ \mu\text{m}$ diameter, respectively, whereas the dashed curve represents a point source. The signals were generated from fluid absorbers using a delta pulse excitation.

while the value of n is close to 1 [87]. The conversion of the acoustic constants from *decibels* to *neper*s is achieved by

$$\alpha_0 = \alpha_{0, dB} \cdot 5 \ln(10) \cdot (10^{-6})^n. \quad (3.21)$$

According to Eq. (3.20), acoustic attenuation affects the various frequency components differently and has a greater effect on the high frequencies. Thus, the bandwidth is narrowed, accompanied by a broadening of the time signals and a reduction of their amplitude [86]. Figure 3.4 illustrates the simulated effect of acoustic attenuation in water (blue) and tissue (red) for different source diameters (solid curves: $5\ \mu\text{m}$ diameter, dotted curves: $10\ \mu\text{m}$ diameter) as a function of the propagation distance. For the simulation, the attenuation constants were chosen according to the values presented above and a delta pulse excitation was used. As can be seen from the simulation, the attenuation in tissue is stronger than in water for both absorbers, leading to a more pronounced reduction of the signal bandwidth. In the case of the $5\ \mu\text{m}$ source, the attenuation in water and tissue has the same effect within the first millimeter because of the different values of n , which compensates the larger attenuation constant of tissue. Finally, acoustic attenuation limits the theoretically highest detectable frequencies to $\sim 300\ \text{MHz}$ for $3\ \text{mm}$ propagation distance in water, as can be seen from the point source simulation (dashed blue line). This has implications on the highest detectable frequencies for transducers with a certain focal distance. Furthermore, it can be concluded that acoustic attenuation ultimately limits the imaging depth of optoacoustic mesoscopy to a few millimeters for absorbers with a size of $< 10\ \mu\text{m}$. However, for the imaging of tissue, the limiting factor of the penetration depth is typically the absorption of the visible laser light, which is also in the order of a few millimeters.

3.2.6 Focused ultrasound transducers and detection geometry

Piezoelectric ultrasound detectors

As discussed in the previous sections, optoacoustic signals are broadband with frequencies spanning tens of megahertz in the case of optoacoustic mesoscopy. Therefore, an accurate

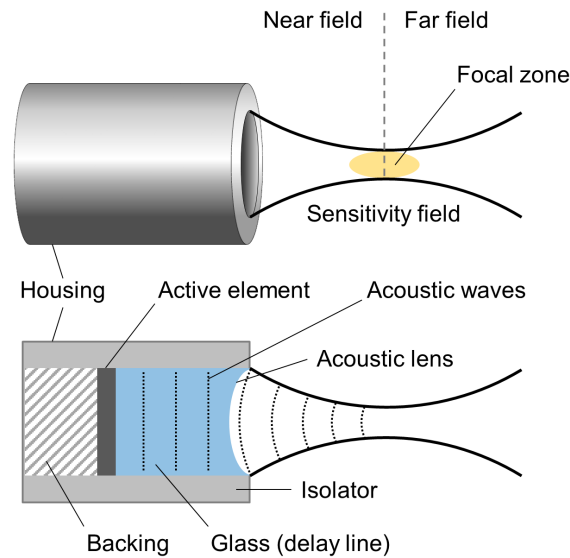


Figure 3.5: Components of spherically focused ultrasound transducers based on a glass lens.

sensing of such signals requires broadband detection with high sensitivity and dynamic range [73]. Typically, focused piezoelectric ultrasound transducers are used as acoustic detectors in high-resolution optoacoustic imaging. The central part of a transducer is a piezoelectric active element, which converts pressure waves into voltage signals that can be further electronically processed and recorded. Its working principle is based on the piezoelectric effect, i.e. the re-orientation of molecular dipole moments upon mechanical deformation by pressure waves, leading to a voltage difference proportional to the deformation amplitude [88].

In order to increase the sensitivity and to facilitate certain scanning schemes, ultrasound transducers can be focused in one or two dimensions. Cylindrically focused transducers have a wide acceptance angle in one dimension and are focused in the perpendicular direction, resulting in an approximate 2D sensitivity field. Such a geometry is useful for scanning schemes based on linear arrays, where signals outside of the focal plane are suppressed. On the other hand, spherically focused transducers have a narrow acceptance angle in all directions and a conical sensitivity field, which converges to a focal point with maximum detection sensitivity. In this geometry, the signals around the focal volume can be considered to originate from the central acoustic axis, whereas signals outside of the narrow double-conical sensitivity field are not detected⁸ [73].

Acoustic focusing can be achieved by either shaping the active element with a cylindrical or spherical curvature or by using an acoustic lens together with a flat active element. Since the central frequency of ultrasound transducers is inversely proportional to the thickness of the piezoelectric medium, high-frequency detectors are based on thin active elements of a few tens of micrometers [87]. Because such thin piezoelectric elements are difficult to manufacture in a curved geometry, high-frequency ultrasound transducers for optoacoustic mesoscopy or microscopy applications are typically realized using an acoustic lens.

⁸ In fact, the sensitivity fields of ultrasound transducers exhibit several spatial side lobes, which are, however, typically weak compared to the main lobe and can therefore be neglected in most applications.

Another distinct feature of high-frequency transducers is the material of their active element. Whereas most low-frequency active elements are made of piezoceramics (e.g. lead zirconate titanate - PZT) or composite materials (i.e. piezoceramics in a polymer matrix), thin piezoelectric layers are commonly realized using polymers (e.g. polyvinylidene fluoride - PVDF) [88]. The ultrasound detectors used throughout this work are based on single crystal lithium niobate ($LiNbO_3$), which can be utilized for frequencies in the range of approximately 50–200 MHz.

Figure 3.5 illustrates the configuration of the spherically focused ultrasound transducers used in this work. The active element is grown on quartz glass (SiO_2), which has a length of several millimeters and acts as a delay line to temporally separate the optoacoustic waves from laser induced signals. The acoustic lens is formed by a concave cavity in the glass that shapes a spherically focused sensitivity field. In order to convert the spherical acoustic waveforms emanating from the focus into plane waves that simultaneously hit the entire active element, the lens curvature is larger than the reciprocal focal distance. Furthermore, no matching layers are used, which increases the detection bandwidth but at the same time reduces the sensitivity due to the considerable acoustic mismatches between water ($c = 1500$ m/s, $\rho = 1000$ kg/m³), glass ($c_l \approx 6000$ m/s, $\rho \approx 2200$ kg/m³) and lithium niobate ($c_l \approx 6900$ m/s, $\rho \approx 4600$ kg/m³) [89]. The backing behind the active element absorbs reverberations and determines the sensitivity and bandwidth of the detector via its matching to the piezoelectric element [73].

Sensitivity field and detection geometry

The sensitivity field volume between lens and focus is referred to as the near field of the transducer and is characterized by a series of local maxima and minima. On the other hand, the volume beyond the focus represents the far field and yields a smooth sensitivity gradient. Figure 3.6 illustrates the detection geometry of a spherically focused 100 MHz transducer with 1.5 mm active element diameter and focal distance and a detection bandwidth of approximately 20–180 MHz. A simulation of the sensitivity field using the Field II package [90, 91] is shown in Figure 3.6(a), whereas the detector is located on the left side of the panel. In Figure 3.6(b), the experimental measurement of a black 18 μ m suture at an axial position of ± 200 μ m and ± 500 μ m with respect to the focus is illustrated (see section 3.3.1 for a description of the experimental setup). For each axial distance, which was adjusted by moving the transducer up and down, the transducer was perpendicularly scanned over the suture to form B-scans with a length of 1 mm. The x -axis represents the time axis of the A-scans, which was converted to the depth dimension via the known speed of sound in water. As can be observed from the measurement, the profile of the suture is point like in the focus but gets projected as arcs outside of the focal zone. The size of the arcs scales with the axial distance (defocus), whereas the tips of the arcs point towards the focus in the near as well as the far field. Furthermore, the signals coincide with the double-conical shape of the sensitivity field as depicted in Figure 3.6(a). These projections occur because the different times of flight of the optoacoustic signals increase with the lateral displacement from the acoustic axis. Figure 3.6(c) shows the one-dimensional profile through (b) along the central acoustic axis (see black arrows). The signal from the focus has the highest amplitude due to the maximum focal gain, whereas the signals get weaker with increasing axial distance. Furthermore, the shapes of the signals differ between the near and the far field, which is the result of the spatial impulse response (SIR) of the transducer. The SIR describes the distortion of measured acoustic signals originating from out-of-focus locations, which do not hit the area of the

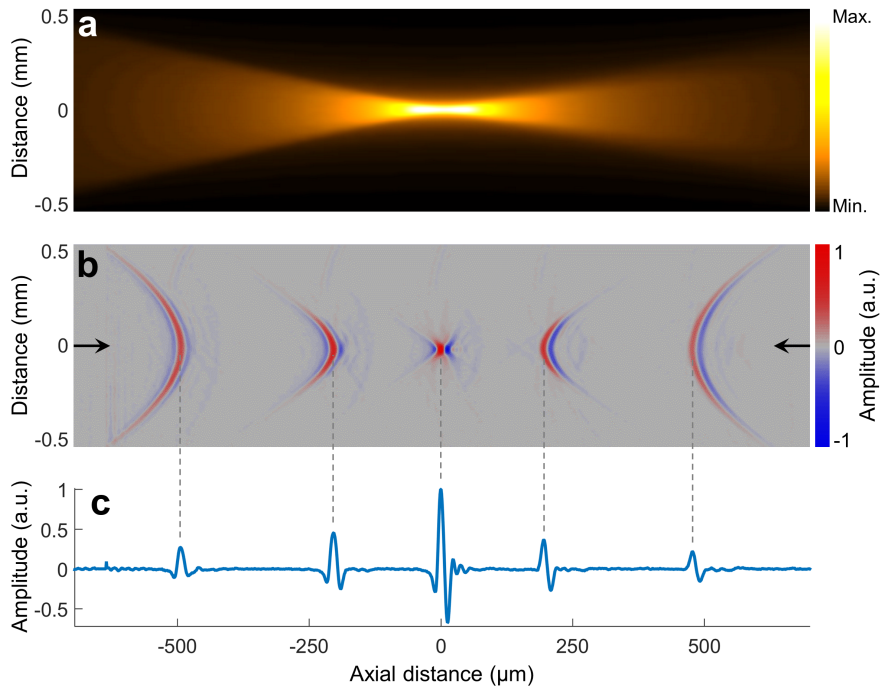


Figure 3.6: Detection geometry of spherically focused transducers. (a) Simulation of the sensitivity field of a 100 MHz transducer with 1.5 mm active element diameter and focal distance. The detector is located on the left. (b) Experimental measurement of a black 18 μm suture at five different depths using a transducer with parameters matching the ones from the simulation. B-scans with 1 mm range are stacked to illustrate the sensitivity field of the transducer. (c) One-dimensional profile of the suture measurements along the central acoustic axis, as indicated by the black arrows in (b).

active element simultaneously. For signals from the far field, the outer parts of the active element are reached earlier than the inner part and vice versa for near field signals. The temporal elongation of the measured optoacoustic signals caused by the SIR leads to a dampening of the high frequencies and therefore a degradation of the axial resolution with increasing lateral and axial distance of the source to the acoustic focus [73].

Scanning schemes in high-resolution optoacoustic imaging

Most of the optoacoustic mesoscopy imaging systems, including the RSOM modality presented in this chapter, rely on a single spherically focused transducer. Tomographic imaging is achieved by mechanically scanning the detector and recording the optoacoustic signals at different positions. The most common scanning schemes involve a spherical, cylindrical or planar geometry. In the latter, which is used for all mesoscopy implementations discussed in this work, the transducer is laterally scanned in a plane above the illuminated sample. As illustrated in Figure 3.7(a), the optoacoustic signals are typically detected from the far field beyond the acoustic focus in the case of tomographic imaging. As will be discussed in the next section, the out-of-focus detection requires reconstruction methods to restore the original shape of the absorbers from the measured arc-shaped signals. On the other hand, the signals from the focal volume can be directly stacked to form a 3D volume, which either requires thin samples or a low NA transducer with an extended focal zone. Figure 3.7(b) shows an exemplary B-scan of chicken breast tissue using the RSOM system introduced in section 3.3.1. The skin (highlighted by red arrows)

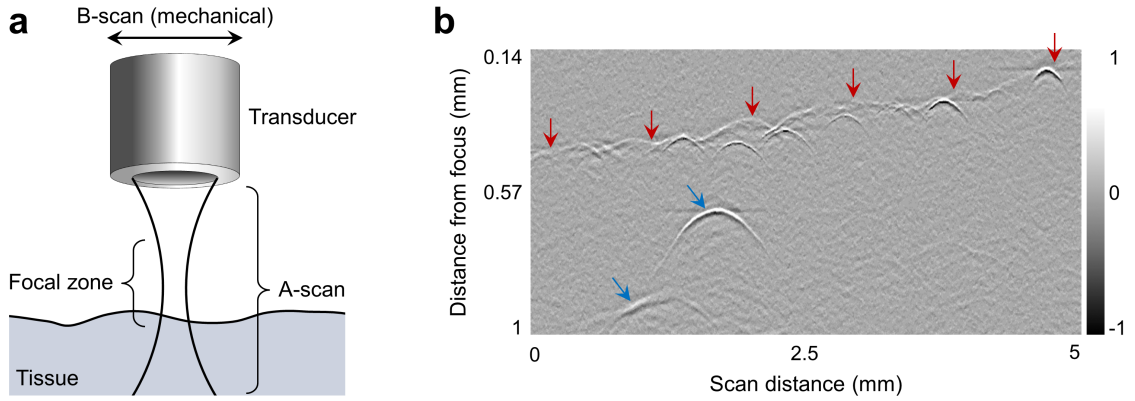


Figure 3.7: Scanning in optoacoustic mesoscopy. (a) Linear scanning scheme, which is also used in RSOM. (b) B-scan of chicken breast tissue using the RSOM system. Red arrows indicate the skin surface, whereas the blue arrows highlight deeper blood vessels.

is clearly visible through the strong optoacoustic signals from superficial blood vessels. Moreover, bigger blood vessels beneath the skin (see blue arrows) are observed. Since the sample was placed in the positive defocus of the transducer, all signals yield the characteristic arc shape. The image was spatially highpass and temporally bandpass filtered (see section 3.3.1) to improve the visibility.

3.2.7 Spatial resolution in optoacoustic mesoscopy

In optoacoustic mesoscopy, the spatial resolution depends on the properties of the employed focused ultrasound transducer. In the case of a planar scanning geometry and a spherically focused detector with a central frequency f_{ac} , the lateral resolution is defined by the FWHM of the acoustic focus:

$$R_{lat} = FWHM_{ac} = 0.71 \frac{\lambda_{ac}}{NA_{ac}}, \quad (3.22)$$

where $\lambda_{ac} = c/f_{ac}$ is the acoustic wavelength at the central frequency and NA_{ac} denotes the numerical aperture of the transducer [10]. The numerical aperture can be approximated as

$$NA_{ac} = n_c \sin(\varphi) = n_c \sin \left[\tan^{-1} \left(\frac{D}{2F} \right) \right] \approx n_c \frac{D}{2F}, \quad (3.23)$$

where n_c is the refractive index of the coupling medium, φ represents the half opening angle of the transducer, D is the aperture (i.e. the diameter of the acoustic lens or the curved active element) and F denotes the focal distance. In case of water coupling with a refractive index of $n_c = 1.33$, the lateral resolution can therefore be written as

$$R_{lat} \approx 1.07 \lambda_{ac} \frac{F}{D}. \quad (3.24)$$

This expression of the lateral resolution is only valid within the acoustic focal zone, as the signals outside are projected as elongated arcs (see previous sections). The -3 dB

depth of the focal zone can be estimated as [88]

$$D_{foc} \approx 7.2 \lambda_{ac} \left(\frac{F}{D} \right)^2. \quad (3.25)$$

Furthermore, Eq. (3.24) was derived for the central frequency of the detector, which represents a good approximation in most of the cases. However, it should be mentioned that the true lateral resolution is compromised by the low frequency components of the detected signals and is slightly worse than predicted by Eq. (3.24) [59].

On the other hand, the axial resolution of optoacoustic mesoscopy is proportional to the detection bandwidth BW_{det} of the transducer and can be expressed as

$$R_{ax} \approx 0.88 \frac{c}{BW_{det}}. \quad (3.26)$$

This approximation is based on the assumptions that the signal bandwidth is larger than the detection bandwidth and that the latter has a Gaussian profile [92]. Moreover, it takes the entire time signal into account, i.e. all positive and the negative peaks. However, the true axial resolution is better than predicted by Eq. (3.26), because the positive and negative peaks of closely successive signals mutually cancel. The leading peak of the first signal and the last peak of the second signal can often still be distinguished even though the absorber distance is smaller than the temporal width of the individual signals (see section 5.4 and appendix B for a more detailed discussion).

3.2.8 The backprojection reconstruction method

As demonstrated and discussed in the previous sections, the widening of the sensitivity field of focused ultrasound transducers outside of the focal zone results in a lateral elongation of imaged structures and thus in a degradation of the lateral resolution. However, many applications of optoacoustic mesoscopy require the capturing of out-of-focus signals over a range of up to several millimeters. In order to map the arc-shaped signals back to the original absorber dimensions and to achieve a constant lateral resolution over the entire scanning depth, tomographic reconstruction methods are employed. These reconstruction techniques can be divided into two main categories: numerical or model-based inversion approaches and analytical methods [93]. Model-based reconstruction techniques use a system dependent forward model to calculate acoustic fields originating from arbitrary optoacoustic sources. The final reconstructed 3D volume or image is obtained by iterative optimization procedures as the best match to the detected signals [94]. Model-based algorithms offer higher reconstruction accuracy in many cases and allow for the incorporation of detector properties into the model. However, they are time and memory consuming and are typically used for tomographic applications involving only a few hundreds or thousands of projections.

In contrast to tomography, optoacoustic mesoscopy approaches capture hundreds of thousands of projections to image millimeter-sized FOVs with a resolution tens of micrometers. Most of these approaches, including RSOM, employ the backprojection algorithm, an analytical reconstruction method that is easy to implement, fast and memory-efficient. In the backprojection method, the A-scans recorded at each detector position \vec{r}_i are projected onto concentric spherical shells by using the TOF information of the signals and the speed of sound c in the medium. This procedure corresponds to the inverse

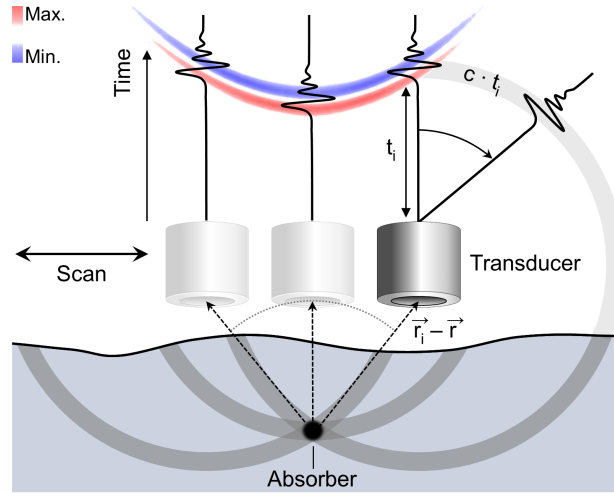


Figure 3.8: Principle of the backprojection reconstruction method with a planar detection geometry. The optoacoustic signals detected at positions \vec{r}_i and time instants t_i are projected back onto concentric spherical shells with radius $c \cdot t_i$ and summed up in the 3D reconstruction grid.

spherical Radon transform⁹ and projects the signals at time instant t_i to all positions they could have emerged from [94]. Finally, the backprojected signals are summed up at each voxel of the 3D reconstruction grid, which usually involves a 3D interpolation of the time signals onto the discrete grid. Figure 3.8 visualizes the technique for a planar scanning geometry as used in RSOM, where the detected hyperbolic signal shapes (red and blue colors) of spherical absorbers are mapped back to the original spherical structures (black dot).

For spherical, cylindrical and planar detection geometries, an analytical backprojection formula for the initial pressure $p_0^{(b)}(\vec{r})$ has been introduced in [95], which writes

$$p_0^{(b)}(\vec{r}) = 2 \iint_{\Omega_0} \frac{d\Omega_i}{\Omega_0} \left[p_\delta(\vec{r}_i, t) - t \frac{\partial p_\delta(\vec{r}_i, t)}{\partial t} \right]_{t=|\vec{r}-\vec{r}_i|/c}. \quad (3.27)$$

Here,

$$b(\vec{r}_i, t) = 2 p_\delta(\vec{r}_i, t) - 2 t \frac{\partial p_\delta(\vec{r}_i, t)}{\partial t} \quad (3.28)$$

represents the backprojected quantity, whereas $p_\delta(\vec{r}_i, t)$ denotes the optoacoustic signal excited by a delta pulse and detected by a point detector at position \vec{r}_i . The factor $d\Omega_i/\Omega_0$ is a solid-angle weighting factor for the contribution of the infinitesimal detector surface dS_0 at each measurement position \vec{r}_i . Furthermore,

$$d\Omega_i = \frac{dS_0}{|\vec{r} - \vec{r}_i|^2} \frac{\vec{n}_s \cdot (\vec{r} - \vec{r}_i)}{|\vec{r} - \vec{r}_i|} \quad (3.29)$$

⁹ The spherical Radon transform assumes that a signal measured at time t_i corresponds to the integral over a spherical shell of radius $c \cdot t_i$. It is the spherical equivalent of the linear Radon transform used in X-ray computed tomography (X-ray CT).

is the infinitesimal solid angle of dS_0 with respect to the reconstruction point at \vec{r} and \vec{n}_s is a unit normal vector to dS_0 pointing towards the source [72]. Ω_0 represents the total solid angle of the detection surface, which is 4π for a perfect spherical or cylindrical and 2π for a perfect planar geometry. The first term of Eq. (3.28) is referred to as the direct term and represents the measured pressure itself. Backprojecting only the direct term

$$b(\vec{r}_i, t) = 2p_\delta(\vec{r}_i, t) \quad (3.30)$$

is called delay-and-sum [96] and is equivalent to the synthetic aperture focusing technique (SAFT) [97]. The second term of Eq. (3.28) acts as a ramp filter, which suppresses low frequency signals [12]. Backprojecting just the derivative term

$$b(\vec{r}_i, t) = -2t \frac{\partial p_\delta(\vec{r}_i, t)}{\partial t} \quad (3.31)$$

is referred to as filtered backprojection and is often the preferred method because it usually results in sharper images due to the accentuation of high frequency components. In the special case where the distance between the source and the detector positions is much larger than the imaged objects (far field approximation), the derivative term dominates and the weighting factor $d\Omega_i / \Omega_0$ becomes independent of \vec{r} and can thus be neglected for visualization purposes [94].

In the far field approximation, Eq. (3.27) can be discretized to assign each voxel at position \vec{r}_k of the reconstruction grid the value

$$p_0^{(dis)}(\vec{r}_k) = \sum_j \left[p(\vec{r}_j, t_i) - t_i \frac{\partial p(\vec{r}_j, t_i)}{\partial t} \right]_{t_i=t_{jk}=\sqrt{(x_j-x_k)^2+(y_j-y_k)^2+(z_j-z_k)^2}/c}, \quad (3.32)$$

where $p(\vec{r}_j, t_{jk})$ is the measured pressure¹⁰ at time t_i and position \vec{r}_j , t_{jk} denotes the TOF between detector position $\vec{r}_j = (x_j, y_j, z_j)^T$ and voxel position $\vec{r}_k = (x_k, y_k, z_k)^T$ and $\partial p(\vec{r}_j, t_i) / \partial t \approx (p(\vec{r}_j, t_i) - p(\vec{r}_j, t_{i-1})) / (t_i - t_{i-1})$ [59, 75].

The backprojection algorithm is based on the assumption of point detectors. Hence, it can not be readily applied to spherically focused transducers, which typically have active element diameters of several millimeters in mesoscopic applications to achieve tight acoustic focusing. This problem can be overcome by assuming the acoustic focus to be a virtual point detector and backprojecting the signals into the conical volumes above and below the focus [98].

3.3 Materials and methods

3.3.1 Experimental designs of RSOM

RSOM can be implemented in two different configurations. The first version was implemented in transmission mode, where the detector and the laser illumination were located on opposite sides of the sample [11] (see Figure 3.9(a)). The laser source was an actively Q-switched pulsed diode-pumped solid state 532 nm laser (Wedge HB532, Brightsolutions

¹⁰ As the time samples t_i of the measured optoacoustic signals usually do not coincide with t_{jk} , the values $p(\vec{r}_j, t_{jk})$ have to be found by interpolation.

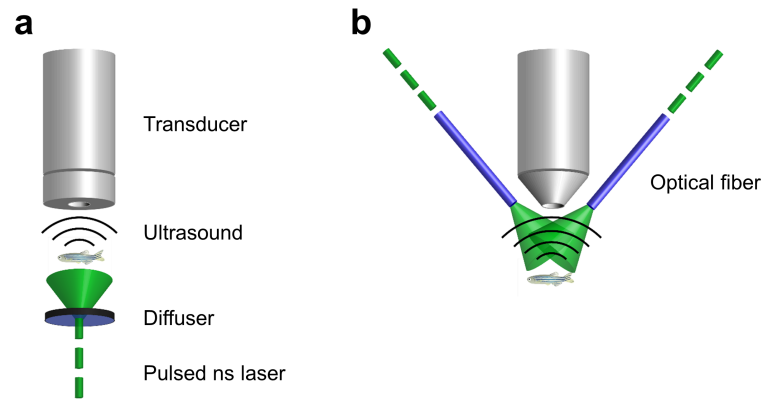


Figure 3.9: Schematic illustration of the two RSOM configurations. (a) Transmission mode design. (b) Epi-illumination mode design. (Adapted from [58].)

SRL; max. repetition frequency: 2 kHz, max. energy per pulse: 1 mJ, pulse width: ~ 1 ns). The laser beam was guided through a diffuser (DG10-600-A, Thorlabs) to expand the beam diameter for homogeneous illumination of the entire sample from below. For fixation purposes, the sample was mounted in pure agar and placed in a water tank with a glass window below the agar block. Optoacoustic signals generated in the sample were detected with a spherically focused 80 MHz ultrasound transducer (Sonaxis; -6 dB bandwidth: 48–108 MHz, active element diameter: 1.5 mm, focal distance: 1.76 mm). The sensor was mounted above the sample to a pair of motorized linear piezo stages (M 683.2U4, Physik Instrumente GmbH & Co. KG) with a travel range of 50 mm and a minimum step size of $0.3 \mu\text{m}$. For acoustic coupling, the water tank was filled with deionized water until the lens of the transducer was immersed. The detector was raster-scanned in the lateral xy -plane above the sample by means of the two linear stages.

The second generation of RSOM was implemented in epi-illumination mode [58] (see Figure 3.9(b)), where illumination and detection were both located on the same side above the sample. Such a configuration allows for large samples or special holder designs to be imaged, including adult zebrafish, tumors grown on mice, cell cultures, etc. In the epi-illumination design, the laser beam was guided onto the sample via a fiber bundle with three arms (1808B, CeramOptec GmbH; NA: 0.22) that were mounted and scanned together with the transducer by the motorized linear stages. To allow for the fibers to be brought closely to the sample, a custom designed conically shaped spherically focused 100 MHz transducer (Sonaxis; -6 dB bandwidth: 44–152 MHz, active element diameter: 1.5 mm, focal distance: 1.65 mm) was used.

In both implementations, the optoacoustic signals were amplified by a low-noise 63 dB amplifier (AU-1291, Miteq) and recorded by a 12-bit high-speed DAQ card (CS122G1, Gage Applied; max. sampling rate: 2 GS/s). A photodiode (DET36A, Thorlabs) collecting laser light reflected from the optical components provided the trigger signal for the data acquisition.

The stage control, signal acquisition and processing as well as the 3D reconstruction was performed in MATLABTM, whereas the image postprocessing was done with Fiji [99].

3.3.2 Scanning scheme and spatial resolution

For imaging, the transducer was raster-scanned in a bi-directional semi-continuous manner above the sample. Along the so-called slow axis, the detector was moved step wise between

successive B-scans, while the latter were continuously scanned along the fast axis. In order to achieve a certain step size Δx between the measurements, the speed of the fast axis stage was set according to

$$v_{stage} = f_{PRF} \cdot \Delta x, \quad (3.33)$$

where f_{PRF} denotes the pulse repetition frequency of the laser. The maximum scanning speed was limited by f_{PRF} and the occurrence of scanning head vibrations at high speeds, which compromised the signals. Because of a delay between the software command to start a B-scan and the actual onset of the stage movement, the alternating B-scans were offset by a step size dependent value and had to be manually corrected.

Furthermore, the DAQ card was used in multi-record mode during the B-scans. More specifically, the A-scans acquired at each measurement position were stored on the internal memory of the DAQ card and transferred to the PC together at the end of each B-scan. Compared to the single-record mode where each A-scan is directly transferred to the PC after acquisition, multi-record acquisition enables scanning at repetition rates of 2 kHz and higher [59].

Because of the Nyquist–Shannon sampling theorem, the spatial sampling step size Δx must be smaller than half of the size of the smallest resolvable feature [30], which corresponds to the lateral resolution of the transducer in the case of RSOM. By imaging 10 μm black polystyrene microspheres (Polybead, Polysciences) embedded in pure agar, the transmission-mode RSOM system equipped with the 80 MHz transducer was characterized to have an axial resolution of 7 μm . The lateral resolution at the focus was found to be 22 μm , whereas a uniform lateral resolution after reconstruction of $\sim 30 \mu\text{m}$ was measured up to a depth of 5 mm [11]. Similarly, the epi-illumination RSOM system was characterized to yield a lateral resolution at the focus of 18 μm and an axial resolution of 4 μm [58]. Thus, the maximum step size in both RSOM systems was $\sim 10 \mu\text{m}$. In practice, a step size of 5 μm was chosen in order to reduce artifacts by oversampling and to increase the SNR, which is proportional to the square root of the number of projections.

3.3.3 Signal processing and reconstruction

Filtering

The measured optoacoustic A-scans were bandpass filtered in the 25–125 MHz range for the 80 MHz transducer and in the 20–180 MHz range for the 100 MHz detector. These ranges differ from the bandwidths provided by the manufacturer because of the receive-only detection mode in optoacoustic imaging and were found to give the best trade-off between noise rejection and SNR¹¹. To reduce ringing artifacts of the filtered signals, an asymmetric bandpass filter was used with a transfer function of the form

$$H(f) = e^{-(f/f_{high})^{n_o}} \cdot \left(1 - e^{-(f/f_{low})^{n_o}}\right), \quad (3.34)$$

where f_{low} and f_{high} denote the low and high cutoff frequencies, respectively, and n_o represents the filter order, which was normally set to four [59]. Additionally, a spatial highpass filter was applied to the B-scans to remove the laser induced optoacoustic signals

¹¹ In section 5.3.2, a method to experimentally measure the detection bandwidth of high-frequency transducers is presented.

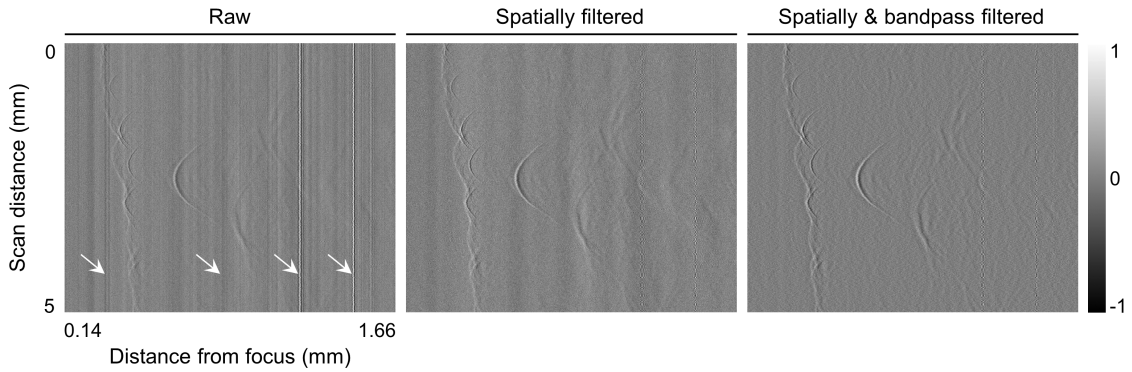


Figure 3.10: Spatial and bandpass filtering of optoacoustic signals. The white arrows indicate laser induced signals occurring at the same time instant. The B-scans were recorded from chicken breast tissue with the epi-illumination system (see section 3.2.7).

that appear as straight lines along the projection dimension. It was realized as an inverted Gaussian centered at zero spatial frequency and multiplied with the 1D spatial FFT of the B-scans. The width of the filter was adjusted to yield an optimum trade-off between effective stripe rejection and maintaining a high SNR at the slowly varying parts of the signals (especially at the tips of the arcs). Figure 3.10 showcases the effect of spatial filtering on the stripe artifacts originating from laser induced signals (see white arrows) and the effect of further bandpass filtering. The B-scan was recorded from the chicken tissue sample shown in Figure 3.7. Finally, a 2D spatial highpass filter was applied to each xy -plane of the reconstruction volume to remove remaining low-frequency artifacts.

Reconstruction using a binary sensitivity field mask

The tomographic reconstruction in RSOM is based on filtered backprojection and the virtual detector technique (see section 3.2.8). In order to increase the reconstruction speed, the interpolation of the optoacoustic signals onto the reconstruction grid was run on a graphics processing unit (GPU). The algorithm performed the 3D interpolation on 2D planes at depths $z_R(i)$, where i is the index of z -positions, and stacked up the resulting interpolated planes to yield a 3D reconstruction volume. In order to reject unwanted signals outside of the sensitivity field, the detector geometry was taken into account by conditioning the backprojected optoacoustic signals before performing the interpolation. Figure 3.11 illustrates the reconstruction geometry of the algorithm. The 2D grid of transducer coordinates was located at the focal points of each measurement position, as defined by the focal time $t_{foc} = F/c + t_{dl}$, where t_{dl} denotes the propagation time of acoustic waves in the glass delay line of the transducer. The virtual detector transformation

$$t_{VD} = t - t_{foc} \quad (3.35)$$

shifted the detection origin of the signals to the focal point and yielded two time and corresponding signal vectors for the near and far field volumes of the sensitivity field, which were separately backprojected into the respective volumes. In the following, the discussion is limited to the backprojection into the far field volume (positive defocus), because this case corresponds to the majority of the RSOM measurements.

In the first version of the reconstruction algorithm, the transducer geometry was accounted for by a binary mask, setting the signals outside of the sensitivity field cone defined by

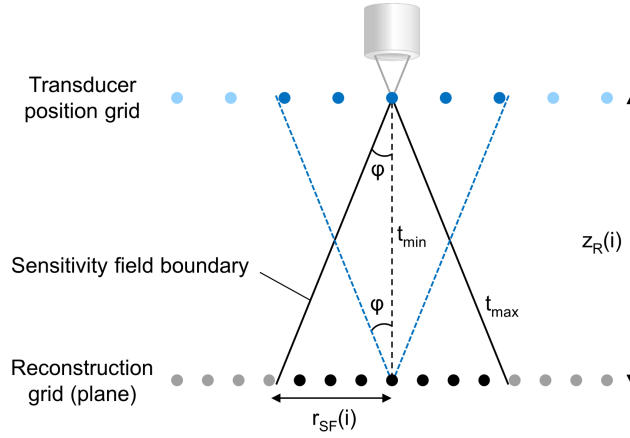


Figure 3.11: Reconstruction geometry in RSOM. Black dots represent grid voxels within the conical sensitivity field for a single transducer position. Dark blue dots correspond to detector positions used for interpolation on a single grid voxel at the central axis.

the half opening angle φ to zero (see Figure 3.11). At a depth $z_R(i)$, the reconstruction grid points located inside the sensitivity field (black dots) were defined by the radius $r_{SF}(i) = z_R(i) \cdot \tan(\varphi)$. The same relationship determined the projections that were used for the interpolation on a specific grid point (dark blue dots). The binary mask for the interpolation was applied by cropping the backprojected signals around a time window between $t_{min}(i) = z_R(i)/c$ and $t_{max}(i) = t_{min}(i)/\cos(\varphi)$.

Reconstruction using a weighted hyperbolic sensitivity field (WHSF) model

The reconstruction with a binary sensitivity field mask yields several inaccuracies. First, it assumes the acoustic focus of the transducer to be point-like, whereas it is rather corresponding to a finite vocal volume. Thus, the binary reconstruction rejects valuable information originating from the focal zone. Second, the sharp cut of the signals at the sensitivity field boundary can lead to ringing artifacts in the reconstruction. Third, since the true sensitivity field amplitude has a smooth radial transition to zero (again, spatial side lobes are neglected in this discussion), the binary mask might dismiss signals outside of the sharp boundary that contributed to the measurements. Finally, the dimensions of the sensitivity field, especially at the focal zone, depend on the frequency content of the measured signals. At higher frequencies, the diameter and length of the focal volume become smaller. Such a frequency dependency cannot be accounted for in case of a point-like focus.

In order to incorporate a realistic model of the transducer into the reconstruction, the sensitivity field was modeled as a hyperboloid. In this geometry, the radial distance $r_{SF}(i)$ at a given depth from the focus $z_R(i)$ was defined by

$$r_{SF}(i) = \frac{d_{foc}}{2} \sqrt{1 + \frac{4 z_R(i)}{d_{foc}^2 \tan^2(\frac{\pi}{2} - \varphi)}}, \quad (3.36)$$

where $d_{foc} = FWHM_{ac}$ is the frequency dependent focal diameter as defined by Eq. (3.22). Figure 3.12 illustrates the idealized sensitivity field geometry (gray) based on a focal point and the hyperbolic geometry for a central frequency of 40 MHz (red) and 100 MHz

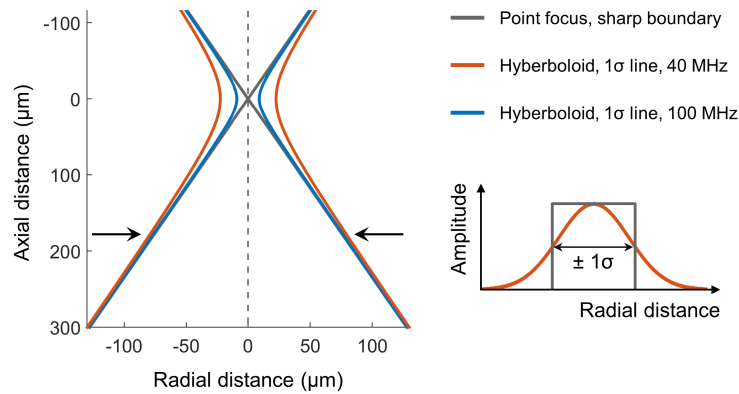


Figure 3.12: Reconstruction in RSOM using a weighted hyperbolic sensitivity field model. The red and blue lines correspond to the $\pm 1\sigma$ levels of the weighted hyperboloids at central frequencies of 40 and 100 MHz, respectively. The gray lines represent the idealized sensitivity field with a point-like focus used in the binary mask model.

(blue), respectively. The hyperboloid features a frequency dependent finite focal diameter and approaches the conical sensitivity field as the distance to the focus increases. Thus, the hyperbolic geometry is expected to have an effect especially on signals originating from the vicinity of the focal volume. Furthermore, a smooth radial amplitude transition from the maximum at the central axis (gray dashed line) to zero was incorporated by weighting the signals with a Gaussian function. The standard deviation of the Gaussian weighted sensitivity field was chosen to coincide with the boundaries of the original cones. Hence, the hyperbolas shown in Figure 3.12 represent the $\pm 1\sigma$ lines of the weighted hyperboloids. Finally, the backprojected signals were weighted with the reciprocal radius of the sensitivity field to account for the increasing number of interpolated projections with an increasing distance to the focus. Without this axial weighting, the signals from greater depths are upscaled compared to signals from the focal region.

Multi-frequency reconstruction and vesselness filtering

As shown in section 3.2.3, the amplitude of optoacoustic signals is proportional to the absorber size under widefield illumination. Furthermore, the high frequencies required to resolve fine structures are more attenuated than low frequencies emitted by bigger objects [100] (see section 3.2.5). As a consequence, large structures yield a higher SNR in optoacoustic images compared to smaller features and often mask fine details.

To improve the visibility of small features in the RSOM reconstruction, a multi-frequency analysis was developed. For this purpose, the detection bandwidth of the employed transducer was divided into several (usually three) sub-bands with equal spacing of the cutoff frequencies¹². These sub-bands were reconstructed sequentially using the respective central frequencies in order to set the corresponding focal diameters $d_{foc}(f)$ for the hyperbolic sensitivity fields. The resulting sub-band reconstructions were processed separately to adjust the visibility of structures on the desired scales and were either summed up or overlaid in different colors. For vasculature imaging, a 2D Frangi vesselness filter [102] was applied to the sub-band images to further reduce noise outside

¹² Alternatively, the sub-bands can be selected to have an equal relative bandwidth in order to reduce ringing artifacts [101].

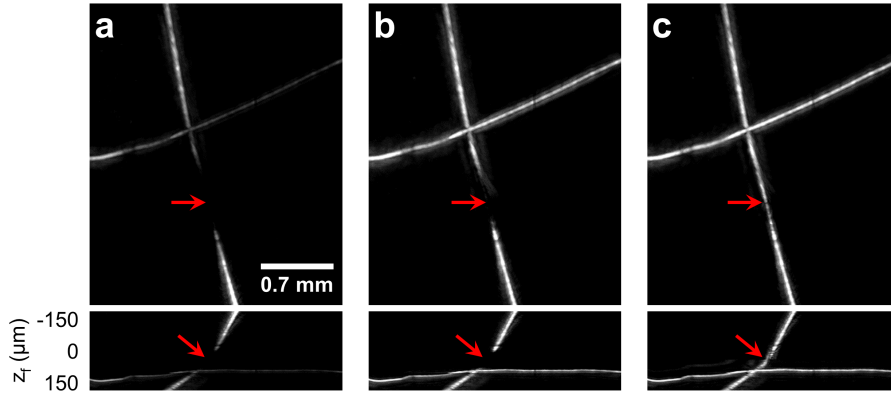


Figure 3.13: RSOM imaging of a 30 μm suture cross phantom. Top and bottom panels illustrate top-view and side-view MAPs, respectively. (a) Binary mask model. (b) Binary mask model incorporating an axial signal weighting. (c) WHSF model. The red arrows indicate signals originating from the focal volume of the detector. z_f denotes the axial distance to the acoustic focus.

of the respective bandwidths and to improve the visibility of the vasculature. The filter scales were adapted to the dimensions of the structures in the respective sub-band images.

3.4 Results

3.4.1 Phantom study

To study the effect of the weighted hyperbolic sensitivity field (WHSF) model on the reconstruction, a 30 μm black suture cross phantom was imaged with the transmission-mode RSOM system. The sutures were embedded in pure agar and one of the sutures was mounted at an angle. The sample was placed in a way to image the horizontal suture in a positive defocus of $\sim 100 \mu\text{m}$, whereas the inclined suture reached through the acoustic focal plane. Figure 3.13 shows maximum amplitude projections (MAP) of the suture cross reconstructed with the original binary mask model (a), the binary mask model including the axial signal weighting (b) and the full WHSF model (c). The upper panels represent the top view, whereas the lower panels correspond to side-view MAPs showing a depth of 300 μm around the focal plane. In the original binary mask reconstruction (a), the horizontal suture has a low SNR, whereas the part of the inclined suture going through the focal volume is not visible. By incorporating an axial weighting (b), the signals closer to the focus are upscaled and the horizontal suture becomes visible, yielding a similar SNR to the inclined suture. However, the signals from the inclined suture corresponding to the focal plane (see red arrows) are still not visible because of the point-like focus of the binary model. Finally, the WHSF model reconstruction (c) is able to visualize the suture within the volume around the focal plane because of the finite focal volume. Furthermore, the laterally weighted sensitivity field leads to a smoother reconstruction of the sample and a reduction of ringing artifacts around the sutures.

3.4.2 Imaging of mouse ear vasculature *ex vivo*

As a next step, the performance of the WHSF reconstruction model was investigated by the transmission-mode RSOM imaging of a mouse ear *ex vivo*. The specimen was excised and mounted in pure agar. Figure 3.14(a) shows a top-view MAP of a $3 \times 3 \text{ mm}^2$

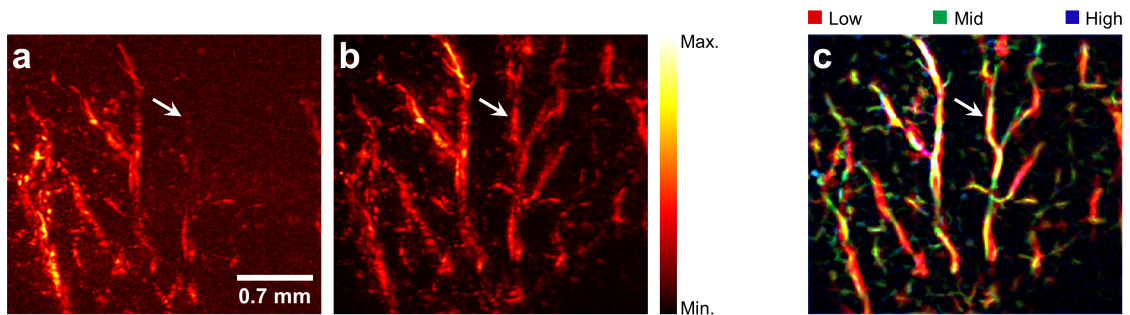


Figure 3.14: RSOM imaging of a mouse ear *ex vivo* using different reconstruction methods. (a) Reconstruction using a binary sensitivity field mask. (b) Reconstruction using the WHSF model. (c) Multi-frequency reconstruction and vesselness filtering showing an overlay of low (red), mid (green) and high (blue) frequencies. The white arrows highlight a blood vessel with different degrees of visibility in the three reconstructions.

FOV, visualizing the vasculature in the ear. For the reconstruction, the original binary mask model without weighting was used. The reconstruction with the WHSF model is depicted in (b), yielding an improved SNR. Moreover, the vasculature in the upper right corner of the FOV is clearly visible in (b), whereas it is mostly masked by noise in the original reconstruction (a). An exemplary vessel that is not observed in (a) but clearly visible in (b) is highlighted by the white arrows. Additionally, a multi-frequency reconstruction was performed, using three sub-bands in the range of 25–58 MHz (low, red color), 58–92 MHz (mid, green color) and 92–125 MHz (high, blue color). An overlay of the three vesselness filtered sub-band images is illustrated in (c). As can be observed, the multi-frequency reconstruction further reduces the noise in the image and leads to an improved visualization of small structures, which are predominantly represented by blue and green colors (high frequencies).

To further demonstrate the small feature enhancement capabilities of the multi-frequency reconstruction, a second excised mouse ear was imaged with the transmission-mode RSOM modality. Figure 3.15(a) depicts a brightfield photograph of an $8 \times 8 \text{ mm}^2$ region of the ear prior to the RSOM imaging. The top-view MAP of the RSOM scan of the same region and using the WHSF reconstruction is presented in (b). A conformity between the vasculature in (a) and (b) can be observed, whereas the RSOM image additionally shows small vascular networks between the prominent vessels. Furthermore, a region characterized by a blurred distribution of blood residue is present in both images, as highlighted by the blue arrows. A $3 \times 3 \text{ mm}^2$ region of interest (ROI) including this blood residue was selected for a second RSOM scan using a step size of $2.5 \mu\text{m}$ for SNR improvement, as shown in (c). The multi-frequency reconstruction using the same frequency bands as in Figure 3.14(c) is depicted as an overlay of the vesselness filtered low (red), mid (green) and high (blue) sub-band images in (d). Similar to Figure 3.14, the multi-frequency reconstruction yields an improved SNR as well as an enhanced visualization of fine details that are mostly masked by low-frequency signals in (c). The fine structure visualization improvement is showcased in (e-f) and (g-h), representing close-ups of two selected ROIs (see white dotted boxes) from the region corresponding to the smeared blood residue. The images of the full bandwidth reconstruction (e) and (g) show blurred low-frequency structures. On the other hand, the corresponding multi-frequency images (f) and (h) visualize fine vessels and details masked by the low-frequency signals in (e) and (g) (indicated by the white arrows).

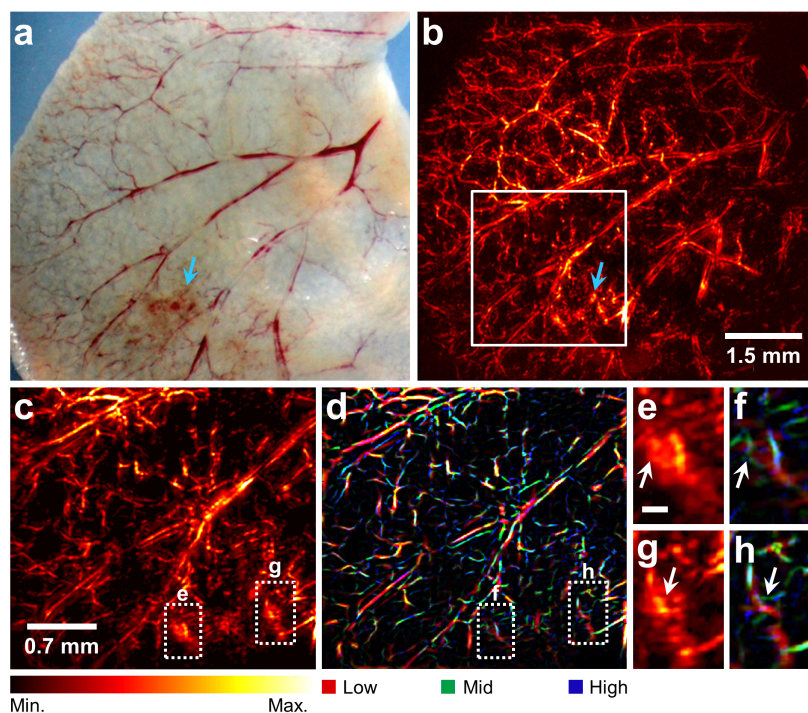


Figure 3.15: RSOM imaging of a mouse ear *ex vivo* comparing the full bandwidth and multi-frequency reconstructions. (a) Brightfield image of the ear. (b) Full bandwidth reconstruction of an $8 \times 8 \text{ mm}^2$ FOV using the weighted hyperbolic sensitivity field model. (c) Scan of a $3 \times 3 \text{ mm}^2$ region of interest (ROI) (indicated by white square in (b)). (d) Multi-frequency reconstruction and vesselness filtering showing an overlay of low (red), mid (green) and high (blue) frequencies. The ROIs marked by the white dotted boxes are shown as close-ups in (e-f) and (g-h). The white arrows highlight small vessels, which are visible in the multi-frequency reconstruction but are masked by low-frequency signals in the broadband scan. Scale bar in (e): $100 \mu\text{m}$.

3.5 Conclusion

This chapter presented a tomographic backprojection method for the 3D reconstruction of RSOM data incorporating a realistic model of the transducer sensitivity field. The developed weighted hyperbolic sensitivity field (WHSF) model has been demonstrated to yield superior results compared to the original reconstruction method using an ideal conical sensitivity field and a binary weighting mask. Through the imaging of a suture phantom, the effects of the axial signal weighting as well as the laterally weighted hyperbolic sensitivity field of the WHSF model were investigated separately. It was confirmed that the axial weighting compensates for an upscaling of signals with axial distance to the focus and leads to an improved visibility of structures closer to the focal plane. Furthermore, the hyperbolic sensitivity field enables the reconstruction of features within the vocal volume, which are not observed if the binary model using a point-like focus is used. These findings were confirmed via the imaging of a mouse ear *ex vivo*, where the WHSF reconstruction yielded an improved SNR and visibility of imaged vasculature compared to the binary mask model. Finally, the developed multi-frequency reconstruction method together with 2D vesselness filtering has been shown to enhance the visibility of small features in RSOM images of mouse ear vasculature by separating fine details from masking low-frequency signals.

In the presented reconstruction algorithm, the GPU based 3D interpolation of the signals on the reconstruction grid was performed for one 2D grid plane at a time. The reconstruction speed could be increased by performing the interpolation directly on a 3D grid. In this case, the sensitivity field could be incorporated by weighting the grid with a simulated 3D map of the transducer's spatial impulse response for each detector position [103]. Furthermore, future implementations might account for a non-uniform optical fluence inside the tissue.

4 Volumetric monitoring of melanophore dynamics *in vivo* using RSOM

In this chapter, the epi-illumination RSOM modality presented previously was applied to the *in vivo* monitoring of endogenous melanophore dynamics and the readout of xenotransplanted frog melanophore stimulation in zebrafish larvae¹. After providing an overview of current limitations and a motivation for this study (section 4.1), a description of melanophore dynamics on the signaling level is given (section 4.2). Next, the sample preparation and the frequency analysis for the identification of cell dynamics related signatures are described (section 4.3) and a simulation of frequency changes upon absorber size change is presented (section 4.4). Subsequently, the results of the *in vitro* and *in vivo* monitoring of melanophore dynamics with RSOM are presented (section 4.5). In the final part (section 4.5.3), the RSOM system is used to sense the stimulation of xenotransplanted frog melanophores in juvenile zebrafish *in vivo*.

4.1 Introduction

Owing to its strong optical absorption over a broad wavelength range (see section 2.1.1), the pigment melanin represents an excellent contrast agent for optoacoustic imaging and has been successfully used in various optoacoustic studies [105–109]. Melanin is present in most organisms, including humans, where it determines the color of skin, hair and eyes. Furthermore, melanin is a major constituent of the skin pigmentation in many non-mammalian vertebrates, including the majority of fish as well as amphibians. In the melanin-containing chromatophores, called melanophores, the pigments are stored in specialized organelles, which are referred to as melanosomes. Certain animals such as cuttlefish or zebrafish are able to adjust their skin color to the environment via a translocation of melanosomes within the melanophores, which is mediated by neuronal and hormonal inputs [110]. In front of a dark background, the dispersion of melanosomes across the melanophores leads to a darker skin color through increased light absorption. Conversely, an aggregation of melanosomes towards the cell centers is triggered by bright background colors, resulting in a lighter appearance of the animals [111].

In zebrafish, melanophores have been demonstrated to show extraordinary behavior such as the migration towards wounds in adult specimens [112]. Moreover, melanoma cells transplanted into adult fish survive and spread, serving as a model to study tumor engraftment and metastasis formation *in vivo* [113]. In order to study processes related to melanophore dynamics including hyperpigmentation and tumor growth, the employed imaging technique has to be able to track and monitor melanophore changes in 3D, *in vivo* and with cellular resolution. However, conventional optical imaging approaches such as brightfield or fluorescence microscopy are limited by the strong light absorption of melanin,

¹ This work was performed in collaboration with Dr. Antonella Lauri, who was responsible for the biology part, and was prepared for publication [104] during the submission of this thesis. The zebrafish used in this study were provided by Prof. Gil Westmeyer.

attenuating light propagating through pigmented tissue. Therefore, the distribution and dynamical changes of multiple melanized structures along the propagation path of light cannot be readily discerned by pure optical techniques [114, 115].

On the other hand, the RSOM modality represents an ideal tool for the 3D monitoring of melanophore dynamics. First, it achieves the necessary spatial resolution to resolve single melanophores, which have a size in the order of 10–40 μm in zebrafish [111]. Second, RSOM relies on widefield illumination, which is less compromised by pigment shadowing, and on acoustic focusing. The latter is little affected by pigmented tissue because acoustic scattering is orders of magnitude weaker than optical scattering and because most tissue components have similar acoustic impedances. Additionally, optoacoustic imaging can provide valuable information in the form of emitted frequencies, which encode the size of measured absorbers (see section 3.2.3). Thus, RSOM offers the ability to study morphological changes of melanophores by identifying specific signatures in the detected frequency spectra (e.g. aggregated melanophores should emit higher frequencies than dispersed cells).

In order to capitalize on the aforementioned abilities, the epi-illumination RSOM system introduced in the previous chapter was applied to the detection of cellular melanophore dynamics, both in frog cells *in vitro* and in zebrafish larvae *in vivo*. The analysis of optoacoustic frequency spectra enabled the distinction of the cellular states of melanophores longitudinally and across entire larvae. Furthermore, by providing a spatially resolved map of frequency shift magnitude, the dynamics of pigmented cells could be quantitatively studied in an entire living fish.

In the final step, the developed detection method of cellular melanophore dynamics was utilized as a readout for stimulated frog melanophores xenotransplanted into the brain of a juvenile zebrafish. This study could pave the way for the development of bioengineered dynamic cell sensors for optoacoustic imaging based on melanosome translocation.

4.2 Background on melanophore pigment translocation

Several classical neurotransmitters and hormones are involved in regulating the translocation of melanosomes inside melanophores, including melatonin, noradrenaline, serotonin and melanocyte stimulating or concentrating hormones (α -MSH and MCH, respectively) [116, 117]. These molecules bind to specialized G-protein-coupled receptors (GPCRs) expressed at the cell surface of melanophores and regulate the intracellular concentrations of cyclic adenosine monophosphate (cAMP) and calcium [111]. These molecules act as secondary messengers and in turn control melanosome translocation inside the cell by influencing the cytoskeletal transport machinery, as illustrated in Figure 4.1(a). More specifically, the translocation movement of melanosomes occurs mainly along radially oriented microtubules, where the associated motor proteins responsible for retrograde (aggregation) and anterograde (dispersion) transport are dynein and kinesin, respectively [118]. Furthermore, randomly oriented actin filaments together with the motor molecule myosin are involved in peripheral melanosome transport. The motor proteins with the highest activity ultimately determine the direction of melanosome transport [119].

In the case of melanosome dispersion, the binding of α -MSH leads to an up-regulation of intracellular cAMP, which in turn results in an activation increase of kinesin. These motor proteins move towards the plus end of the microtubules located at the cell periphery, resulting in an anterograde movement and thus dispersion of melanosomes. As depicted

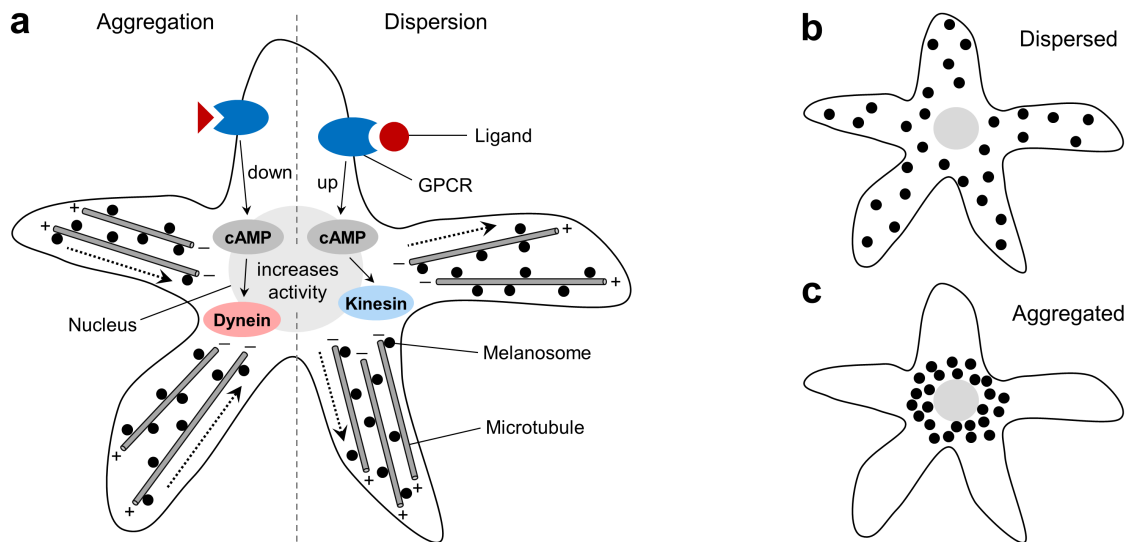


Figure 4.1: Pigment translocation in melanophores. (a) Schematic depiction of the intracellular control of melanosome translocation. The direction of melanosome transport is indicated by the dotted black arrows. (b) Melanophore in the dispersed state. The melanosomes are distributed throughout the cell. (c) Melanophore in the aggregated state, where the melanosomes concentrate around the nucleus.

in Figure 4.1(b), the melanosomes are distributed throughout the melanophores in the dispersed state. On the other hand, melanosome aggregation is triggered by the binding of a dedicated ligand (e.g. MCH), causing a down-regulation of cAMP and a subsequent activation increase of dynein. Such motor molecules transport melanosomes towards the minus end of the microtubules located at the cell center, resulting in a retrograde pigment movement [119]. Figure 4.1(c) illustrates a melanophore in the aggregated state, where the melanosomes are concentrated around the cell nucleus.

In many teleosts and amphibians, the experience of a dark background leads to a secretion of α -MSH by specialized cells in the pituitary gland [120]. Conversely, melanosome aggregation in fish is triggered by a light background through the release of MCH from the hypothalamus [111, 121].

The process of pigment translocation is demonstrated by Figure 4.2 on the example of melanosome aggregation in living 6 dpf wildtype zebrafish larvae following MCH treatment. The brightfield microscopy observation of the head region before and after 10 min treatment with 30 μ mol of rat-derived MCH (M4542, Sigma-Aldrich) is illustrated in (a) and (b), respectively. Close-ups of the regions indicated by the dashed white boxes are provided by the insets, revealing a relocation of melanosomes towards the centers of the melanophores. Here, individual cells are labeled with different colors. Figure 4.2 (c) shows the quantification of the mean pigmented area of single melanophores before and after the MCH treatment. The aggregation resulted in a $\sim 50\%$ reduction in pigmented area size, as found by manual segmentation of individual cells ($n = 25$, error bars denote the respective standard errors of the mean (SEM)).

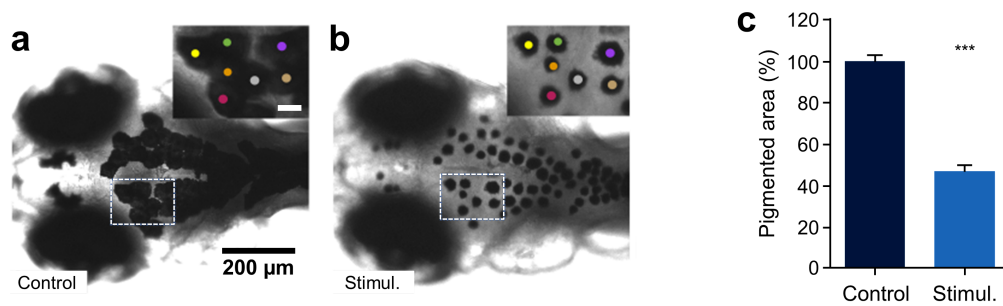


Figure 4.2: Brightfield observation of MCH-mediated melanosome aggregation in zebrafish larvae *in vivo*. (a-b) Melanophores in 6 dpf zebrafish larvae before (a) and after (b) MCH exposure. The insets show magnifications of the regions indicated by the white dashed boxes, whereas the cell identities are color-coded. Scale bar: 30 μm (c) Quantification of the mean pigmented area of single cells before and after MCH treatment (***) indicates $p < 0.001$, paired t-test. Error bars represent standard errors of the mean (SEM)).

4.3 Materials and methods

4.3.1 Setup, sample handling and image processing

For optoacoustic imaging, the epi-illumination RSOM system introduced in chapter 3 was used, incorporating a 100 MHz transducer. Signal processing and 3D reconstruction followed the descriptions in section 3.3. Usually, the step size of the raster-scan was set to 4 μm, corresponding to an acquisition time of about 10 min for a $6 \times 6 \text{ mm}^2$ FOV. For the imaging of xenotransplanted cells *in vivo*, the acquisition speed was increased by using a step size of 10 μm, resulting in an acquisition time of $< 4 \text{ min}$ for a $6 \times 6 \text{ mm}^2$ scan. In contrast to the zebrafish measurements, *Xenopus laevis* cell cultures were imaged in the acoustic focal plane of the transducer such that no tomographic reconstruction was required. The time-resolved signals were cropped around the focal time of the transducer and directly projected along the depth dimension to obtain top-view MAPs.

For imaging, the zebrafish were embedded in 1% low melting agarose inside petri dishes. Acoustic coupling during the control measurements was achieved by filling the petri dish with 'fish water' [122] in case of zebrafish and phosphate buffer saline (PBS) in case of cell culture imaging. For the stimulation of melanosome aggregation, the PBS or fish water was replaced by the respective stimulant solution, which also served as coupling medium. All procedures involving animals conformed to the institutional guidelines and were performed with approval from the Government of Upper Bavaria.

Each set of images comparing measurements before (control) and after stimulation of melanosome aggregation was processed identically and the individual histograms were normalized to saturate a certain percentage of pixels in both images.

4.3.2 Optoacoustic frequency analysis

For the optoacoustic frequency analysis, the raw signals were bandpass filtered and the frequency spectra were summed up to form cumulative power spectra (CPS). The signals were selected for processing according to their maximum amplitude in order to constrain the analysis to melanin related signals. Only signals with a peak amplitude larger than a certain threshold value were considered for further processing. The resulting CPS were smoothed using a moving average filter to remove fine fluctuations while keeping the global trend. Subsequently, the individual CPS were normalized to the areas under the

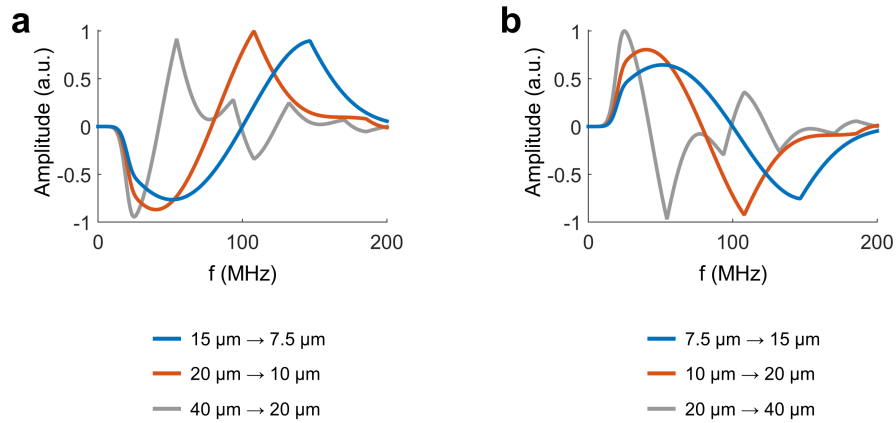


Figure 4.3: Simulation of optoacoustic frequency shifts generated by spherical absorbers with changing size. The difference of the individual frequency spectra in the case of (a) contracting and (b) expanding absorbers are shown. Initial absorber diameters of 15, 20 and 40 μm are illustrated in blue, red and gray colors, respectively. (Adapted from [104].)

curves. Finally, the difference spectra of the CPS were calculated and normalized to the maximum value of the control CPS.

A spatially resolved map of optoacoustic frequency shift magnitude was generated by processing the 3D reconstructions of the imaged zebrafish. The frequency analysis was performed on the signals defined as the 1D depth (z -dimension) profiles at each lateral (xy -dimension) position of the reconstruction grid. First, melanin related signals from the control measurement were selected by choosing signals with a peak amplitude larger than 8% of the maximum amplitude of the whole reconstruction. For each xy -position corresponding to a selected signal, the local CPS was calculated in a neighborhood of 13×13 xy -positions. For the frequency shift map, the individual local CPS were normalized to their peak values instead of the areas for easier thresholding and the local difference spectra were calculated. In the resulting 2D map, pixels were set to zero if the corresponding local difference spectra had a negative minimum value or a maximum value below 8% of the control CPS peak, both in the 70–200 MHz range. Otherwise, the pixels were assigned the peak values of the local difference spectra normalized to the maxima of the control CPS.

4.4 Simulation of frequency shifts generated by absorber size changes

As discussed in section 3.2.3, the size of optical absorbers determines the frequency content of the generated optoacoustic signals. More specifically, smaller objects generate higher optoacoustic frequencies than bigger structures due to the smaller width of the corresponding time signals. Consequently, melanophore aggregation is expected to result in a shift towards higher frequencies in the measured optoacoustic signals following a reduction in pigmented volume. To study the effect of optoacoustic absorber size reduction on the generated frequencies, a simulation was performed assuming fluid spherical absorbers (see appendix A for the used MATLABTM script). The signals were bandpass filtered in the 20–180 MHz range, mimicking the 100 MHz transducer employed in RSOM. Furthermore, acoustic attenuation in water as well as the finite laser pulse width were taken into account. Finally, the frequency spectra were normalized to the areas under the curves

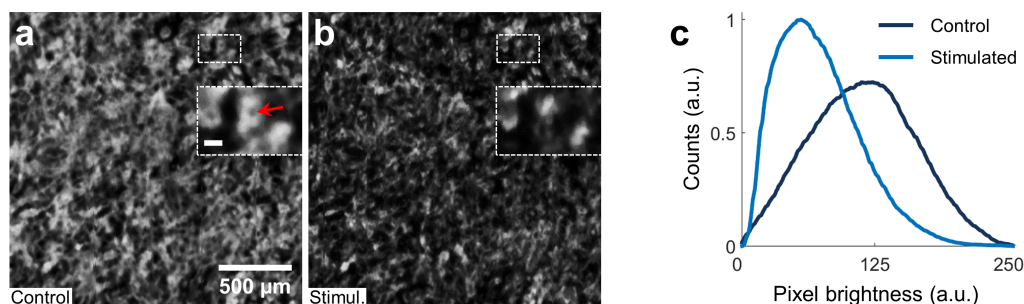


Figure 4.4: Optoacoustic imaging of MCH-mediated melanosome aggregation in cultured *Xenopus laevis* melanophores. Optoacoustic top-view MAPs of the cell layer before (a) and after (b) 40 min of MCH treatment are shown. The insets represent close-ups of the regions marked by the dashed white boxes, showing individual melanophores. The nucleus of one of the cells in the control state is indicated by the red arrow. Scale bar: 50 μm . (c) Normalized pixel brightness histograms of the control (dark blue) and stimulated (light blue) images, showing a shift to lower values upon melanosome aggregation.

and subtracted from each other to form difference spectra.

First, the effect of a reduction in absorber size of 50% was simulated. Figure 4.3(a) shows the difference spectra for an initial absorber diameter of 15, 20 and 40 μm , which are illustrated in blue, red and gray, respectively. A common feature in all spectra is a negative peak at low frequencies followed by a positive peak at higher frequencies. Such a bipolar shape indicates a shift from lower to higher frequencies, whereas the distance between the two peaks in each spectrum scales inversely with the initial absorber diameter. In the case of the 40 μm absorber, additional negative and positive peaks following the initial bipolar signature are observed. These secondary peaks result from sidelobes in the frequency spectra, which are located within the detection bandwidth for frequencies generated by large objects. Second, the converse effect of an increasing absorber diameter was simulated, as shown in Figure 4.3(b). The resulting difference spectra exhibit the inverse shape to the case of absorber shrinkage, yielding a positive peak followed by a negative minimum.

These simulations demonstrate that reduction and increase of absorber sizes result in distinct signatures in the corresponding frequency difference spectra. Consequently, melanosome aggregation and dispersion processes are expected to be identifiable through specific frequency shifts, representing a superposition of numerous single-absorber spectra as depicted in Figure 4.3.

4.5 Results

4.5.1 Melanosome aggregation in frog melanophores *in vitro*

Initially, the ability of RSOM to resolve single melanophores and to capture melanosome dynamics was investigated by imaging a dense layer of wildtype *Xenopus laevis* melanophores, which exhibit cell sizes in the range of 50–100 μm [123]. Figure 4.4(a) shows the top-view MAP of a $2 \times 2 \text{ mm}^2$ region of the cell layer. As can be seen in the inset, the RSOM modality is capable of resolving single melanophores with high contrast as well as the cell nuclei, which are characterized by an absence of optoacoustic signals (see red arrow). To induce melanosome aggregation, the cells were washed with PBS and treated with 30 μmol of MCH for 40 min. The aggregation effect is clearly observed in the optoacoustic scan

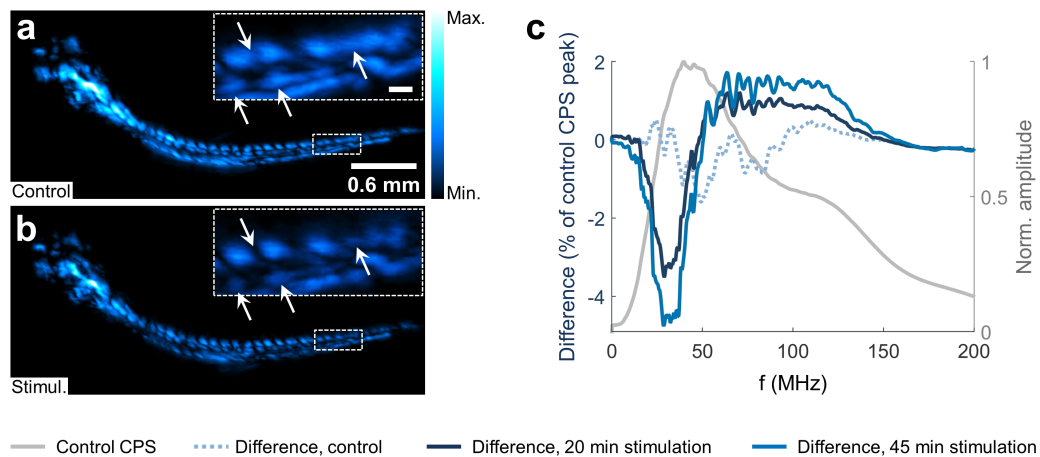


Figure 4.5: Optoacoustic imaging and frequency analysis of a 6 dpf wildtype zebrafish larva *in vivo* before and after MCH treatment. (a-b) Optoacoustic top-view MAPs of the fish before (a) and after (b) 45 min of MCH stimulation. The insets show a magnification of the trunk region indicated by the dashed white boxes. White arrows highlight locations of prominent melanosome aggregation characterized by a reduction of pigmented areas and a widening of intermediate gaps. Scale bar: 50 μm . (c) Optoacoustic frequency analysis of the raw signals. The gray curve represents the CPS of the control measurement. Dark and light blue curves show the difference of the stimulated and control measurements for 20 min and 45 min of MCH stimulation, respectively. The dotted light blue curve corresponds to the difference of two consecutive control measurements. (Adapted from [104].)

of the treated cells, as shown in (b). As a confirmation of the melanosome aggregation detected by RSOM, a shift of the normalized pixel brightness histogram towards lower values is observed in (c). This shift between the control (dark blue) and stimulated (light blue) measurements originates from the reduced total area occupied by signal generating melanin after aggregation.

4.5.2 Frequency based optoacoustic monitoring of melanophore dynamics *in vivo*

Stimulation with MCH

As RSOM could efficiently detect melanosome aggregation in large frog cells *in vitro*, the question was addressed whether melanophore dependent skin lightening could be resolved *in vivo*, where pure optical imaging modalities commonly fail to provide a reliable mapping of melanophores. For this purpose, a 6 dpf wildtype zebrafish larva was imaged *in vivo* with RSOM and treated with 30 μmol of MCH dissolved in fish water. The optoacoustic top-view MAPs of the specimen before and after 45 min of MCH stimulation are presented in Figure 4.5(a) and (b), respectively. Because of their high content of melanin, eyes are easily recognized in the optoacoustic images. Moreover, melanophores forming the different pigmented stripes of the fish yield strong optoacoustic contrast and can be discerned. Similarly to the *in vitro* study, a reduction of apparent melanophore size upon MCH treatment can be observed in (b), resulting from melanosome aggregation in the entire fish. This effect is emphasized by the insets representing close-ups of the region at the tail marked by the dashed white boxes. After the MCH treatment, the gaps between the cells become larger, whereas the sizes of the pigmented areas reduce (see white arrows).

Next, a frequency analysis was performed on the raw signals of the entire specimen. The gray curve in Figure 4.5(c) shows the CPS of the control measurement, which has a peak at around 43 MHz. According to Eq. (3.17), this frequency peak corresponds to an absorber size of $\sim 23 \mu\text{m}$, matching the average size of endogenous zebrafish melanophores [111]. The dark and light blue curves represent the difference spectra (stimulated minus control CPS) after 20 min and 45 min MCH treatment, respectively, which were normalized to the peak value of the control CPS. For the frequency analysis, only melanin-related signals with a peak amplitude $\geq 15\%$ of the global maximum were considered. Both difference spectra feature a pronounced negative peak at ~ 30 MHz and a positive plateau approximately in the 50–140 MHz range. As found from the simulations, such a bipolar shape of the difference spectra indicates a shift towards higher frequencies as a result of melanosome aggregation. Moreover, the curve corresponding to the longer MCH treatment (light blue) exhibits a similar frequency profile as the shorter stimulation (dark blue), albeit with higher peak-to-peak amplitude. The increased amplitude of the 45 min difference spectrum matches the expectation that a longer MCH treatment leads to a stronger melanosome aggregation and hence results in a higher frequency shift magnitude. Finally, the dotted light blue curve in (c) shows the difference spectrum of two consecutive control measurements of the fish (i.e. no stimulation)². Compared to the stimulation curves, it does not show a bipolar shape indicative of a directed frequency shift and yields a lower peak-to-peak amplitude. Hence, it can be concluded that the dynamic aggregation of melanosomes upon MCH treatment yields a clear signature in the optoacoustic frequency spectra and can be captured by RSOM *in vivo* using the developed frequency analysis.

Stimulation through background adaption

In the next step, it was tested whether RSOM could be used to study melanophore dynamics in a more physiologically relevant context. To this end, melanosome dispersion was induced in wildtype zebrafish larvae during background adaption, as skin lightening due to melanosome aggregation naturally occurs during this type of zebrafish behavior [111]. Initially, two 5 dpf wildtype zebrafish were kept in the dark over night to induce melanosome dispersion. The dark adapted fish were subsequently imaged with RSOM on a black background and in darkness to maintain the pigment dispersion. Figure 4.6(a) depicts the optoacoustic top-view MAP of one of the dark adapted fish. Afterwards, the fish were exposed to light for 30 min to trigger melanosome aggregation and imaged again while facing a white background. Melanosome aggregation could be observed in the entire specimen, as can be seen in the optoacoustic image of the light adapted fish shown in (b). Examples of distinctive reduction in pigmented area after background adaption are highlighted by the white arrows in the insets corresponding to the dashed white boxes at the tail. The result of the frequency analysis performed on both imaged specimens is presented in (c). Signals with a peak amplitude of $< 15\%$ of the global maximum were discarded to reduce noise in the CPS. Again, the gray curve represents

² The control measurements were performed with different input range values of the DAQ card. This was done to study the effect of a slight change in the imaging parameters between the scans on the frequency analysis without having to physically alter the settings of the RSOM components. Furthermore, because of the different noise levels near the bandpass filter cutoff frequencies, the control difference spectrum is only shown in the range of 15–150 MHz, where it is accurate to be compared to the stimulation curves.

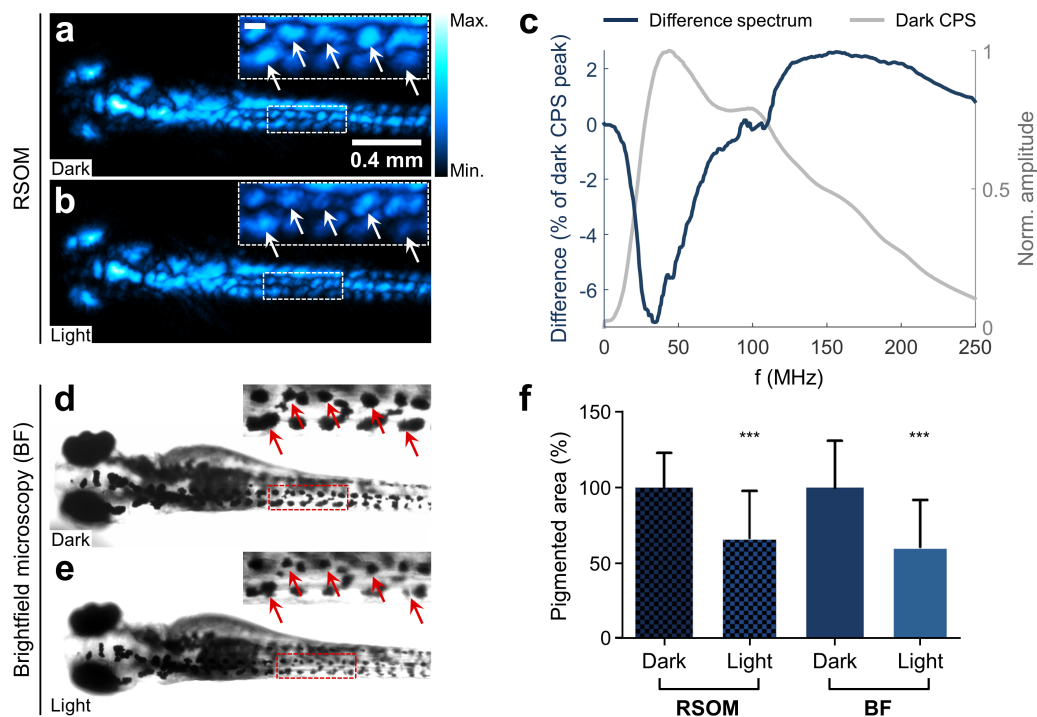


Figure 4.6: Optoacoustic imaging and frequency analysis of light background-induced melanosome aggregation in dark-adapted 5 dpf zebrafish larvae *in vivo*. (a-c) **RSOM imaging.** Top-view MAPs are shown for the dark (a) and light (b) background adapted zebrafish. Insets depict a magnified region at the tail, as indicated by the dashed white boxes. Arrows indicate prominent changes in pigmented area. Scale bar: 50 μ m. (c) Frequency analysis of the raw signals. The gray curve shows the CPS of the dark adapted fish, whereas the blue curve represents the difference of light and dark state CPS. (d-e) **Brightfield microscopy observation of background induced melanosome aggregation in the same specimens after the RSOM imaging.** (d) Dark adapted fish. (e) Light adapted fish showing global melanosome aggregation. Insets and red arrows mark the same cells and clusters as in (a-b). (f) **Quantification of the mean pigmented area of melanophores and cell clusters before and after background adaption in the insets of the RSOM and brightfield images** (***) indicates $p < 0.001$, paired t-test. Error bars represent the SEM). (Adapted from [104].)

the CPS of the dark adapted (i.e. dispersed) state, whereas the blue curve shows the difference of the light and dark adapted CPS. As for the MCH stimulation, a clear shift towards higher optoacoustic frequencies can be observed, indicative of a contraction of the effective absorber sizes as 'seen' by the RSOM modality and matching the simulation results discussed in section 4.3.

Following the RSOM imaging, the same specimens were adapted again to darkness and the background adaption experiment was repeated under a brightfield microscope. The brightfield images of the same fish that is shown in (a-b) are presented in Figure 4.6(d) and (e), corresponding to the dark and light adapted state, respectively. A similar degree of melanosome aggregation as in the RSOM measurement was observed. Besides validating the aggregation effect seen in the optoacoustic images, the brightfield experiment also served as a blindness test, since melanosome translocation is triggered through visual stimuli. The aggregation observed in the brightfield images therefore confirms that the zebrafish were not blinded or affected by the laser irradiation during the RSOM scans.

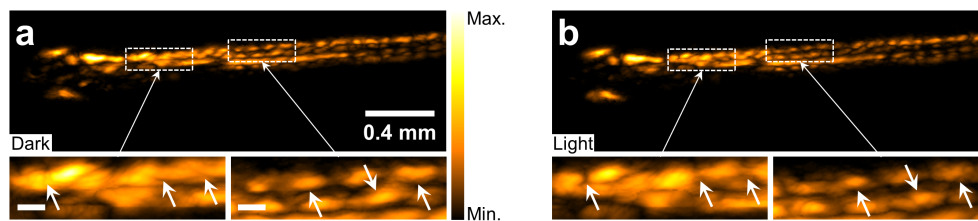


Figure 4.7: 3D optoacoustic imaging of light background-induced melanosome aggregation in a dark-adapted 5 dpf wildtype zebrafish larva *in vivo*. MAPs along a 60° side view of the 3D reconstruction are shown for the dark (a) and light (b) adapted fish. The arrows in the insets mark locations of prominent aggregation effects. Scale bars: $50\ \mu\text{m}$. (Adapted from [104].)

The melanophores marked by the red arrows correspond to the same cells highlighted in the optoacoustic images, demonstrating that RSOM is indeed capable of imaging single pigmented cells and clusters in zebrafish *in vivo*. Finally, the melanophores visible in the four insets were manually segmented to extract the pigmented area of each cell or cluster. Figure 4.6(f) illustrates the mean pigmented areas in the optoacoustic and brightfield images before and after background adaption (RSOM: $n = 9$, brightfield: $n = 19$, error bars denote the respective SEM). A reduction of $\sim 40\%$ upon melanosome aggregation was found for both modalities, confirming once more that RSOM can reliably capture melanophore dynamics *in vivo*.

The key advantage of RSOM in tracking melanophores compared to other optical modalities is the high tissue penetration and its insusceptibility to shadowing effects due to the broad illumination. Hence, it is possible to observe melanosome translocation simultaneously at different depths and under different angles from the 3D reconstructions. This feature is showcased by Figure 4.7, which illustrates 60° view MAPs of the reconstructed dark (a) and light (b) adapted fish. From this perspective, all pigment stripes can be discerned otherwise partially disguised in the top-view images or under other angles. Again, melanosome aggregation is observed in several cells, as indicated by the white arrows. This 3D method can prove valuable when imaging dynamic melanophores *in vivo* as compared to conventional optical microscopy approaches, whose volumetric information is limited as discussed above.

Frequency shift map of background-adaption-induced melanosome aggregation

The developed frequency analysis was so far only applied to the raw signals of entire data sets. Thus, the observed frequency shifts were indicative of the average strength of melanosome aggregation in the whole specimens. In order to test whether certain anatomical locations in the fish generated stronger frequency shifts than other regions and whether these locations coincide with regions showing a strong reduction of pigmented areas, a 2D map of frequency shift magnitude was created (see section 4.3.2). This analysis was performed on the other specimen of the two zebrafish imaged with RSOM during background adaption as shown previously. Additionally, in both the dark and light adapted optoacoustic images, the pigment clusters in the trunk region of the fish were manually segmented and the pigmented areas were obtained. From the results, a 2D area change map was created and compared to the frequency shift map. Figure 4.8 illustrates the different 2D maps calculated from the zebrafish. The bottom panel represents the top-view MAP of the head region (eyes not shown) and the trunk, serving as anatomical

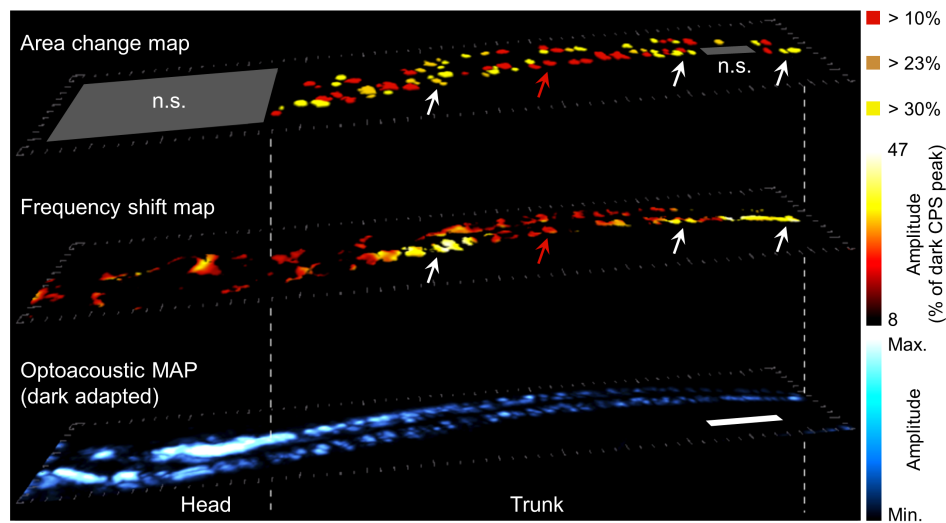


Figure 4.8: 2D mapping of melanophore aggregation via optoacoustic frequency shifts during background adaption in zebrafish larvae *in vivo*. Bottom panel: optoacoustic top-view MAP of the head and trunk region of the fish. Scale bar: 300 μm . Middle panel: 2D map of optoacoustic frequency shift magnitude. White and red arrows mark regions of strong and weak frequency shifts, respectively. Top panel: 2D map of pigmented area change during background adaption based on manual segmentation. The gray boxes indicate regions that could not be reliably segmented (n.s.). Red, fawn and yellow colors represent area changes of 10, 23 and 30 %, respectively. (Adapted from [104].)

reference. The frequency shift map is shown in the mid panel, where red areas indicate weak frequency shifts and yellow to white colors represent strong shifts. As can be observed, the strongest frequency shifts during background adaption originated from defined regions in the trunk and the tail of the fish (see white arrows), whereas only little shifts occurred in the head region. The top panel depicts the segmentation based area change map, where gray boxes (labeled as 'n.s.') indicate regions that could not be reliably segmented. Red, fawn and yellow colors denote area changes of 10, 23 and 30 %, respectively³. When comparing both maps in the trunk region, a correlation between higher or lower frequency shift magnitudes and larger or smaller area changes can be identified. For instance, the clusters showing a reduction in pigmented areas of more than 23 % and 30 % probably contributed the most to the global frequency shift observed after background adaption (see Figure 4.6). Furthermore, an extended region exhibiting small area changes can be correlated to low frequency shift magnitudes (indicated by the red arrows).

The results demonstrate that RSOM is capable of providing spatially resolved information about melanophore dynamics *in vivo* in a non-invasive manner and without the need of tracking single cells.

4.5.3 Bioengineered pigment clustering sensors for dynamic optoacoustic imaging

In the previous section, the RSOM modality together with the frequency analysis was successfully utilized to monitor melanophore translocation *in vivo*. In the next step, this capability was further exploited to serve as a non-invasive and label-free readout of the

³ These particular values were chosen because they resulted in an optimum visualization.

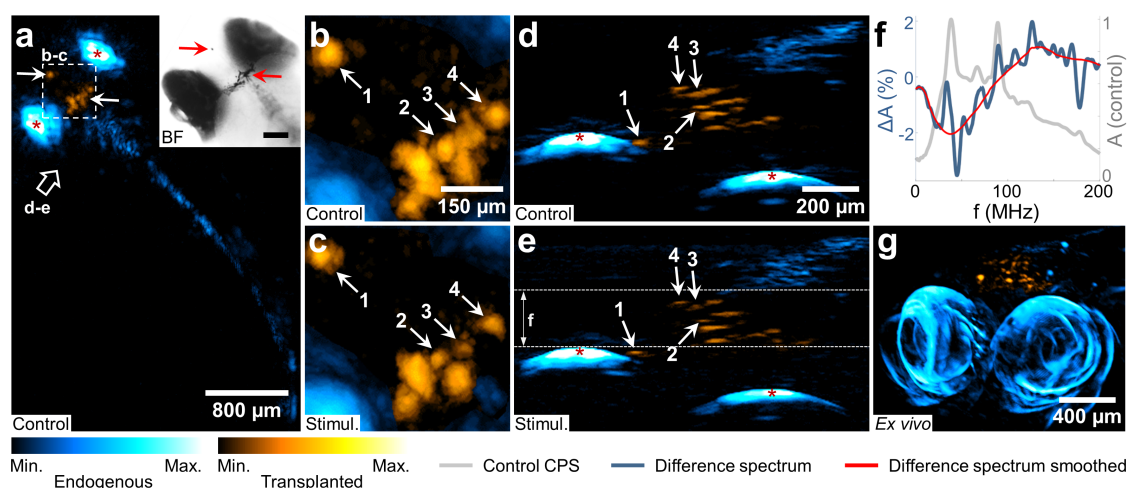


Figure 4.9: Optoacoustic *in vivo* monitoring of melatonin-triggered melanosome aggregation in wildtype *Xenopus melanophores* xenotransplanted into a juvenile Casper™ zebrafish brain. (a) RSOM top-view MAP of the untreated fish, showing the native pigments in blue and the transplanted melanophores in orange. The inset represents a brightfield microscopy (BF) image of the head region. Scale bar: 200 μm . Red and white arrows mark the xenotransplanted cells. (b-c) Close-ups of the head region indicated by the dashed white box in (a). The images illustrate the transplanted cells before (b) and after (c) melatonin stimulation, showing a clear melanosome aggregation. The white numbered arrows label four transplanted cells for reference purposes. (d-e) MAPs of a 90° side view of the head region where the same four transplanted cells are labeled. (f) Optoacoustic frequency analysis of the raw signals corresponding to the volume highlighted by the dashed white lines in (e). The gray curve shows the CPS of the control measurement, whereas the blue curve represents the difference spectrum and the red curve illustrates a local regression fit to the difference spectrum. (g) Multi-orientation RSOM (MORSOM) scan of the fish after the RSOM imaging *ex vivo*, serving as an anatomical reference. (Adapted from [104].)

aggregation response of wildtype *Xenopus laevis* melanophores xenotransplanted into the midbrain of a juvenile Casper™ zebrafish [124] upon stimulation with the hormone melatonin.

Figure 4.9 summarizes the results of the RSOM imaging and frequency analysis of melatonin-induced pigment aggregation in wildtype transplanted frog (WTF) melanophores *in vivo*. The top-view MAP of the control measurement of the zebrafish before melatonin stimulation is shown in (a). Throughout this figure, endogenous pigments are illustrated in blue, whereas WTF melanophores are shown in orange colors. As can be seen in (a), the eyes (labeled with ‘*’) as well as endogenous pigments along the tail are observed, while the transplanted cells are identified in the head region between the eyes. The inset in (a) depicts a brightfield microscopy image of the head region of the same specimen. Red and white arrows label the transplanted cells in both images for reference purposes. Figures 4.9(b-c) represent close-ups of the WTF cell containing head region indicated by the dashed white square before (b) and after (c) 30 min treatment with externally administered melatonin. Four single transplanted melanophores are labeled with numbered white arrows to facilitate visual comparison. From the close-ups, a clear reduction of visualized absorber sizes can be observed, resulting from melanosome aggregation in the WTF cells.

Capitalizing on the tomographic nature of RSOM, the triggered melanosome aggregation can additionally be studied in 3D. Figures 4.9(d-e) show MAPs from a 90° angle of the

head region of the fish, as indicated by the big white arrow in (a). The transplanted melanophores are distributed throughout a depth of approximately $300\ \mu\text{m}$ of the brain. Furthermore, an absorber contraction effect can be seen also from this angle.

As indicated by the dashed white lines in (e), a frequency analysis was conducted using the raw signals corresponding to the volume occupied by the WTF cells. In (f), the CPS of the control measurement is illustrated in gray, whereas the difference spectrum is shown in blue. The red curve represents a local regression fit to the difference spectrum to highlight the global trend. As in the previous cases, the difference spectrum yields the bipolar shape indicative of a shift from lower to higher frequencies, matching the overall shape of the absorber contraction simulations (see section 4.3).

Finally, the zebrafish was imaged with a multi-orientation implementation of RSOM (MORSOM⁴, [125]) *ex vivo*, as depicted in Figure 4.9(g), where the sample was rotated by 360° in 10° steps between successive RSOM scans. Such a multi-view approach overcomes the 3D imaging restrictions of RSOM originating from the limited angular acceptance of the single element transducer, which is in the order of $50\text{--}60^\circ$. As can be seen from the side-view MAPs in (d-e), the axial resolution of RSOM is much better than the lateral resolution, yielding elongated structures along the xy -plane. Furthermore, vertical structures (i.e. oriented along the acoustic axis) cannot be visualized due to the directivity of optoacoustic signals⁵. Thus, only the upper and lower edges of the zebrafish eyes are visible, whereas the side walls do not appear in the reconstruction. Whereas RSOM imaging proved sufficient for the analysis of melanophore dynamics, the MORSOM technique might facilitate the identification of transplanted cells, as it provides an isotropic spatial resolution and the visualization of arbitrarily orientated structures. Consequently, Figure 4.9(g) provides a superior visualization of the zebrafish eyes and the WTF cells and serves as an anatomical reference to the RSOM images.

4.6 Conclusion and outlook

In this chapter, epi-illumination RSOM has been demonstrated to be suitable for the non-invasive and label-free monitoring of dynamic melanophore changes in entire zebrafish larvae *in vivo* based on the strong optoacoustic signal generation of melanin. The RSOM modality yielded sufficient contrast and cellular resolution to visualize individual melanophores in 3D and was confirmed not to interfere with the physiological behavior of zebrafish during the imaging. As shown for hormonal stimulation and background adaptation, the analysis of optoacoustic frequency shifts in the raw datasets revealed an aggregation of melanosomes in the entire specimens. Furthermore, a spatially resolved 2D map of frequency shift magnitude provided a quantitative insight into melanophore

4 For MORSOM imaging, the sample was mounted in an agar column held by a syringe with 4.5 mm inner diameter. The syringe was connected to a rotation stage (RS-40, PI MICOS), which rotated the sample by 360° in defined steps around an axis orthogonal to the acoustic axis of the detector. At each angular position, an RSOM scan was performed within a plane parallel to the rotation axis using a conically shaped 50 MHz transducer (Sonaxis; $-6\ \text{dB}$ bandwidth: $10\text{--}90\ \text{MHz}$, active element diameter: $3\ \text{mm}$, focal distance: $3\ \text{mm}$). The 3D reconstructions from the different angular views were finally combined to yield an isotropic spatial resolution of $\sim 17\ \mu\text{m}$ in the plane orthogonal to the sample rotation axis and $\sim 44\ \mu\text{m}$ along the rotation axis dimension, as characterized in [125].

5 Due to the superposition of optoacoustic signals from neighboring locations, objects with high aspect ratios (e.g. blood vessels) emit directed acoustic waves similarly to the radiation of electromagnetic waves by antennas [73]. Therefore, elongated structures of flat surfaces can only be detected in a perpendicular orientation within the acceptance angle of the transducer.

dynamics without the necessity of tracking individual cells.

Overall, the developed method can prove valuable in studying dynamic changes of melanophores in 3D compared to pure optical techniques, which have limited 3D monitoring capabilities in the case of pigmented cells.

In the second part, the developed method for the detection of cellular melanophore dynamics was applied to the *in vivo* imaging of wildtype frog melanophores, which were xenotransplanted into a juvenile zebrafish brain. The RSOM technique could resolve the transplanted cells and was able to detect melanosome aggregation upon external melatonin stimulation through changes of visualized pigmented area and by a characteristic shift of optoacoustic frequencies. Furthermore, the MORSOM imaging of the fish provided a superior visualization of anatomical features and melanophores and could serve as an anatomical reference to identify transplanted cells.

Being able to capture melanosome relocation in xenotransplanted cells could open the door for the development of bioengineered dynamic whole-cell sensors for optoacoustic imaging. Up to now, few good examples exist for genetically controlled contrast agents sensible to endogenous ligands and used in adult animals [126]. By genetically modifying and overexpressing specific receptors in the melanophores transplanted into living organisms, melanosome aggregation could be triggered by certain endogenous ligands, such as dopamine, and enable an optoacoustic readout of the cell response [127]. Such pigment clustering sensors based on the amplification via GPCR signal transduction could provide extraordinarily high sensitivity of potentially up to nanomolar concentrations of hormones or neurotransmitters *in vivo*.

5 Transmission-mode optoacoustic microscope

This chapter presents the development of a transmission-mode optoacoustic microscope and is based on [128] and [129]. After providing a detailed description of the setup and the image formation procedure (section 5.2), the characterization of the laser source, transducer and overall spatial resolution of the system is discussed (section 5.3). In the results part (section 5.4), the imaging of model organisms as well as the correction of the transducer's electrical impulse response (EIR) is shown. Finally, the development of an all-optical optoacoustic microscope based on an optical fiber detector is presented (section 5.5), including a characterization of the sensor and imaging results from model organisms *ex vivo*.

5.1 Introduction

In the previous chapter, the RSOM modality has been demonstrated to achieve sufficient resolution to visualize single pigmented cells in zebrafish within the whole specimens, i.e. through the entire depth of more than one millimeter in the case of a juvenile specimen (see Figure 4.9) and within FOVs of several millimeter length. However, since the spatial resolution of RSOM is determined by the acoustic focusing capabilities and because the involved acoustic wavelengths are typically $> 10 \mu\text{m}$, optoacoustic mesoscopy does not achieve sub-micrometer resolutions necessary for identifying sub-cellular features.

On the other hand, high-resolution optoacoustic imaging can be implemented based on focused illumination as used in point-scanning laser microscopy. Since the focusing of light with an objective lens is much tighter than acoustic focusing with a transducer, the lateral resolution of such an implementation is exclusively governed by the optical focusing capabilities as defined by Eq. (2.14). Consequently, this mode of optoacoustic imaging is called optical-resolution optoacoustic microscopy or simply optoacoustic microscopy (OM). The axial resolution of OM is still defined by the detection bandwidth of the ultrasound transducer (see Eq. (3.26)) and therefore usually at least one order of magnitude lower than the optical resolution in the lateral dimension.

Optoacoustic microscopy represents a powerful alternative to pure optical microscopy approaches with respect to the imaging of chromophores because its contrast is based on optical absorption, which includes fluorophores but also all molecules that relax mainly via non-radiative processes and other contrast agents such as nanoparticles [130]. However, one of the main assets of OM is its label-free nature in the visualization of endogenous tissue chromophores, including mainly hemoglobin and melanin in the visible spectral range, but also DNA [131] or lipids [132] when using ultraviolet or near-infrared excitation, respectively (see Figure 2.5). As already mentioned in section 1.3, multi-wavelength excitation OM further allows for the extraction of metabolic parameters such as the oxygen saturation of blood based on the different absorption spectra of oxy- and deoxyhemoglobin [25]. Another unique feature of the optoacoustic microscopy is the detection of ultrasound waves instead of light, which leads to an increased penetration depth compared to pure optical techniques of up to 1 mm in tissue [10]. Furthermore, because the speed of sound in tissue is five orders of magnitude smaller than the speed of

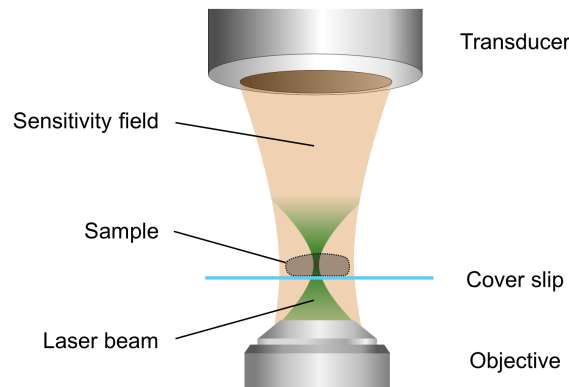


Figure 5.1: Illumination and detection geometry in transmission-mode OM.

light, optoacoustic signals originating from different depths can be separated in time, as opposed to light detection based optical microscopy. Consequently, optical sectioning in OM can be realized by simply windowing the time-resolved signals. For the same reason, depth-scanning around small structures is usually not required in OM as optoacoustic signal generation occurs within several tens of micrometers of axial distance to the focal spot.

Figure 5.1 depicts the illumination and detection geometry of optoacoustic microscopy in a typical transmission-mode configuration. The excitation laser beam is focused by a microscope objective lens into the examined sample, which rests on a microscopy cover slip. The generated optoacoustic signals are detected from the other side by a high-frequency ultrasound transducer that is spherically focused for sensitivity maximization, with the acoustic and optical foci overlapping. With transmission-mode OM, sub-micrometer lateral resolutions can be easily reached by using high-NA objectives, as there is no restriction on the working distance or the objective immersion medium. For this reason, transmission-mode OM has been traditionally employed to reach sub-cellular resolutions in thin specimens, such as single cells [133], mouse ears [134] or larvae of small animal models [135].

Alternatively, OM can be implemented in epi-illumination mode, where illumination and detection of the sample are performed from the same side. Such a configuration allows for larger specimens to be imaged *in vivo*, including mouse brains [136], eyes [137] or tumors [138]. However, epi-illumination usually comes at the price of lateral resolution, since larger working distances and thus lower numerical apertures are required for the illumination optics to accommodate the ultrasound detection unit. Moreover, the larger propagation distances of optoacoustic signals result in an increased acoustic attenuation of high frequencies, setting limits on the achievable axial resolution.

Point-scanning of the laser focus in epi-illumination OM is typically realized by moving the scanning head while leaving the sample fixed. On the other hand, transmission-mode OM relies either on the mechanical scanning of the sample while keeping illumination and detection fixed or by raster-scanning the laser focus similarly to classical confocal or multiphoton microscopy, in most cases by means of scanning mirrors. The latter has the advantage of an increased acquisition speed compared to mechanical scanning approaches, but requires out-of-focus detection, which yields a lower sensitivity and a loss of high frequencies at the FOV borders due to the spatial impulse response (SIR) of the detector. In this chapter, the development of a transmission-mode optoacoustic microscope is presented. The OM system was designed in transmission-mode in order to facilitate

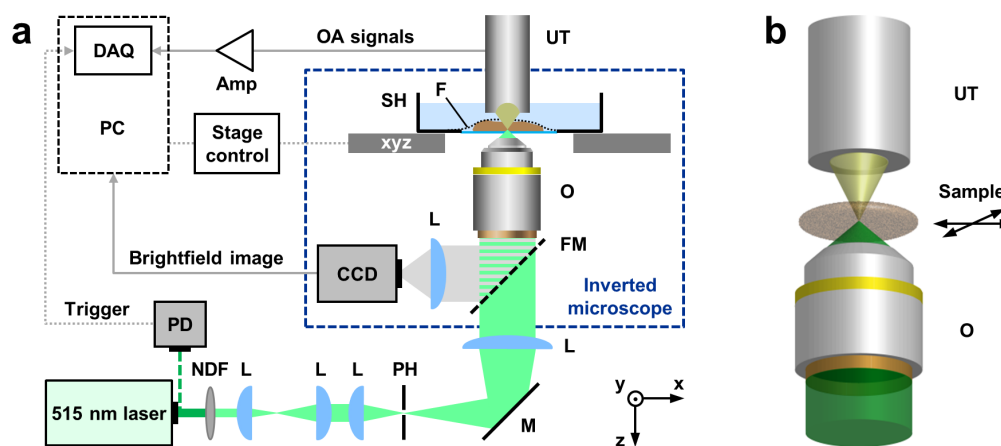


Figure 5.2: Experimental setup. (a) Scheme of the OM system. (b) OM scanning configuration. **Abbreviations:** Amp: Amplifier, DAQ: Data acquisition card, F: Plastic foil, FM: Flippable mirror, L: Plano-convex lens, M: Silver mirror, NDF: Neutral density filter, O: Objective lens, OA: Optoacoustic, PD: photodiode, PH: Pinhole, SH: Sample holder, UT: Ultrasound transducer, xyz: Motorized *xyz*-stage. ((b) adapted from [139].)

sub-micrometer imaging suitable for the combination with multiphoton microscopy (see next chapter). Additionally, the OM system was used for the characterization of high-frequency transducers, which is traditionally a challenging task regarding the creation of point sources. The developed system furthermore served as a platform to perform a pilot study on the suitability of optoacoustic microscopy based on an optical fiber detector, which could open up new opportunities in OM with respect to epi-illumination implementations or specialized detection schemes.

5.2 Materials and methods

5.2.1 Experimental setup

The developed optoacoustic microscope is schematically depicted in Figure 5.2(a). A photograph of the system can be found in appendix C.

The excitation source was a passively Q-switched pulsed diode-pumped solid state laser (Flare HP PQ Green 2 k-500, Innolight GmbH; repetition frequency: 1.25 kHz, energy per pulse: 570 μ J, pulse width: 2.15 ns) with a wavelength of 515 nm. The laser beam was attenuated by a combination of neutral density filters and guided into a modified inverted microscope (AxioObserver.D1, Zeiss). Since diffraction limited focusing requires the back aperture of the objective with a diameter of 10 mm to be completely filled, the initial beam was expanded 32 times by several telescopic lens configurations to reach a final diameter of \sim 15 mm. A 25 μ m pinhole was placed at the focal spot of one of the Keplerian beam expanders in order to spatially filter the beam, which was focused into the sample by a 0.25 NA air-immersion objective (PLN 10X, Olympus). The samples were placed inside a glass bottom petri dish with a glass thickness of 170 μ m (D60-30-1.5-N, IBL). Furthermore, the samples were either fixed to the glass by means of a piece of 10–20 μ m thick polyethylene plastic foil or inside agar, which was filled into the glass bottom well for polymerization. For optoacoustic signal detection, a spherically focused ultrasound transducer (Sonaxis; -6 dB bandwidth: 48–108 MHz, active element diameter: 1.5 mm) with \sim 80 MHz central frequency and 1.76 mm focal distance was employed. The

detector was located in transmission-mode above the sample in a confocal and coaxial alignment with respect to the optical focus and was mounted on a set of manual linear stages for xy - (8MT167-25LS, Standa) and z -positioning (PT1, Thorlabs).

Acoustic coupling was achieved by a drop of deionized water between transducer and sample. In case of plastic foil for fixation, ultrasound gel was inserted between sample and foil for gapless acoustic coupling. The sample holder was mounted on a pair of motorized xy -stages (MLS203-2, Thorlabs) together with a piezoelectric z -stage (MZS500-E, Thorlabs), which were used to position and scan the sample in three dimensions with sub-micrometer precision. After being detected by the transducer, the optoacoustic signals were amplified by a low-noise 63 dB amplifier (AU-1291, Miteq) and digitized by a high-speed 12-bit DAQ card (CS121G2, Gage Applied; max. sampling rate: 1 GS/s)¹. The trigger signal for the data acquisition was provided by a photodiode (DET36A, Thorlabs), which collected scattered light at the output of the laser.

For brightfield examination of the sample, a CCD camera (AxioCam ICc 1, Zeiss) was used. The illumination was provided by a white light LED lamp that could be positioned above the sample.

5.2.2 Acquisition and image formation

The time-resolved optoacoustic signals were digitized with a sampling rate of 1 GS/s to ensure a sufficient temporal representation². In order to reject (mostly electronic) noise outside of the sensitive frequency range of the transducer, the signals were bandpass filtered in the range of 25–125 MHz using the filter function defined by Eq. (3.34). Finally, the envelope of the bipolar optoacoustic signals was calculated using the Hilbert transform. Through this procedure, the original axial dimension of the imaged absorbers is maintained when performing a side-view MAP, which otherwise removes the negative part of the signals.

In order to demonstrate the effect of the Hilbert transform, a black 18 μm suture was imaged with the OM system using a step size of 1 μm and five averages per position (see Figure 5.3). A raw A-scan of the suture is shown in Figure 5.3(a) (black curve), representing the depth profile of the suture. The second signal at $z = 100 \mu\text{m}$ represents the reflection of the optoacoustic wave from the upper surface of the glass slide. The red dotted curve shows the Hilbert transform of the signal, corresponding to its envelope. Figure 5.3(b) compares the FWHM of the raw and Hilbert transformed peaks to the real diameter of the suture of 18 μm , which was determined by the lateral profile of the suture, as well as by measuring the diameter using a calibrated brightfield microscope. As can be observed in the bar graph, the positive peak of the raw signal results in a too small value of the diameter (6.2 μm), whereas the Hilbert transform yields a value close to the correct diameter (18.3 μm). A side-view MAP of the suture using the raw and Hilbert transformed signals is presented in Figure 5.3(c) and (d), respectively. The right structure at larger z corresponds again to the reflection from the glass slide.

In contrast to RSOM, the detected optoacoustic signals in OM originate from a confined double-conical volume around the optical focus. Because this excitation volume is much

1 For the measurements shown in Figure 5.3, 5.7 and 5.8(b), an 8-bit DAQ card was used (Cobra Max CS23G8, Gage Applied; max. sampling rate: 1.5 GS/s).

2 This is typically achieved by oversampling the signals at 5–10 times the highest detected frequency [140], which is in the order of 150 MHz in case of the employed transducer (see section 5.3.2). Thus, a sampling rate of 1 GS/s corresponds to an oversampling factor of > 6 .

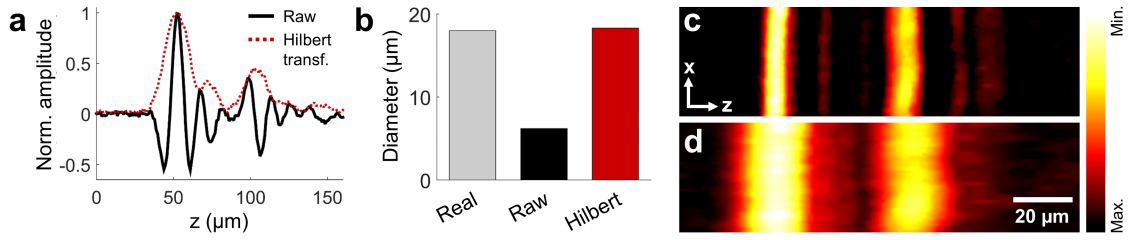


Figure 5.3: Hilbert transform of optoacoustic signals. (a) A-scan of a black 18 μm suture (black curve) and the corresponding Hilbert transform (red dotted curve). (b) Bar graph displaying the FWHM of the raw (black) and Hilbert transformed (red) peaks compared to the real diameter (gray) of the suture. (c-d) Side-view MAPs of the suture using the raw and Hilbert transformed signals, respectively. The signatures on the right side as well as the second peak in (a) represent reflections of the optoacoustic signals from the glass slide.

smaller than the acoustic focus of the employed transducer ($\sim 23 \mu\text{m}$ lateral and $\sim 200 \mu\text{m}$ axial extent at the central frequency of 80 MHz), no tomographic reconstruction is required. Furthermore, no spatial highpass filtering of stripe artifacts in the B-scans had to be used, since the laser pulses with energies at the sample of $< 100 \text{ nJ}$ were not strong enough to induce parasitic optoacoustic signals in the transducer. An image was formed by laterally moving the sample in discrete steps by means of the sample holding xyz -stage. At each xy -position, the time-resolved optoacoustic signals were recorded, averaged for SNR enhancement and cropped around the focal depth. Depending on the sample, the windowed signals had a length of several tens to a few hundreds of nanoseconds. Since in OM the A-scans directly represent depth profiles, a 3D volume of optical absorption in the sample was obtained by multiplying the time signals with the speed of sound in water (typically a value of 1510 m/s was used in order to take into account a slight heating of the water drop by the laser irradiation of the sample). The maximum lateral resolution was confined to a slice with a thickness of approximately $10 \mu\text{m}$, corresponding to the confocal parameter of the focused laser beam (see Eq. (2.8)), whereas the lateral resolution within the 3D volume gradually decreased with increasing axial distance to the optical focus.

The control of the stages, signal acquisition and processing, synchronization of the different devices, as well as the generation of 3D datasets was performed in MATLABTM. Image postprocessing was done with Fiji and involved standard operations such as windowing, median filtering, interpolation and Gaussian blurring of the entire images. Whenever quantitative values were extracted from images, the raw and unprocessed data was used.

5.2.3 Alignment of transducer and optical excitation

The coaxial and confocal alignment of transducer and laser beam had to be performed prior to every sample examination. For this purpose, a drop of black nail polish was placed on the glass slide next to the samples, which generated strong optoacoustic signals through an extended depth. After coarse positioning of laser focus and detector, the fine adjustment was achieved by maximizing the amplitude of the optoacoustic signal from the polish while matching the TOF of the signal to the focal distance of the transducer including the acoustic propagation time in the glass delay line. The optimization process involved the manual adjustment of the optical focus position and the x -, y - and z - positions of the transducer by means of the manual stages, as well as visual inspection via the DAQ-card oscilloscope program.

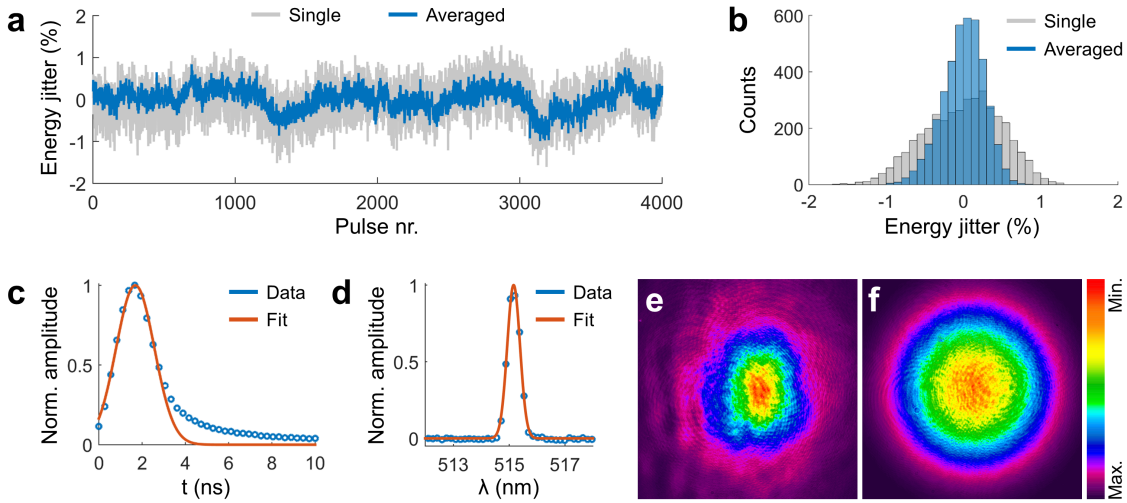


Figure 5.4: Characterization of the 515 nm laser. (a) Measured pulse energy jitter for single pulses (gray curve) and after 20 averages (blue curve). (b) Histogram representation of the curves in (a). (c) Recording of a laser pulse with a fast photodiode (blue circles) fitted with a Gaussian function (red curve). (d) Wavelength spectrum of the laser (blue circles) fitted with a Gaussian function (red curve). (e-f) Profile of the beam before (e) and after (f) spatial filtering with the 25 μm pinhole.

5.3 Characterization

5.3.1 Laser source

Figure 5.4 summarizes the characterization of the used 515 nm laser. To accurately determine the pulse width and energy jitter, a series of laser pulses was recorded with an ultra-fast photodiode (G4176-03, Hamamatsu; rise time: 30 ps). Additionally, a 12-bit DAQ card with a sampling rate of 3.6 GS/s was used for this measurement (ADQ412, SP Devices). All pulses were fitted with a Gaussian curve to extract the peak amplitudes and FWHM. The percentage difference of the individual peak amplitudes from the mean value of the series is shown as a gray curve in Figure 5.4(a) for 4000 pulses. The data shows a pulse energy jitter in the range of $\pm 1\%$ with a standard deviation of 0.54%. To study the effect of signal averaging on the energy fluctuations between different scans, the peak amplitudes after averaging 20 pulses were recorded (blue curve). The averaged pulses yielded a standard deviation of 0.31%, which corresponds to a reduction of the pulse energy jitter by 43%. Figure 5.4(b) shows the histograms corresponding to the pulse series in (a). Furthermore, from the averaged data a mean pulse width of 2.15 ns could be determined. Figure 5.4(c) depicts an averaged laser pulse (blue dots) fitted with a Gaussian function (red curve, $R^2 = 0.972$, data points with $t > 3.2$ ns excluded from the fit). Next, the spectral profile of the laser was measured with a spectrometer (DSA491000, Qwave) as 515.2 nm with a spectral linewidth of 0.55 nm, as shown by Figure 5.4(d) (red curve represents Gaussian fit, $R^2 = 0.996$).

Finally, the effect of spatially filtering the laser beam by means of the 25 μm pinhole is demonstrated in Figure 5.4(e-f). A beam profiler (SP620U, Ophir) was used to record the spatial 2D intensity profiles of the laser beam before and after the passing through the pinhole. The original beam (e) showed a non-circular profile together with intensity fluctuations of higher spatial frequencies. On the other hand, the spatially filtered beam (f) had a circular profile devoid of any severe fluctuations, leading to an improved focusing

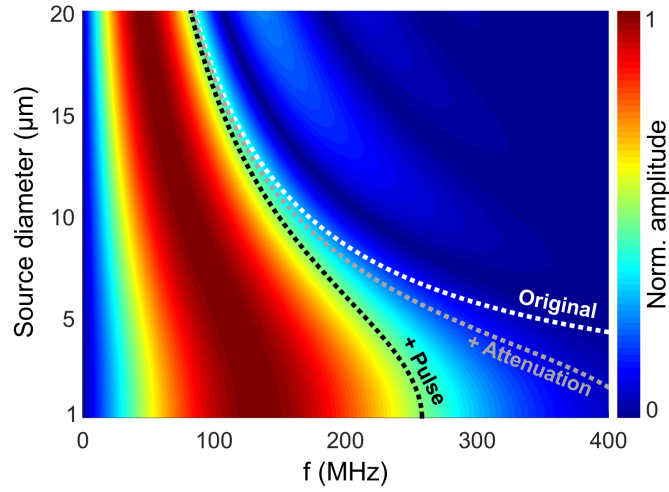


Figure 5.5: Simulation of optoacoustic frequencies reaching the 80 MHz transducer as a function of the source diameter incorporating acoustic attenuation and 2.15 ns laser pulses. The black dotted curve follows the -6 dB high cutoff frequencies of the spectra. The white and light gray curves denote the corresponding -6 dB high cutoff frequencies of the original unaffected signals and the ones only subject to acoustic attenuation, respectively.

at the sample³.

5.3.2 Transducer detection bandwidth and electrical impulse response

Generally, optoacoustic signals recorded by ultrasound transducers are distorted and thus do not correspond to the original pressure waves generated in the sample. First, as discussed in section 3.2.5, ultrasound waves experience acoustic attenuation while propagating through sample and coupling medium towards the detector, leading to a reduction in amplitude and bandwidth of the measured signals. Furthermore, the optoacoustic signals are distorted by a number of effects that can be mathematically represented as a convolution with the original waves [141]. The voltage signal $s_d(\vec{r}_d, \vec{r}, t)$ measured by a transducer at position \vec{r}_d and produced by a point source emitting the pressure wave $p_\delta(\vec{r}_d, \vec{r}, t)$ at position \vec{r} and time t can be expressed as

$$s_d(\vec{r}_d, \vec{r}, t) = p_\delta(\vec{r}_d, \vec{r}, t) * H_t(t) * EIR(t) * SIR(\vec{r}_d, \vec{r}, t), \quad (5.1)$$

where $H_t(t)$ corresponds to the temporal profile of the laser pulse, $EIR(t)$ denotes the electrical impulse response (EIR) and $SIR(\vec{r}_d, \vec{r}, t)$ the spatial impulse response (SIR) of the transducer [142, 143]. In the case of a point source at the acoustic focus of a spherically focused transducer, such as in the presented OM configuration, the SIR reduces to $SIR(\vec{r}_d, \vec{r}, t) = \delta(t)$, since the entire active element is excited simultaneously [73].

In order to study the effect of the 2.15 ns pulses of the 515 nm laser on optoacoustic frequencies detectable by the employed 80 MHz transducer, a simulation was performed using the script mentioned in section 3.2.4. The frequencies generated by optoacoustic sources with the same material properties as the surrounding water are displayed for

³ The small circular diffraction patterns in the profiles originated from impurities on the optical elements of the beam profiler.

different diameters in Figure 5.5. In this model, acoustic attenuation in water along the 1.76 mm focal distance of the transducer and a pulse width of 2.15 ns were incorporated. The black dotted curve marks the -6 dB high-frequency cutoff of the spectra. The corresponding -6 dB curves for the original (undistorted) signals as well as for the signals only experiencing acoustic attenuation are depicted by the white and light gray curves, respectively. As can be seen from the simulation, acoustic attenuation limits the highest detectable frequencies to slightly above 400 MHz, whereas the finite pulse width further reduces the highest frequencies to < 300 MHz. However, as the 80 MHz transducer cannot detect frequencies above 200 MHz, it is minimally affected by the pulse duration $H_t(t)$ and, thus, the 515 nm laser represents a suitable excitation source for the OM system. The next step of the transducer characterization was the determination of the detection bandwidth by measuring the EIR of the detector. In general, piezoelectric transducers have a finite detection bandwidth governed by the properties of their components, such as active element, backing material, electronics, etc. [73]. Quantitative knowledge of the bandpass behavior of the employed transducer is, however, crucial for imaging applications, because it allows for an efficient reduction of electronic noise by means of software bandpass filters, which are adapted to the real detection bandwidth. Furthermore, since the bandwidth of optoacoustic signals depends on the size of the respective sources, transducers with an appropriate frequency response have to be chosen for the imaging of specific structures. Typically, the manufacturers of ultrasound detectors characterize their devices via the so-called pulse-echo (PE) method, where the transducer emits an acoustic response to a delta voltage pulse and records the same pulse after being reflected from a surface [74]. On the other hand, optoacoustic imaging relies on passive detection only, which typically leads to a larger detection bandwidth than characterized by the manufacturer. Thus, the characterization of ultrasound transducers for optoacoustic imaging should rely on measuring acoustic waves with a flat or known frequency spectrum generated by the photoacoustic effect itself [142]. A common technique to generate such a spectrum is the detection of a point source, often an absorbing microsphere with a diameter much smaller than the axial resolution of the transducer. Under this condition, the frequency spectrum of the point source signal is approximately linear within the detection bandwidth of the transducer. In the case of a point absorber excited by a delta pulse, the optoacoustic signal fulfills $p_\delta(\vec{r}_d, \vec{r}, t) \propto \partial\delta(t)/\partial t$ (see Eq. (3.16)) and thus Eq. (5.1) implies that [73]

$$s_d(\vec{r}_d, \vec{r}, t) \propto \delta(t) * \frac{\partial EIR(t)}{\partial t} = \frac{\partial EIR(t)}{\partial t}. \quad (5.2)$$

Hence, the EIR of the detector can be calculated by integrating the measured signal over time [143]:

$$EIR(t) = \int_0^t s_d(\vec{r}_d, \vec{r}, t') dt'. \quad (5.3)$$

For high-frequency focused transducers employed in OM featuring axial resolutions of only a few micrometers, the point source requirement poses a major challenge. The reason is the inherently small signal amplitude produced by such sources as well as the sample preparation and reproducibility. Consequently, another approach based on the focusing of the laser on a thin absorbing layer was chosen for the generation of an optoacoustic point source [144]. Figure 5.6(a) illustrates the experimental setting. The sample was a standard 170 μm cover slip coated with a 250 nm layer of gold using electron beam

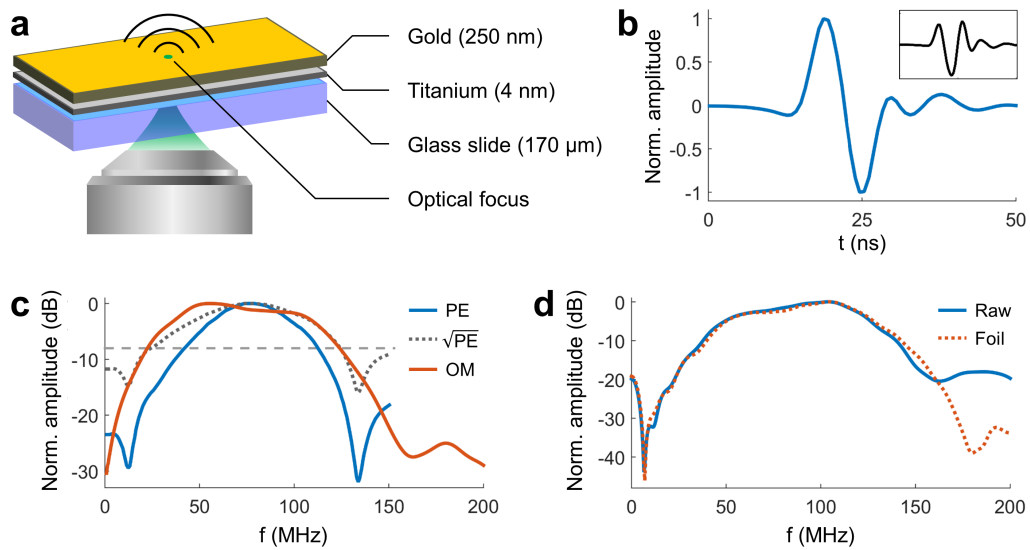


Figure 5.6: Measurement of the transducer detection bandwidth and electrical impulse response. (a) Schematic sketch of the gold layer sample and the measurement configuration. (b) Measured EIR using 1000 averages. The inset shows the corresponding time signal. (c) Detection bandwidth of the transducer measured with OM (red curve) compared to the spectrum provided by the manufacturer obtained with the PE method (blue curve). The square root of the PE spectrum is shown by the gray dotted graph. The light gray dashed line denotes the -8 dB amplitude, corresponding to a bandwidth of 25–125 MHz of the measured spectrum. (d) Effect of plastic foil on the recorded optoacoustic signals. The graphs show the frequency spectra of measured signals without (blue curve) and with (red dashed curve) the foil inserted between sample and transducer.

physical vapor deposition. A 4 nm film of titanium served as adhesion layer between glass and gold. Because the skin depth of gold for a wavelength of 515 nm is ~ 20 nm [145], the effective size of the point source was ~ 20 nm axially and < 1 μm laterally⁴. The transducer was acoustically coupled to the gold surface by a drop of deionized water. Figure 5.6(b) shows the EIR of the 80 MHz transducer using 1000 averages. The back curve in the inset represents the corresponding time signal. The detection bandwidth as obtained by the Fourier transform of the EIR is depicted by the red curve in (c). The previously mentioned software bandpass filter range of 25–125 MHz corresponds to the -8 dB cutoff frequencies of the measured spectrum (denoted by the gray dashed horizontal line) and was consistently found to yield the best results in the OM measurements. For comparison, the PE detection bandwidth provided by the manufacturer is illustrated by the blue curve. The PE spectrum appears narrower than the spectrum measured by OM, which can be explained by the transmission-receive process corresponding to twice a convolution of the acoustic signal with the EIR. To demonstrate this relation, the square root of the manufacturer PE spectrum is shown as a gray dotted curve, approximating the receive-only frequency spectrum. It is found to correspond well with the measured OM spectrum within the first -10 dB.

Additionally, the gold sample was used to characterize the attenuation effect of plastic foil, which was used for sample fixing purposes, on the detected optoacoustic frequencies.

⁴ A 0.45 NA objective (Plan Apochromat 10X, Zeiss) was used for this measurement, featuring a theoretical focal diameter of ~ 600 nm.

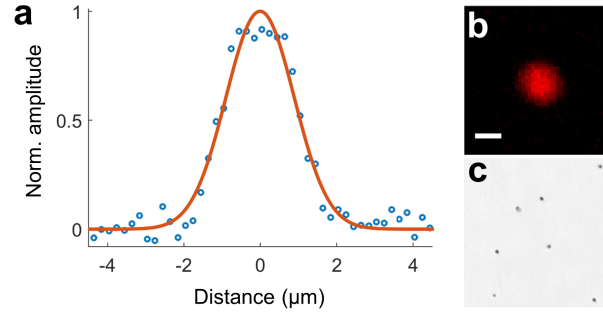


Figure 5.7: Lateral resolution characterization of the optoacoustic microscope. (a) Measured profile across a single $2.8 \mu\text{m}$ black microsphere (blue dots) fitted with a Gaussian function (red curve). (b) Top-view MAP of the sphere. Scale bar: $2 \mu\text{m}$. (c) Brightfield image of several microspheres embedded in agar.

Figure 5.6(d) shows the two frequency spectra of optoacoustic signals recorded without (blue curve) and with (red dashed curve) foil inserted between gold sample and transducer. The spectrum after transmission through foil is almost identical to the raw spectrum within the first 160 MHz, whereas an attenuation effect can be observed for higher frequencies. This frequency range corresponds mainly to the first side lobe of the detector and does not contribute significantly to the amplitude of recorded signals. Thus, it can be concluded that optoacoustic signals are not affected by plastic foil in this implementation of OM. The gold plate method can readily be used for the characterization of other high-frequency transducers, which is a task otherwise tedious and difficult to reliably repeat. Moreover, this technique may be applied to the characterization of the SIR of high-frequency transducers, as well as the effect of different materials and detection geometries on the detectable frequencies.

5.3.3 Spatial resolution

According to Eq. (2.14), the lateral resolution of OM is defined by the FWHM of the optical focus. It was experimentally determined by imaging a black $2.8 \mu\text{m}$ polystyrene microsphere (Polybead, Polysciences) with a scanning step size of $0.2 \mu\text{m}$, five signal averages and a pulse energy at the focus of $\sim 3 \text{ nJ}$. The microspheres were treated in an ultrasonic bath to prevent agglomerations, embedded in pure agar and mounted inside a glass bottom petri dish. Usually, the resolution of a microscopy modality is obtained by imaging a point source, which directly delivers the PSF. In this case however, the size of the microsphere was comparable to the achievable spatial resolution of the OM system and thus the PSF could not be directly measured. In order to derive the lateral resolution from the measured sphere profile, the scanning process was approximated to be described by a convolution of the Gaussian laser focus profile with the real optoacoustic sphere profile resulting from the excitation with an infinitely small laser beam. Additionally, the original sphere profile was assumed to be Gaussian shaped as well, with the nominal sphere diameter $d_{nom} = 2.8 \mu\text{m}$ corresponding to $\pm 3\sigma$. Under these assumptions, the lateral resolution R_{OM} could be analytically expressed as

$$R_{OM} = \sqrt{d_{exp}^2 - \left(\frac{1}{3} \sqrt{2 \ln(2)} d_{nom} \right)^2}, \quad (5.4)$$

where d_{exp} is the FWHM of the measured microsphere profile. Figure 5.7(a) shows the cross-sectional profile of a single microsphere. The Gaussian fit (red curve, $R^2 = 0.971$) yielded a FWHM of $d_{exp} = 2.1 \mu\text{m}$, resulting in a lateral OM resolution of $R_{OM} = 1.8 \mu\text{m}$. This value exceeds the theoretical FWHM of the Airy disk, predicted by Eq. (2.14) to be $1.1 \mu\text{m}$, by a factor of ~ 1.7 . The deviation can be explained by optical imperfections of the laser beam, optical aberrations and the slight underestimation of the lateral resolution by setting the nominal sphere diameter equal to $\pm 3\sigma$ of the original profile. The top-view MAP of the imaged microsphere is shown in Figure 5.7(b) and a brightfield microscopy image of a few spheres embedded in agar is provided by Figure 5.7(c).

On the other hand, the axial resolution in OM is determined by the detection bandwidth of the employed transducer. However, calculating the axial resolution via Eq. (3.26) or experimentally determining it by measuring the FWHM of the Hilbert transformed peak in the time signal would result in a too large value. The reason for this is the fact that optoacoustic signals are bipolar. Thus, if two bipolar optoacoustic signals approach each other temporally, the negative peak of the first and the positive peak of the second signal mutually cancel, leaving the positive and negative peaks of the first and second signals, respectively⁵. The Hilbert transform of this added signal would still show two distinct peaks up to a temporal distance smaller than the FWHM of the envelope of a single signal. A numerical simulation of this situation using the measured signal shown in the inset of Figure 5.6(b) is provided in appendix B. A better estimation of the axial resolution is therefore given by the FWHM of the first positive peak of an optoacoustic point source signal⁶. With this method, the axial resolution of the 80 MHz transducer was found to be $\sim 7 \mu\text{m}$ in [11] (data not shown) by measuring a $10 \mu\text{m}$ black microsphere.

5.4 Results

5.4.1 Imaging of model organisms *ex vivo*

To demonstrate the imaging capabilities of the developed OM system, two model organisms were imaged *ex vivo*, a mouse ear and an 11 dpf zebrafish larva (huC::GCamP5G). Besides their applicability to studying skin, as well as vascular structure, function and related diseases [10, 146, 147], mouse ears represent ideal samples to investigate the ability of the OM modality to visualize objects of different sizes at different depths. On the other hand, zebrafish larvae contain melanophores, which strongly absorb light in the entire visible range, and are otherwise transparent. Thus, they can be used to study the imaging performance at cellular resolution and the resulting images can be compared to brightfield microscopy images.

A $360 \times 360 \mu\text{m}^2$ region of the mouse ear was scanned with a step size of $1.8 \mu\text{m}$ and 40 signal averages within ~ 70 min. The pulse energy at the sample was $\sim 42 \text{ nJ}$ ⁷. Figure 5.8(a) represents the top-view MAP of the OM scan, where the depth of the signals is represented by different colors. The image shows blood vessels of different size through a depth of $125 \mu\text{m}$.

⁵ In fact, the number of positive and negative peaks depends on the size of the object and the transducer properties. However, optoacoustic signals always have positive and negative peaks, which can cancel each other. Thus, this argument can be generalized to any optoacoustic signals.

⁶ In this case, point-like refers to the bandwidth-derived axial resolution of the ultrasound transducer.

⁷ The mouse ear was measured with the 0.45 NA objective. The corresponding lateral resolution characterization is presented in section 6.3.1.

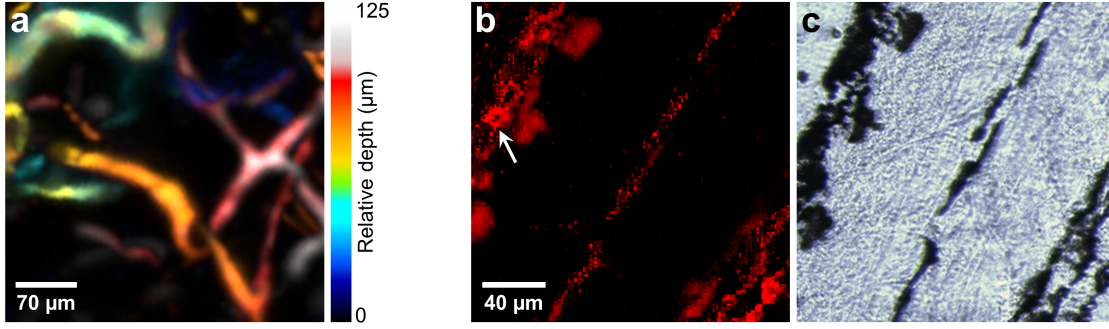


Figure 5.8: OM imaging of model organisms *ex vivo*. (a) Mouse ear vasculature recorded through a depth of 125 μm (depth color coded). (b) Top-view MAP of the trunk region of a 11 dpf zebrafish larva showing melanocytes forming the pigmented stripes of the fish. (c) Corresponding brightfield microscopy image. ((b) adapted from [128].)

Figure 5.8(b) shows the OM top-view MAP in a $200 \times 200 \mu\text{m}^2$ FOV at the trunk of the zebrafish. The step size was $2 \mu\text{m}$, the signals were averaged five times and the pulse energy at the focus was reduced to $\sim 6 \text{ nJ}$ in order to prevent damage from the specimen. The total acquisition time was $\sim 18 \text{ min}$. In the OM image, the pigmented stripes of the zebrafish are visible, revealing single melanophores and even cell nuclei (highlighted by the white arrow), which lack melanosomes and are thus characterized by the absence of optoacoustic signals. A brightfield microscopy image of the same region is presented in Figure 5.8(c), matching with the OM image but showing considerably less contrast variations within the melanized regions due to the strong absorption of transmitted light⁸.

5.4.2 Electrical impulse response correction

Ultrasound transducers act like bandpass filters owing to their finite detection bandwidth. This effect leads to a distortion of the recorded optoacoustic signals and can be mathematically described as a convolution with the EIR (see Eq. (5.1)). Consequently, the original optoacoustic signals can be partially restored by a deconvolution with the EIR, provided that the latter can be accurately measured. A standard method to perform such a deconvolution while taking noise into account is the Wiener deconvolution [73]. In the frequency domain, with $S_o(f)$ and $S_d(f)$ denoting the Fourier transformed original (undistorted) and measured signals, respectively, the Wiener deconvolution is described as

$$S_o(f) = \frac{S_d(f)}{EFR(f)} \cdot \frac{|EFR(f)|^2}{|EFR(f)|^2 + NSPR(f)}, \quad (5.5)$$

where the so-called electrical frequency response EFR is the Fourier transform of the EIR and $NSPR$ is the noise to signal power ratio $NSPR(f) = |N(f)|^2 / |S_o(f)|^2$ of the mean power spectral density of the noise $N(f)$ and the undistorted signal [148].

The EIR of the 80 MHz transducer has been measured with the gold layer sample, as discussed in section 5.3.2, and could therefore be utilized to correct the OM data for distortions due to the finite detection bandwidth. For this study, a phantom comprising 20, 30 and 40 μm sutures in a triangular configuration embedded in agar was measured.

⁸ It has to be mentioned that the brightfield modality of this system did not achieve the same performance as optimized brightfield microscopes using Köhler illumination.

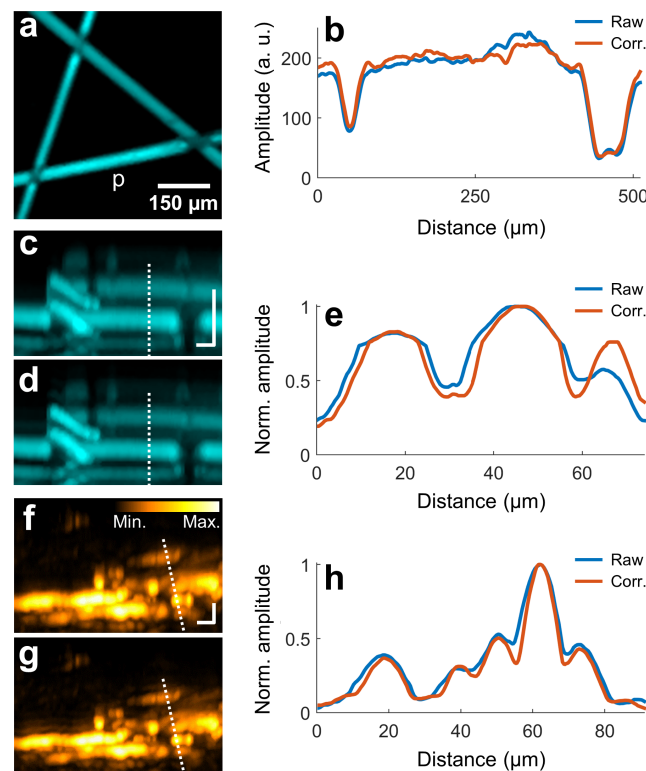


Figure 5.9: Electrical impulse response correction. (a-e) Phantom of 20, 30 and 40 μm sutures. (a) Optoacoustic top-view MAP of the phantom. (b) Lateral profiles along the 'p'-labeled suture in (a), showing the amplitudes of the raw (blue) and EIR corrected (red) data. (c-d) Side-view MAPs of the sutures using the raw (c) and corrected (d) data. Scale bar: 50 μm . (e) Raw (blue) and EIR corrected (red) axial profiles along the white dashed lines in (c-d). **(f-h) Mouse ear *ex vivo*.** (f-g) Side-view MAPs of the ear before (f) and after (g) EIR correction. Scale bar: 30 μm . (h) Corresponding profiles along the dashed white lines in (f-g) for the raw (blue) and corrected (red) data.

Figure 5.9(a) shows the top-view MAP of the phantom. The signals were averaged 40 times and the step size was 5 μm to allow for a bigger FOV of $500 \times 500 \mu\text{m}^2$ to be scanned. The profiles along the suture marked with the label 'p' in (a) for the raw (blue curve) and EIR corrected (red curve) data is presented in Figure 5.9(b). The raw profile is slightly inclined, showing larger amplitudes towards the right side, whereas the corrected curve is leveled. Figures 5.9(c-d) depict side-view MAPs of the phantom with a depth of 110 μm using the raw (c) and EIR corrected (d) signals. Axial profiles along the white dashed lines are plotted in (e), revealing larger amplitude variations and thus better contrast for the corrected profile. Furthermore, the width of the peaks is reduced with respect to the raw data. It can therefore be concluded that the EIR correction leads to a better representation of the sample, results in a better contrast and improves the axial resolution of the transducer. To validate these findings in a biological sample, the mouse ear data presented in Figure 5.8(a) was used for the EIR correction. Figures 5.9(f-g) show the raw and corrected side-view MAPs of the ear with a depth of 205 μm , respectively. The profiles corresponding to the white dashed lines in (f-g) are illustrated in (h). As for the suture phantom, the EIR corrected profile yields larger amplitude variations and a reduced peak width.

In conclusion, the EIR correction method presented in this section based on the EIR

measurement using the gold layer sample was demonstrated to improve the axial resolution and image quality for phantoms as well as biological samples in OM.

5.5 All-optical optoacoustic microscope using an optical fiber detector

This section presents the development of an optoacoustic microscope using optical detection⁹ and is based on [149].

5.5.1 Motivation for optical sensors

The use of piezoelectric ultrasound transducers is widespread in optoacoustic microscopy due to their high sensitivity, robust design and commercial availability [25]. On the other hand, optical sensors have been increasingly used in high-resolution optoacoustic imaging in recent years [138, 150–153], due to a number of limitations of piezoelectric detection schemes for specific applications.

First, the sensitivity of piezoelectric detectors decreases with the size of their active element, whereas optical sensors can be miniaturized without significant sensitivity losses [25]. Even though OM has been achieved using sub-millimeter sized piezoelectric transducers [154], their fabrication is complicated and requires custom designs. Furthermore, optical detectors are less vulnerable to certain experimental conditions, such as electromagnetic disturbances or laser irradiation of the transducer element or housing, which can cause noise or parasitic optoacoustic signals [149, 155]. Finally, common piezoelectric transducers are bulky and opaque, impeding the implementation of epi-illumination OM. While optoacoustic microscopy in transmission mode, such as the system presented in this chapter, achieves a high lateral resolution due to the use of high-NA objectives, its applicability is limited to thin samples due to space restrictions. In contrast, epi-illumination mode OM employs an illumination and detection from the same side. Previous methodologies based on piezoelectric detectors relied on acoustical-optical beam combiners [156], ring-shaped transducers with central illumination [157] or reflection objectives [158]. However, these designs suffered from degraded sensitivity, low illumination or detection NA and design constraints [25]. Transparent and miniaturized optical sensors can overcome such limitations and are therefore suitable for epi-illumination OM.

Previous studies discussed and implemented π -phase-shifted fiber Bragg grating (π -FBG) sensors for optoacoustic detection [153, 155, 159]. The active area of these sensors consists of a periodic change of the refractive index (grating) within an optical fiber, leading to a bandgap in the transmission spectrum, the location of which depends on the grating period Λ [155]. A discontinuity of the length equivalent to a phase change of π at the center of the Bragg grating acts like a Fabry-Pérot interferometer (FPI) and creates an ultra-narrow transmission notch centered in the reflective bandgap. Optoacoustic waves incident on the π -FBG cause transient changes in Λ , which in turn lead to wavelength shifts of the transmission notch. These shifts are finally detected by interferometric systems and translated into voltage signals for data acquisition [160].

So far, π -FBG sensors have not been demonstrated for the optoacoustic imaging of biological specimens. To study the suitability of these detectors in OM and in order to pave the way for future epi-illumination applications, the transducer of the OM system

⁹ The optical sensor and interferometry system were developed by Prof. Amir Rosenthal and the detection part of the all-optical microscope was designed and operated by Georg Wissmeyer.

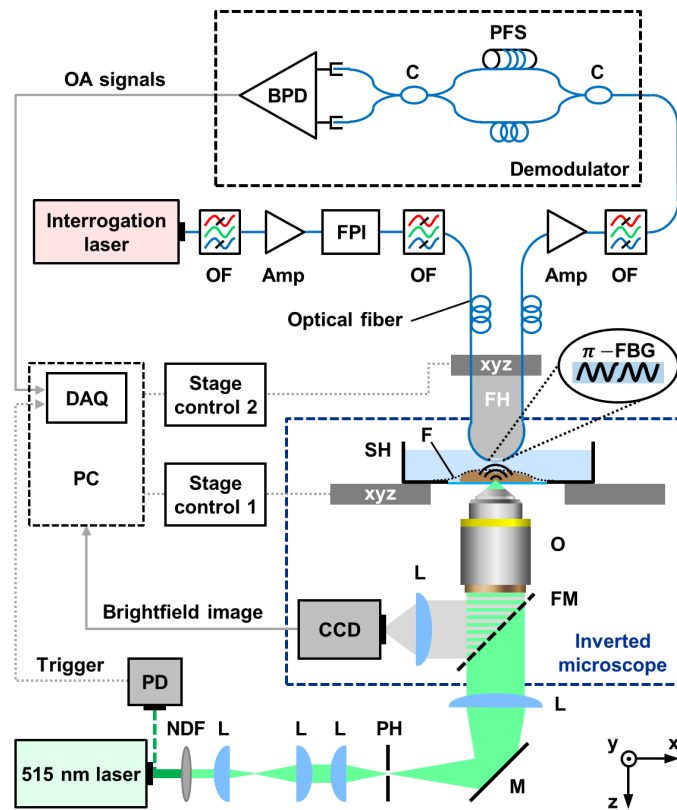


Figure 5.10: Scheme of the fiber detector based all-optical optoacoustic microscope. Amp: Erbium doped optical amplifier, BPD: Balanced photodiode, C: 50/50 coupler, DAQ: Data acquisition card, F: Plastic foil, FH: Fiber holder, FM: Flippable mirror, FPI: Fabry-Pérot interferometer, L: Plano-convex lens, M: Silver mirror, NDF: Neutral density filter, O: Objective, OF: Optical filter, PD: photodiode, PFS: Piezoelectric fiber stretcher, PH: 25 μm pinhole, SH: Sample holder, UT: Ultrasound transducer, xyz: Motorized *xyz*-stage.

introduced in the previous sections was replaced by an optical π -FBG sensor for the detection of optoacoustic signals.

5.5.2 Experimental setup

Figure 5.10 depicts a schematic of the all-optical optoacoustic microscope. With respect to the setup, acquisition and scanning scheme described in section 5.2.1, only the detection part was changed. The optical fiber containing the π -FBG sensor (TeraXion Inc.; total diameter: 250 μm) was fixed on a 3D-printed holder, which was attached to a motorized *xyz*-stage (M-683.2, M-501.1, Physik Instrumente). The effective sensing area of the π -FBG with a length of 270 μm around the discontinuity of the Bragg grating was placed at the tip of the printed holder and placed directly above the sample and the illumination focus. The interferometric detection of the optoacoustic signals was based on coherence-restored pulse interferometry (CRPI), and is discussed in detail in [153] and [161].

The interrogation part of the CRPI system is shown on the left side of the π -FBG holder in Figure 5.10. A pulsed 1550 nm laser with a repetition rate of 250 MHz (Menlo Laser TC-1550 M-comb, Menlo Systems GmbH) was coupled into the optical fiber sensor to interrogate the π -FBG, which had a transmission notch at 1549 nm. To match the notch, the wideband laser was bandpass filtered (C-band tunable bandpass filter, Optoplex

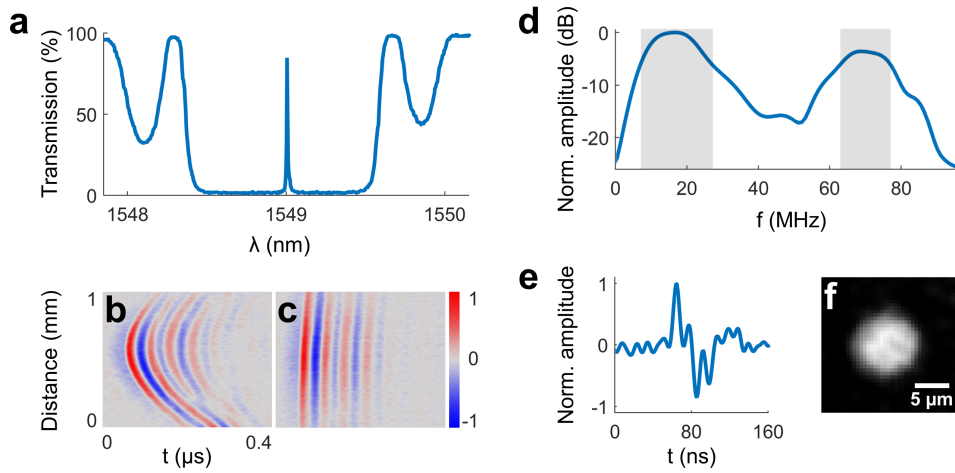


Figure 5.11: Characterization of the π -FBG sensor. (a) Transmission spectrum of the π -FBG around the notch, recorded with a tunable CW laser. (b-c) Optoacoustic signals recorded from black varnish. B-scans are shown for sensor scans (b) perpendicular to and (c) along the fiber axis. Positive and negative amplitude values are colored in red and blue, respectively. (d) Frequency response of the CRPI system, where the regions with an amplitude above -6 dB are highlighted by gray shaded boxes. The source was a $10\ \mu\text{m}$ black polystyrene microsphere. (e) Corresponding time signal recorded at the center of the sphere. (f) Top-view MAP of a single microsphere. ((d-f) adapted from [149].)

Corp.) to a $0.4\ \text{nm}$ band around $1549\ \text{nm}$, amplified (C-band EDFA optical fiber amplifier, Amonics Ltd.) and filtered again to reduce optical noise from the amplifier. Further reduction of optical noise was achieved by an FPI (Optical Frequency Synthesizer, Menlo Systems GmbH) with a free spectral range of $1\ \text{GHz}$, which was actively locked on the frequency comb of the interrogation laser. This procedure led to a transmission of every fourth peak of the frequency comb and thus increased the repetition rate of the π -FBG interrogation to $1\ \text{GHz}$. The sensor transmission signal, encoding the spectral shifts upon acoustic perturbation, was amplified, bandpass filtered and demodulated using a Mach-Zehnder interferometer. The phase difference between the interferometer arms was actively stabilized against low-frequency drifts using a piezoelectric fiber stretcher (PZ3-PM, Optiphase) at one of the arms [162]. Finally, the time-varying phase differences resulting from spectral shifts of the notch were translated into voltage signals via a balanced photodiode (PDB450C, Thorlabs).

5.5.3 Characterization of the optical sensor

The characterization of the π -FBG sensor and the CRPI system is shown in Figure 5.11. The transmission spectrum of the π -FBG was recorded with a tunable CW laser (TL1550-B-PM, Thorlabs) and yielded a bandgap of $\sim 1.4\ \text{nm}$ and a $-3\ \text{dB}$ notch width of $8\ \text{pm}$, as shown in Figure 5.11(a). To study the sensitivity field of the optical sensor, the excitation laser was focused on a layer of black nail polish to create a strong optoacoustic signal. The sensor was moved across the sample in two line scans perpendicular and parallel to the fiber axis. Figure 5.11(b) and (c) illustrates the corresponding B-scans over a length of $1\ \text{mm}$ for the perpendicular and parallel sensor movement, respectively, where both the positive (red) and negative (blue) amplitude values are shown. The perpendicular scan shows the typical arc shape, indicating a radially outward pointing sensitivity field of the sensor. On the other hand, the parallel scan yields an almost constant time-of-flight

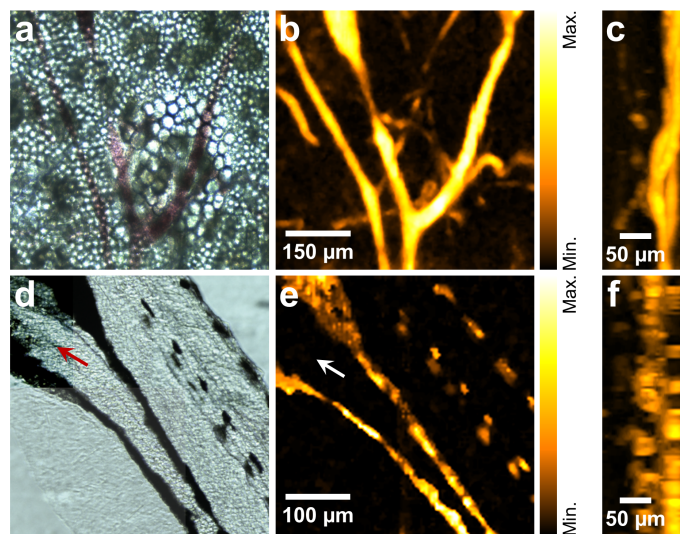


Figure 5.12: Imaging of model organisms with the all-optical optoacoustic microscope. (a-c) **Excised mouse ear.** (a) Brightfield image and (b) optoacoustic top-view MAP showing vasculature at different depths. (c) Side-view MAP of the ear with a total depth of $140\ \mu\text{m}$. (d-f) **Wildtype zebrafish larva *ex vivo*.** (d) Brightfield image and (e) optoacoustic top-view MAP at the trunk of the fish showing single melanocytes and pigmented structures. (f) Corresponding side-view MAP with a total depth of $140\ \mu\text{m}$. (Adapted from [149].)

of the acoustic signals over the $1\ \text{mm}$ translation distance with declining amplitudes at the edges. This profile could originate from the dimensions of the π -FBG ($270\ \mu\text{m}$ effective sensing length compared to a core diameter of $125\ \mu\text{m}$) and additionally could be a result of surface waves traveling along the fiber with a high speed of sound [159]. To characterize the detection bandwidth and axial resolution of the CRPI system, the optoacoustic signal of a $10\ \mu\text{m}$ black polystyrene microsphere was measured using 150 averages and the frequency response was calculated as described in section 5.3.2.

The frequency spectrum is shown in Figure 5.11(d) and reveals a peak sensitivity at around $17\ \text{MHz}$ and two distinct bands above $-6\ \text{dB}$ at $7\text{--}27\ \text{MHz}$ and $63\text{--}77\ \text{MHz}$, as depicted by the gray shaded areas in the graph. The locations of these bands in the frequency response originate from certain resonances and depend on the geometry of the fiber detector and the acoustic impedance matching of its coating and the coupling medium [149]. The time signal corresponding to the frequency spectrum is presented in Figure 5.11(e). From the FWHM of the first positive peak, an axial resolution of the CRPI detection system of $\sim 11\ \mu\text{m}$ could be determined. Since the optical focusing was not changed, the all-optical microscope had a lateral resolution of $\sim 1.8\ \mu\text{m}$, as found in section 5.3.3. Finally, a single microsphere was imaged with a step size of $0.5\ \mu\text{m}$, a pulse energy of $\sim 12\ \text{nJ}$ and 150 signal averages. The top-view MAP of the bead is depicted in Figure 5.11(f), showing sufficient contrast to clearly identify the outline of the sphere.

5.5.4 Imaging results

In order to investigate the imaging capabilities of the developed all-optical optoacoustic microscope, a mouse ear and a 10 dpf wildtype zebrafish larva were imaged *ex vivo*. Both optoacoustic scans were performed with $5\ \mu\text{m}$ step size and 150 signal averages. The results are illustrated by Figure 5.12. The mouse ear was excised directly after

sacrificing the animal and the severed blood vessels were cauterized to minimize blood loss. Figure 5.12(a) shows the brightfield microscopy image of a $600 \times 600 \mu\text{m}^2$ region of the ear. The corresponding optoacoustic image was recorded with a pulse energy of $\sim 100 \text{ nJ}$ and is presented in (b) as a top-view MAP, displaying vasculature in different layers of the ear. A side-view MAP, depicted in (c), shows the same layered structure with the prominent big vessels below smaller vasculature. The contrast is similar to piezoelectric detection based OM, proving that the π -FBG sensor is suitable for imaging vasculature. This is especially interesting as it might pave the way for intravascular applications, which require detectors with a small footprint.

Figures 5.12(d-f) present the imaging of a $400 \times 400 \mu\text{m}^2$ region at the trunk of the zebrafish. The brightfield observation of the specimen is depicted in (d), where prominent melanin patterns can be observed as dark structures. The OM scan of the same FOV was performed with $\sim 16 \text{ nJ}$ pulse energy at the focus and is shown in (e). The optoacoustic image essentially visualizes the same melanized structures and single melanophores as the brightfield recording. However, dark features in the brightfield image that can probably not be attributed to any pigmented structures, such as the area indicated by the red arrow, do not appear in the optoacoustic image (indicated by the white arrow), because it exclusively visualizes optical absorption. The side-view MAP of the recorded volume is depicted in (f).

5.5.5 Summary and future plans

For the first time, biological specimens have been imaged in OM with a π -FBG sensor. The results look similar to conventional OM images, showing good contrast and anatomical conformity with corresponding brightfield recordings.

These findings are promising with respect to a possible upgrade of the OM system from current transmission mode to epi-illumination mode in order to enable the imaging of large specimens at arbitrary positions. Alternatively, the π -FBG sensor could be used in a side-looking configuration together with a galvo-mirror-based scanning of the laser beam inside the sample for rapid acquisition. Finally, this study could be a first step towards optoacoustic intravascular applications, where the small size of the optical sensor would represent a major advantage compared to so far commonly used piezoelectric transducers.

5.6 Conclusion and outlook

The developed OM system was demonstrated to achieve a sub-cellular lateral resolution allowing to resolve nuclei in endogenous zebrafish melanophores. The lateral resolution can be readily increased by using a higher NA objective at the expense of field of depth. Additionally, the imaging of mouse ear vasculature showed that the OM modality is capable of label-free deep-tissue imaging, simultaneously visualizing blood vessels through a depth of $> 100 \mu\text{m}$ without the necessity of depth-scanning. Consequently, the developed OM system is suitable for an integration of multiphoton microscopy (see next chapter), which achieves a similar spatial resolution and imaging depth.

Furthermore, the measurement of the transducer's EIR by means of the gold sample as well as the successful demonstration of a correction for the detection frequency response disclosed a promising way of characterizing high-frequency transducers, which is traditionally a tedious task. If used together with a fast laser-scanning approach, the presented method could be utilized to characterize the 3D SIR of ultrasound transducers. Such a measurement could in turn promote reconstruction algorithms used in optoacoustic

mesoscopy applications that take the detector properties into account (see section 3.3.3). Up to now, the detector models employed in optoacoustic mesoscopy are based on simulations or theoretical calculations and are expected to benefit from an exact knowledge of the 3D SIR of the used high-frequency transducers.

6 Integrated multiphoton and multiscale optoacoustic microscope (IMMSOM)

This chapter presents the combination of the previously introduced OM system discussed with multiphoton microscopy and is based on [139] and [163]¹. First, a motivation for multimodal microscopy schemes as well as the state of the art are provided (section 6.1), before the different label-free modalities of the hybrid system are presented and described (section 6.2). Next, the system is characterized (section 6.3) and multiscale optoacoustic imaging is demonstrated on the *ex vivo* imaging of a zebrafish larva (section 6.4.1). Finally, the full multiscale and multicontrast performance of the developed hybrid microscope is showcased on the *ex vivo* imaging of model organisms (sections 6.4.2 and 6.4.3) and a human carotid atheroma sample (section 6.4.4).

6.1 Introduction

The last few decades have seen a tremendous growth and sophistication of optical microscopy techniques due to advances in various technological fields, such as optical components, laser sources, detectors and fluorescent labels. As a result of this development, researchers can access a vast pool of high-resolution imaging tools to study structure and function of all different aspects and parts of biological systems. On the other hand, each of these microscopy modalities relies on a specific contrast mechanism and can thus visualize only a limited number of features with a fixed spatial resolution and within a limited imaging volume. However, biological organisms are highly complex systems with mutually interacting sub-units of different structure and scale. Consequently, many biological applications, such as studying development and the spatial heterogeneity of diseases, require the simultaneous capturing of cellular, tissue and whole-organism level features and processes, as well as their mutual interactions [5]. Therefore, a number of requirements have to be met by an ideal imaging scheme for such applications.

First, the concurrent visualization of different structural features can only be achieved by multiple labeling or by the combination of several imaging modalities to extend the range of accessible contrast mechanisms. In OM, multimodal imaging has been achieved in combination with various techniques, such as optical coherence tomography [164], pulse-echo ultrasound imaging [157], fluorescence confocal microscopy [165], multiphoton microscopy [128, 166, 167] or quantitative phase-contrast microscopy [168].

Second, the capturing of structures and processes ranging in dimension from nanometers to millimeters requires multiscale imaging capabilities with variable spatial resolution and imaging volume. However, due to the limitation of ballistic light excitation, the maximum achieved imaging depth of conventional microscopy techniques does usually not exceed a few hundred microns even in tissue. To overcome this limitation, several mesoscopic imaging approaches achieving resolutions of tens of micrometers have been

¹ The multiphoton system was developed by Dr. George Tserevelakis.


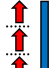
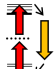


Label-free modality	Contrast mechanism	Typical biological structures	Lateral resolution	Axial resolution	Imaging depth
SHG 	Birefringence	Collagen, myosin fibrils	$\sim 1.5 \mu\text{m}$	$\sim 6 \mu\text{m}$	$< 0.5 \text{ mm}$
THG 	Optical inhomogeneity	Lipid droplets, membranes	$\sim 1.5 \mu\text{m}$	$\sim 6 \mu\text{m}$	$< 0.5 \text{ mm}$
TPEF 	Auto-fluorescence	Elastin, lysosomes	$\sim 1.5 \mu\text{m}$	$\sim 6 \mu\text{m}$	$< 0.5 \text{ mm}$
OM 	Optical absorption	Vessels, melanin	$\sim 1 \mu\text{m}$	$\sim 6 \mu\text{m}$	$< 1 \text{ mm}$
RSOM 	Optical absorption	Vessels, melanin	$< 30 \mu\text{m}$	$\sim 6 \mu\text{m}$	$< 5 \text{ mm}$

Table 6.1: Comparison of the label-free imaging modalities of IMMSOM. (Adapted from [139].)

developed, including mesoscopic fluorescence tomography (MFT) [57], RSOM [58] and other optoacoustic mesoscopy techniques [67, 68, 169] (see section 2.5).

Third, an appropriate imaging method should rely on label-free contrast to minimize photodamage in the specimens. As discussed in section 1.2, the artificial labeling of specimens, either via exogenous agents or through introducing genetically expressed fluorescent proteins such as GFP, can interfere with physiological functions of the examined biological organisms [7]. Furthermore, the excitation light potentially creates altered molecules such as reactive oxygen species [8], which can be toxic to the organism (phototoxicity), and inevitably leads to photobleaching, therefore setting limits on the total observation time (see section 2.3.6). Since optoacoustic imaging visualizes optical absorption, it is ideal to image endogenous tissue chromophores, such as melanin or hemoglobin.

Finally, the observation of biological processes on multiple temporal scales requires a fast acquisition speed and long-term imaging capabilities [5]. To achieve this goal, several rapid-acquisition OM methods have been introduced, based on laser-scanning by means of galvanometric mirrors [170] or microelectromechanical systems (MEMS) [136], fast stage-scanning [171] and light-sheet illumination [172].

In order to meet the first three requirements, the OM system presented in chapter 5 was combined with transmission-mode RSOM and multiphoton microscopy, incorporating two-photon excitation fluorescence (TPEF), second-harmonic generation (SHG) and third-harmonic generation (THG) microscopy. This integrated multiphoton and multiscale optoacoustic microscope (IMMSOM) combines five label-free² high-resolution imaging modalities (see Table 6.1) and operates at different geometrical scales by integrating microscopic and mesoscopic modes into one device. Besides the label-free nature of the multiphoton modalities, the larger penetration depth compared to fluorescence microscopy facilitates the combination with OM, achieving imaging depths of several hundreds of

² In case of TPEF, label-free refers to intrinsic autofluorescence.

micrometers. On the other hand, the RSOM modality allows for scanning two orders of magnitude larger FOVs compared to conventional microscopy and reaches penetration depths of several millimeters. At the same time, multimodal imaging enables the concurrent visualization of various biological features with complementary contrast. The scanning volume and spatial resolution can be dynamically selected through switching between RSOM and the microscopy modalities, lending the developed IMMSOM system a unique zoom-in ability.

6.2 Experimental setup

The IMMSOM setup is schematically depicted in Figure 6.1(a), a photograph can be found in appendix C. The microscopy modalities employed two different laser sources, which were both coupled into an inverted microscope. A flip mount mirror inside the last beam expander was used in order to switch between OM and multiphoton scans. The entire system was situated on an optical table that was actively isolated from external vibrations by a pneumatic system (PTS603, Thorlabs).

6.2.1 Optoacoustic microscope

Compared to the OM system introduced in the previous chapter, the OM sub-system of IMMSOM used a higher NA objective (Plan Apochromat 10X, Zeiss; numerical aperture: 0.45 NA), which was also used for multiphoton microscopy, and motorized stages for the transducer alignment. The OM scanning scheme is illustrated in Figure 6.1(c).

6.2.2 RSOM modality

For RSOM scans, the sample position remained fixed, whereas the 80 MHz transducer was raster-scanned laterally above the sample using two motorized linear piezo stages (M 683.2U4, Physik Instrumente GmbH & Co. KG). The microscope objective was replaced by an ordinary lens in order to achieve a broad illumination of the sample by the opening cone of the full power laser beam, which was focused below the sample holder (see Figure 6.1(d)). The lens and the objective for the microscopy modalities could be easily interchanged by means of an objective revolver. For 3D imaging, the sample or structures to be imaged were placed in the positive defocus of the transducer. A short-range but compact z -stage (M 501.1DG, Physik Instrumente GmbH & Co. KG) allowed for vertical positioning of the transducer. This xyz -scanning unit was mounted upside down on a massive frame to minimize image artifacts caused by vibrations during the raster-scan. The RSOM scanning scheme followed the pattern illustrated by Figure 6.1(b).

For signal processing and 3D reconstruction, the filtering techniques and the GPU-based WHSF backprojection algorithm introduced in section 3.3.3 were used. The final images were corrected for the uneven Gaussian-shaped laser illumination through division by a 2D Gaussian. For both optoacoustic modalities, the stage control, transducer alignment, signal acquisition and processing, as well as the reconstruction was performed in MATLAB[™].

6.2.3 Multiphoton microscope

The three multiphoton microscopy modalities used an Yb-based solid state femtosecond laser with a wavelength of 1043 nm (YBIX, Time-Bandwidth; pulse width: 170 fs, average

power: 2.8 W, repetition frequency: 84.4 MHz). The laser beam was attenuated and reduced in diameter by a two-lens telescope to fit the size of a following set of high-precision galvanometric scanning mirrors (6215H, Cambridge Technology). Subsequently, the beam was reflected by a shortpass dichroic mirror (DMSP805R, Thorlabs) and expanded six times by a 4f telescopic lens configuration, before it was finally coupled into the inverted microscope and focused into the sample. The galvo mirrors were used to raster-scan the laser focus in the xy -plane inside the specimen and followed a scanning scheme as illustrated by Figure 6.1(b). For focal plane selection and z -scanning to generate 3D stacks, the sample holding piezo-stage was used. Figure 6.1(e) depicts the scanning configuration for multiphoton microscopy. For a resolution of 300×300 pixels and a galvo line-scan frequency of 400 Hz, the achieved frame rate was around 0.6 s. Final images were averaged 30 times to increase the SNR. Both, SHG and TPEF signals generated at the focus were collected back through the objective and transmitted through the shortpass dichroic mirror. The desired wavelengths for SHG and TPEF recordings were selected by an appropriate narrow bandpass dielectric interference filter (FB520-10, Thorlabs) and a longpass colored glass filter (FGL550, Thorlabs), respectively. Finally, the non-linear optical signals were detected via an ultra-sensitive photomultiplier tube (PMT) (H9305-03, Hamamatsu), amplified and digitized by a 16-bit DAQ card (PCIe 6363, National Instruments; max. sampling rate: 1 MS/s). Compared to SHG and TPEF radiation, the THG signals with a UV wavelength of ~ 348 nm were emitted mainly in forward direction [52]. Therefore, a second detection channel was designed in transmission-mode, accommodating a 0.79 NA aspherical condenser lens (ACL25416U, Thorlabs), a bandpass color glass filter (FGUV5, Thorlabs) and a second identical PMT. For the accurate interchange of ultrasound transducer and THG channel, magnetic mounts (SB1, Thorlabs) were used to connect the respective detector holders to the xyz -stage unit. The synchronization of the multiphoton devices and the data acquisition were performed using custom designed LabVIEW programs. Final image processing for all modalities was done with Fiji and involved operations such as windowing, median filtering, interpolation, gamma correction and Gaussian blurring of the entire images.

6.3 Characterization

6.3.1 Spatial resolution

The spatial resolution of the OM modality using the 0.45 NA objective was determined by imaging a black polystyrene microsphere with 954 nm diameter embedded in agar, following the same procedure as discussed in section 5.3.3. The sphere was scanned in $0.2 \mu\text{m}$ steps in an $8 \times 8 \mu\text{m}^2$ FOV with a pulse energy of ~ 12 nJ and five signal averages. Figure 6.2(a) shows the Gaussian fitted lateral (blue, $R^2 = 0.997$) and axial (black, $R^2 = 0.993$) profiles of the microsphere. The two insets depict the top-view (top panel) and side-view (bottom panel) MAPs of the imaged microsphere. The FWHM of the lateral profile was 910 nm, corresponding to a lateral resolution of 829 nm according to Eq. (5.4). The theoretical value predicted by Eq. (2.14) was 584 nm. As in the previous chapter, the difference in expected and measured resolution probably arises from beam imperfections, optical aberrations and a slight underestimation of the measured resolution by the deconvolution assumption. The axial profile corresponds to the positive peak of the raw signals, yielding a FWHM and thus an axial resolution of $5.78 \mu\text{m}$. This number is in a good agreement with the value determined in [11]. In the same article, the FWHM of the acoustic focus of the 80 MHz transducer was found to be $\sim 30 \mu\text{m}$ up to 5 mm of

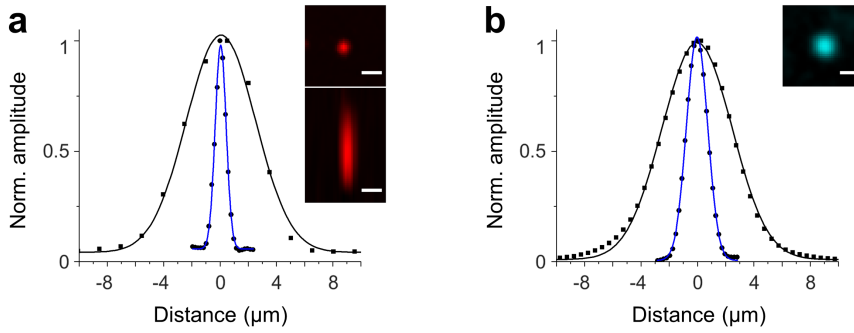


Figure 6.2: Spatial resolution characterization of the IMMSOM microscopy modalities. (a) OM measurement of a black 954 nm microsphere. The insets show MAPs of the imaged sphere in top (top) and side (bottom) view. Gaussian fitted profile plots are illustrated by the blue (lateral) and black (axial) curves. (b) Measurements of a 100 nm fluorescent nanobead with TPEF and a glass-air optical interface with THG. The inset shows the lateral view of the nanobead. Blue and black curves represent the Gaussian fitted profiles of the sphere (lateral, TPEF) and the glass-air interface (axial, THG), respectively. Scale bars: 2 μm . (Adapted from [139].)

depth, corresponding to the lateral resolution of the RSOM modality of IMMSOM. The axial resolution of RSOM was the same as for OM.

For multiphoton microscopy, the lateral and axial resolutions were characterized using two different approaches. The lateral resolution was estimated through the TPEF imaging of a 100 nm fluorescent bead (TetraSpeck Fluorescent Microspheres Size Kit, Invitrogen). Figure 6.2(b) shows the respective Gaussian fitted lateral profile (blue, $R^2 = 0.999$). The FWHM of the profile was 1.75 μm , corresponding directly to the lateral resolution because the bead acted as a point source (see section 2.2.2). This value is twice as large as the OM resolution, owing to the longer wavelength of the employed femtosecond laser of 1043 nm compared to 515 nm for the OM laser. The theoretical diameter of the diffraction limited spot was 1.18 μm according to Eq. (2.14). A top-view MAP of the nanobead is shown by the inset in (b), representing the transverse PSF of the multiphoton system. On the other hand, the axial resolution of the non-linear modalities was determined by measuring the THG profile at the glass-air interface of a standard 170 μm cover slip, as shown by the black curve in Figure 6.2(b). The FWHM of the Gaussian fit ($R^2 = 0.998$) was 5.84 μm , corresponding to the confocal parameter of the beam [173] and thus to the axial resolution. The pulse energy for both measurements was ~ 1.3 nJ.

For this analysis, the raw images were smoothed with a weak Gaussian blurring filter in order to eliminate an angular dependence of the profile widths. Hence, the true spatial resolution of the OM and multiphoton modalities was slightly better than estimated in this section.

6.3.2 Co-registration of the imaging volumes

As the optoacoustic and multiphoton modalities used different laser sources, the optical foci and therefore the FOVs of the different IMMSOM modalities exhibited slight offsets in all three dimensions in the order of tens of micrometers. In order to co-register the scanning volumes of the sub-modalities, an 18 μm suture cross phantom was imaged with RSOM, OM and THG microscopy, as illustrated by Figure 6.3. The FOVs of all non-linear modalities were scanned by the same laser and were thus identical. A top-view MAP of the RSOM scan is presented in (a), showing an extended FOV of 2.3×2.3 mm².

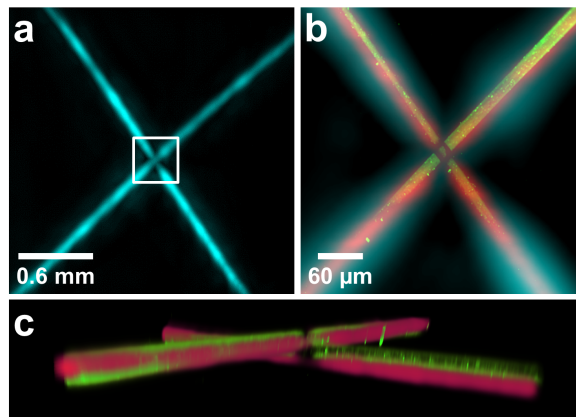


Figure 6.3: Offset characterization of the IMMSOM modalities by the multi-modal imaging of an $18\ \mu\text{m}$ suture cross phantom. (a) Top-view MAP of the RSOM reconstruction. The white box indicates the FOV of microscopy scans. (b) Overlay of the RSOM (cyan), OM (red) and THG (green) MAPs after offset correction. (c) Offset-corrected 3D overlay of the OM and THG reconstructions. (Adapted from [163].)

Figure 6.3(b) shows an offset-corrected overlay of the OM (red color) and THG (green color) scans with the zoom-in of the RSOM image (cyan color) within the white box indicated in (a). The difference in lateral resolution between RSOM and the microscopy modalities is reflected by the larger diameter of the imaged sutures. The three scans show a good correspondence of the suture orientation, which is also validated in 3D for the OM and THG reconstructions, as illustrated by Figure 6.3(c). From these scans, the mutual lateral and axial offsets were determined and corrected for prior to each IMMSOM measurement. The final co-registration of all images was performed with Fiji.

6.4 Results

6.4.1 Multiscale optoacoustic zebrafish imaging

First, the ability of IMMSOM to perform multiscale optoacoustic imaging with RSOM and OM and to accurately relate the resulting images was investigated. For this purpose, a 5 dpf wildtype zebrafish larva was measured. With RSOM, a FOV of $3 \times 3\ \text{mm}^2$ covering the entire fish was scanned using a step size of $4\ \mu\text{m}$. Figure 6.4(a) depicts the top-view MAP of the RSOM reconstruction. A MAP from a 65° side view is presented in (b). In the two images, the eyes (E), yolk (Y), swim bladder (B) and the melanophore patterns along body and tail forming the yolk sac stripe (YS), ventral stripe (VS), dorsal stripe (DS) and central stripes (CS) of the zebrafish can be identified. For the high-resolution OM scan, a ROI at the tail of the fish was selected, as indicated by the white box in (a). The inset in (a) represents a zoom-in on the respective RSOM image. Even though single melanocytes can be identified in this close-up, sub-cellular features cannot be resolved due to the lateral resolution of RSOM of $20\text{--}30\ \mu\text{m}$. The OM image of the same region is shown in Figure 6.4(c), visualizing single melanocytes of the dorsal (lower stripe) and central (upper stripe) pigmented stripes with sub-cellular resolution. The pulse energy at the sample was $\sim 13\ \text{nJ}$. A brightfield microscopy image of this FOV is provided by (d) as a reference. The blue and red arrows mark the same two exemplary melanocytes throughout the images for comparison. Evidently, the OM scan could only visualize melanophores around the relatively thin focal plane, whereas with RSOM it was possible

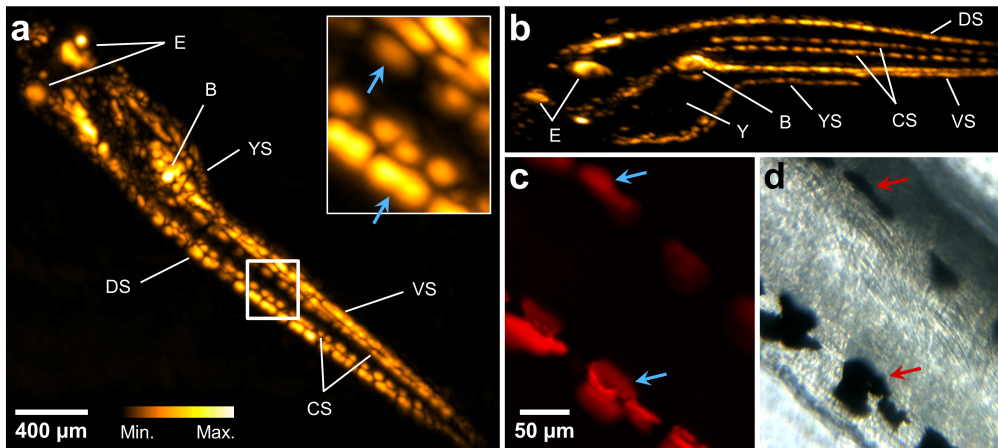


Figure 6.4: multiscale optoacoustic imaging of a wildtype zebrafish larva *ex vivo*. (a-b) RSOM scan of the entire specimen. MAPs are shown in top view (a) and 65° side view (b). The eyes (E), yolk (Y), swim bladder (B) and the melanophore patterns forming the yolk sac stripe (YS), ventral stripe (VS), dorsal stripe (DS) and central stripes (CS) can be identified. The white box in (a) indicates the FOV where high-resolution scans with optoacoustic (c) and brightfield (d) microscopy were performed. The inset in (a) shows a zoom-in of the RSOM image on the same region. Two identical melanophores are highlighted with blue and red arrows as reference. (Adapted from [163].)

to map the pigment distribution of the whole specimen. In this manner, the optoacoustic multiscale implementation of IMMSOM was able to combine the advantages of mesoscopic and microscopic imaging into one device. Moreover, by comparing the RSOM and OM images of the same FOV, it can be concluded that the developed system achieved high structural conformity between the different scales, which is important for relating RSOM via OM to the multiphoton scans.

6.4.2 Hybrid mouse ear imaging

Next, the full multiscale and multicontrast imaging capabilities of IMMSOM were studied by the hybrid imaging of an excised mouse ear. Figure 6.5 summarizes the multimodal imaging of the ear, which was embedded in pure agar inside a glass bottom dish. The first step involved an RSOM scan of a $2 \times 2 \text{ mm}^2$ FOV with a step size of $3 \mu\text{m}$ and an acquisition time of ~ 6 min. A top-view MAP of the reconstruction, visualizing vasculature through the entire thickness of the mouse ear of about $350 \mu\text{m}$, is illustrated in Figure 6.5(a). Additionally, to capitalize on the inherent multiscale nature of RSOM, a multi-frequency reconstruction was conducted as introduced in section 3.3.3. For this purpose, the high frequencies in the 75–125 MHz band were reconstructed and the resulting MAP processed separately to enhance the visibility of small features and vessels. The overlay of the full detection band (red color), representing mainly the bigger vessels, and the high frequencies (cyan color), showing small features otherwise masked by low-frequency structures or noise, is presented in Figure 6.5(b). To highlight the effect of the multi-frequency reconstruction, a small region indicated by the white dashed box is magnified as an inset and compared to the full-bandwidth reconstruction shown in (a). The multi-frequency inset contains small vessels (highlighted by the arrows), which are not observed in the respective inset in (a). Subsequently, the zoom-in ability of IMMSOM was exploited to select a ROI of $375 \times 375 \mu\text{m}^2$ at the branching of a big vessel for

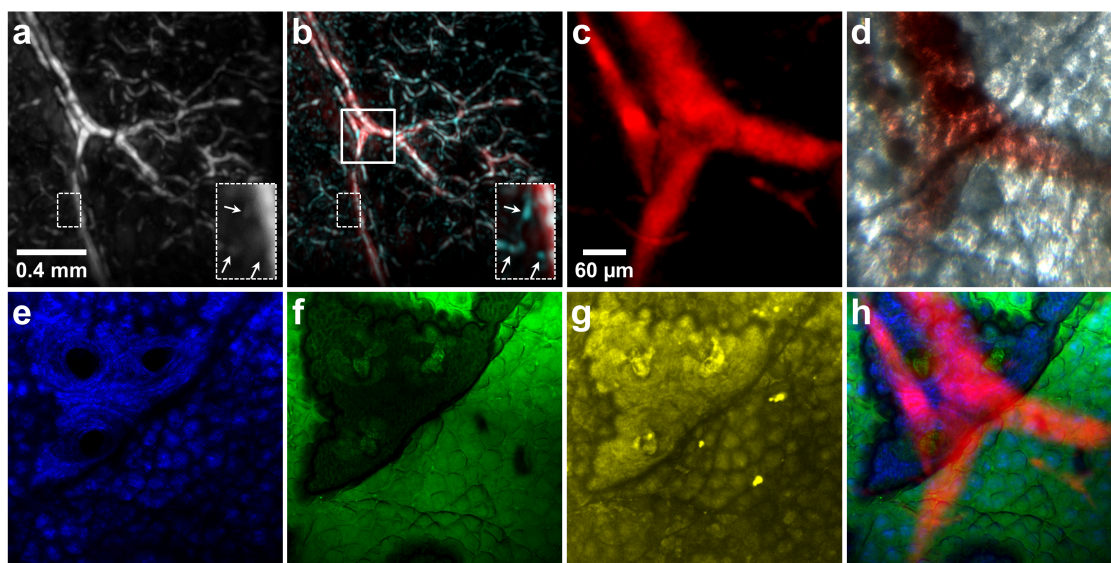


Figure 6.5: Hybrid label-free imaging of a mouse ear *ex vivo*. (a) RSOM top-view MAP of an extended volume showing vasculature of different size. (b) Overlay of the full detection bandwidth (red) and high frequencies (cyan). The insets depict a magnified region marked with the dashed white boxes. White arrows highlight the enhancement of small vessels by multi-frequency reconstruction (b). The white square indicates the selected ROI for microscopy scans with the (c) OM (vessels), (d) brightfield microscopy, (e) SHG (collagen), (f) THG (keratinocytes and hair follicles) and (g) TPEF (elastin) modalities. (h) Overlay of the OM, SHG and THG images. (Adapted from [139].)

multimodal microscopy imaging, as indicated by the white square in (b). For the OM scan, a step size of $1.8\ \mu\text{m}$, a pulse energy of $\sim 85\ \text{nJ}$ and 40 signal averages were used. The corresponding top-view MAP is shown in (c), visualizing the branching and some small vessels with high contrast.

Multiphoton scans of the same region were performed through a depth of $50\ \mu\text{m}$ with $2\ \mu\text{m}$ vertical steps, a pixel size of $0.5\ \mu\text{m}$, $\sim 1.3\ \text{nJ}$ pulse energy and 30 averages. Maximum intensity projections (MIP) are presented for (e) SHG, (f) THG and (g) TPEF measurements. The SHG image (e) displays the collagen constituting the dermis layer of the ear skin [174]. Due to their non-centrosymmetry and intrinsic birefringence, collagen fibrils represent strong sources of SHG signal generation [175]. A pronounced region in the upper left corner containing three holes can be observed. This area is surrounded by collagen patterns following the keratinocyte locations of the epidermis layer. Thus, it can be concluded that the stratum corneum of the ear skin represented a mono-layer of cells. The gaps between the patterns correspond to the intercellular boundaries, which probably reduced the laser focusing due to an increased scattering and hence lead to a decreased signal generation in the collagen layer underneath. In the THG image (f), the keratinocytes populating the stratum corneum of the epidermis are clearly visible. The signals arose from the optical interface between this outermost layer of the stratified squamous epithelium and the cover slip. Additionally, an area characterized by the absence of cells and weak signal generation is observed, matching with the smooth region in the SHG image. It contains three well-defined structures, which can be identified as hair follicles. Finally, the TPEF image (g) shows the autofluorescence arising mainly from elastin contained in the extracellular matrix of the dermis layer [174] and from the bulb regions of the hair follicles [176,177]. While it follows essentially the collagen distribution,

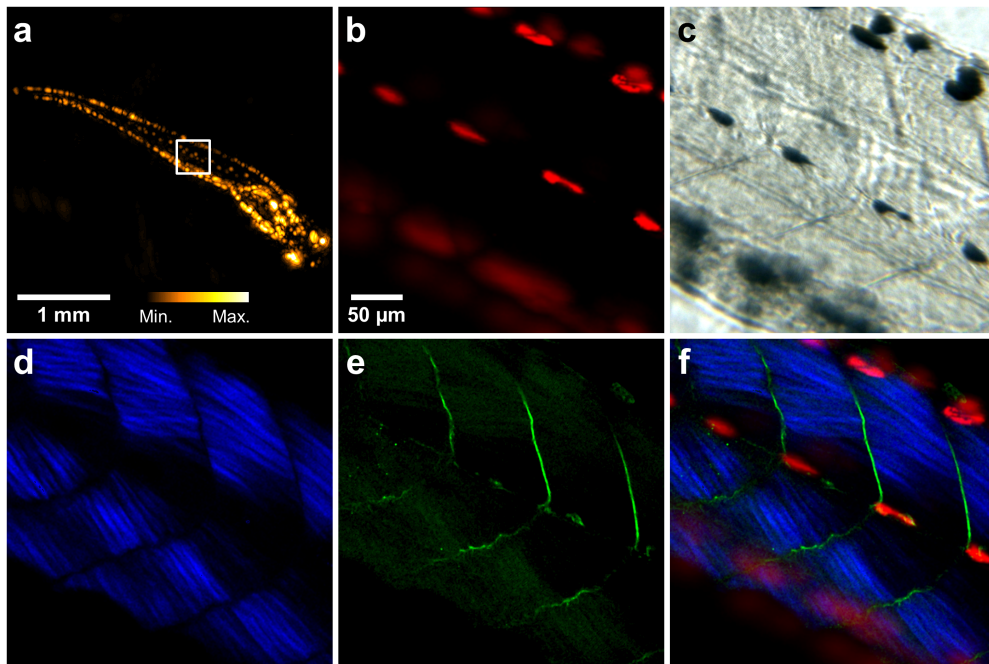


Figure 6.6: Hybrid label-free imaging of a wildtype zebrafish larva *ex vivo*. (a) RSOM top-view MAP of the zebrafish, visualizing the global pigment distribution, eyes and inner organs. Microscopy images were obtained from the ROI indicated by the white box. Imaging was performed with the (b) OM (melanocytes), (c) brightfield microscopy, (d) SHG (muscles) and (e) THG (connective tissue) modalities. (f) Overlay of the OM, SHG and THG images. (Adapted from [139].)

the hair follicles yield strong signals compared to the SHG image. An overlay of the OM, SHG and THG images is illustrated in Figure 6.5(h), displaying a high contrast complementarity between the different scans. A brightfield microscopy image of the same region is shown in (d) as a reference.

6.4.3 Hybrid zebrafish imaging

To demonstrate the performance of IMMSOM on a second model organism, a 6 dpf wildtype zebrafish larva was imaged *ex vivo*. The RSOM image of the entire specimen, representing the top-view MAP of the full detection bandwidth for a scanning region of $4 \times 4 \text{ mm}^2$, is depicted in Figure 6.6(a). The step size was $5 \mu\text{m}$ and the scan took ~ 10 min. As discussed in section 6.4.1, the RSOM image visualizes the global pigment distribution and other anatomical features of the fish. Subsequent microscopy scans were performed within a selected ROI of $315 \times 315 \mu\text{m}^2$ (indicated by the white box in (a)) at the trunk of the larva. The OM scan was carried out with $1.8 \mu\text{m}$ step size, $\sim 8 \text{ nJ}$ pulse energy and 40 signal averages within ~ 65 min. The corresponding top-view MAP is illustrated in Figure 6.6(b), showing single melanocytes around the focal plane. The lower melanized stripe was out of focus and is thus characterized by low amplitude and blurred shape.

Figures 6.6(d) and (e) depict the SHG and THG images, respectively. The multiphoton scan parameters were similar to the mouse ear imaging, whereas the pulse energy had to be reduced to $\sim 0.5 \text{ nJ}$ due to the strong non-linear absorption of melanin. Consequently,

saturated pixels from the pigments were removed from the multiphoton images in order to improve the visibility. Furthermore, the images represent single slices of the recorded stacks at the approximate same depth as the focal plane during the OM measurement. The SHG image (d) reveals the musculature of the fish tail, owing to the strong SHG signal generation by myosin fibrils contained in the sarcomeres – the functional units of muscles [178]. Moreover, the different muscle segments (myomeres) constituting the musculature can be distinguished and single myofibrils are resolved. On the other hand, the THG signals (e) originated mainly from the gaps between the myomeres and can thus be identified as the vertical myosepta, which represent thin sheets of connective tissue that separate and support the myomeres and to which the myofibrils are attached. Figure 6.6(f) shows an overlay of the OM, SHG and THG images. As for the mouse ear, the triple-modal image is characterized by a strong contrast complementarity, simultaneously visualizing three different anatomical structures without the necessity of labeling. A brightfield microscopy image (c) serves as a reference and shows the pigments, as well as indications of the vertical myosepta.

6.4.4 Hybrid human carotid atheroma imaging

Finally, the IMMSOM system was used for the hybrid imaging of a human carotid atheroma slice³. These patient samples, acquired through carotid thrombendarterectomy, yield valuable information about carotid artery atherosclerosis, which is a main cause of ischemic stroke. It results from an atheromatous plaque, which accumulates chronically within the subendothelial layer (intima) of the affected artery, becomes complicated and creates a thrombotic luminal occlusion leading to cerebral ischemia [180,181]. Understanding atheroma pathophysiology and characterizing the involved histological components is critical for the development of prevention and treatment strategies and requires the complementary interrogation of the different plaque tissue constituents and their interactions. Some earlier approaches used multiphoton microscopy for the label-free imaging of atheroma samples, however these techniques did not incorporate OM for the detection of blood embeddings [182,183].

As depicted by Figure 6.7(a), advanced atheromatous plaques can be divided into different structural sub-regions: the shoulders, a thin fibrous cap and a large lipid-rich necrotic core. Figure 6.7(b) shows a brightfield image of the entire 10 μm thick atheroma slice, acquired with a microscope slide scanner (Aperio CS2, Leica). The constricted lumen, the shoulders, as well as the cap and the large necrotic core can be identified. In order to localize a ROI for multimodal imaging, a 10 \times 10 mm² coarse OM image with a step size of 100 μm was acquired. The resulting image is presented in (c), revealing a congruence of yellow-brown intraplaque patterns on the brightfield image (b) and OM signals, corresponding to blood embeddings. In order to visualize the topological structure of the lipid core, a ROI was selected and imaged with the IMMSOM microscopy modalities. The OM scan, depicted in (d), was performed using a 100 MHz transducer (Sonaxis; –6 dB bandwidth: 42–149 MHz, active element diameter: 3 mm, focal distance: 3 mm) and 20 averages⁴. It reveals the blood residue distribution in the core, appearing

3 This section is based on [179]. The laser-scanning OM implementation was developed by Markus Seeger.

4 The OM scan was performed using galvo scanning and streaming like continuous data acquisition with a 12-bit DAQ card (ADQ412, SP Devices; max sampling rate per channel: 3.6 GS/s), which is described in more detail in [179]. This implementation of OM is, however, not part of this thesis.

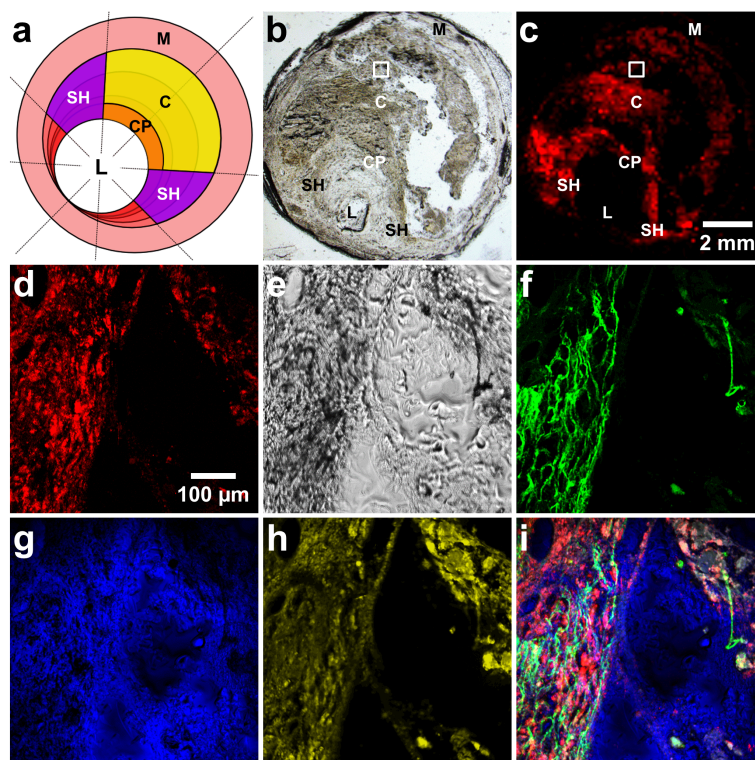


Figure 6.7: Hybrid imaging of a human carotid atheroma slice. (a) Schematic illustration of a typical atherosclerotic vascular cross-section. **Abbreviations:** C: Core, CP, Cap, L: Lumen, M: Media, SH: Shoulder. (b) Widefield BF image of the atheroma slice used for IMMSOM imaging. (c) Coarse OM scan of the entire sample. The white box indicates the selected ROI at the lipid core region. **(d-i) Multimodal imaging of the core region.** (d) OM, (e) brightfield microscopy, (f) SHG, (g) THG and (h) TPEF scans of the same FOV. (i) Overlay of the OM and multiphoton images, where the TPEF signals are shown in white color. (Adapted from [179].)

in clusters. The overall tissue morphology is shown by the THG image (g) and by the brightfield microscopy image (e), whereas the darker areas in the latter correspond to the regions generating strong OM signals. The SHG scan (f) visualizes the collagen fibers inside the core, which appear to be widened and split up into smaller fibrils. Finally, the TPEF image (h) reveals elastin in the extracellular matrix of the tissue. The structures visible in the upper right corner cannot be assigned with OM or THG signals and could therefore represent foam cells, which are known to be prominent in the necrotic lipid core and moreover generate TPEF signals [184]. The overlay of OM, SHG, THG and TPEF (white color) signals is depicted in (i). A fine interleaving of collagen fibrils and blood embeddings in the order of 10–20 μm can be observed, indicating an advanced degradation of overall tissue morphology.

As can be concluded by the imaging results, IMMSOM has the capability to reveal information regarding collagen, elastin and blood residues as well as their mutual interaction without the need for staining. Due to the lack of requiring multiple slices to obtain the components of interest (i.e. collagen, elastin, blood and overall cell distribution) by histological staining techniques, a precise topological co-registration was achieved. This application might be useful to assess the severity of degradation and the potential risk of rupture in atheromatous plaques.

6.5 Conclusion and outlook

For the first time, label-free multiscale and multimodal high-resolution imaging has been demonstrated with a single device. The developed IMMSOM system offers the possibility to scan entire specimens or large structures of several millimeters length with high spatial resolution and to dynamically zoom into interesting regions for imaging with micrometer resolution. It therefore bears great potential for developmental biology studies, providing a comprehensive view of complementary anatomical features at different scales, whereas RSOM facilitates high-resolution imaging beyond the optical diffusion limit. These capabilities are expected to enhance our understanding of morphological processes, simultaneously capturing cellular, tissue and organ level organization in developing organisms. Moreover, IMMSOM has been successfully demonstrated on the label-free imaging of histopathological samples. Hence, it is expected to become a valuable tool for the assessment and examination of tissue samples, where staining procedures might be disadvantageous for the integrity and co-registration of the different structures to be visualized.

At the current stage, the *in vivo*⁵ application of IMMSOM is limited to small specimens, such as early-stage zebrafish or mouse ears, due to its transmission-mode configuration. As already discussed in section 5.5, an implementation of the system in epi-illumination mode, e.g. using an optical fiber detector, could overcome these constraints. However, this would probably come at the cost of the RSOM modality, which could not easily be changed to an epi-illumination configuration in the inverted microscope. Furthermore, by employing several excitation wavelengths (e.g. by a tunable dye laser), a more comprehensive differentiation of various tissue structures based on their characteristic absorption spectra, such as oxy- and deoxyhemoglobin or melanin, might be achieved [185]. Finally, in order to meet the fourth requirement discussed in the introduction (a high temporal resolution for the imaging of rapid biological processes), the acquisition speed of IMMSOM has to be increased. For the OM modality, this can be accomplished by fast laser-scanning using a high-repetition-rate laser and streaming-like acquisition. A further increase of the imaging speed could be realized by the simultaneous recording of optoacoustic and SHG or TPEF signals.

5 Up to this point, OM and IMMSOM imaging has only been demonstrated *ex vivo*. As will be discussed in chapter 7, *in vivo* imaging of mouse ears has been accomplished in the context of frequency-domain OM and can be readily employed in future IMMSOM applications.

7 Laser-scanning frequency-domain optoacoustic microscope (FD-OM)

In this chapter, the development of a transmission-mode optoacoustic microscope operating in the frequency-domain (FD) is presented¹. After providing a theoretical background on signal generation, SNR limitations and IQ demodulation (section 7.2), the experimental setup is introduced (section 7.3). Subsequently, the characterization of the laser source and FOV as well as a simulation of monofrequent sensitivity fields of the transducer are discussed (section 7.4). Next, FD-OM imaging is demonstrated on phantoms and model organisms *ex vivo* and *in vivo* (section 7.5). Finally, the combination of FD-OM with the previously introduced multiphoton microscope is presented (section 7.5.5).

7.1 Introduction

Optoacoustic microscopy is typically realized in the time-domain (TD) using short pulsed laser sources, such as the OM system presented in chapter 5. Optoacoustic signals are generated within the duration of a laser pulse (usually 1–10 ns) and recorded in the microsecond range following the excitation process [14]. A key feature of this OM implementation is the TOF information contained in the ultrasound waves that are emitted by local absorbers in the sample. This information enables the localization of imaged structures with respect to the transducer and to other signal generating optoacoustic sources. Furthermore, absorbers at different depths can easily be separated by temporal windowing of the signals, e.g. in vascular imaging applications where out-of-focus vessels can mask capillaries at the focal plane. Another advantage of TD-OM is the high SNR owing to the excitation of broadband optoacoustic signals with high-energy pulses, typically in the range of 1–100 nJ. The short duration of the pulses leads to an efficient generation of signals from a broad range of optical absorbers, distributing the pulse energy over an extended frequency range. Additionally, high repetition rate laser sources enable fast imaging, e.g. based on galvo scanning, as discussed in section 6.1.

However, high-speed OM implementations in the time-domain are relatively complex systems because of the required synchronization of the pulsed laser source, scanning device and data acquisition. Moreover, apart from the combination of several usually expensive laser lines, multi-wavelength approaches are so far limited to dye lasers, which suffer from rapid chemical degradation of the dyes or to expensive optical parametric oscillators, both of which requiring additional pump laser sources.

On the other hand, optoacoustic waves can also be generated as localized signals in the frequency-domain by using intensity-modulated continuous wave (CW) lasers. Instead of creating acoustic signals that are localized in time but broad in frequency space, the pressure fields generated in FD approaches have one or more sharply defined frequency

¹ The work was initiated by Dr. Stephan Kellnberger and Dr. George Tserevelakis and was prepared for publication [186] during the submission of this thesis.

	Ease of use	Costs	SNR	Axial resolution	TOF	Imaging speed	Instabilities / noise	Multi-wavelength
TD	-	-	++	Yes	Yes	++	Pulse energy jitter	-
FD	++	+	-	Requires frequency sweep	No	+	Laser induced, electronic	++

Table 7.1: Comparison of TD and FD high-speed optoacoustic microscopy.

components but are extended in time. In the simplest FD implementation, the CW source is modulated with a sinusoidal function, giving rise to one defined frequency component [15,16,187,188]. The key advantage of FD-OM is the use of cheap excitation sources, such as diode lasers or even single laser diodes (see Table 7.1). This low-cost feature facilitates the combination of several laser lines to perform multi-wavelength imaging. Furthermore, due to the continuous operation of the lasers, fast imaging applications are easy to implement. However, a considerable disadvantage is the inherently low SNR in FD optoacoustic imaging (see section 7.2.2). To compensate for the weak signals, most methodologies rely on slow lock-in detection, which impeded the implementation of fast scanning FD-OM in the past. Another limitation is the missing TOF information in FD-OM and thus the lack of axial resolution. As opposed to TD imaging, parasitic laser induced signals cannot be separated from real optoacoustic signals having the same frequency, as they are smeared out in time. Moreover, monofrequent FD-OM does not impart depth information due to the 2π -phase ambiguity of sinusoidal signals. Some approaches were able to overcome this restriction by using pulse compression based on frequency-swept (chirped) laser modulation [189–192], which imprints time information onto the frequencies. The TOF of the signals can be restored by using a cross-correlation with reference signals from the modulated laser source. However, these methods cannot be considered pure FD implementations, since the detection is still performed as a TD operation. Another technique to restore depth information in FD-OM is the use of several modulation frequencies within the detection bandwidth of the employed detector [193], which, however, increases the acquisition time. By performing a discrete inverse fast Fourier transform (iFFT) of the frequency-domain signals, the corresponding time profiles carrying depth information can be recovered.

Despite the successful implementation of FD-OM imaging techniques based on lock-in detection, high-speed imaging of biological samples has not been demonstrated. Furthermore, previous applications used either *ex vivo* samples [15] or contrast agents to enhance the SNR [16]. Therefore, a laser-scanning frequency-domain optoacoustic microscope using a simplified acquisition scheme based on IQ-demodulation was developed. In contrast to existing approaches, the developed FD-OM acquires amplitude and phase information at multiple modulation frequencies to enable the depth-resolved visualization of optical absorption. The excitation at more than one frequency additionally expands the range of absorber sizes that can be effectively measured. Moreover, the rapid acquisition allows for higher laser powers to be employed within exposure safety limits, which significantly increases the SNR achieved with FD-OM. Consequently, FD-OM was used for the first time to perform label-free imaging of biological specimens *in vivo*. Finally, the FD-OM modality was combined with multiphoton microscopy for high-speed *in vivo* multicontrast imaging.

7.2 Theoretical background

7.2.1 Governing equations in the frequency-domain

The description of the generation and propagation of periodic pressure waves is more convenient in the frequency-domain [191]. By Fourier transforming the optoacoustic wave equation (3.5), the inhomogeneous Helmholtz equation is obtained as

$$\left(\nabla^2 + \frac{\omega^2}{c^2}\right)\hat{p}(\vec{r}, \omega) = -i\omega \frac{\Gamma}{c^2} \hat{H}(\vec{r}, \omega), \quad (7.1)$$

where ω is the angular frequency and $\hat{p}(\vec{r}, \omega)$ and $\hat{H}(\vec{r}, \omega)$ denote the Fourier transforms of the acoustic pressure field $p(\vec{r}, t)$ and the heating function $H(\vec{r}, t)$, respectively. For monofrequent modulation of the CW laser source with a frequency $\omega_{mod} = 2\pi f_{mod}$, the TD heating function can be written as

$$H(\vec{r}, t) = \eta_h \mu_a(\vec{r}) I_0(\vec{r}) [1 + \cos(\omega_{mod} t)], \quad (7.2)$$

with $I_0(\vec{r})$ representing the time-averaged light intensity [15]. Hence, the respective Fourier transformed heating function is given by

$$\hat{H}(\vec{r}, \omega) = \eta_h \mu_a(\vec{r}) I_0(\vec{r}) \left[\delta(\omega) + \frac{1}{2}\delta(\omega + \omega_{mod}) + \frac{1}{2}\delta(\omega - \omega_{mod}) \right]. \quad (7.3)$$

The first term in the bracket represents the static (DC) component of the modulation function. Similarly to the TD case, the forward solution of the FD wave equation can be obtained by the Green's function approach, with the respective Green's function being

$$\hat{G}(\vec{r} - \vec{r}', \omega) = \frac{1}{4\pi} \frac{e^{-i(\frac{\omega}{c}|\vec{r} - \vec{r}'| + \phi_a)}}{|\vec{r} - \vec{r}'|}, \quad (7.4)$$

where ϕ_a is a phase constant due to the conversion of modulated excitation light to pressure waves by thermoelastic expansion [194]. The FD forward solution of Eq. (7.1) can then be formulated as

$$\hat{p}(\vec{r}, \omega) = -i \frac{\omega \Gamma}{4\pi c^2} \iiint_V d^3\vec{r}' \hat{H}(\vec{r}', \omega) \frac{e^{-i(\frac{\omega}{c}|\vec{r} - \vec{r}'| + \phi_a)}}{|\vec{r} - \vec{r}'|}. \quad (7.5)$$

In the case of a point source that is w.l.o.g. located at the origin, the heating function simplifies to $\hat{H}(\vec{r}, \omega) = \hat{H}(\omega) \cdot \delta(\vec{r})$ and the forward solution takes the form

$$\hat{p}(r, \omega) = -i \frac{\omega \Gamma}{4\pi c^2 r} \hat{H}(\omega) e^{-i(\frac{\omega}{c}r + \phi_a)}, \quad (7.6)$$

which is the Fourier transform of Eq. (3.15). From the forward solution, it can be seen that FD optoacoustic signals have the same frequency content as the modulated laser excitation and that the amplitude of the signals depends linearly on the modulation frequency. In the case of monofrequent modulation, as described by Eq. (7.3), the optoacoustic waves

oscillate at the laser modulation frequency ω_{mod} . Furthermore, the DC term in Eq. (7.3) does not contribute to the signal, as the corresponding frequency is zero. Therefore, the amplitude of FD optoacoustic signals depends on the modulation depth of the employed laser source.

7.2.2 SNR considerations

In this section, an estimation of the SNR achievable with FD-OM compared to the TD method is provided [15, 25].

Signal generation efficiency

For pulsed laser excitation as used in TD-OM, the temporal intensity profile can be approximated as a Gaussian function:

$$I_{pulse}(t) \approx \frac{\phi_p}{\sigma_p \sqrt{2\pi}} e^{-t^2/2\sigma_p^2}. \quad (7.7)$$

Here, ϕ_p denotes the light fluence per pulse and σ_p is the standard deviation of the Gaussian pulse, which relates to the FWHM pulse width τ_p through $\tau_p = 2\sqrt{2\ln(2)}\sigma_p$. According to Eq. (3.15), for a point source the optoacoustic pressure is proportional to the time derivative of the heating function and thus the light intensity: $p_{\delta r}(r, t) \propto \partial I(r, t) / \partial t$. Hence, by using Eq. (7.7) the TD maximum pressure amplitude can be estimated as

$$p_{max,pulse}(r) = \gamma(r) \frac{8\ln(2)\phi_p}{\sqrt{2\pi}e\tau_p^2}, \quad (7.8)$$

with $\gamma(r) = \Gamma \eta_h \mu_a(r) / 4\pi c^2 r$. On the other hand, the heating function in the case of monofrequent laser modulation for FD-OM is given by Eq. (7.2) and the respective maximum pressure amplitude is

$$p_{max,CW}(r) = \gamma(r) \omega_{mod} I_0(r). \quad (7.9)$$

In order to compare Eq. (7.8) and (7.9), the exposure limits for pulsed and CW excitation as defined by the American national standard institute (ANSI) are used. For skin surface irradiation in the visible range, the respective exposure limits are $\phi_{p,ANSI} = 20 \text{ mJ/cm}^2$ for nanosecond pulses and $I_{0,ANSI} = 1.1 \cdot t_e^{-0.75} \text{ W/cm}^2$ for a CW exposure time t_e in the range between 100 ns and 10 s [195].

Figure 7.1(a) shows the ratio of the maximum pressure amplitudes $p_{max,pulse}/p_{max,CW}$ as a function of the CW exposure time t_e using $I_0 = I_{0,ANSI}(t_e)$. A pulse width of 2.15 ns was selected according to the specifications of the 515 nm laser of the TD-OM system (see chapter 5) and the FD-OM modulation frequency was set to 50 MHz. Based on this calculation, in fast acquisition FD-OM applications where the CW exposure time per measurement position is in the range of 1–50 μs , $p_{max,pulse}$ is 55–80 dB higher than $p_{max,CW}$. The reason is that pulsed excitation is more efficient in optoacoustic signal generation due to the simultaneous excitation of a broad frequency range and steeper temporal slopes of the intensity profiles. In tomographic FD imaging applications, the difference in pressure amplitude is in the order of 120 dB because the ANSI limit is considerably lower for long CW exposure times ($I_{0,ANSI} = 200 \text{ mW/cm}^2$ for $t_e > 10 \text{ s}$) [15].

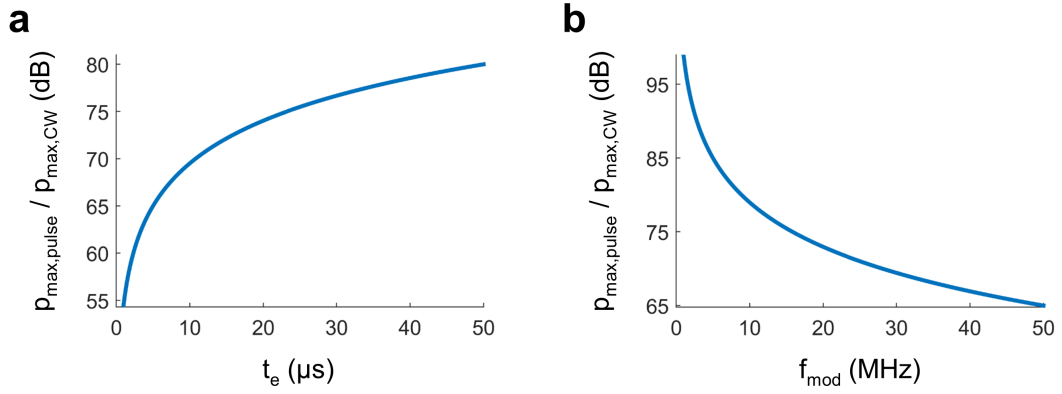


Figure 7.1: Optoacoustic signal strength comparison between TD-OM and FD-OM. (a) Ratio of the maximum pressure amplitudes for pulsed and CW excitation as a function of CW exposure time t_e , using $I_{0,ANSI}(t_e)$ and the values $\tau_p = 2.15$ ns and $f_{\text{mod}} = 50$ MHz. (b) Ratio of the maximum pressure amplitudes as a function of the modulation frequency, using an exposure time of $t_e = 5$ μs .

Figure 7.1(b) depicts $p_{\max,pulse}/p_{\max,CW}$ as a function of the modulation frequency ω_{mod} for an exposure time of $t_e = 5$ μs .

Noise and signal bandwidth

In all optoacoustic measurements, noise is a combination of different sources including acoustic thermal noise from the medium, thermal noise from the transducer, electronic noise from the amplifier and other electronic components, as well as laser induced optoacoustic signals created in the matching layer and the active element of the transducer [187]. Whereas in TD-OM, laser-induced acoustic peaks can be identified and removed via digital filters, these parasitic signals have the same frequency as the optoacoustic signals from the source in FD-OM and reduce the SNR. The same is true for electronic noise from the modulation source, which should therefore be properly shielded or isolated. For broadband transducers, the dominating factor in the overall noise is the thermal noise generated by the transducer itself [25]. It can be modeled as Johnson noise, which is defined by the Nyquist equation as

$$\bar{V}_N = \sqrt{4k_B T \Delta f}, \quad (7.10)$$

where \bar{V}_N is the root mean square (rms) noise voltage, k_B denotes the Boltzmann constant, T is the temperature and Δf represents the detection bandwidth [196].

Because the noise amplitude scales with the square root of the detection bandwidth, narrowband detection in FD-OM can compensate for the previously discussed difference in signal strength. In TD-OM, the detection bandwidth of typically employed high-frequency transducers is in the range of 100 MHz. For a FD-OM detection bandwidth in the kilohertz range, the SNR is increased compared to TD-OM by approximately two orders of magnitude, corresponding to 30–40 dB [15]. If a lock-in amplifier is used for detection, the difference can be increased to 60 dB and beyond, potentially exceeding the absolute SNR achievable with TD-OM, though at the expense of acquisition speed.

Finally, the SNR can be further enhanced by using dedicated detectors resonating at the desired modulation frequency, such as quartz-enhanced tuning forks (QTF). However,

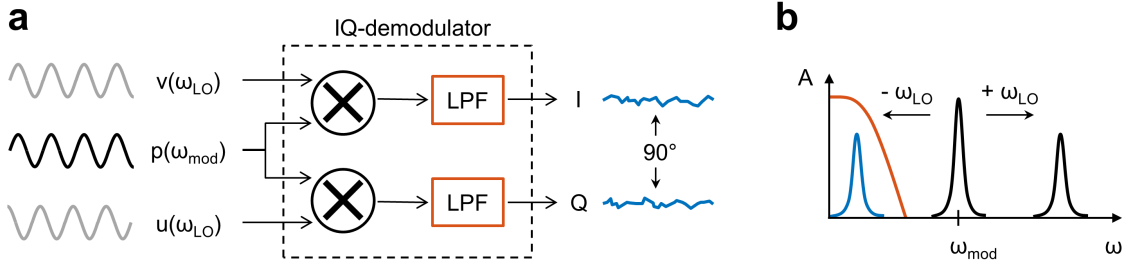


Figure 7.2: Principle of IQ-demodulation for FD optoacoustic imaging. (a) Operation principle of the IQ-demodulator in homodyne detection mode ($\Delta\omega^- = 0$), yielding time-constant quadrature voltage signals I and Q . The '×'-symbol denotes a multiplication (mixing) of the recorded optoacoustic signal $p(\omega_{mod})$ with local oscillator (LO) reference signals $v(\omega_{LO})$ and $u(\omega_{LO})$. LPF: Lowpass filter. (b) Up and downmodulation of the original modulation frequency peak. The red curve indicates the lowpass filter range.

such a detection scheme confines FD-OM to a single frequency, which limits the range of excitable structures and does not allow for retrieving depth information.

7.2.3 Principles of IQ-demodulation

The aim of typical FD-OM systems is to measure the amplitude of monofrequent optoacoustic signals in order to generate 2D amplitude images of optical absorption around the acoustical or optical focal plane [15,16]. However, to restore depth information in FD imaging, the phase of the optoacoustic signals has to be recorded additionally [194,197]. This can be achieved by using a lock-in amplifier for detection, which is however expensive. Alternatively, the optoacoustic signals oscillating in the MHz range can be directly recorded and subsequently Fourier transformed. The drawback is the high frequency of the signals, which requires fast sampling at more than twice the modulation frequency and thereby poses limitations in terms of integration time and computer memory. Furthermore, the Fourier transformation of MHz signals is time demanding and therefore not suitable for fast-imaging applications.

To enable the fast recording of both, amplitude and phase of FD optoacoustic signals, an acquisition scheme based on IQ-demodulation was used. Figure 7.2(a) illustrates the working principle of the IQ-demodulator. The detected optoacoustic voltage signal with the frequency ω_{mod} is divided and each signal is multiplied (mixed) with local oscillator (LO) reference signals having a frequency ω_{LO} . The two LO signals are set to have a 90° phase difference² and can be expressed as

$$\begin{aligned} v(\omega_{LO}) &= \sin(\omega_{LO} t) \\ u(\omega_{LO}) &= \cos(\omega_{LO} t). \end{aligned} \quad (7.11)$$

The optoacoustic signal is given by

$$p(\omega_{mod}) = A \sin(\omega_{mod} t + \phi), \quad (7.12)$$

where A denotes the amplitude and ϕ the phase of the measured signal relative to the

² Such a set of signals is referred to as 'in quadrature'.

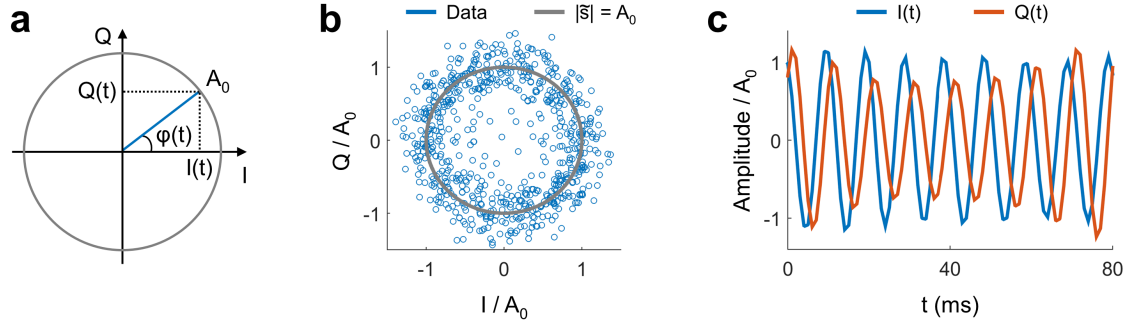


Figure 7.3: I and Q signals in heterodyne detection. (a) Phasor diagram visualizing the relationship of $I(t)$, $Q(t)$, A_0 and $\varphi(t)$. (b) Experimental measurement of I and Q values (blue circles) from black polish, downmodulated to 100 Hz. The scatter plot represents the complex plane illustrated in (a), whereas the gray circle denotes $A_0 = \sqrt{I(t)^2 + Q(t)^2}$. (c) Time courses of the measured I (blue) and Q (red) signals.

LO signals, which depends on the axial distance of the absorber to the detector³. The multiplication yields two new quadrature signals I and Q , which are of the form

$$\begin{aligned} I(\Delta\omega^-, \Delta\omega^+, t) &= A_0 \left[\cos(\Delta\omega^- t + \phi) - \cos(\Delta\omega^+ t + \phi) \right] \\ Q(\Delta\omega^-, \Delta\omega^+, t) &= A_0 \left[\sin(\Delta\omega^- t + \phi) + \sin(\Delta\omega^+ t + \phi) \right]. \end{aligned} \quad (7.13)$$

Here, $\Delta\omega^- = \omega_{mod} - \omega_{LO}$ and $\Delta\omega^+ = \omega_{mod} + \omega_{LO}$ are the down and upmodulated frequency components, respectively, originating from the multiplication process and $A_0 = \frac{A}{2}$. The high-frequency component $\Delta\omega^+$ is removed by a lowpass filter, as depicted in Figure 7.2(b). Thus, the resulting I and Q signals are downmodulated to the frequency $\Delta\omega^-$, which is referred to as 'heterodyne detection' in the case of $\Delta\omega^- \neq 0$. I and Q can generally be represented as the real and imaginary components of a complex phasor

$$\tilde{s}(t) = A_0 e^{i\varphi(t)} = I(t) + iQ(t), \quad (7.14)$$

with $\varphi(t) = \Delta\omega^- t + \phi$, describing a circle with radius A_0 in the complex plane, as depicted in Figure 7.3(a). This relationship is validated experimentally by measuring the optoacoustic signal of black polish with the FD-OM system (see next section) modulated at 50 MHz and downmodulated to $\Delta\omega^- = 100$ Hz. Figure 7.3(b) shows the recorded Q values plotted against the respective I values (blue circles), which corresponds to the complex plane illustrated in (a). The values are distributed around a circle with constant amplitude $A_0 = \sqrt{I(t)^2 + Q(t)^2}$ after bandpass filtering the signals in the 80–120 Hz range. The corresponding time courses of I and Q over 80 ms are shown in Figure 7.3(c), where the 90° phase difference of the quadrature signals can be observed.

In order to enable the high-speed recording of A and ϕ with the FD-OM system, the

³ ϕ is not to be confused with the instantaneous and time dependent phase of the optoacoustic signal itself. The constant phase ϕ depends on the modulation frequency and can be written as $\phi = \phi_a + \phi_{el}$. ϕ_a is the phase constant introduced in Eq. (7.4) and accounts for the fact that the modulated laser light is converted into a pressure wave, which travels through the medium to be detected by the transducer and converted into a voltage signal. ϕ_{el} represents the phase difference between LO and optoacoustic signal due to different electronic components such as cables and amplifier.

LO and modulation frequency are set to be equal, in which case $\Delta\omega^- = 0$ (homodyne detection) and which results in time-independent I and Q signals

$$\begin{aligned} I &= A_0 \cos(\phi) \\ Q &= A_0 \sin(\phi). \end{aligned} \quad (7.15)$$

From these constant voltage signals, the amplitude and time-invariant phase of the optoacoustic signal are directly obtained as

$$A = 2 \sqrt{I^2 + Q^2} \quad (7.16)$$

$$\phi = \varphi = \tan^{-1} \left(\frac{Q}{I} \right), \quad (7.17)$$

which can be recorded at an arbitrarily low sampling frequency.

7.3 Materials and methods

7.3.1 Experimental setup

The experimental setup of the developed FD-OM system is schematically illustrated in Figure 7.4. It was based on the IMMSOM setup described in chapter 6, incorporating the same inverted microscope, multiphoton modalities and the respective components and devices. A photograph of the optical system can be found in appendix C.

The excitation source of the FD-OM modality was a CW diode laser (A350, Omicron-Laserage) emitting at 488 nm with a maximum output power of 200 mW. The laser diode current was modulated by a fast function generator (DG5252, Rigol) using a sinusoidal waveform. After being expanded and spatially filtered by a 50 μm pinhole, the intensity-modulated beam passed through a neutral density filter wheel for adjustable attenuation. Subsequently, the FD-OM laser was coupled into the beam path of the multiphoton laser by means of a longpass dichroic mirror (DMLP650, Thorlabs). Finally, the beam was guided onto the galvo mirror set of the multiphoton modality, expanded and focused into the sample by the 0.45 NA objective. The generated monofrequent optoacoustic signals were detected by a conically shaped 50 MHz transducer (Sonaxis; active element diameter: 3 mm, focal distance: 3 mm) that could capture frequencies in a range of ~ 5 –95 MHz. The laser scanning was performed within the sensitivity field of the detector in the positive defocus. For homodyne detection, the previously amplified optoacoustic signals were multiplied with a LO reference signal using an IQ-demodulator (AD8333, Analog Devices; RF frequency range: DC to 50 MHz, lowpass filter cutoff frequency: 40 kHz). The LO signal was provided by the same function generator used for modulating the diode laser. For digitizing the time-constant I and Q signals, the 16-bit DAQ card of the multiphoton system was employed.

7.3.2 Acquisition and image formation

The DAQ card was also used to generate and deliver the voltage waveforms (see Figure 6.1(b)) to the galvo mirror controller. Sampling of the input signals and output waveform voltages was performed simultaneously. To account for the initial delayed movement of the galvo mirrors at the beginning of each scan, the first pixels had to

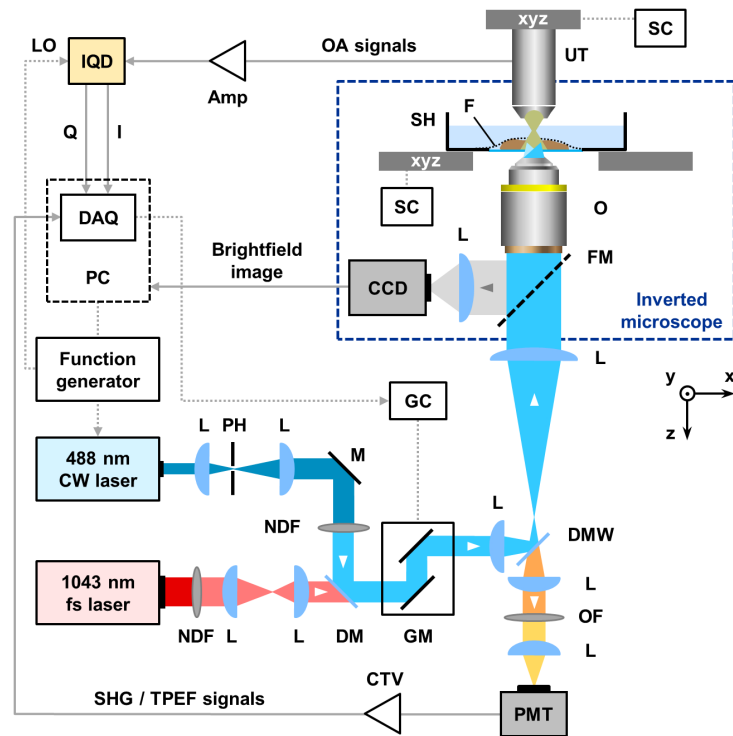


Figure 7.4: Scheme of the hybrid FD-OM and multiphoton microscopy setup. **Abbreviations:** A: Amplifier, CTV: Current to voltage converter and amplifier, DAQ: Data acquisition card, DMW: Dichroic mirror wheel, F: Plastic foil, FM: Flippable mirror, GC: Galvo mirror controller, GM: Galvo mirrors, IQD: IQ-demodulator, L: Plano-convex lens, LO: Local oscillator signal, NDF: Neutral density filter, O: Objective lens, OA: Optoacoustic, OF: Optical filter, PH: Pinhole, PMT: Photomultiplier tube, xyz: Motorized xyz -stage, SC: Stage controller, SH: Sample holder, UT: Ultrasound transducer. (Adapted from [186].)

be removed. The FOV of the scan was controlled by the maximum amplitude of the galvo waveforms, whereas the pixel size was determined by the galvo scan frequency and the sampling rate. The time required for a single scan of 300×300 pixels was ~ 0.6 s, using a bi-directional scanning frequency of 400 Hz. The corresponding pixel dwell time was $4.2 \mu\text{s}$, just above the time constant of the IQ-demodulator's lowpass filter of $\sim 4 \mu\text{s}$. According to the discussion in section 7.2.2, an exposure time of $4.2 \mu\text{s}$ results in a ratio of the maximum TD and FD signal amplitudes of 64 dB at the respective ANSI limits, assuming a pulse width of 2.15 ns and a modulation frequency of 50 MHz. On the other hand, a detection bandwidth of ~ 40 kHz gives rise to a 34 dB improvement in SNR compared to a ~ 90 MHz detection bandwidth in the pulsed mode (see Eq. (7.10)). For a further SNR enhancement by 20 dB, 100 averages were acquired on a per-image basis within 1 min.

The scan was repeated several times using different modulation frequencies within the reception bandwidth of the transducer. In this manner, the I and Q values for a number of modulation frequencies were recorded for each pixel and the corresponding amplitude and phase values were calculated according to Eq. (7.16) and (7.17). The maximum modulation frequency was limited to 50 MHz by the input bandwidth of the IQ-demodulator. Figure 7.5 illustrates the acquisition scheme of the FD-OM system compared to conventional pulsed mode OM. An absorber excited by a delta pulse emits an optoacoustic signal spanning a frequency range that depends on the absorber geometry. In FD-OM,

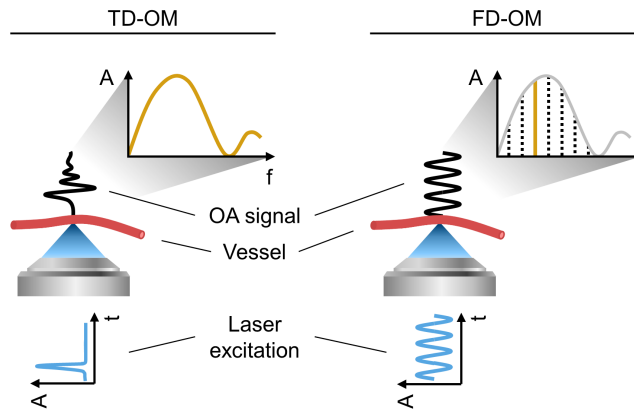


Figure 7.5: Comparison of signal generation in TD-OM and FD-OM. The orange curves denote the frequency content of the respective generated optoacoustic signals. In FD-OM, the modulation frequency is swept (gray dashed lines) within the detection bandwidth of the transducer. The light gray curve in the FD-OM frequency graph illustrates the frequency response of the excited vessel. OA: Optoacoustic. (Adapted from [186].)

the absorber is sequentially scanned with a number of distinct excitation frequencies. The amplitude at each of these frequencies depends on the excitation frequency spectrum of the absorber (i.e. how efficiently the absorber can be excited at a particular frequency) and thus varies between structures of different size. For example, a $30\ \mu\text{m}$ suture yields the maximum FD optoacoustic amplitude at a modulation frequency of $\sim 50\ \text{MHz}$ due to the underlying excitation frequency spectrum.

For simple 2D imaging, the amplitude images for each single frequency were summed up and the final images were corrected for the transducer's uneven sensitivity field using a suitable 2D Gaussian function. By taking the phase of each modulation frequency into account, the depth information could partially be restored by performing an iFFT. The resulting pseudo-TD signals were Hilbert transformed and processed similarly to the method used in TD-OM (see section 5.2.2). Due to the 2π -phase ambiguity of FD optoacoustic signals, the 3D reconstructions following the iFFT operation showed several repetitive patterns in depth and had to be windowed accordingly.

For hybrid FD-OM and multiphoton imaging, the co-registration of the different modalities was achieved by imaging a suture cross phantom with all modalities and finding the mutual lateral and axial offsets, as analogously described in section 6.3.2. Additionally, a drop of black polish was placed next to the samples for adjusting the transducer and illumination co-alignment prior to each measurement. The transducer was centered within the laser-scanning FOV by imaging the cross-section of the sensitivity field at the focus and correcting the lateral offsets with the motorized transducer holding *xyz*-stages.

The control of the FD-OM system as well as the acquisition and Gaussian correction was performed in MATLABTM. The volume rendering of the iFFT based 3D reconstructions was achieved using AmiraTM.

7.3.3 Sample mounting and *in vivo* experiments

The sample preparation and mounting for small specimens and phantoms followed the procedure described in chapter 5. In order to enable the *in vivo* imaging of mouse ear vasculature, a custom designed holder was produced with a 3D printer (a photograph can be found in appendix C). The holder could be mounted on top of the sample holding

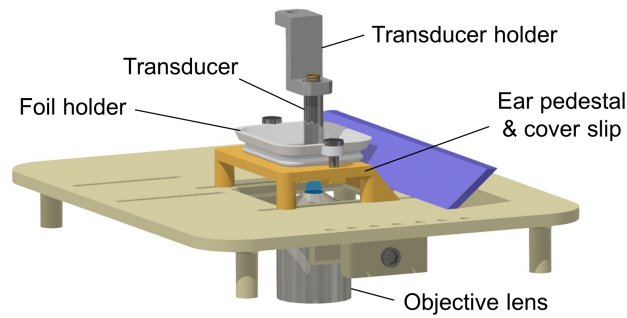


Figure 7.6: 3D printed mouse ear holder for *in vivo* experiments.

xyz-stage and had a central opening for the objective lens. Figure 7.6 illustrates the design of the *in vivo* holder. A pedestal (orange) was located above the objective, accommodating a cover slip and on top of it the mouse ear. The mouse rested between the pedestal and a rack (blue) that could be adjusted to fit the size of the mouse. A piece of plastic foil was fixed to a frame (white), which was pressed on the pedestal from above to flatten and fixate the ear that was squeezed between cover slip and foil. For gapless acoustic coupling, centrifuged ultrasound gel was inserted between ear and plastic foil and the foil frame was filled with deionized water.

The mice (HSD:Athymic Foxn1nude) were anesthetized using 2% of isoflurane. A mobile snout piece delivered the gas to the animal during the experiment, while the body temperature was maintained using a heating lamp. All procedures were approved by the District Government of Upper Bavaria.

7.4 Characterization

7.4.1 Laser source

In order to characterize the CW laser, the beam profile was recorded with a profiler (SP620U, Ophir) before and after spatial filtering with the 50 μm pinhole, as shown in Figure 7.7(a) and (b), respectively. The filtered beam shows a smooth and circular profile, appropriate for diffraction limited focusing. Next, the wavelength of the laser was measured by a spectrometer (DSA491000, Qwave) as 487.3 nm with a spectral linewidth of 1.15 nm.

As discussed in section 7.2.1, the modulation depth of the CW laser determines the amplitude of FD optoacoustic signals. It is defined as the peak amplitude AC_{pk} divided

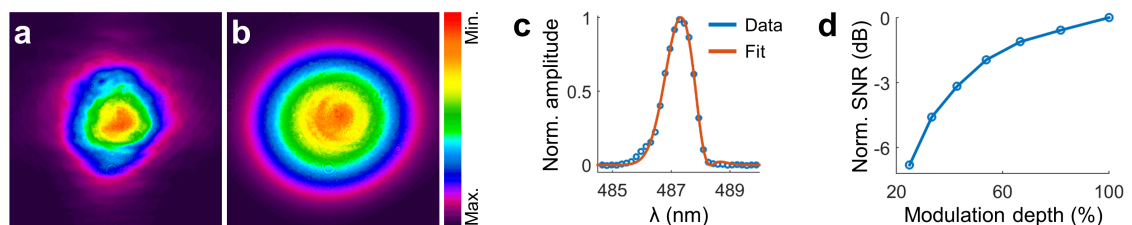


Figure 7.7: Characterization of the 488 nm CW laser. (a-b) Profile of the beam before (a) and after (b) spatial filtering with a 50 μm pinhole. (c) Wavelength spectrum (blue circles) fitted with a double Gaussian function (red curve, $R^2 = 0.997$). (d) SNR measurement of a 50 μm suture using different laser modulation depths AC_{pk} / DC .

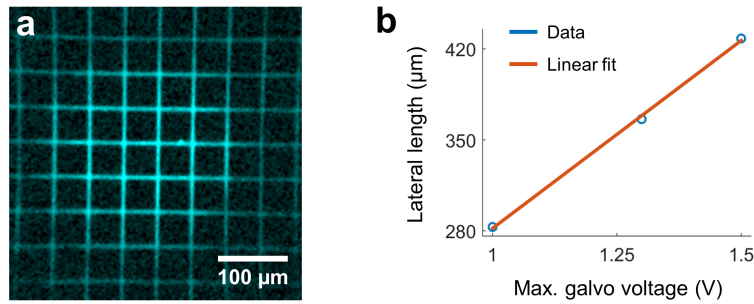


Figure 7.8: FOV and field distortion characterization using a black grid sample. (a) Optoacoustic image of the grid representing the sum of the single frequency images (10–50 MHz). (b) Characterization of measured lateral length of the scanning FOV as a function of the maximum amplitude of the galvo voltage waveform. The red line shows a linear fit to the data (blue circles).

by the offset DC of the modulated waveform. To ensure a maximum SNR, the laser was characterized by the manufacturer to have a modulation depth $> 98\%$ up to a modulation frequency of 200 MHz. To demonstrate the effect of the modulation depth on the achieved SNR, a $50\ \mu\text{m}$ black suture was imaged at a modulation frequency of 30 MHz using modulation depths varying from 20–100%. The modulation depth was artificially changed by introducing different DC offsets with the function generator, while the high-level voltage was kept constant. Figure 7.7(d) shows the measured SNR calculated from the imaged suture as the mean value of the signal divided by the standard deviation of the image noise for different modulation depths. As can be observed from the data, a modulation depth of 30% leads to a reduction of the achieved SNR by $\sim 6\ \text{dB}$.

7.4.2 FOV and field distortion

Next, in order to determine the laser scanning FOV for a given maximum amplitude of the voltage waveform transferred to the galvo mirrors, a distortion grid sample (R1L3S3P, Thorlabs) with a grid spacing of $50\ \mu\text{m}$ was measured. Figure 7.8(a) shows the amplitude summed image for a modulation of 10–50 MHz with 10 MHz steps, displaying the grid lines of the sample. In this measurement, the uneven sensitivity field was not corrected for. The image yields a FOV of $420 \times 420\ \mu\text{m}^2$ at a positive defocus of $400\ \mu\text{m}$, while the respective peak amplitude of the galvo waveform was 1.5 V. To characterize the dependency of the scanning FOV on the maximum galvo voltage, the grid measurement was repeated for different voltage values, as depicted by Figure 7.8(b)). The red curve represents a linear fit to the data ($R^2 = 0.999$), yielding a slope of $289 \pm 9.11\ \mu\text{m}/\text{V}$ and an intercept of $-7.00 \pm 11.7\ \mu\text{m}$.

Additionally, the grid sample was used to study field distortions introduced by the galvo mirror configuration. In Figure 7.8(a), a slight pincushion distortion can be observed, where the outer grid lines appear to be bent inwards (see section 2.2.3). However, for a FOV of $420 \times 420\ \mu\text{m}^2$ or smaller, the distortion is only weakly pronounced and can therefore be neglected.

7.4.3 Sensitivity field simulation for monofrequent excitation

Finally, the properties of the transducer sensitivity field in the case of monofrequent excitation was investigated. Focused piezoelectric transducers generally have a finite

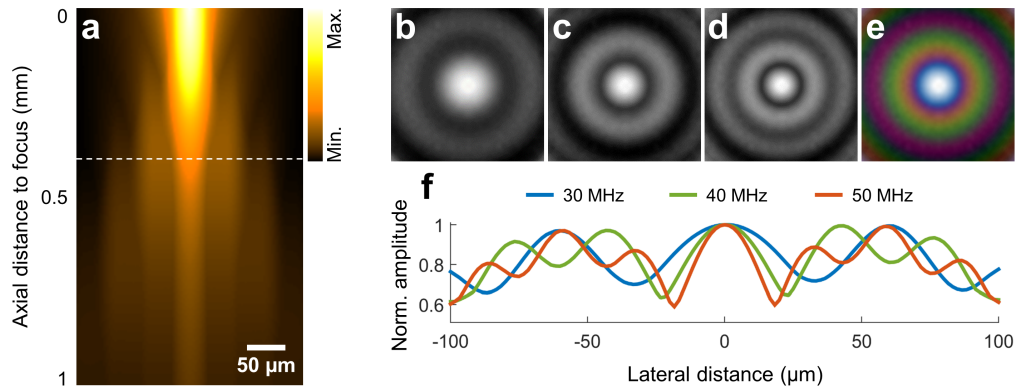


Figure 7.9: Simulation of the transducer sensitivity field for CW excitation at different modulation frequencies. (a) Side-view MAP of the 50 MHz sensitivity field in the positive defocus. Gaussian corrected 2D cross-sections 400 μm behind the focus (see dashed white line in (a)) are shown for (b) 30 MHz, (c) 40 MHz and (d) 50 MHz modulation frequencies. (e) Overlay of (a-c). (f) Cross-sectional 1D profiles through the centers of the single frequency images showing mutually interleaving amplitude minima and maxima. Blue, green and red colors represent 30, 40 and 50 MHz, respectively. (Adapted from [186].)

active element, which can either be curved to achieve focusing or a flat active element is accompanied by a plano-concave acoustic lens. Therefore, the path difference between the source and the different parts of the active element depends on the source location and can lead to constructive or destructive interference of the arriving optoacoustic signals. Due to the rotation symmetry around the transducer axis, the resulting maxima and minima in the sensitivity field are concentric around the same axis. Furthermore, the destructive interference condition depends on the frequency of the acoustic waves and thus on the modulation frequency.

In order to qualitatively simulate the sensitivity field of the 50 MHz transducer for CW excitation at different modulation frequencies, the Field II package was used. The speed of sound was set to 3200 m/s to compensate for the propagation of the acoustic waves through ~ 3 mm of glass, which leads to a refocusing of the waves on the active element in the case of excitation in the positive defocus. In the glass delay line, the path differences are inverted due to the refocusing and the interference effects are partially compensated due to the high speed of sound in glass (> 5000 m/s). Figure 7.9(a) illustrates a side-view MAP of the simulated 50 MHz sensitivity field through a depth of 1 mm after the focus. Figures 7.9(b-d) show $200 \times 200 \mu\text{m}^2$ cross-sections of the sensitivity field at a positive defocus of 400 μm (see dashed white line in (a)) for 30, 40 and 50 MHz modulation frequencies, respectively. The images were divided by a 2D Gaussian mask to improve the visibility of the interference rings. As expected, the spatial frequency of the amplitude oscillations increases with the modulation frequency. Figure 7.9(e) represents the overlay of the single frequency images (blue: 30 MHz, green: 40 MHz, red: 50 MHz). The respective 1D profiles through the centers of the 2D sensitivity fields are illustrated in (f), showing an interleaving of the maxima and minima for the different modulation frequencies⁴. As a result, the single frequency images obtained with FD-OM are expected to show frequency dependent amplitude oscillations that smooth out in the summed-up images.

⁴ Note that the y -axis begins at a value of 0.5.

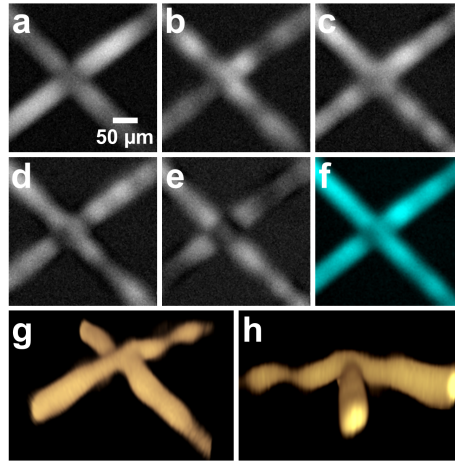


Figure 7.10: FD-OM imaging of a 50 μm suture cross phantom. The sample was imaged at different modulation frequencies: (a) 30 μm , (b) 35 μm , (c) 40 μm , (d) 45 μm and (e) 50 μm . (f) Sum of (a-e). (g-h) 3D reconstruction of the suture cross following an iFFT based on amplitude and phase information and subsequent Hilbert transform. (Adapted from [186].)

Moreover, the finite excitation volume around the optical focus leads to an interference of optoacoustic waves from different depths. This effect causes an additional amplitude oscillation as a function of the scanning position, being superimposed on the oscillations induced by the finite active element. However, the destructive interference condition requires an axial extent of the imaged absorbers of a few tens of micrometers, which is large compared to the confocal parameter of the focused 488 nm beam of $\sim 4 \mu\text{m}$. Therefore, the finite active element is expected to have a greater influence on the amplitude oscillations than the finite excitation volume.

7.5 Results

7.5.1 Suture phantom imaging and 3D reconstruction

The performance of the developed FD-OM system was initially evaluated by imaging a 50 μm black suture cross phantom using five different modulation frequencies ranging from 30 to 50 MHz⁵. The FOV was $290 \times 290 \mu\text{m}^2$ with a pixel size of $0.97 \mu\text{m}$. Figures 7.10(a-e) show the single frequency amplitude images from (a) 30 MHz to (e) 50 MHz in 5 MHz steps. Amplitude fluctuations changing with the modulation frequency can be observed, confirming the simulation results shown in section 7.4.3. The amplitude summation of all frequencies is illustrated in (f), yielding a smooth appearance of the sutures, which is also predicted by the sensitivity field simulations.

To demonstrate the 3D imaging capability of multi-frequency FD-OM, the recorded amplitude and phase information was used together with the iFFT method described in section 7.3.2. Figures 7.10(g-h) represent different views of the resulting 3D reconstruction of the suture cross phantom. The relative position in depth can clearly be identified, as

⁵ The suture phantom was measured using a fiber coupled 808 nm CW laser (A350, Omicron-Laserage) and the 80 MHz transducer of the OM system. All other samples were imaged using the components described in section 7.3.1.

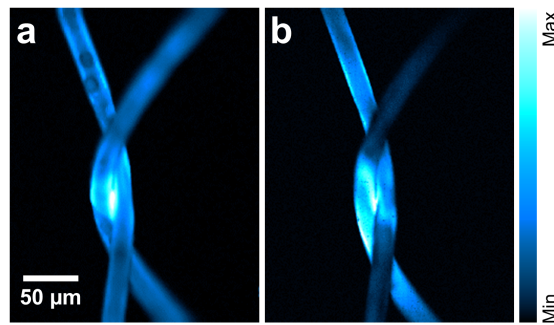


Figure 7.11: Comparison of the SNR achieved in FD and TD optoacoustic microscopy. (a) FD-OM amplitude summed image of a 40 μm suture knot phantom. (b) TD-OM scan of the same phantom. (Adapted from [186].)

well as local bendings and deformations of the suture matching the amplitude variations in (f). The results demonstrate the suitability of FD-OM in retrieving relative depth information by using multiple modulation frequencies as well as the phase information of the optoacoustic signals.

7.5.2 SNR comparison to TD-OM

Next, the SNR achieved with CW excitation in the FD-OM system was compared to pulsed excitation using the TD-OM modality introduced in chapter 5. For this purpose, a 40 μm suture knot phantom was imaged with FD-OM in the frequency range of 10–50 MHz using nine modulation frequencies and an average power of 18 mW at the sample. Figure 7.11(a) illustrates the amplitude summed image of the FD-OM scan, yielding an SNR of 45 dB.

For the TD-OM scan, the galvo scan implementation mentioned in the hybrid atheroma imaging part (see section 6.4.4 and [179]) was used together with a 532 nm diode-pumped solid state laser (SPOT-10-200-532, Elforlight Ltd; pulse width: 1.4 ns; actively Q-switched) at a repetition rate of 20 kHz. The sample was scanned in an equivalent manner to the previous FD imaging, using the same transducer, FOV, defocus position and objective as well as a pulse energy at the sample of ~ 10 nJ. The top-view MAP of the TD-OM scan of the suture phantom is shown in Figure 7.11(b). No signal averaging was performed and an SNR of 39 dB was determined from the image. Consequently, the experimentally measured difference in SNR between FD-OM and TD-OM was ~ 6 dB. For the settings used in both measurements, a similar SNR could therefore be achieved by using four signal averages in the TD-OM scan.

From Eq. (7.9) and (7.8), the theoretically predicted SNR difference for the laser parameters provided above was estimated to be -2 dB, which is in agreement with the experimental value. For this calculation, the averaging in FD-OM, the difference in laser wavelengths yielding different focal diameters as well as the respective input bandwidths (~ 40 kHz in FD-OM and ~ 90 MHz in TD-OM) were taken into account. It can therefore be concluded that the FD-OM system achieves an SNR comparable to typical TD-OM implementations.

7.5.3 Zebrafish eye imaging *ex vivo*

Following the imaging of phantom samples, the FD-OM system was used for the observation of biological specimens. Figure 7.12 shows the FD-OM imaging of an eye of a 5 dpf

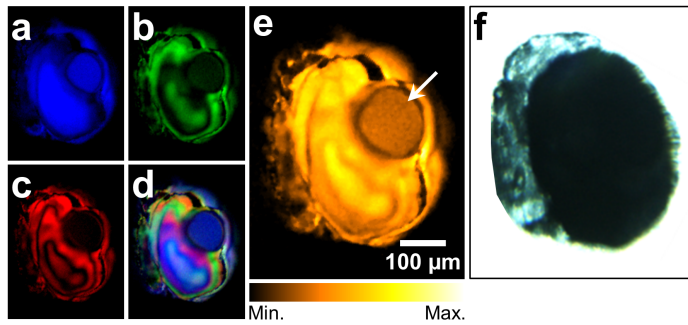


Figure 7.12: FD-OM imaging of a wildtype zebrafish eyeball *ex vivo*. (a–c) Summed-up images for (a) 10–20 MHz, (b) 25–35 MHz and (c) 40–50 MHz modulation frequencies. Frame (d) corresponds to the overlay of (a–c), whereas (e) shows the summed-up image of all frequencies. The white arrow marks the lens of the eye. (f) Brightfield microscopy image of the eyeball. (Adapted from [186].)

wildtype zebrafish larva *ex vivo*. The specimen was recorded at nine equally distributed frequencies in the range of 10–50 MHz using an average power of ~ 5.7 mW and a pixel size of $1.55 \mu\text{m}$. Zebrafish eyes contain a retinal pigment epithelium – a melanized cell monolayer that supports and protects the retinal photoreceptors [198, 199], resulting in a strong light absorption over a broad spectral range. The latter optical property in combination with the well-defined geometrical structure of the eyeballs render them an ideal specimen for optoacoustic measurements. Figures 7.12(a–c) depict the summed low (blue color, 10–20 MHz), mid (green color, 25–35 MHz) and high (red color, 40–50 MHz) frequency images, respectively. Due to the defined geometry of the eyeball, the images show pronounced amplitude oscillations. The spatial distribution of these oscillations vary between the different frequencies and mutually interleave, as can be seen in the overlay image (d). Similar to the suture phantom, the interleaving pattern of the amplitude variations leads to a smooth signal distribution of the image representing the amplitude summation of all frequencies, illustrated in (e). The circular structure in the center of the eyeball (indicated by the white arrow) corresponds most probably to the lens. It represents a large structure ($> 60 \mu\text{m}$ at 5 dpf [200]) compared to the thin melanized layer of the eye that can consequently only be excited at relatively low modulation frequencies. This fact is reflected by the imaging results, showing no significant signal contribution at modulation frequencies higher than 20 MHz. A brightfield microscopy image of the imaged eye is provided by (f) for reference.

7.5.4 Mouse ear vasculature imaging *in vivo*

As a next step, the developed system was used to image the vascular network in a mouse ear *in vivo*, which was achieved for the first time in a label-free manner using FD-OM. The average power at the sample was ~ 18 mW. Since the optical focus was approximately $150 \mu\text{m}$ deep inside the ear, the effective average power per area at the skin surface was $\sim 200 \text{ W}/\text{cm}^2$, which is well below the ANSI skin exposure limit of $12 \text{ kW}/\text{cm}^2$ for a microsecond pixel dwell time in the visible range [195]. In order to cover a larger region, nine adjacent ROI with a FOV of $360 \times 360 \mu\text{m}^2$ were scanned and stitched together with an overlap of $\sim 60 \mu\text{m}$. The pixel size was $1.2 \mu\text{m}$ and the modulation frequencies were identical as for the zebrafish eye measurement. Each ROI took a scan time of 9 min including all frequencies, resulting in an overall acquisition time of ~ 80 min.

Figure 7.13(a) depicts the stitched mosaic of the different summed-up images, visualizing

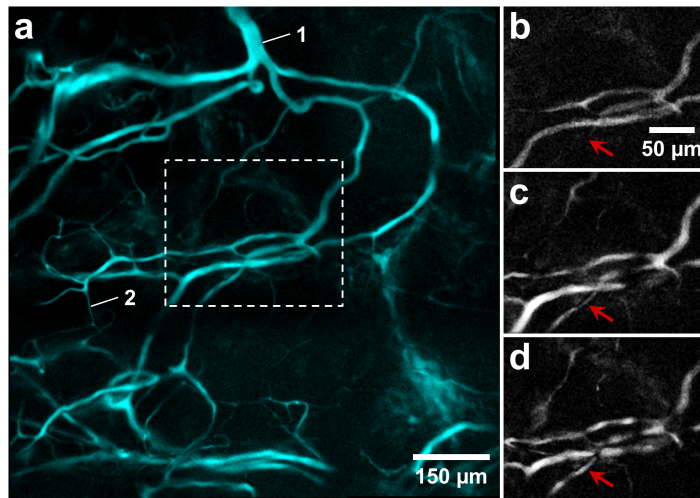


Figure 7.13: FD-OM imaging of the vascular network in a mouse ear *in vivo*. (a) Stitched mosaic of 9 adjacent ROIs, representing the amplitude summation of the single frequency scans in the 10–50 MHz range. The labels '1' and '2' mark vessels of $\sim 33 \mu\text{m}$ and $\sim 5 \mu\text{m}$ diameter, respectively. (b-d) Single frequency images at (b) 10 MHz, (c) 30 MHz and (d) 50 MHz of the region indicated by the white dashed box in (a). The red arrows indicate a capillary exhibiting varying degrees of signal amplitude for the different modulation frequencies. (Adapted from [186].)

vasculature in the mouse ear in an overall FOV of $960 \times 960 \mu\text{m}^2$. As can be seen from the image, vessels of different sizes were successfully captured simultaneously based on the excitation with several modulation frequencies. The diameters of the observed vessels range from $\sim 33 \mu\text{m}$ (see label '1') down to $\sim 6 \mu\text{m}$ (see label '2'), which represents the smallest capillaries present in vascular networks. Up to 12 branchings are identified between the vessels labeled with '1' and '2', respectively. The blurred structures visible in the mosaic correspond to blood vessels located outside of the optical focus. Figures 7.13(b-d) depict single frequency scans at 10, 30 and 50 MHz, respectively, of the region indicated by the white dashed box in (a). From these scans it can be seen that the amplitudes of the signals from different vessels show a strong dependence on the modulation frequency. This effect is showcased by the red arrows highlighting a capillary that does not appear at 10 MHz but has an increasing signal amplitude from 30 to 50 MHz. Again, signal amplitude fluctuations attributed to the interference of monofrequent optoacoustic signals are apparent in (b-d), which are smoothed out in the summed-up image (a).

7.5.5 Hybrid FD-OM and multiphoton mouse ear imaging *in vivo*

Finally, the full fast-scanning multicontrast imaging performance was demonstrated by the hybrid FD-OM and multiphoton imaging of a mouse ear *in vivo*. Similarly to the procedure described in the previous section, a mosaic of 3×3 ROIs was scanned with each modality and stitched together to form the final image with a total FOV of $1.18 \times 1.18 \text{ mm}^2$. Figure 7.14(a) depicts the brightfield microscopy image of the scanned region, showing a 3-fold branching of a prominent vessel, as well as keratinocytes and hair follicles characterized by dark shadows. The summed-up FD-OM image, acquired with the same parameters as in the previous section, is illustrated in (b), showing the vasculature within the scanning region. The laser was focused on a network of smaller vessels, while the larger branching vessel was out of focus and appears as a blurred shadow

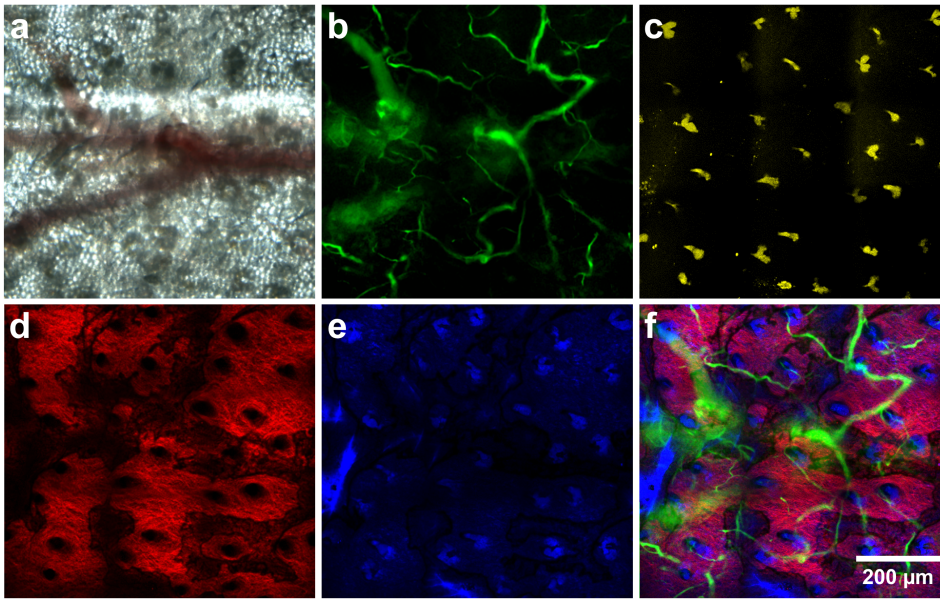


Figure 7.14: Hybrid FD-OM and multiphoton imaging of a mouse ear *in vivo*. The images represent stitched mosaics of 3×3 adjacent ROIs. (a) Brightfield microscopy image. (b) Summed-up FD-OM image of the vascular network in the ear. (c) TPEF scan visualizing hair follicles. (d) SHG image of the collagen structure in the dermis layer of the skin. (e) THG scan showing hair follicles and the tissue morphology. (f) Overlay of (b), (d) and (e).

in the image. Subsequently, the FOV was scanned with the multiphoton modalities using a pulse energy of 0.77 nJ at the sample and selecting an appropriate focal depth for each modality. Figure 7.14(c) represents the TPEF signals originating from the bulb regions of hair follicles, which are known to yield strong autofluorescence signals [176, 177]. The SHG scan is shown in (d), visualizing the collagen in the dermis of the ear. The locations of hair follicles can be identified by the absence of signal, forming distinct 'holes'. Finally, the THG image (e) visualizes the hair follicles and the overall tissue morphology. An overlay of the FD-OM, SHG and THG images is provided by (f), yielding a strong contrast complementarity without the use of any labeling.

7.6 Conclusion and outlook

The FD-OM system introduced in this chapter presents a novel laser-scanning OM implementation which operates in the frequency-domain using modulated CW lasers. It is based on potentially cheap and stable light sources and a simple acquisition scheme using IQ-demodulation. The recording of time-independent signals enables easy data synchronization and acquisition for fast imaging as opposed to laser-scanning TD approaches based on pulsed laser sources. Moreover, compared to traditional single frequency FD optoacoustic techniques, the developed system allows for the visualization of structures largely varying in size, as well as for 3D imaging thanks to the interrogation at multiple optical modulation frequencies. Due to the high frame rate of ~ 1.7 Hz, allowing for high laser power to be used within the ANSI limits, a comparable SNR to TD-OM approaches can be achieved, as has been also demonstrated experimentally. The developed system allowed for the first time to visualize the vascular network in a mouse ear *in vivo* using the

FD-OM technique. Finally, the novel integration of the FD-OM system into a multiphoton microscope demonstrated high contrast complementarity and the label-free visualization of a range of anatomical features. Owing to the short acquisition times of all modalities, hybrid images of skin constituents and the underlying vascular network could be generated *in vivo* within an extended FOV via the stitching of adjacent scans.

In the presented implementation, the laser modulation was limited to 50 MHz by the high frequency cut-off of the IQ-demodulator input. The frequency range can be readily extended by using IQ-demodulators with a larger input bandwidth to allow for the efficient imaging of micrometer sized structures. Furthermore, the availability of a wide range of CW laser lines allows for a cost-efficient multi-wavelength extension of FD-OM, offering novel molecular and functional insights into rapid biological processes on a microscopic scale. Beyond that, simultaneous excitation with different lasers could be attained by applying distinct modulation frequencies to each wavelength and using several IQ-demodulators in parallel. Such a scheme can effectively separate optoacoustic signals originating from different wavelengths without the need for complicated temporal interleaving of pulses as in comparable time-domain approaches.

8 Visualization of microcirculatory blood flow *in vivo* with FD-OM

This chapter presents the application of the developed frequency-domain optoacoustic microscope on the visualization of microcirculatory blood flow *in vivo* via the detection of optoacoustic Doppler shifts and is based on [186]. First, the current status and limitations of the most common blood flow measurement techniques are discussed (section 8.1) and the Doppler shift detection method is introduced (section 8.2). Subsequently, the characterization of Doppler shift detection capabilities is presented and different approaches are compared (section 8.3). In the following results section (8.4), the *in vivo* measurement of microcirculatory blood flow is demonstrated by monitoring flow during a terminal experiment and by presenting a single vessel flow profile and a 2D flow map.

8.1 Motivation and status quo

Analyzing microcirculatory blood flow (microflow) can play a key role in early disease indication and treatment [1, 2]. In general, the microcirculation is of great importance to organ function through its regulation of blood pressure and temperature, tissue oxygenation, as well as the delivery of nutrients and removal of waste metabolites. Because of this dependency, a large number of different pathological conditions can be related to functional and morphological alterations of the microcirculation, such as cancer, diabetes and Alzheimer's [201–203].

The growing awareness of the scientific and clinical relevance of studying microflow over the past decades was accompanied by a rapid development of appropriate imaging techniques [204]. A well-established method for the non-invasive imaging of blood perfusion is laser Doppler imaging (LDI). In LDI, the average velocities of red blood cells (RBC) within a certain tissue volume are determined by measuring the optical Doppler shifts of reflected laser light [205]. Another technique of imaging microflow, but faster and with slightly higher spatial resolution than LDI, is laser speckle imaging (LSI). It uses speckle patterns that are created by the reflection of coherent laser light by the rough skin surface. Relative blood flow velocities can be deduced by the analysis of temporal intensity variations of the image speckles [11]. Furthermore, the medical need for cheap and easy-to-use diagnostic tools for microcirculatory blood perfusion imaging has led to the development of orthogonal polarization spectroscopy (OPS) [206]. OPS facilitates non-invasive microcirculation imaging through the skin surface by rejecting polarized light reflected from the skin and accepting diffusively backscattered light from deeper structures [207]. Usually, OPS is implemented in a portable device that can access surfaces of different internal organs. LDI, LSI and OPS have been successfully demonstrated in various animal models [12,13] and clinical applications [208–212]. However, these optical techniques are based on the detection of backscattered light, which introduces various artifacts [207] and severely limits their resolution, imaging depth and sensitivity to small capillaries due to the strong light scattering of tissue [213].

Instead of using coherent light for microflow imaging, Doppler ultrasound imaging (DUS)

relies on detecting Doppler shifts of ultrasonic waves by means of piezoelectric transducers to extract blood flow velocities and has been applied to various human diseases [203]. However, DUS imaging at the capillary level is hampered by the strong acoustic reflections from tissue boundaries and by speckle artifacts.

A common feature of the previously presented imaging modalities is the range of accessible vessel diameters for flow measurements, which is mostly above $50\ \mu\text{m}$ [203]. In order to facilitate microflow imaging of smaller vessels down to the capillary level, several high resolution modalities have been developed. Doppler optical coherence tomography (DOCT) – the optical equivalent to DUS – has been used to image microflow in different animal models [214,215], as well as in clinical applications, such as ophthalmology [216]. A fundamental limitation originates from the 1D nature of the measured signals. The real 3D flow velocity has to be estimated, which is prone to errors [203]. Moreover, background scattering and motion artifacts reduce the SNR and impede flow speed measurements below $\sim 1\ \text{mm/s}$ [217]. In order to overcome angular dependence and background artifacts, several advanced variants of DOCT have been developed, such as speckle variance OCT (svOCT), correlation mapping OCT (cmOCT) [201] or Doppler optical micro-angiography (DOMAG) [217]. These recent methods, however, suffer from the requirement of *a priori* structural knowledge of the tissue [203], bulk motion artifacts and extensive data post-processing [201], respectively.

In the past years, promising progress has been made in using OM for the non-invasive label-free visualization of microflow *in vitro* and *in vivo* [218]. In contrast to the aforementioned modalities, which exclusively rely on either optical or acoustical backscattering, OM is based on optical absorption. Because of the specific light absorption by RBCs, OM provides good SNR, as well as high imaging depth compared to pure scattering based techniques. In TD-OM, transverse flow velocities can be measured and are usually derived from a correlation based analysis of signal intensity fluctuations in successive A-scans [213,219–221]. Although TD flow imaging has been mostly demonstrated on phantoms, first examples of successful *in vivo* applications include mouse ear and chick embryo microvasculature [221,222]. A shortcoming of TD-OM flow measurements is the necessity of additional A-scans to be acquired for the correlation analysis compared to conventional OM, which is time and memory consuming. Moreover, the flow direction can only be detected by mechanically scanning the sample back and forth. On the other hand, OM flow measurements in the frequency-domain are achieved by directly measuring the acoustic Doppler shift introduced by moving absorbers. Doppler FD-OM has been so far only accomplished in tube phantoms [223–225], due to the low amplitudes of Doppler shifted signals from RBCs. Apart from the weak signals, a limitation of this implementation is the angular acceptance of the Doppler measurements, which is confined to the narrow forward opening angle of the ultrasound detector.

To demonstrate the *in vivo* microflow imaging capabilities of Doppler OM, the developed FD-OM system was used for the detection of optoacoustic Doppler shifts from moving absorbers in phantom experiments. Based on the results, it was possible for the first time to image microcirculatory blood flow *in vivo* in a mouse ear based on lock-in detection, paving the way for the translation of Doppler OM from the laboratory to the clinic.

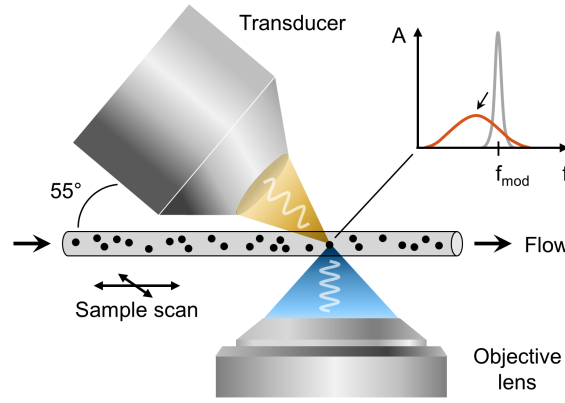


Figure 8.1: FD-OM Doppler shift detection scheme. (Adapted from [186].)

8.2 Optoacoustic Doppler shift detection method

An optical absorber moving at a speed v_a and illuminated by a CW laser modulated with frequency f_{mod} will emit an optoacoustic wave that is Doppler shifted by

$$\Delta f_{OA} = f_{mod} \frac{v_a}{c} \cos(\Theta_D) \quad (8.1)$$

with respect to f_{mod} [223]. Here, the so-called Doppler angle Θ_D denotes the angle between the direction of absorber movement and the detector axis. The Doppler shift of the modulated light exciting the absorber can be neglected in this calculation, since the respective component is proportional to the absorber speed divided by the speed of light in the medium, which is several orders of magnitude smaller than v_a/c .

As can be seen from Eq. (8.1), a Doppler angle of less than 90° is required in order to detect Doppler shifts. For this reason, the FD-OM system introduced in the previous chapter was used in a Doppler shift detection geometry as depicted by Figure 8.1. The conically shaped 50 MHz transducer (see previous chapter) was positioned in a $\sim 55^\circ$ angle with respect to the sample holder accommodating the mouse ears for *in vivo* measurements or flow phantoms. Such an angle corresponds to a reduction in detectable Doppler shift by $\sim 43\%$. For SNR optimization, the acoustical and optical foci were co-aligned. The angle of $\sim 55^\circ$ was a trade-off between decreasing the Doppler angle and increasing the space between transducer and sample in the confocal configuration. For microflow imaging, the sample was step wise scanned in the xy -plane by means of the sample holding stage and the Doppler shifts were analyzed at each position.

Two techniques can be used in order to detect Doppler shifts with the FD-OM system. First, the IQ-demodulator can be employed for heterodyne measurements. In contrast to the homodyne detection scheme used for FD-OM imaging where the detected pressure signal is downmodulated to DC by setting $\omega_{LO} = \omega_{mod}$, in heterodyne measurements the signal is downmodulated from the MHz range to a lower frequency that is more convenient and faster to analyze. Following the discussion in section 7.2.3, the heterodyne downmodulation process yields two quadrature voltage signals

$$\begin{aligned} I(\Delta\omega^-, t) &= A_0 \cos(\Delta\omega^- t + \phi) \\ Q(\Delta\omega^-, t) &= A_0 \sin(\Delta\omega^- t + \phi), \end{aligned} \quad (8.2)$$

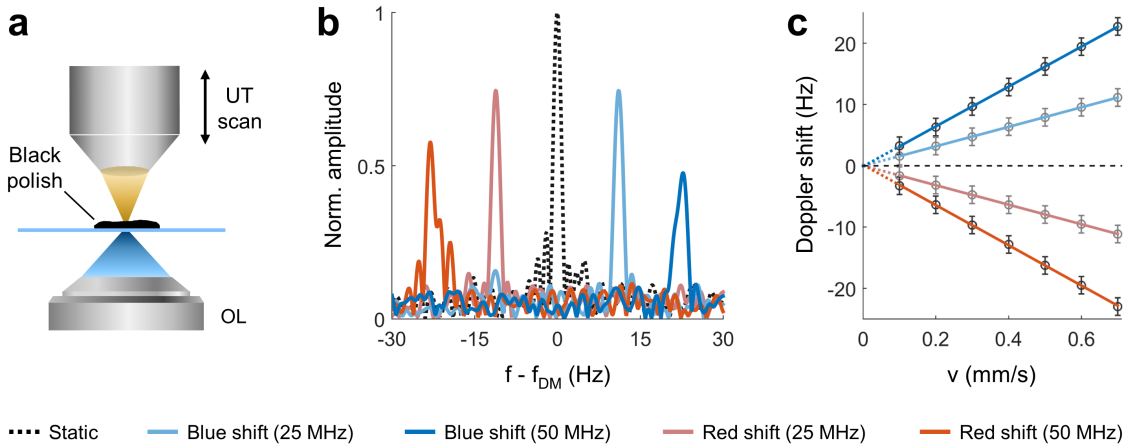


Figure 8.2: Doppler shift detection using black nail polish and a moving detector.

(a) Experimental setting and detection geometry. **Abbreviations:** OL: Objective lens, UT: Ultrasound transducer. (b) Doppler shifted frequency spectra for 25 MHz (light colors) and 50 MHz (dark colors) laser modulation at a transducer speed of 0.7 mm/s. The spectra are normalized to the static peak (gray dashed curve). (c) Doppler shift values as a function of transducer speed. The lines represent linear fits to the data, while the dotted lines are extensions of the fits to a speed of zero.

where $\Delta\omega^- = \omega_{mod} - \omega_{LO}$ represents the frequency to which the optoacoustic signal is downmodulated. The resulting time dependent I and Q signals can be readily Fourier transformed and analyzed. In this manner, Doppler shifts are identified by movements of the downmodulated peak around $\Delta\omega^-$ in the Hz range. Additionally, the Doppler shifted signals experience spectral broadening (see Figure 8.1) due to the opening angle of the transducer and a distribution of flow velocities [218]. This broadening is proportional to the flow speed and ultimately limits the highest detectable flow speed as the peak approaches the noise level for large Doppler shifts [226]. On the other hand, the lowest detectable flow speed depends on the acquisition time of the system, which is inversely proportional to the frequency resolution.

Instead of using the IQ-demodulator for heterodyne detection, Doppler shifts can be directly recorded by a spectrum analyzer, which measures the frequency spectrum around $f_{mod} = \omega_{mod} / 2\pi$ with high sensitivity. However, such devices are usually more expensive and slower than IQ-demodulators.

8.3 Characterization

In order to investigate the suitability of heterodyne IQ-demodulation for *in vivo* blood flow imaging and to establish the method, a number of phantom experiments were conducted.

8.3.1 Black varnish and moving transducer

As a first step towards establishing FD-OM Doppler imaging, the Doppler shifts of optoacoustic signals from black nail polish were measured and characterized. For this purpose, the 50 MHz transducer was positioned in a 90° configuration in transmission mode, as depicted in Figure 8.2(a). The transducer holding *xyz*-stage was used for moving the detector along the *z*-direction with different velocities ranging from 0.2–0.7 mm/s. Blue and red shifts were generated by moving the transducer towards and away from

the polish during illumination, respectively. The acquisition time for all single scans was 0.7 s. To validate the linear dependency of Δf_{OA} on f_{mod} according to Eq. (8.1), the measurement was performed using two modulation frequencies of 25 MHz and 50 MHz, while downmodulating the signals to $f_{DM} = \Delta\omega^- / 2\pi = 100$ Hz. Figure 8.2(b) shows the red and blue shifted optoacoustic signals measured at both modulation frequencies for a stage velocity of 0.7 mm/s. The gray dashed line represents a static scan as a reference, showing a sharp peak at f_{DM} . The light blue and red peaks at lower frequencies correspond to the 25 MHz signals, respectively. For 50 MHz modulation (dark blue and red curves), the peaks are shifted to higher frequencies and show a slight broadening. Figure 8.2(c) shows the full characterization for all velocities and both modulation frequencies. The data were fitted with linear functions ($R^2 > 0.999$) using the same color code as described in (b), whereas the colorbars correspond to the frequency resolution of the measurements. The dotted line segments are linear extensions of the fitted lines, which are found to meet at the origin as expected (mean intercept: 0.02 ± 0.07 Hz). Moreover, the values for the red and blue shifts are equidistant from f_{DM} and increase linearly with the modulation frequency. The results are in excellent agreement with the predictions by Eq. (8.1). Moreover, from the fitted linear functions an average speed of sound in the medium of 1549 ± 2 m/s is extracted, being close to the speed of sound in water (~ 1510 m/s at 30°C), which was used for acoustic coupling.

8.3.2 Carbon particles flowing in a tube

In the next step, it was investigated whether optoacoustic Doppler shifts can also be detected for micrometer sized absorbers flowing in a liquid medium, resembling red blood cells with a diameter of 7–8 μm and a thickness of 2–3 μm moving in the blood stream. A suspension of glassy carbon particles (484164, Sigma-Aldrich; diameter: 2–12 μm) in distilled water with a volume fraction of 10% was used as absorbers. To avoid sedimentation, the mass density of the water was increased to ~ 1.45 g/cm³ by adding an appropriate amount of sodium polytungstate (71913, Sigma-Aldrich), matching the density of the carbon particles [223]. Additionally, 1–2% of polyoxyethylenesorbitan monolaurate (Tween 20, Sigma-Aldrich) was added to the suspension in order to reduce the aggregation of the particles by a reduction of the surface tension of water. The experimental setting is illustrated in Figure 8.3(a). The suspension was manually pumped through a plastic tubing (PTFE Extruded Special, Zeus Inc.) with 300 μm inner and 500 μm outer diameter by means of a syringe. The focus of the 50 MHz detector was co-aligned with the optical focus of the laser inside the tube. A Doppler angle of almost 0° for Doppler shift maximization was achieved by a co-axial alignment with the tangent of the tube at the point of optical illumination. Blue and red shifts were generated by pumping the carbon particles towards or away from the transducer, respectively.

First, the Doppler shifts were detected by a spectrum analyzer (FSC 3, Rohde & Schwarz) within a frequency range of 100 Hz around the modulation peak and an integration time of ~ 4 s. A modulation frequency of 15 Hz was chosen because optoacoustic frequencies above ~ 20 MHz were attenuated by the 100 μm thick tube walls, as was found by measuring the frequency spectrum of black ink inside the tube (data not shown). Figure 8.3(b) shows two exemplary red shifted (red color) and blue shifted (blue color) frequency spectra measured by the spectrum analyzer. The gray dashed curve represents a static measurement for reference purposes. The blue and red shifted spectra yield a reduced amplitude at the modulation frequency and a broadened distribution of 10–20 Hz at higher and lower frequencies, respectively. The effect of the Doppler broadening on the

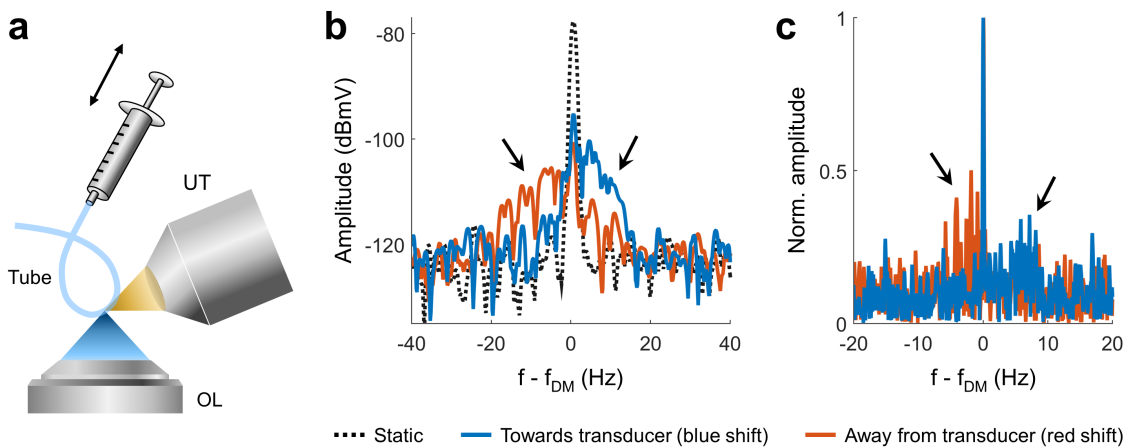


Figure 8.3: Doppler shift detection using black carbon particles flowing in a tube. (a) Experimental setting and detection geometry. **Abbreviations:** OL: Objective lens, UT: Ultrasound transducer. (b) Doppler shift detection with a spectrum analyzer at 15 MHz laser modulation. Red and blue shifted frequency spectra are shown in red and blue colors, respectively. The gray curve represents a static measurement. (c) Doppler shift detection with the IQ-demodulator. Red and blue shifted spectra are shown, whereas the static spectrum is masked and thus not visible. The Doppler peaks in (b) and (c) are indicated by black arrows.

overall signal amplitude, setting limits on the highest detectable flow speed, can clearly be observed.

After successfully measuring flow in the tube phantom with the spectrum analyzer, the IQ-demodulator was used for heterodyne detection in the next step. The 15 MHz optoacoustic signal was downmodulated to 100 Hz and an integration time of 5 s was used. Figure 8.3(c) illustrates red and blue shifted frequency spectra recorded with the IQ-demodulator, whereas the respective Doppler peaks are highlighted by the black arrows. As can be seen from the spectra, the IQ-demodulator yielded a lower SNR compared to the spectrum analyzer. In fact, most of the recorded spectra did not show any recognizable Doppler signatures. It can therefore be concluded that the IQ-demodulator is not suitable for *in vivo* blood flow detection due to its limited sensitivity, as the optoacoustic Doppler signatures of red blood cells are several orders of magnitude weaker than for the carbon particles [226]. On the other hand, the spectrum analyzer measurement yielded clear Doppler shifts and an SNR of 10–20 dB for an integration time of ~ 4 s. Accordingly, blood flow measurements should be conducted using ultra-narrowband detection over a frequency range of several tens of Hz. For this reason, a digital lock-in amplifier (UHFLI, Zürich Instruments; Max. input frequency: 600 MHz) incorporating a spectrum analyzer module was used for *in vivo* Doppler shift recordings.

8.3.3 Doppler shift calibration

After having established the appropriate flow detection method, the optoacoustic Doppler shifts generated at known flow speeds measured with the *in vivo* scan geometry (see Figure 8.1) were characterized. A similar carbon particle suspension with a volume fraction of 20 % was used to generate Doppler shifts inside a microfluidic chip (01-0175-0138-02, microfluidic ChipShop). The channel had a depth of 200 μm , a diameter of 1 mm and was covered by a 140 μm cycloolefin co-polymer lid (TOPASTM). A syringe pump (540060, TSE Systems) was used to generate flow with known speeds inside the channel.

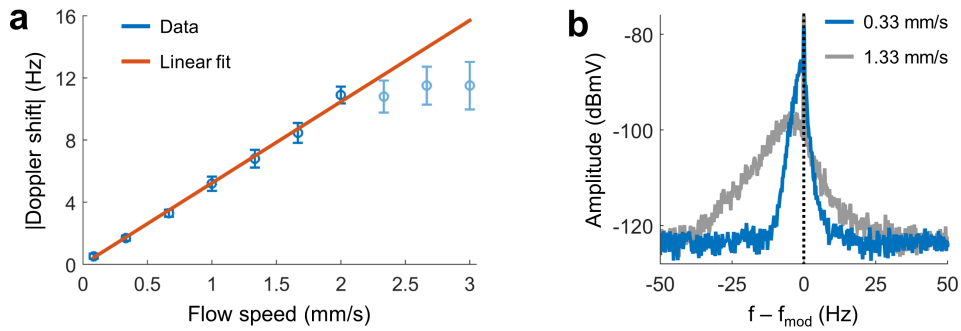


Figure 8.4: Doppler shift calibration. (a) Characterization of experimentally measured optoacoustic Doppler shifts as a function of flow speed. The data points correspond to the mean values of ten consecutive measurements and the error bars represent the respective standard deviations. The red line shows a linear fit to the data that was forced to go through the origin and where the last three data points (light blue color) were excluded. (b) Averaged frequency spectra around the modulation frequency (black dotted line) for flow speeds of 0.33 mm/s (blue curve) and 1.33 mm/s (gray curve).

To achieve similar measurement conditions as for the *in vivo* experiments, the chip was mounted on top of the mouse holder (see Figure 7.6) using the same transducer holder and configuration. The integration time of the lock-in amplifier was 9.6 s, corresponding to a frequency resolution and thus a lower Doppler shift detection limit of ~ 0.1 Hz for this setting. The modulation frequency was 15 MHz and the average power at the chip was ~ 18 mW. Figure 8.4(a) shows the measured optoacoustic Doppler shifts for different flow speeds ranging from 0.08–3.0 mm/s¹. The data points represent the mean Doppler shift values of ten consecutive measurements for each flow speed, which were extracted by fitting double-Gaussian functions to the spectra after smoothing with a moving average filter. The error bars denote the respective standard deviations of the ten measurements. Because the particles were pumped away from the transducer, the shifts correspond to the absolute values of the Doppler red shifts. The red line represents a linear fit to the data ($R^2 = 0.996$) that was forced to go through the origin and where the last three data points (light blue color) were excluded. For flow speeds higher than 2 mm/s, the Doppler shifts were underestimated by the measurements due to a strong Doppler broadening causing a low SNR. Thus, this value represents the maximum flow speed that can be detected with the modulation and acquisition settings provided above. From the slope of the linear fit (5.23 ± 0.15 Hz/mm s⁻¹), a Doppler angle of $58 \pm 1^\circ$ is calculated, assuming a speed of sound of 1510 m/s, which is in very good agreement with the adjusted transducer angle of $\sim 55^\circ$. Figure 8.4(b) illustrates two exemplary averaged frequency spectra for flow speeds of 0.33 mm/s (blue curve) and 1.33 mm/s (gray curve). The spectrum corresponding to the higher flow speed yields a larger Doppler shift and a stronger Doppler broadening. It can be concluded that the FD-OM system can accurately pick up flow speeds within the range of 0.08–2.0 mm/s, which corresponds to the flow speeds present in capillaries and small vessels [221], by using the spectrum analyzer module of the lock-in amplifier. The minimum and maximum detectable flow speeds can be further adjusted by changing the integration time of the lock-in amplifier and the modulation frequency of the laser.

1 In order to avoid focusing at the slope of the parabolic flow profile, the laser was slightly defocused to illuminate a larger volume of the channel. Thus, the flow speeds were assumed to correspond to the average of the flow profile, which is half the maximum speed at the tip of the profile.

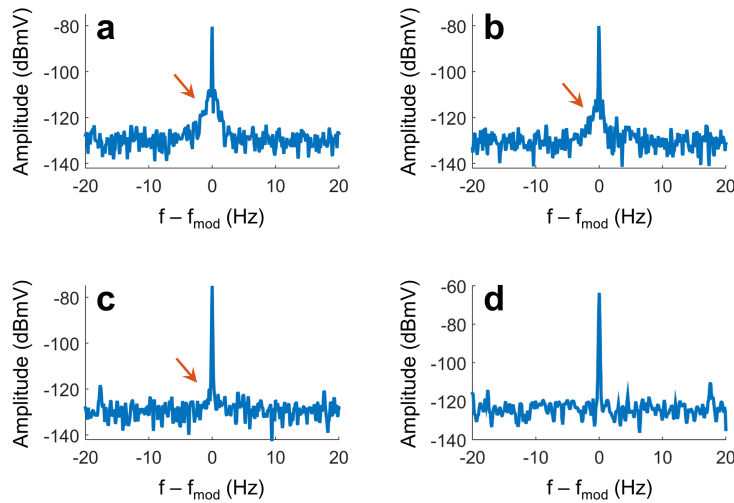


Figure 8.5: Blood flow monitoring of a single vessel in a mouse ear during a terminal experiment. (a-c) Frequency spectra around the modulation peak directly before starting the overdose (a), after 10 min (b) and *post mortem* (c). The red arrows indicate the blood flow induced Doppler peak. (d) Static reference measurement of black polish using the same settings. (Adapted from [186].)

8.4 Results

For the *in vivo* experiments presented in the following sections, the mice (HSD:Athymic Foxn1nude) were anesthetized and handled according to the description in section 7.3.3. All procedures were approved by the District Government of Upper Bavaria. For all measurements described in this section, the average power of the laser at the sample was 18 mW. With respect to all presented 2D images, the transducer was located at the bottom side with the acoustic lens pointing towards the images.

8.4.1 Blood flow monitoring during terminal experiment

In order to examine the *in vivo* flow detection capacity of the FD-OM system, the blood flow inside a single vessel of a mouse ear was monitored during a terminal experiment. First, a ROI was selected by performing a galvo scan with the FD-OM system to identify a suitable blood vessel for the flow measurements. Subsequently, the laser was focused into a $\sim 15 \mu\text{m}$ vessel and frequency spectra were recorded from point measurements with the lock-in amplifier at different time instances. The laser was modulated at 50 MHz and the integration time was ~ 33 s. During the experiment, the mouse was sacrificed by an overdose of isoflurane and the Doppler shifts were monitored. Figure 8.5 (a-c) shows the frequency spectra of the measurements directly before administering the overdose (a), after 10 min (b) and *post mortem* (c). As highlighted by the red arrows, a clear Doppler peak underneath the static signal at the modulation frequency is observed. The Doppler peak shows a reduced width after 10 min (b) and disappears in the *post mortem* spectrum (c), which clearly indicates blood flow in the vessel as the source. The frequency spectrum shown in Figure 8.5(d) represents a static reference measurement of black polish prior to the *in vivo* experiment with identical settings. It yields the same flat distribution around the modulation peak, validating that the observed Doppler peaks in the *in vivo* measurements did not originate from noise.

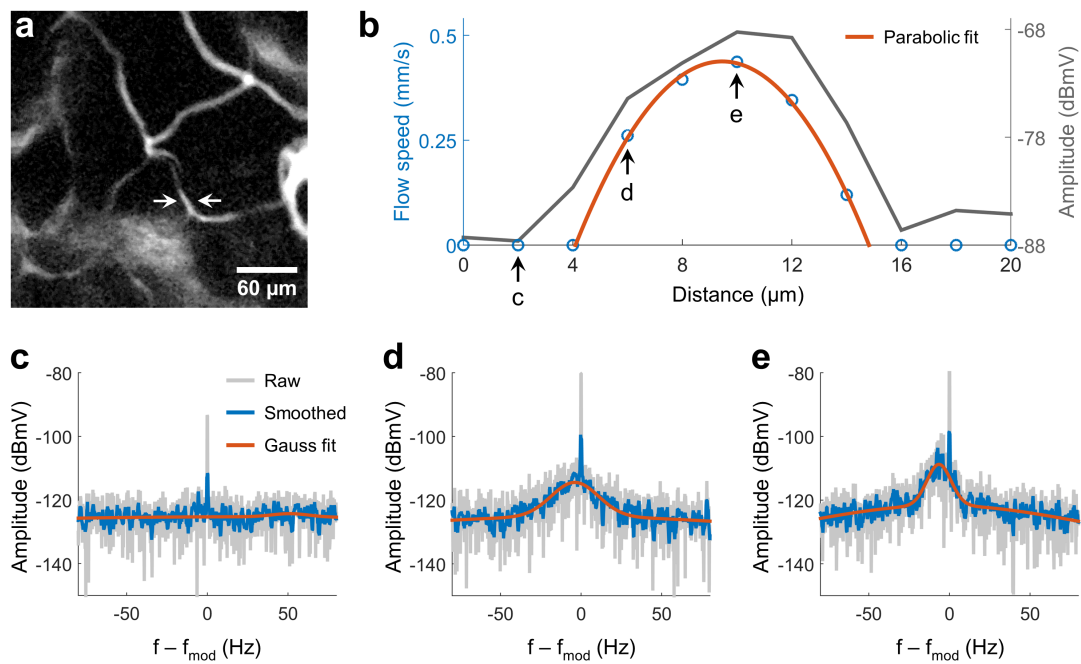


Figure 8.6: Blood flow profile of a single vessel in a mouse ear *in vivo*. (a) Galvo scan image of a $300 \times 300 \mu\text{m}$ FOV representing the amplitude sum of all frequencies. The white arrows indicate the location of the profile scan. (b) Profile scan across a single vessel showing the peak amplitude (gray curve) and the measured blood flow speed (blue circles). The red curve represents a parabolic fit to the flow speed data. (c-d) Frequency spectra obtained at the profile positions labeled with the black arrows in (b). The raw data (gray) was smoothed with a moving average filter (blue) and fitted with a double Gaussian (red curve). (Adapted from [186].)

8.4.2 Vessel flow profile and 2D blood flow map *in vivo*

In the final experiment, the question was addressed, whether the FD-OM system is capable of mapping microcirculatory blood flow across single vessels and in an entire 2D region of a mouse ear. As a first step, a $300 \times 300 \mu\text{m}^2$ FOV was imaged using the galvo scan mode and a frequency range of 10–50 MHz. Since the transducer was tilted by $\sim 55^\circ$ for the flow measurements, the galvo scan had to be performed within the asymmetric sensitivity field of the inclined detector. The alignment of galvo scanning FOV and transducer sensitivity field was performed prior to the vasculature imaging by measuring black polish placed next to the ear. The summed-up galvo scan image is illustrated in Figure 8.6(a), where the white arrows indicate the location of the profile scan across a single vessel. A modulation frequency of 42 MHz² and an integration time of 9.6 s were chosen for the flow scans. Figure 8.6(b) shows the peak amplitude (gray curve) and blood flow (blue circles) profiles of the vessel, acquired in $2 \mu\text{m}$ steps. The peak amplitude profile yielded a FWHM vessel diameter of $\sim 10 \mu\text{m}$. Regarding the Doppler analysis, the recorded frequency spectra were smoothed using a moving average filter and fitted with a double Gaussian, whereas the values corresponding to the central static peak were

² This particular modulation frequency was selected because the galvo scan showed a high SNR at 40 MHz but also yielded considerable electronic noise at that frequency. Consequently, the modulation frequency was increased by 2 MHz.

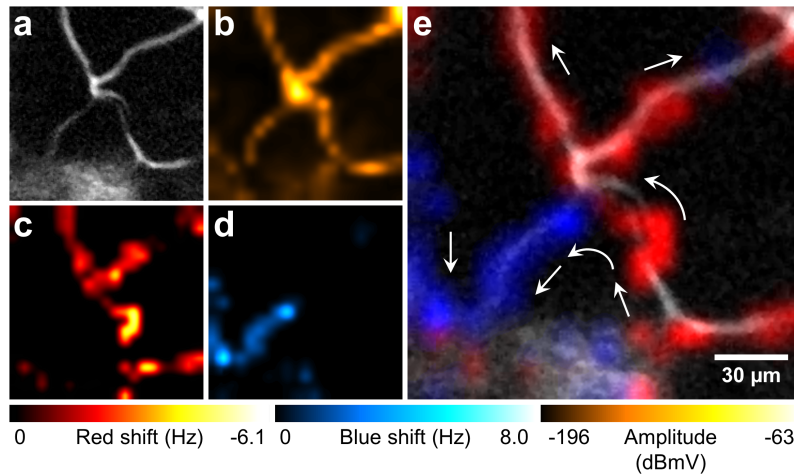


Figure 8.7: 2D blood flow mapping in a mouse ear *in vivo*. (a) Galvo scan image of the flow scan ROI. (b) Peak amplitude image of the flow scan. (c-d) Flow maps showing the Doppler red shift (c) and blue shift (d) values. (e) Overlay of the galvo scan image (gray), red shift (red) and blue shift (blue) maps. The arrows indicate the blood flow directions in the different vessels. (Adapted from [186].)

excluded from the fit³. For the flow profile, all Doppler shift values were set to zero if the respective Gauss fits had a too low R^2 value or peak amplitude. The Doppler shift data was fitted with a parabolic function ($R^2 = 0.997$), as represented by the red curve in (b). Finally, the measured Doppler red shift values were scaled down to a modulation frequency of 15 MHz, as this value was used in the flow calibration measurements, and translated into blood flow speeds by the calibration fit function shown in Figure 8.4. As can be seen from the fit, the measured flow profile follows a parabolic shape with a peak flow speed of ~ 0.44 mm/s. Figures 8.6(c-e) illustrate three exemplary frequency spectra corresponding to the line-scan positions of the profile indicated by the labeled black arrows in (b).

Subsequently, a 2D blood flow scan was performed in a $160 \times 160 \mu\text{m}$ region within the FOV shown in Figure 8.6(a) using the same settings as for the profile scan and a step size of $8 \mu\text{m}$. Figure 8.7(a) shows the galvo scan image of the selected FOV, whereas the 2D-interpolated peak amplitude map of the flow scan is presented in (b). At each measurement position, the optoacoustic Doppler shift was extracted. Figure 8.7(c) and (d) show the 2D-interpolated Doppler red shift and blue shift maps, respectively, representing mutually distinct areas of the scanned ROI. The images were gamma-corrected for better visibility but not saturated in order to keep the relation of brightness and Doppler shift, as shown by the respective color bars. The relationship between Doppler shifts and thus blood flow direction on the one hand and vessel anatomy on the other hand becomes more apparent in the overlay image presented in (e). Here, the galvo scan image is shown in gray color, whereas red and blue shifts are depicted in red and blue colors, respectively. The overlay image reveals the blood flow direction in the capillaries, as indicated by the white arrows. In this manner, the blood flow map does not only provide valuable information regarding the microcirculation, but furthermore facilitates the identification

³ For the spectrum corresponding to a distance of $14 \mu\text{m}$ in Figure 8.6(b), the data in the range of -15 to -5 Hz was excluded from the Gaussian fit because it could clearly be identified as noise compromising the fit.

of the vessel morphology. For example, by looking at (a) alone, it is difficult to judge whether the imaged vessel network represents a branching or a crossing of several blood vessels. However, as can be concluded from the blood flow map, the vessel in the lower part of the image probably does not bifurcate, but continues from the right to the left side and merges with another vessel coming from above. On the other hand, the branching at the center presumably belongs to a separate vessel which originates from an out-of-focus plane not visible in the image.

8.5 Conclusion and outlook

In conclusion, FD-OM was demonstrated for the first time to be suitable for *in vivo* microflow imaging. Detection based on IQ-demodulation was proven not to be sensitive enough for *in vivo* applications in a tube phantom experiment. On the other hand, Doppler shift detection using a lock-in amplifier based spectrum analyzer was shown to be appropriate for this purpose. The integration of the blood flow sensing capabilities into a microscopic imaging framework allowed for the unique generation of 2D microflow maps *in vivo*.

Together with the hybrid optoacoustic and multiphoton imaging ability presented in the previous chapter, the FD-OM methodology offers novel insights into structure and function of microvascular networks. This work therefore paves the way for a translation of the FD-OM modality from the laboratory into the clinics, where simple and cheap hardware might facilitate an application in human studies.

In order to reduce the laser exposure time, the SNR of the blood flow measurements could be increased by employing a dedicated ultrasound detector. Since the Doppler measurements require only a single modulation frequency, a transducer resonating at a narrow band around the laser modulation can considerably boost the achieved sensitivity. Furthermore, Doppler shifts $\Delta\omega$ can as well be detected by analyzing the phase differences $\Delta\phi$ induced by moving absorbers: $\Delta\omega = \Delta\phi/T$, where T denotes the time between two sequential scans [227]. Such a phase-resolved detection scheme could be highly sensitive especially to small flow speeds and might present an alternative to direct Doppler shift measurements.

9 Summary and conclusion

9.1 Conclusive summary

This work was dedicated to the advancement of high-resolution optoacoustic imaging. The thesis presented the results and discussed the implications of this endeavor at different fronts of development and application. In the following, a conclusive summary is given based on the four goals defined in section 1.4.

1. Improvement and further development of existing high-resolution optoacoustic imaging techniques

The first part of the thesis was concerned with the tomographic reconstruction used in raster-scan optoacoustic mesoscopy (RSOM). The original backprojection algorithm assumed a point-like acoustic focus and a binary mask for the transducer sensitivity field. While such a binary mask model effectively suppresses signals originating from outside the sensitivity field, it fails to reconstruct structures close to the focus and up-scales signals with increasing distance to the focus. To incorporate a more realistic model of the detector, a weighted hyperbolic sensitivity field (WHSF) was implemented together with an axial weighting. The WHSF model was demonstrated to yield superior reconstruction results compared to the binary mask model, especially for structures close to the acoustic focus. Furthermore, a method was introduced based on the reconstruction of multiple frequency bands to capitalize on the broadband nature of optoacoustic signals commonly detected in high-resolution applications. The simultaneous reconstruction of the full signal bandwidth often results in a masking of small features by low-frequency signals, which generally have a higher amplitude than the high-frequency components. The multi-frequency reconstruction allowed for a separation of low- and high-frequency components and an improved visualization of small features and details. The presented methods illustrate the necessity of using realistic detector models and taking into account the frequency dimension in optoacoustic mesoscopy, leading to improved visualization results.

In the mid part of the thesis, the development of a transmission-mode optoacoustic microscope was presented. The OM system was used together with a custom-designed gold sample to characterize the electrical impulse response (EIR) of the transducer, which is a task not readily achieved with high-frequency detectors due to the difficulties of reliably detecting sub-micrometer sized point sources. The measured EIR was further used to correct the recorded optoacoustic signals for the finite frequency response of the transducer, leading to an improvement in axial resolution. Owing to the convenience and reliability, this method could become a standard in characterizing high-frequency ultrasound transducers for mesoscopy or microscopy applications and could be even used to experimentally determine their 3D spatial impulse response. Additionally, the developed OM system was used together with an optical fiber detector based on a π -phase-shifted fiber Bragg grating for the imaging of biological organisms *ex vivo*, yielding similar results as with traditional piezoelectric-transducer-based detection. This pilot

study could pave the way towards all-optical epi-illumination optoacoustic microscopy, enabling the imaging of large specimens at arbitrary locations.

The final part of the thesis focused on frequency-domain optoacoustic microscopy (FD-OM), an implementation of OM that relies on monofrequent excitation by modulated CW lasers and on the detection of optoacoustic signals at the same frequency. Traditionally, FD-OM uses a single modulation frequency for imaging, as well as lock-in detection because of the inherently low SNR. The shortcomings of such an approach are the long acquisition time and the lack of axial resolution and depth information. In order to overcome these limitations, the developed FD-OM system was implemented based on IQ-demodulation instead of lock-in detection, which enabled a fast and direct read-out of amplitude and phase of the detected monofrequent optoacoustic signals. Building upon this acquisition scheme, FD-OM could be realized using fast laser-scanning by means of galvanometric mirrors, which not only tremendously increased the image frame rate to more than 1 Hz, but additionally enabled high laser powers to be employed, which significantly increased the achieved SNR. Furthermore, the fast acquisition allowed for the use of multiple discrete modulation frequencies within a reasonable total imaging time of a few minutes (including averaging). As demonstrated by the imaging of phantoms and model organisms, the multiple-frequency imaging approach could simultaneously visualize objects ranging from a few to several tens of micrometers, which is not attainable with conventional single-frequency FD-OM. Moreover, the recording of amplitude as well as phase at different modulation frequencies using IQ-demodulation facilitated the restoration of limited depth information and thus 3D reconstruction capabilities. Finally, the increased acquisition speed together with the superior multi-frequency acquisition scheme allowed for the first time to perform label-free imaging of mouse ear vasculature *in vivo*. These findings suggest that FD-OM might indeed become a serious alternative to conventional time-domain OM approaches.

2. Combination of optoacoustic microscopy and mesoscopy with other optical microscopy techniques

The OM modality developed in this work was successfully integrated into a hybrid device together with multiphoton microscopy, which incorporated two-photon excitation fluorescence (TPEF), second-harmonic generation (SHG) and third-harmonic generation (THG) microscopy. The OM and multiphoton modalities were shown to achieve comparable spatial resolutions and imaging depths. Moreover, by exploiting four fundamentally different label-free contrast mechanisms, the hybrid microscope was able to visualize a broad range of structures in biological specimens, such as melanin and hemoglobin (OM), elastin (TPEF), collagen and myosin (SHG) as well as cell membranes and other structural surfaces (THG), without the need for external labeling. Furthermore, building upon the scalability of optoacoustic imaging, the RSOM modality was implemented in the hybrid microscope using the same laser and detector. Additionally to the multicontrast ability, the integrated multiphoton and multiscale optoacoustic microscope (IMMSOM) thus allowed for label-free imaging at different geometrical scales, a requirement crucial for many biological studies, e.g. understanding development or disease heterogeneity.

One of the limitations of IMMSOM was the mechanical scanning scheme of the OM modality. Whereas the RSOM and multiphoton scans had total acquisition times of a few minutes, the OM scan typically took one hour or more, depending on the FOV. To overcome this bottleneck in acquisition speed, the developed FD-OM modality was from the beginning set up within the IMMSOM system, using the galvo mirrors of the

multiphoton microscope for laser-scanning. This design enabled the combination of FD-OM and multiphoton microscopy for label-free multimodal imaging at high frame rates. The gain in imaging speed in turn facilitated the hybrid imaging of mouse ears *in vivo*, simultaneously visualizing vasculature, hair follicles, keratinocytes and collagen.

3. Development of novel optoacoustic microscopy implementations based on simple and cost-effective technologies

The laser-scanning in OM could be also implemented in the time domain (TD-OM) using a pulsed laser source. However, the synchronization of galvo mirror movement, laser pulses and acquisition is a complicated task which moreover requires a fast and expensive kHz laser in order to provide a true speed improvement. On the other hand, laser-scanning with the developed IQ-demodulation based FD-OM system is considerably easier to realize because time-constant voltage signals (I and Q) are acquired, which do not require synchronization with the DAQ or the galvo mirrors.

Another simplification of FD-OM compared to conventional OM concerns the simultaneous imaging at multiple wavelengths. Multi-wavelength TD-OM so far requires dye lasers suffering from a rapid degradation of the dyes or expensive optical parametric oscillators. Both kinds of sources have to be pumped by additional lasers, which further increases the overall costs. In contrast, FD-OM relies on cheap CW laser sources, which are available at various wavelengths throughout the visible and near-infrared spectrum. Furthermore, the combination of several laser lines is significantly facilitated by the IQ-demodulation scheme, as different wavelengths can be modulated at different frequencies and separately demodulated for simultaneous acquisition. Such a concurrent imaging at multiple wavelengths would require the complicated interleaving of pulses from different laser sources in the time domain.

Finally, FD-OM enables the direct imaging of flow via the detection of optoacoustic Doppler shifts, which was successfully demonstrated in phantoms using the developed FD-OM system. With the goal to eventually image blood flow *in vivo*, different methods to detect optoacoustic Doppler shifts were investigated and characterized. As a result, heterodyne detection with the IQ-demodulator was shown to be in principle able to capture Doppler shifts, albeit with insufficient SNR for *in vivo* applications. On the other hand, Doppler shift detection with a lock-in amplifier used in frequency-sweep mode (similar to a spectrum analyzer) proved to achieve sufficient SNR and consequently was found to be appropriate for blood flow imaging *in vivo*.

4. Application of the high-resolution optoacoustic modalities to biological imaging

Besides the technological development, the high-resolution optoacoustic modalities covered in this work were applied to the imaging of biological specimens. At the mesoscopic scale, epi-illumination RSOM was used to monitor dynamic responses of endogenous melanophores in zebrafish larvae *in vivo*, induced by hormonal treatment and background adaptation. RSOM could identify single melanophores and capture stimulated melanosome aggregation *in vitro* and *in vivo* via amplitude changes in the optoacoustic data. It was further hypothesized that a change in the effective pigmented volume as 'seen' by RSOM is reflected in the optoacoustic frequency spectra. After such a frequency shift effect was characterized via simulations of contracting and expanding optical absorbers, similar signatures were indeed observed during measurements of melanosome aggregation in fish *in vivo* by applying a frequency analysis to the raw data. Most importantly, the RSOM

imaging procedure was demonstrated not to interfere with the physiological functions of the fish, which is crucial for the reliability of the developed method. Subsequently, the developed frequency analysis was used to create a spatially resolved 2D map of frequency shift magnitude indicative of the strength of melanosome aggregation during a background adaption experiment *in vivo*. This non-invasive and label-free frequency analysis technique could prove useful in developmental biology studies or for investigating processes such as hyperpigmentation and tumor growth, where pure optical approaches commonly fail to reliably track pigment dynamics in 3D due to the strong optical absorption of melanin. On the other hand, the label-free capturing of melanophore dynamics *in vivo* and in 3D could open the door for the development of bioengineered dynamic whole-cell sensors for optoacoustic imaging. As a first step towards this goal, RSOM together with the developed frequency analysis was successfully used to monitor the dynamics of wildtype xenotransplanted frog melanophores in a juvenile zebrafish brain, which were stimulated with the hormone melatonin. By genetically modifying and overexpressing specific receptors in the melanophores, the dynamic response could be triggered by specific endogenous ligands of interest, such as dopamine, and picked up by optoacoustic mesoscopy.

At the microscopic level, FD-OM was used for imaging microcirculatory blood flow based on the detection of optoacoustic Doppler shifts. The developed method enabled the measurement of a parabolic flow profile of a single capillary in terms of absolute flow speeds as well as a 2D map of microflow in a vascular network of a mouse ear. As the Doppler shifted signals are extraordinarily weak, blood flow imaging in the frequency-domain has not been achieved before *in vivo*. On the other hand, blood flow imaging in the time domain is feasible but typically requires additional measurements as well as mechanically moving the sample or scanning unit back and forth to discriminate between the flow directions. The FD-OM approach not only allows for direct Doppler shift measurements to determine blood flow direction and speed, but also relies on cost-efficient and simple hardware. This is an important criterion for a future translation of the method into the clinics, where the imaging of microcirculatory blood flow might give novel insights into the regulation of blood pressure and temperature, tissue oxygenation or the delivery of nutrients in the context of various diseases, including cancer and diabetes.

9.2 General outlook

Optoacoustic microscopy (including mesoscopy) in itself bears great potential for biomedical imaging by visualizing a huge range of absorbing molecules and enabling the label-free measurement of functional and metabolic parameters at depths exceeding the limits of conventional microscopy. However, a major direction for future development will be the integration of optoacoustic microscopy into hybrid imaging systems in order to complement the observations of complex samples with absorption-based contrast and the unique optoacoustic supplement of frequency-related and spectral information. The extent to which optoacoustic microscopy will be successful in invading the realm of widespread and standardized microscopy in biomedical imaging is expected to depend on a number of factors, all of which were addressed by the underlying thesis.

First, the complexity of optoacoustic microscopy systems has to be reduced in order to facilitate an easy integration in existing microscopy setups. The bottleneck of this aim is clearly the ultrasound detection unit, which requires close proximity to the examined sample as well as acoustic coupling. One possible solution could be the miniaturization

of the ultrasound detector, e.g. by using optical fiber detectors similar to the π -FBG sensor presented in this work. Second, the implementation of optoacoustic microscopy should enable arbitrary samples to be measured. Once again, the use of optical detectors can play a crucial role by allowing for versatile positioning of the sensor or by facilitating epi-illumination based setups that achieve sub-micrometer resolutions owing to their small footprint. Third, the optoacoustic microscopy components should come at low costs and small form factors.

Frequency-domain optoacoustic microscopy could play a major role in this integration process. It has the potential to achieve similar performances as conventional optoacoustic microscopy approaches at considerably lower costs and complexity. Ultimately, the future technological development in terms of fast or tunable pulsed laser sources and high-speed digitizers is going to decide whether FD-OM will establish itself as an alternative or even superior solution to conventional time-domain approaches.

Irrespective of the technological advancement, it can already be concluded that optoacoustic microscopy will play an important role in biomedical imaging in the years to come and that it will contribute its part to the endeavor of the scientific community to answer the big questions about nature by uncovering the microscopic world.

A MATLAB™ script for the simulation of optoacoustic signals

```

function [p, t, pf, f] = SimSignal(d, object, pulse_FWHM, ...
                                attenuation)

%+++++%%%%%%%%%%%%%%%%%%%%%%%%%%%%%%%%%%%%%%%%%%%%%%%%%%%%%%%%%%%%%%%%%%%%%%%%+++++
% MATLAB version: R2015a
%
% Input parameters:
% d:          Absorber diameter [um]
% object:     Absorber type: 1) liquid sphere
%             2) solid sphere
%             3) solid cylinder
% pulse_FWHM: Laser pulse width (FWHM) [ns] (0: off)
% attenuation: Acoustic attenuation flag (0: off)
%             Prog. distance has to be set in the code
%
% Output parameters:
% p:          Simulated time signal
% t:          Time vector
% pf:         Simulated frequency spectrum
% f:          Frequency vector
%+++++%%%%%%%%%%%%%%%%%%%%%%%%%%%%%%%%%%%%%%%%%%%%%%%%%%%%%%%%%%%%%%%%%%%%%%%%+++++

if nargin < 4
    attenuation = 1;
end
if nargin < 3
    pulse_FWHM = 2.2;
end
if nargin < 2
    object = 1;
end

% Simulation parameters:
nS      = 512;          % Number of time samples
Fs      = 2e9;          % Sampling frequency [Hz]
dt      = 1/Fs;        % Time resolution [s]
t0      = -nS/2*dt:dt:nS/2*dt; % Time vector [s]
df      = 1/(t0(end)-t0(1)); % Frequency resolution [Hz]
f0      = 0:df:Fs;     % Frequency vector [Hz]
R       = 1e-9;

% Coupling medium:
v_sur   = 1500;        % Speed of sound (SoS) [m/s]
rho_sur = 1000;       % Density [kg/m^3]

```

```

% Acoustic attenuation:
z_t    = 0;                % Propag. distance in tissue [m]
z_w    = 1650;            % Propag. distance in water [m]

% Absorber parameters:
v_abs  = 2200;            % SoS in absorber [m/s]
v_trans = 0;              % Transverse SoS in absorber [m/s]
rho_abs = 1140;           % Density of absorber [kg/m^3]

r      = d/2*1e-6;        % Radius of absorber [m]

% Laser pulse width (standard deviation) [s]:
pulse_sig = pulse_FWHM/(2*sqrt(2*log(2)))*1e-9;

if object == 1                % Signal of a fluid sphere
    p0 = heaviside(r - abs(R-v_sur*t0)).*((R-v_sur*t0)/(2*R));

    % Convolve signal with Gaussian laser pulse:
    if pulse_FWHM
        g = normpdf(t0, 0.0, pulse_sig);
        p = conv(p0, g, 'same');
    else
        g = p0;
        p = p0;
    end

    [pf, f] = FFT_t2f(p, t0);    % FFT
    pf      = abs(pf);

    t      = t0;
else
    % Reduced variables [dimensionless]:
    q      = 4*pi*f0*r/v_abs;
    rho_0  = rho_abs/rho_sur;
    v_0    = v_abs/v_sur;
    v_t    = 2*v_trans/v_abs;

    switch object
        case 2                % Signal of a solid sphere
            Nom    = (sin(q) - q.*cos(q))./q.^2;
            Denom  = (1 - rho_0 + rho_0*v_t^2./q.^2).*sin(q)./q ...
                - (1 + rho_0*v_t^2./q.^2).*cos(q) ...
                + 1i*rho_0*v_0*((1 - v_t^2./q.^2).*sin(q) ...
                + v_t^2./q.*cos(q));

            case 3            % Signal of a solid cylinder
                Nom    = besselj(1,q)./q.*besselh(0,v_0*R/r*q);
                Denom  = besselj(1,q).*besselh(0,v_0*q) ...
                    - rho_0*v_0*besselh(1,v_0*q).*(besselj(0,q) ...
                    - v_t^2/2*besselj(1,q)./q);
        end

    pf0 = 1i * Nom./Denom;

    % Simulate acoustic attenuation in tissue and water:

```

```

if attenuation
    AO_t = 1.06;           % Tissue att. coeff. [dB/MHz/cm]
    AO_w = 0.00217;      % Water att. coeff. [dB/MHz/cm]

    m_t = 1.0;
    m_w = 2.0;

    A_t = log(10^(AO_t/20))*1e-4; % [dB] -> [Np]
    A_w = log(10^(AO_w/20))*1e-10;

    % Frequency dependent attenuation:
    pf0 = pf0 .* exp(-A_t*f0.^m_t*z_t*1e-6) ...
        .* exp(-A_w*f0.^m_w*z_w*1e-6);
end

pf0(1) = [];           % 1st entry is NaN
f0(1) = [];

[p0, t] = FFT_f2t(pf0, f0); % iFFT
p0 = ifftshift(p0);

% Convolve signal with Gaussian laser pulse:
if pulse_FWHM
    g = normpdf(t, mean(t), pulse_sig);
    p = conv(p0, g, 'same');
else
    g = p0;
    p = p0;
end

[pf, f] = FFT_t2f(p, t); % FFT
pf = abs(pf);

% Flip and center signals:
p = p(end:-1:1);

switch object
case 2
    t = (t - mean(t)) - r/v_sur;
case 3
    t = (t - mean(t));
end
end
end

function [fs, f] = FFT_t2f(s, t) % FFT function
Fs = 1/(t(2) - t(1));
NFFT = 16*2^nextpow2(length(t));

fs = fft(s, NFFT);
fs = 2*fs(1:NFFT/2+1);

f = Fs/2*linspace(0, 1, NFFT/2+1);
end

```

```
function [s, t] = FFT_f2t(ss, f) % iFFT function
df = f(2) - f(1);
NFFT = 2^nextpow2(length(f));

s = ifft(ss, NFFT, 'symmetric')*NFFT;
s = 2*s(1:NFFT);

t = linspace(0, 1, NFFT)/(2*df);
end
```

B Numerical axial resolution simulation

The axial resolution of an optoacoustic imaging system depends on the transducer reception bandwidth and can be either determined theoretically by using Eq. (3.26) or experimentally by measuring the FWHM of the signal envelope (Hilbert transform) from a point source. However, both methods result in a too large value for the axial resolution because the positive and negative peaks of two optoacoustic signals in close proximity add up and partially cancel. The envelope of the added signal still shows distinct peaks when the temporal distance of the two signals is smaller than the FWHM of the envelope of the single signal.

This effect is demonstrated by Figure B.1, which shows a numerical simulation of two temporally approaching optoacoustic point source signals (dashed blue curves) and its effect on the envelope (red curve) of the added signal. The optoacoustic signal used in the simulation was experimentally measured with the 80 MHz transducer using the gold layer sample, as shown in the inset of Figure 5.6(b). The two signals were manually shifted, added up and the envelope was calculated using the Hilbert transform. Figure B.1 shows the situation for a temporal distance between the signals of (a) 40 ns, (b) 30 ns, (c) 20 ns, (d) 10 ns, (e) 5 ns and (f) 2.5 ns. As can be observed, the envelope of the added signal yields two distinct peaks up to a separation of 5 ns, which corresponds to an axial distance of $\sim 8 \mu\text{m}$ and matches the value determined in [11]. On the other hand, Eq. (3.26) results in a value of $\sim 15 \mu\text{m}$, whereas the FWHM of the single signal envelope yields $\sim 20 \mu\text{m}$.

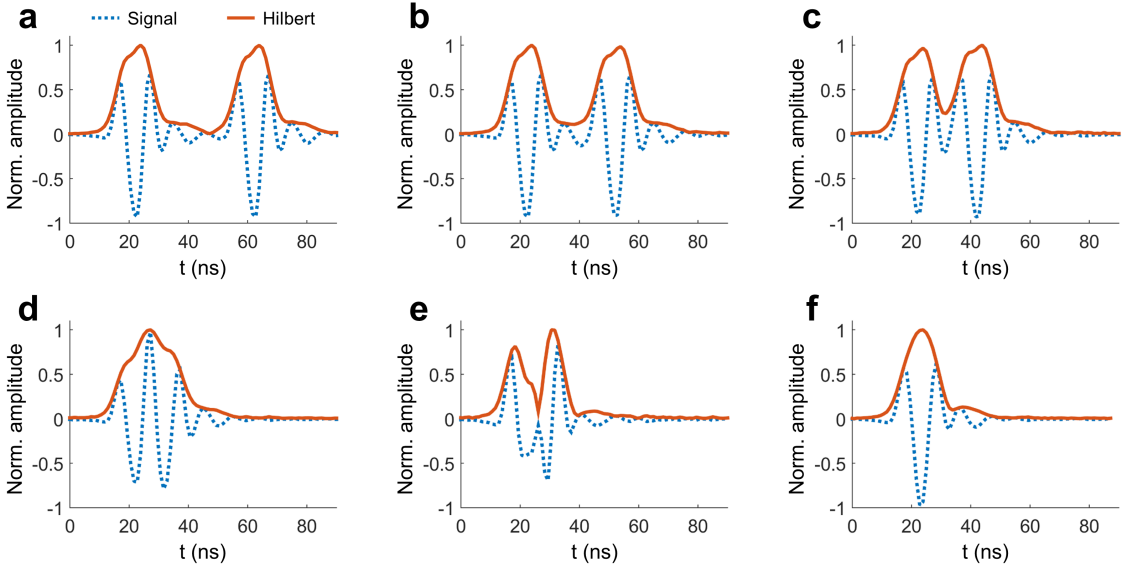


Figure B.1: Numerical axial resolution simulation. Dashed blue curves: Two temporally approaching optoacoustic point source signals that are manually shifted and added. The signal was experimentally measured with the gold layer sample (see Figure 5.6(b)). Red curve: Envelope (Hilbert transform) of the added signal. Temporal distances between the two signals of (a) 40 ns, (b) 30 ns, (c) 20 ns, (d) 10 ns, (e) 5 ns and (f) 2.5 ns are shown.

Estimation method	Axial resolution value (μm)
Calculation using Eq. (3.26)	15
FWHM of point source signal envelope	20
FWHM of first point source signal peak	5
FWHM of first microsphere signal peak [11]	7
Numerical simulation	8

Table B.1: Comparison of axial resolution values for the 80 MHz transducer estimated by different methods.

Both methods evidently underestimate the true axial resolution of the transducer. For this reason, the FWHM of the first peak of the single signal represents a better estimation of the axial resolution, having a value of $\sim 5 \mu\text{m}$. Table B.1 collects the axial resolution values estimated by the different methods.

As can be seen in Figure B.1(d), there is an intermediate situation during the approach of the two signals where the total envelope does not feature distinct peaks. The reason is that the used point source signal exhibits a negative and two positive peaks instead of the characteristic bipolar N-shape shown in Figure 3.3, which add up constructively at this particular temporal distance. The deviation from the N-shape results from the finite detector bandwidth (EIR), which cuts off parts of the frequency spectrum and thus distorts the measured signal.

One method to quantitatively determine the axial resolution would be to define a specific metric, e.g. the contrast-to-noise ratio of the total envelope, calculate its value for several temporal distances and set a threshold which defines the axial resolution. Such a quantitative characterization was used in [134]. However, the minimum axial distance of two optoacoustic signals that still yields two distinguishable peaks in the summed envelope depends on the shape of the optoacoustic signal used in the characterization. The temporal shape of optoacoustic signal in turn depends on the size and shape of the absorber and on the propagation medium. Hence, the experimentally determined axial resolution will be different for point source signals obtained from reference samples such as thin layers or microspheres and objects measured in biological tissue. Consequently, it is not possible to determine a value for the axial resolution of an optoacoustic imaging system that applies to all experimental conditions, but rather to provide a realistic estimation.

C Photographs of the optoacoustic microscopy systems

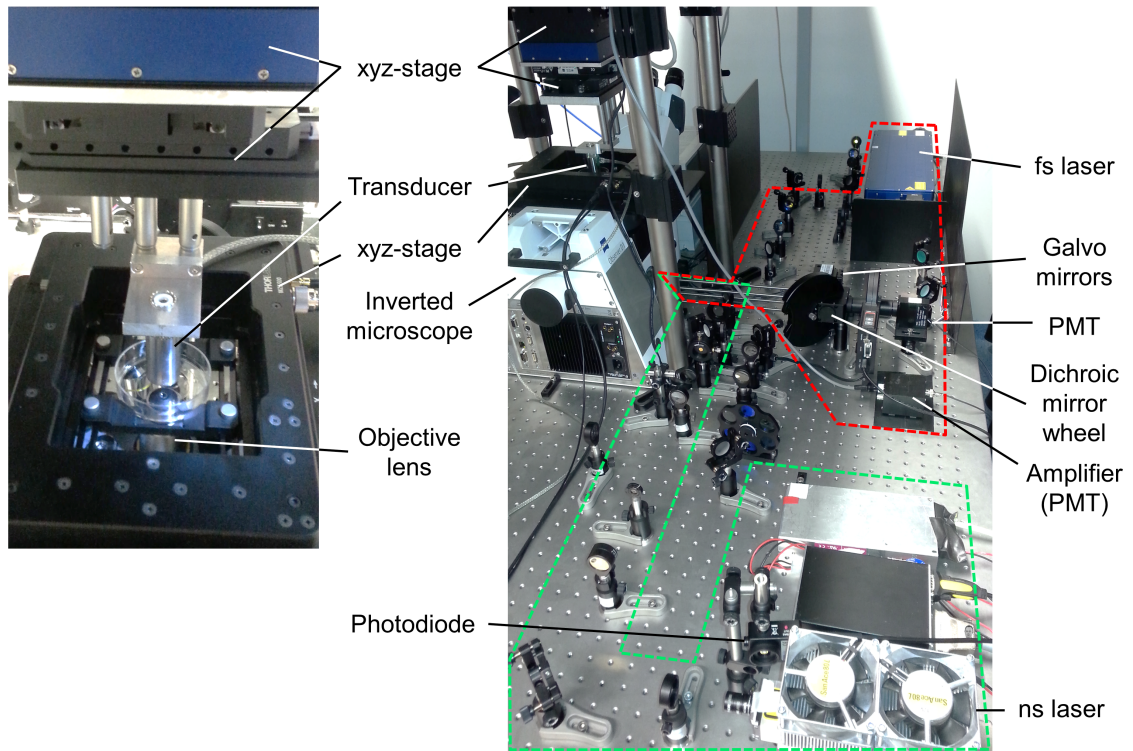


Figure C.1: IMMSOM system and scanning unit. Green box: OM beam path. Red box: Multiphoton microscopy beam path.

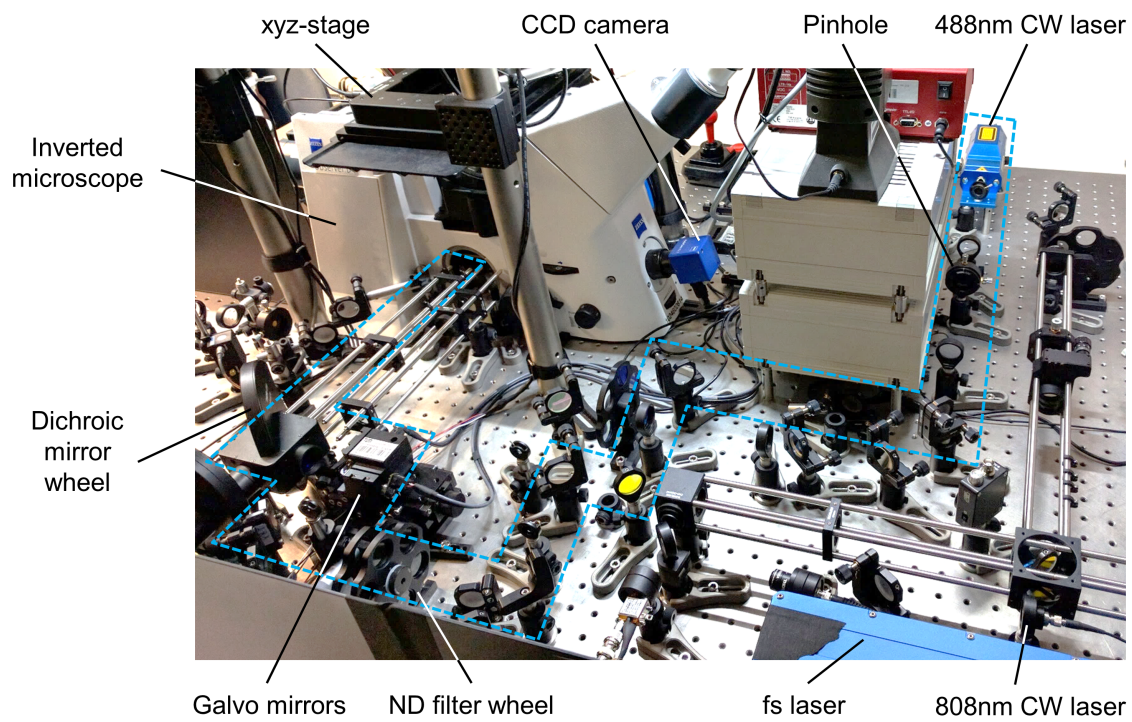


Figure C.2: FD-OM system. Blue box: Beam path of the 488 nm CW laser. The 808 nm beam path is not shown.

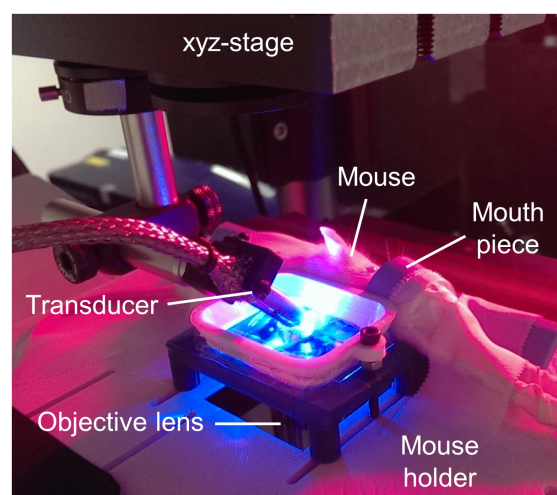


Figure C.3: FD-OM *in vivo* mouse ear holder during blood flow scan.

D Published material and reprint permissions

Most of the results presented in this work has been previously published in different articles or are being prepared for publication in the near future.

- In chapter 3, Figure 3.9 was adapted from [58] (© 2014 Optical Society of America). The experimental development as well as the performance characterization of the transmission-mode and epi-illumination mode RSOM systems was previously published in [11] (© 2013 Optical Society of America) and [58], respectively. Furthermore, parts of the introduction and theory section as well as Figure 3.1 were adapted and prepared for publication in a book chapter [228] during the submission of this thesis.
- The results presented in chapter 4 were in preparation for publication [104] during the submission of this thesis.
- In chapter 5, the resolution characterization has been published in [128] (© 2014 Optical Society of America) and [129] (© 2015 SPIE), whereas the OM zebrafish image has been adapted from the hybrid OM and multiphoton image presented in [128]. The results presented in section 5.5 have been published in [149] (© 2016 Optical Society of America).
- The figures shown in chapter 6 were adapted from the publications [139] (© 2015 Nature Publishing Group) and [163] (© 2016 SPIE). The hybrid atheroma results were published in [179] (© 2016 Elsevier).
- The results presented in chapters 7 and 8 were in preparation for publication [186] during the submission of this thesis.

Permissions to reproduce text passages and illustrations are granted through the author rights in the copyright transfer agreements for the above mentioned publications and have been additionally obtained in written form through email contact to the editorial boards.

Figure 2.13 was taken from [47] (© S. Ruzin and H. Aaron, UC Berkely) and adapted. Permission was granted through email contact.

Acknowledgments

This work is among other things a result of the guidance and support of many different people and a few lines are not remotely enough to appropriately express my gratitude for their professional and private contributions over the past three and a half years.

First of all, I would like to gratefully thank my advisor Prof. Vasilis Ntziachristos for giving me the opportunity to work in the exciting field of high-resolution optoacoustic imaging. Despite having a background in particle physics, he offered me the chance to dive into a completely new field and to learn so many new and fascinating things. It was an honor to learn from his deep and comprehensive expertise in the field of imaging and to experience the scientific spirit and visions that he imparted to the people working around him. He always granted me the freedom and encouraged me to work towards my own ideas and approaches, but at the same time constantly provided me with guidance, support and an open door. I really appreciated this spirit and the enjoyable working atmosphere.

Furthermore, I would like to thank Prof. Gil Westmeyer for the great and productive collaboration as well as for his constant support and guidance. With his visions and motivation, he showed me how to bring the best out of my research.

For being part of my thesis committee and providing me with valuable feedback, I want to thank Prof. Gil Westmeyer and Prof. Sibylle Ziegler.

During my Ph.D., I have had the fortune to meet a number of people that not only have been great co-workers, but that above all have become good friends over the years.

First and foremost I have to thank Dr. Murad Omar, who introduced me to the field of optoacoustic imaging and who has been my mentor throughout my work. We spent numerous hours in the lab working with RSOM and had many good moments and discussions from the first day on. He helped me with the development of the OM system and also taught me the value of laser safety, why marzipan beats nougat and how to employ the word 'use'.

I am very glad to have met Dr. George Tserevelakis, with whom I not only shared the microscopy lab and several publications, but also inspiring conversations and a great time. We had a very close and fruitful collaboration in the development of the multimodal TD-OM and FD-OM systems and from him I learned the basic concepts of optical microscopy as well as the power of γ .

My thanks furthermore goes to Dr. Ara Ghazaryan, who worked with me on the multiphoton setup and on certain OM implementations. He improved the overall working conditions at the institute with his positive character and particularly my personal well-being by establishing a constant supply chain with Sujuk. Without him, my Ph.D. would have been far less bright.

Finally, I want to thank Markus Seeger, who joined the IMMSOM project during the last year of my Ph.D. and who upgraded the OM modality to enable fast laser-scanning. He not only was a true OCD companion, but we moreover shared our fondness for multispectral imaging, Wolfgang Ambros, 472 Hz and styrodur. I am very grateful for

the fantastic time and collaboration we have had together.

For their valuable comments and corrections regarding this thesis I am deeply indebted to Dr. Murad Omar and Markus Seeger, who have reviewed the whole text, but also to Dr. George Tserevelakis and Dr. Antonella Lauri, who have revised specific chapters.

I am much obliged to Dr. Antonella Lauri, who collaborated with me on the RSOM melanophore project and who spent many hours with me in the lab preparing samples or running RSOM measurements. We had a very good relationship throughout the years and my research profited considerably from her experience and knowledge. With her quiet and precise manner of working as well as her ethical imperative, I will always remember her as a role model for a good scientist.

Special thanks goes to Georg Wissmeyer, with whom I collaborated for the optical fiber sensor based OM project and to Roman Shnaiderman for the numerous interesting and elucidating discussions about OM and the one or the other program. Working with both of them in the lab was a unique and hilarious experience that I will keep in good memory. Additionally, I wish to thank Dr. Andriy Chmyrov for his support. His profound knowledge in the field of optical microscopy helped me with the refinement of the various optoacoustic microscopy systems.

I am furthermore indebted to Dr. Stephan Kellnberger for his support in the beginning of my Ph.D. and for the many helpful work-related and funny private discussions we have had. I particularly remember the look of his engineering lab, which alleviated my initial nostalgia after the transition from a particle physics to an imaging institute.

Moreover, I want to thank Ludwig Prade, a fellow FD sufferer who helped me a lot with understanding the conceptual framework of FD imaging and with electronics-related problems. He was also a fellow physics student with whom I spent many funny moments over the past years.

Two persons I want to especially thank are Mathias Schwarz, who started his Ph.D. together with me, and Hailong He, who joined the institute a few weeks later. We shared the office for a long time, helped each other a lot in the first months of our work and influenced one another throughout our Ph.D.

Additionally, I would like to thank Dr. Jaya Prakash for his feedback regarding FD-OM flow measurements, Dr. Angelos Karlas for his help with flow phantoms for FD-OM, Marwan Muhammad for borrowing me his lock-in amplifier, Stratis Tzoumas for his valuable feedback on the optoacoustic monitoring of melanophore dynamics, Marco Mette for his help and constructive ideas regarding the design of the FD-OM *in vivo* mouse ear holder, Juan Osorio for developing a GUI for RSOM image processing, Jacob Wierzbowski for producing the gold layer sample using EBPVD and Dr. Andreas Bühler for his help in understanding the principles of optoacoustic imaging at the beginning of my Ph.D. For the good time and a lot of funny conversations, I would like to thank Maximilian Koch, Dmitry Bozhko, Dr. Pouyan Mohajerani, Dr. Gael Diot, Ivan Olefir, Thomas Fehm, Andrei Chekkoury, Carlos Cruz Perez, Sheryl Roberts, Yuanhui Huang, Dr. Miguel Pleitez, Dr. Juan Aguirre, Dr. Josefine Reber and Dr. Nicolas Bézière.

I wish to particularly thank Florian Jurgeleit for his help with the *in vivo* FD-OM mouse experiments, Sarah Glasl for her assistance with *in vivo* RSOM measurements of mice, Uwe Klemm for his help with the preparation of cell samples for RSOM and Anja Stelzl for her help with zebrafish and cell cultures for the RSOM melanophore project. Besides their scientific help and support, we also had a lot of fun in and outside the lab.

I would further like to express my gratitude to Susanne Stern, Zsuzsanna Öszi, Dr. An-

dreas Brandstaetter, Martina Riedl, Dr. Doris Bengel, Dr. Julia Niefnecker, Dr. Christiane Ogorek, Silvia Weinzierl and Dr. Barbara Schroeder, who provided immediate, patient and competent help in all kinds of different matters, including organizational issues, animal experiments and purchasing orders. Without their great work and support, this thesis would not have been possible.

For their swift and uncomplicated help with all matters regarding the Ph.D. program 'Medical Lifescience and Technology', I would like to thank Desislava Zlatanova and Dr. Katrin Offe.

Finally, I am eternally grateful for the ceaseless love and support of my family. The unconditional help and endorsement of my parents and my brother laid the foundation of my work and gave me the space to define myself over the years. My wife Leila backed me up with admirable selflessness throughout my entire academic career, from the early days in school to the end of my Ph.D. Without her, I would not be the person that I am today and I will never forget what she did for me. My son Karim, who was born at the beginning of my Ph.D., has been my bright spot and source of joy during the last three and a half years. He helped me to come down in difficult situations and to put my work and life into perspective. However, the reconciliation of my scientific work and private life would not have been feasible to this degree without the constant help of my mother-in-law Eika, who abandoned a part of her life to facilitate ours. This applies especially to the recent period, which culminated in the completion of this thesis and in the birth of my second son Robin. It is ultimately these people that give true meaning to my work and endeavor.

List of publications

First author publications

1. G. J. Tserevelakis*, **D. Soliman***, M. Omar and V. Ntziachristos, “Hybrid multiphoton and optoacoustic microscope,” *Optics Letters*, vol. 39, no. 7, pp. 1819–1822, 2014.
2. **D. Soliman***, G. J. Tserevelakis*, M. Omar and V. Ntziachristos, “Combining microscopy with mesoscopy using optical and optoacoustic label-free modes,” *Scientific Reports*, vol. 5, 2015.

In preparation

3. S. Kellnberger*, G. J. Tserevelakis*, **D. Soliman***, M. Seeger, H. Yang, A. Karlas, L. Prade, and V. Ntziachristos, “Amplitude and phase optoacoustic microscopy at multiple modulation frequencies”.
4. A. Lauri*, **D. Soliman***, M. Omar, A. Stelzl, V. Ntziachristos and G. G. Westmeyer, “Photoacoustic pigment relocalization sensor (PaPiReS)”.

Second author publications

5. M. Omar, **D. Soliman**, J. Gateau and V. Ntziachristos, “Ultrawideband reflection-mode optoacoustic mesoscopy,” *Optics Letters*, vol. 39, no. 13, pp. 3911–3914, 2014.
6. J. Aguirre, M. Schwarz, **D. Soliman**, A. Buehler, M. Omar and V. Ntziachristos, “Broadband mesoscopic optoacoustic tomography reveals skin layers,” *Optics Letters*, vol. 39, no. 21, pp. 6297–6300, 2014.
7. M. Omar, M. Schwarz, **D. Soliman**, P. Symvoulidis and V. Ntziachristos, “Pushing the optical imaging limits of cancer with multi-frequency-band raster-scan optoacoustic mesoscopy (RSOM),” *Neoplasia*, vol. 17, no. 2, pp. 208–214, 2015.
8. G. Wissmeyer, **D. Soliman**, R. Shnaiderman, A. Rosenthal and V. Ntziachristos, “All-optical optoacoustic microscope based on wideband pulse interferometry,” *Optics Letters*, vol. 41, no. 9, pp. 1953–1956, 2016.
9. M. Seeger, A. Karlas, **D. Soliman**, J. Pelisek and V. Ntziachristos, “Multimodal optoacoustic and multiphoton microscopy of human carotid atheroma,” *Photoacoustics*, vol. 4, no. 3, pp. 102–111, 2016.

* Equal contribution.

In preparation

10. M. Schwarz, **D. Soliman**, M. Omar, A. Buehler, J. Aguirre and V. Ntziachristos, "Optoacoustic dermoscopy of the human skin: Tuning excitation energy for optimal detection bandwidth with fast and deep imaging in vivo," *IEEE Transactions on Medical Imaging*, in print.
11. R. Shnaiderman, G. Wissmeyer, M. Seeger, **D. Soliman**, H. Estrada, D. Razanski, A. Rosenthal and V. Ntziachristos, "Intravital hybrid optical-optoacoustic microscopy based on fiber Bragg grating interferometry," submitted to *Optica*.

Conference proceedings

12. M. Omar, **D. Soliman** and V. Ntziachristos, "Retrieving small features in reflection-mode raster-scan optoacoustic mesoscopy (RSOM) using multi-frequency reconstruction," *Proc. SPIE 9323, Photons Plus Ultrasound: Imaging and Sensing 2015*, p. 932326, 2015.
13. **D. Soliman***, G. J. Tserevelakis*, M. Omar and V. Ntziachristos, "Hybrid label-free multiphoton and optoacoustic microscopy (MPOM)," *Proc. SPIE 9539, Opto-Acoustic Methods and Applications in Biophotonics II*, p. 953908, 2015.
14. M. Omar, **D. Soliman** and V. Ntziachristos, "High-resolution epi-illumination raster-scan optoacoustic mesoscopy for imaging of model organisms and microvessels," *Proc. SPIE 9539, Opto-Acoustic Methods and Applications in Biophotonics II*, p. 95390U, 2015.
15. **D. Soliman***, G. J. Tserevelakis*, M. Omar, V. Ntziachristos, "Combined label-free optical and optoacoustic imaging of model organisms at mesoscopy and microscopy resolutions," *SPIE 9708, Photons Plus Ultrasound: Imaging and Sensing 2016*, p. 9708105, 2016.
16. M. Omar, M. Schwarz, **D. Soliman**, P. Symvoulidis and V. Ntziachristos, "Imaging melanin cancer growth in vivo using raster scan optoacoustic mesoscopy (RSOM) at 50 MHz and 100 MHz," *SPIE 9708, Photons Plus Ultrasound: Imaging and Sensing 2016*, p. 970825, 2016.
17. M. Schwarz, J. Aguirre, **D. Soliman**, A. Buehler and V. Ntziachristos, "Unmixing chromophores in human skin with a 3D multispectral optoacoustic mesoscopy system," *SPIE 9708, Photons Plus Ultrasound: Imaging and Sensing 2016*, p. 9708155, 2016.

Book chapters

18. M. Omar, **D. Soliman** and V. Ntziachristos, "Multimodal optoacoustic imaging," in C. Kuntner, Y. Hämişch, *Image Fusion: I spy with my little eye, Volume 5: Image Fusion in pre-clinical Imaging*, submitted to *Springer*.

* Equal contribution.

Bibliography

- [1] G. Karp, *Molekulare Zellbiologie*. Springer, 2005.
- [2] D. Ganten and K. Ruckpaul, *Grundlagen der Molekularen Medizin*. Springer, 2008.
- [3] S. W. Paddock and K. W. Eliceiri, *Laser scanning confocal microscopy: history, applications, and related optical sectioning techniques*. Springer New York, 2014.
- [4] V. Ntziachristos, “Going deeper than microscopy: the optical imaging frontier in biology,” *Nature Methods*, vol. 7, no. 8, pp. 603–614, 2010.
- [5] P. J. Keller, “Imaging morphogenesis: technological advances and biological insights,” *Science*, vol. 340, no. 6137, p. 1234168, 2013.
- [6] W. R. Zipfel, R. M. Williams, and W. W. Webb, “Nonlinear magic: multiphoton microscopy in the biosciences.” *Nature Biotechnology*, vol. 21, no. 11, pp. 1369–1377, 2003.
- [7] X. Zhang and F. L. Kiechle, “Hoechst 33342 Alters Luciferase Gene Expression in Transfected BC3H-1 Myocytes,” *Archives of Pathology & Laboratory Medicine*, vol. 127, no. 9, pp. 1124–1132, 2003.
- [8] L. Greenbaum, C. Rothmann, R. Lavie, and Z. Malik, “Green fluorescent protein photobleaching: a model for protein damage by endogenous and exogenous singlet oxygen,” *Biological Chemistry*, vol. 381, no. 12, pp. 1251–1258, 2000.
- [9] T. Bernas, M. Zarebski, R. R. Cook, and J. W. Dobrucki, “Minimizing photobleaching during confocal microscopy of fluorescent probes bound to chromatin: role of anoxia and photon flux,” *Journal of Microscopy*, vol. 215, no. 3, pp. 281–296, 2004.
- [10] J. Yao and L. V. Wang, “Photoacoustic microscopy,” *Laser and Photonics Reviews*, vol. 7, no. 5, pp. 758–778, 2013.
- [11] M. Omar, J. Gateau, and V. Ntziachristos, “Raster-scan optoacoustic mesoscopy in the 25-125 MHz range,” *Optics Letters*, vol. 38, no. 14, pp. 2472–2474, 2013.
- [12] L. V. Wang and H.-I. Wu, *Biomedical Optics: Principles and Imaging*. John Wiley & Sons, 2007.
- [13] P. Beard, “Biomedical photoacoustic imaging,” *Interface Focus*, vol. 1, no. 4, pp. 602–631, 2011.
- [14] S. Kellnberger, “Thermoacoustic Imaging in time and frequency domain. Theory and experiments,” Ph.D. dissertation, Technical University of Munich, 2012.
- [15] K. Maslov and L. V. Wang, “Photoacoustic imaging of biological tissue with intensity-modulated continuous-wave laser,” *Journal of Biomedical Optics*, vol. 13, no. 2, p. 024006, 2008.
- [16] X. Liu, R. Wen, Y. Li, and S. Jiao, “Optical coherence photoacoustic microscopy (OC-PAM) with an intensity-modulated continuous-wave broadband light source,” *Journal of Optics*, vol. 18, no. 6, p. 064001, 2016.

- [17] D. J. Segelstein, "The complex refractive index of water," Master's thesis, University of Missouri - Kansas City, 1981.
- [18] W. Demtröder, *Experimentalphysik 3: Atome, Moleküle und Festkörper*. Springer, 2010.
- [19] R. Gross and A. Marx, *Festkörperphysik*. Walter de Gruyter GmbH & Co KG, 2014.
- [20] G. Wedler, *Lehrbuch der physikalischen Chemie*. WILEY-VCH Verlag GmbH, 2004.
- [21] W. Demtröder, *Experimentalphysik 2: Elektrizität und Optik*. Springer, 2006.
- [22] S. L. Jacques, "Melanosome absorption coefficient," <http://omlc.org/spectra/melanin/mua.html>, accessed July 21 2016.
- [23] S. A. Prahl, "Tabulated Molar Extinction Coefficient for Hemoglobin in Water," <http://omlc.org/spectra/hemoglobin/summary.html>, accessed July 21 2016.
- [24] S. A. Prahl, "Optical Absorption of Fat," <http://omlc.org/spectra/fat>, accessed July 21 2016.
- [25] J. Yao and L. V. Wang, "Sensitivity of photoacoustic microscopy," *Photoacoustics*, vol. 2, no. 2, pp. 87–101, 2014.
- [26] A. Chmyrov, "Photo-induced dark states in fluorescence spectroscopy - investigations & applications," Ph.D. dissertation, KTH Royal Institute of Technology, Stockholm, 2010.
- [27] P. Meredith and J. Riesz, "Radiative relaxation quantum yields for synthetic eumelanin," *Photochemistry and Photobiology*, vol. 79, no. 2, pp. 211–216, 2004.
- [28] D. M. Jameson, *Introduction to fluorescence*. Taylor & Francis, 2014.
- [29] B. R. Masters and P. So, *Handbook of biomedical nonlinear optical microscopy*. Oxford University Press on Demand, 2008.
- [30] J. Mertz, *Introduction to optical microscopy*. Roberts, 2010.
- [31] S. L. Jacques, "Optical properties of biological tissues: a review," *Physics in Medicine and Biology*, vol. 58, no. 11, pp. R37–61, 2013.
- [32] H. J. Eichler and J. Eichler, *Laser: Bauformen, Strahlführung, Anwendungen*. Springer, 2010.
- [33] M. Muller, *Introduction to confocal fluorescence microscopy*. SPIE press, 2006.
- [34] M. A. Ortega Delgado and A. F. Lasagni, "Reducing field distortion for galvanometer scanning system using a vision system," *Optics and Lasers in Engineering*, vol. 86, pp. 106–114, 2016.
- [35] M. W. Davidson, "Introduction to Microscope Objectives," <http://www.microscopyu.com/articles/optics/objectiveintro.html>, accessed July 25 2016.
- [36] V. Ntziachristos, A. Leroy-Willig, and B. Tavittian, *Textbook of in vivo Imaging in Vertebrates*, 2007.
- [37] J. W. Lichtman and J.-A. Conchello, "Fluorescence microscopy," *Nature Methods*, vol. 2, no. 12, pp. 910–919, 2005.
- [38] J.-A. Conchello and J. W. Lichtman, "Optical sectioning microscopy," *Nature Methods*, vol. 2, no. 12, pp. 920–931, 2005.

- [39] M. Monici, "Cell and tissue autofluorescence research and diagnostic applications," *Biotechnology Annual Review*, vol. 11, pp. 227–256, 2005.
- [40] M. W. Davidson, "Numerical Aperture and Resolution," <https://micro.magnet.fsu.edu/primer/anatomy/numaperture.html>, accessed July 27 2016.
- [41] W. R. Leo, *Techniques for Nuclear and Particle Physics Experiments: A How-To Approach*. Springer Science & Business Media, 1994.
- [42] M. W. Davidson, "Photobleaching," <http://micro.magnet.fsu.edu/primer/java/fluorescence/photobleaching>, accessed July 31 2016.
- [43] G. J. Tserevelakis, "Nonlinear optical procedures for the diagnostics and processing of biological samples by using ultra-short laser pulses," Ph.D. dissertation, University of Crete, Heraklion, 2013.
- [44] F. Helmchen and W. Denk, "Deep tissue two-photon microscopy," *Nature Methods*, vol. 2, no. 12, pp. 932–940, 2005.
- [45] M. Weber, M. Mickoleit, and J. Huisken, "Light sheet microscopy," *Methods in Cell Biology*, vol. 123, pp. 193–215, 2014.
- [46] D. K. Toomre, M. F. Langhorst, and M. W. Davidson, "Introduction to Spinning Disk Confocal Microscopy," <http://zeiss-campus.magnet.fsu.edu/articles/spinningdisk/introduction.html>, accessed July 30 2016.
- [47] S. Ruzin and H. Aaron, "1P vs 2P fluorescence imaging," <http://microscopy.berkeley.edu/courses/TLM/2P/index.html>, accessed July 31 2016.
- [48] M. Sheik-Bahae and M. P. Hasselbeck, "Third Order Optical Nonlinearities," in *OSA Handbook of Optics IV*, 2000.
- [49] F. J. Ávila, O. del Barco, and J. M. Bueno, "Polarization dependence of aligned collagen tissues imaged with second harmonic generation microscopy," *Journal of Biomedical Optics*, vol. 20, no. 8, p. 086001, 2015.
- [50] G. J. Tserevelakis, E. V. Megalou, G. Filippidis, B. Petanidou, C. Fotakis, and N. Tavernarakis, "Label-free imaging of lipid depositions in *C. elegans* using third-harmonic generation microscopy," *PLoS ONE*, vol. 9, no. 1, 2014.
- [51] Y. Barad, H. Eisenberg, M. Horowitz, and Y. Silberberg, "Nonlinear scanning laser microscopy by third harmonic generation," *Applied Physics Letters*, vol. 70, no. 8, pp. 922–924, 1997.
- [52] G. J. Tserevelakis, S. Psycharakis, B. Resan, F. Brunner, E. Gavgiotaki, K. Weingarten, and G. Filippidis, "Femtosecond laser nanosurgery of sub-cellular structures in HeLa cells by employing Third Harmonic Generation imaging modality as diagnostic tool," *Journal of Biophotonics*, vol. 5, no. 2, pp. 200–207, 2012.
- [53] K. N. Anisha Thayil, E. J. Gualda, S. Psilodimitrakopoulos, I. G. Cormack, I. Amat-Roldán, M. Mathew, D. Artigas, and P. Loza-Alvarez, "Starch-based backwards SHG for in situ MEFISTO pulse characterization in multiphoton microscopy," *Journal of Microscopy*, vol. 230, no. 1, pp. 70–75, 2008.
- [54] J. Huisken and D. Y. R. Stainier, "Selective plane illumination microscopy techniques in developmental biology." *Development*, vol. 136, no. 12, pp. 1963–1975, 2009.
- [55] J. Sharpe, "Optical projection tomography as a new tool for studying embryo anatomy," *Journal of Anatomy*, vol. 202, no. 2, pp. 175–181, 2003.

- [56] V. Ntziachristos, J. Ripoll, L. V. Wang, and R. Weissleder, “Looking and listening to light: the evolution of whole-body photonic imaging,” *Nature Biotechnology*, vol. 23, no. 3, pp. 313–320, 2005.
- [57] C. Vinegoni, C. Pitsouli, D. Razansky, N. Perrimon, and V. Ntziachristos, “In vivo imaging of *Drosophila melanogaster* pupae with mesoscopic fluorescence tomography.” *Nature Methods*, vol. 5, no. 1, pp. 45–47, 2008.
- [58] M. Omar, D. Soliman, J. Gateau, and V. Ntziachristos, “Ultrawideband reflection-mode optoacoustic mesoscopy.” *Optics Letters*, vol. 39, no. 13, pp. 3911–4, 2014.
- [59] M. A. Omar, “Multi-scale thermoacoustic imaging methods of biological tissues,” Ph.D. dissertation, Technical University of Munich, 2015.
- [60] A. A. Oraevsky, S. L. Jacques, and F. K. Tittel, “Determination of tissue optical properties by piezoelectric detection of laser-induced stress waves,” in *Proc. SPIE 1882, OE/LASE’93: Optics, Electro-Optics, & Laser Applications in Science & Engineering. International Society for Optics and Photonics*, 1993, pp. 86–101.
- [61] A. A. Oraevsky, R. Esenaliev, S. L. Jacques, S. Thomsen, and F. K. Tittel, “Lateral and z-axial resolution in laser optoacoustic imaging with ultrasonic transducers,” in *Proc. SPIE 2389, Photonics West’95. International Society for Optics and Photonics*, 1995, pp. 198–208.
- [62] R. A. Kruger, P. Liu, Y. Fang, and R. C. Appledorn, “Photoacoustic ultrasound (PAUS)–reconstruction tomography,” *Medical Physics*, vol. 22, no. 10, pp. 1605–1609, 1995.
- [63] C. Lutzweiler and D. Razansky, “Optoacoustic imaging and tomography: Reconstruction approaches and outstanding challenges in image performance and quantification,” *Sensors*, vol. 13, no. 6, pp. 7345–7384, 2013.
- [64] J. J. S. Salichs, “Analysis of optoacoustic efficiency and study of heterogeneous solid tumors with mesoscopic multispectral optoacoustic tomography,” Ph.D. dissertation, Technical University of Munich, 2014.
- [65] L. V. Wang and S. Hu, “Photoacoustic Tomography: In Vivo Imaging from Organelles to Organs,” *Science*, vol. 335, no. 6075, pp. 1458–1462, 2012.
- [66] D. Razansky, C. Vinegoni, and V. Ntziachristos, “Imaging of mesoscopic-scale organisms using selective-plane optoacoustic tomography,” *Physics in Medicine and Biology*, vol. 54, no. 9, pp. 2769–2777, 2009.
- [67] A. Chekkoury, J. Gateau, W. Driessen, P. Symvoulidis, N. Bézière, A. Feuchtinger, A. Walch, and V. Ntziachristos, “Optical mesoscopy without the scatter: broadband multispectral optoacoustic mesoscopy,” *Biomedical Optics Express*, vol. 6, no. 9, pp. 3134–3148, 2015.
- [68] H. F. Zhang, K. Maslov, G. Stoica, and L. V. Wang, “Functional photoacoustic microscopy for high-resolution and noninvasive in vivo imaging.” *Nature Biotechnology*, vol. 24, no. 7, pp. 848–851, 2006.
- [69] M. Omar, M. Schwarz, D. Soliman, P. Symvoulidis, and V. Ntziachristos, “Pushing the Optical Imaging Limits of Cancer with Multi-Frequency-Band Raster-Scan Optoacoustic Mesoscopy (RSOM),” *Neoplasia*, vol. 17, no. 2, pp. 208–214, 2015.
- [70] L. V. Wang, “Tutorial on photoacoustic microscopy and computed tomography,” *IEEE Journal on Selected Topics in Quantum Electronics*, vol. 14, no. 1, pp. 171–179, 2008.

- [71] C. Li and L. V. Wang, "Photoacoustic tomography and sensing in biomedicine," *Physics in Medicine and Biology*, vol. 54, no. 19, pp. R59–R97, 2009.
- [72] M. Xu and L. V. Wang, "Photoacoustic imaging in biomedicine," *Review of Scientific Instruments*, vol. 77, no. 4, pp. 1–22, 2006.
- [73] A. B. Bühler, "Multi-Spectral Optoacoustic Tomography: Methods and Applications," Ph.D. dissertation, Technical University of Munich, 2014.
- [74] M. A. Áraque Caballero, "Incorporating Sensor Properties in Optoacoustic Imaging," Ph.D. dissertation, Technical University of Munich, 2012.
- [75] D. Querios, "Image Reconstruction in Optoacoustics," Ph.D. dissertation, Technical University of Munich, 2014.
- [76] J. Laufer, A. Jathoul, M. Pule, and P. Beard, "In vitro characterization of genetically expressed absorbing proteins using photoacoustic spectroscopy," *Biomedical Optics Express*, vol. 4, no. 11, pp. 2477–90, 2013.
- [77] D. K. Yao, C. Zhang, K. Maslov, and L. V. Wang, "Multiphoton fluorescence microscopy of the live kidney in health and disease Multiphoton fluorescence microscopy of the live kidney in health and disease," *Journal of Biomedical Optics*, vol. 19, no. 1, p. 017007, 2014.
- [78] E. Bossy and S. Gigan, "Photoacoustics with coherent light," *Photoacoustics*, vol. 4, no. 1, pp. 22–35, 2016.
- [79] L. I. Grossweiner, J. B. Grossweiner, and B. G. Rogers, *The science of phototherapy: an introduction*, L. R. Jones, Ed. Dordrecht: Springer, 2005.
- [80] I. N. Bronstein, K. A. Semendjajew, G. Musiol, and H. Mühlig, *Taschenbuch der Mathematik*. Verlag Harry Deutsch, 2006.
- [81] J. D. Jackson, *Classical electrodynamics*. Wiley, 1999.
- [82] A. a. Oraevsky and A. a. Karabutov, "Ultimate Sensitivity of Time-Resolved Opto-Acoustic Detection," in *Proc. SPIE 3916, BiOS 2000 The International Symposium on Biomedical Optics*, 2000, pp. 228–239.
- [83] M. I. Khan and G. J. Diebold, "The photoacoustic effect generated by an isotropic solid sphere," *Ultrasonics*, vol. 33, no. 4, pp. 265–269, 1995.
- [84] M. I. Khan and G. J. Diebold, "The photoacoustic effect generated by laser irradiation of an isotropic solid cylinder," *Ultrasonics*, vol. 34, no. 1, pp. 19–24, 1996.
- [85] B. Treeby and B. Cox, "Fast, tissue-realistic models of photoacoustic wave propagation for homogeneous attenuating media," in *Proc. of SPIE, Photons Plus Ultrasound: Imaging and Sensing*, vol. 7177, 2009, pp. 1–10.
- [86] X. L. Deán-Ben, D. Razansky, and V. Ntziachristos, "The effects of acoustic attenuation in optoacoustic signals," *Physics in Medicine and Biology*, vol. 56, no. 18, pp. 6129–6148, 2011.
- [87] T. L. Szabo, *Diagnostic ultrasound imaging: inside out*. Academic Press, 2004.
- [88] R. S. Cobbold, *Foundations of biomedical ultrasound*. Oxford University Press, 2006.
- [89] J. M. Cannata, T. A. Ritter, W.-H. Chen, and K. K. Shung, "Design of focused single element (50-100 MHz) transducers using lithium niobate," *Ultrasonics Symposium, 2000 IEEE*, vol. 2, pp. 1129–1133, 2000.

- [90] J. A. Jensen and N. B. Svendsen, "Calculation of Pressure Fields from Arbitrarily," *IEEE Transactions on Ultrasonics, Ferroelectrics, and Frequency Control*, vol. 39, no. 2, pp. 262–267, 1992.
- [91] J. A. Jensen, "Field: A Program for Simulating Ultrasound Systems," in *10th Nordic-Baltic Conference on Biomedical Imaging*, vol. 4, 1996, pp. 351–353.
- [92] C. Zhang, "Submicron-resolution Photoacoustic Microscopy of Endogenous Light-absorbing Biomolecules," Ph.D. dissertation, Washington University in St. Louis, 2014.
- [93] A. Rosenthal, V. Ntziachristos, and D. Razansky, "Acoustic Inversion in Optoacoustic Tomography: A Review," *Current Medical Imaging Reviews*, vol. 9, pp. 318–336, 2013.
- [94] A. Rosenthal, V. Ntziachristos, and D. Razansky, "Model-based optoacoustic inversion with arbitrary-shape detectors," *Medical Physics*, vol. 38, no. 7, pp. 4285–4295, 2011.
- [95] M. Xu and L. V. Wang, "Universal back-projection algorithm for photoacoustic computed tomography," *Physical Review E - Statistical, Nonlinear, and Soft Matter Physics*, vol. 71, no. 1, pp. 1–7, 2005.
- [96] C. G. Hoelen and F. F. de Mul, "Image reconstruction for photoacoustic scanning of tissue structures," *Applied Optics*, vol. 39, no. 31, pp. 5872–5883, 2000.
- [97] C. K. Liao, M. L. Li, and P. C. Li, "Optoacoustic imaging with synthetic aperture focusing and coherence weighting," *Optics Letters*, vol. 29, no. 21, pp. 2506–2508, 2004.
- [98] M.-L. Li, H. E. Zhang, K. Maslov, G. Stoica, and L. V. Wang, "Improved in vivo photoacoustic microscopy based on a virtual-detector concept," *Optics Letters*, vol. 31, no. 4, pp. 474–476, 2006.
- [99] J. Schindelin, I. Arganda-Carreras, E. Frise, V. Kaynig, M. Longair, T. Pietzsch, S. Preibisch, C. Rueden, S. Saalfeld, B. Schmid, J.-Y. Tinevez, D. J. White, V. Hartenstein, K. Eliceiri, P. Tomancak, and A. Cardona, "Fiji: an open-source platform for biological-image analysis," *Nature Methods*, vol. 9, no. 7, pp. 676–682, 2012.
- [100] M. Omar, D. Soliman, J. Gateau, and V. Ntziachristos, "Retrieving small features in reflection-mode raster-scan optoacoustic mesoscopy (RSOM) using multi-frequency reconstruction," in *Proc. SPIE 9323, Photons Plus Ultrasound: Imaging and Sensing 2015*, 2015, p. 932326.
- [101] M. Omar, M. Schwarz, D. Soliman, P. Symvoulidis, and V. Ntziachristos, "Imaging melanin cancer growth in-vivo using raster-scan optoacoustic mesoscopy (RSOM) at 50 MHz and 100 MHz," in *Proc. SPIE 9708, Photons Plus Ultrasound: Imaging and Sensing 2016*, 2016, p. 97080S.
- [102] A. F. Frangi, W. J. Niessen, K. L. Vincken, and M. A. Viergever, "Multiscale vessel enhancement filtering," in *International Conference on Medical Image Computing and Computer-Assisted Intervention*, vol. 1496. Berlin: Springer, 1998, pp. 130–137.
- [103] J. Turner, H. Estrada, M. Kneipp, and D. Razansky, "Improved optoacoustic microscopy through three-dimensional spatial impulse response synthetic aperture focusing technique," *Optics Letters*, vol. 39, no. 12, pp. 3390–3393, 2014.

- [104] A. Lauri, D. Soliman, M. Omar, A. Stelzl, V. Ntziachristos, and G. G. Westmeyer, "Photoacoustic pigment relocalization sensor (PaPiReS)," *in preparation*.
- [105] J. Staley, P. Grogan, A. K. Samadi, H. Cui, M. S. Cohen, and X. Yang, "Growth of melanoma brain tumors monitored by photoacoustic microscopy," *Journal of Biomedical Optics*, vol. 15, no. 4, p. 040510, 2010.
- [106] A. Krumholz, S. J. Vanvickle-Chavez, J. Yao, T. P. Fleming, W. E. Gillanders, and L. V. Wang, "Photoacoustic microscopy of tyrosinase reporter gene in vivo," *Journal of Biomedical Optics*, vol. 16, no. 8, p. 080503, 2011.
- [107] C. Qin, K. Cheng, K. Chen, X. Hu, Y. Liu, X. Lan, Y. Zhang, H. Liu, Y. Xu, L. Bu, X. Su, X. Zhu, S. Meng, and Z. Cheng, "Tyrosinase as a multifunctional reporter gene for Photoacoustic/MRI/PET triple modality molecular imaging," *Scientific Reports*, vol. 3, p. 1490, 2013.
- [108] A. P. Jathoul, J. Laufer, O. Ogunlade, B. Treeby, B. Cox, E. Zhang, P. Johnson, A. R. Pizzey, B. Philip, T. Marafioti, M. F. Lythgoe, R. B. Pedley, M. a. Pule, and P. Beard, "Deep in vivo photoacoustic imaging of mammalian tissues using a tyrosinase-based genetic reporter," *Nature Photonics*, 2015.
- [109] M. Kneipp, H. Estrada, A. Lauri, J. Turner, V. Ntziachristos, G. G. Westmeyer, and D. Razansky, "Volumetric tracking of migratory melanophores during zebrafish development by optoacoustic microscopy," *Mechanisms of Development*, vol. 138, pp. 300–304, 2015.
- [110] K. W. Jeon, M. Friedlander, J. Jarvik, and R. Fujii, "Cytophysiology of Fish Chromatophores," *International Review of Cytology*, vol. 143, pp. 191–255, 1993.
- [111] D. W. Logan, S. F. Burn, and I. J. Jackson, "Regulation of pigmentation in zebrafish melanophores," *Pigment Cell Research*, vol. 19, no. 3, pp. 206–213, 2006.
- [112] M. Levesque, Y. Feng, R. Jones, and P. Martin, "Inflammation drives wound hyperpigmentation by recruiting pigment cells to sites of tissue damage," *Disease Models & Mechanisms*, vol. 6, pp. 508–515, 2013.
- [113] A. M. Taylor and L. I. Zon, "Zebrafish tumor assays: the state of transplantation," *Zebrafish*, vol. 6, no. 4, pp. 339–346, 2009.
- [114] T. Yamashita, T. Kuwahara, S. González, and M. Takahashi, "Non-invasive visualization of melanin and melanocytes by reflectance-mode confocal microscopy," *Journal of Investigative Dermatology*, vol. 124, no. 1, pp. 235–240, 2005.
- [115] R. C. Tryon and S. L. Johnson, "Clonal and lineage analysis of melanocyte stem cells and their progeny in the zebrafish," *Progenitor Cells: Methods and Protocols*, vol. 916, pp. 181–195, 2012.
- [116] L. E. Nery and a. M. Castrucci, "Pigment cell signalling for physiological color change," *Comparative Biochemistry and Physiology Part A: Physiology*, vol. 118, no. 4, pp. 1135–1144, 1997.
- [117] M. T. Teh and D. Sugden, "An endogenous 5-HT(7) receptor mediates pigment granule dispersion in *Xenopus laevis* melanophores," *British Journal of Pharmacology*, vol. 132, no. 8, pp. 1799–808, 2001.
- [118] A. R. Reilein, I. S. Tint, N. I. Peunova, G. N. Enikolopov, and V. I. Gelfand, "Regulation of organelle movement in melanophores by protein kinase A (PKA), protein kinase C (PKC), and protein phosphatase 2A (PP2A)," *Journal of Cell Biology*, vol. 142, no. 3, pp. 803–813, 1998.

- [119] S. Salim and S. a. Ali, *Melanophores: Smooth muscle cells in disguise*. INTECH Open Access Publisher, 2012.
- [120] H. Vaudry, N. Chartrel, L. Desrues, L. Galas, S. Kikuyama, A. Mor, P. Nicolas, and M. C. Tonon, "The pituitary-skin connection in amphibians. Reciprocal regulation of melanotrope cells and dermal melanocytes," *Annals of the New York Academy of Sciences*, vol. 885, no. 1, pp. 41–56, 1999.
- [121] D. Dulcis and N. C. Spitzer, "Illumination controls differentiation of dopamine neurons regulating behaviour," *Nature*, vol. 456, no. 7219, pp. 195–201, 2008.
- [122] C. Nusslein-Volhard and R. Dahm, *Zebrafish*. Oxford University Press, 2002.
- [123] D. Sudgen and S. J. Rowe, "Protein kinase C activation antagonizes melatonin-induced pigment aggregation in *Xenopus laevis* melanophores," *The Journal of Cell Biology*, vol. 119, no. 6, pp. 1515–1521, 1992.
- [124] R. M. White, A. Sessa, C. Burke, T. Bowman, J. LeBlanc, C. Ceol, C. Bourque, M. Dovey, W. Goessling, C. E. Burns, and L. I. Zon, "Transparent Adult Zebrafish as a Tool for In Vivo Transplantation Analysis," *Cell Stem Cell*, vol. 2, no. 2, pp. 183–189, 2008.
- [125] M. Omar, J. Rebling, K. Wicker, T. Schmitt-Manderbach, M. Schwarz, J. Gateau, H. Lopez-Schier, T. Mappes, and V. Ntziachristos, "Optical imaging of post-embryonic zebrafish using multi orientation raster scan optoacoustic mesoscopy," *Light: Science & Applications*, vol. 6, no. e16186, 2017.
- [126] A. Muller, V. Joseph, P. a. Slesinger, and D. Kleinfeld, "Cell-based reporters reveal in vivo dynamics of dopamine and norepinephrine release in murine cortex," *Nature Methods*, vol. 11, no. 12, pp. 1245–52, 2014.
- [127] S. Rogan and B. Roth, "Remote control of neuronal signaling," *Pharmacological Reviews*, vol. 63, no. 2, pp. 291–315, 2011.
- [128] G. J. Tserevelakis, D. Soliman, M. Omar, and V. Ntziachristos, "Hybrid multiphoton and optoacoustic microscope." *Optics Letters*, vol. 39, no. 7, pp. 1819–22, 2014.
- [129] D. Soliman, G. J. Tserevelakis, M. Omar, and V. Ntziachristos, "Hybrid label-free multiphoton and optoacoustic microscopy (MPOM)," in *Proc. SPIE 9539, Opto-Acoustic Methods and Applications in Biophotonics II*, 2015, p. 953908.
- [130] J. Weber, P. C. Beard, and S. E. Bohndiek, "Contrast agents for molecular photoacoustic imaging," *Nature Methods*, vol. 13, no. 8, pp. 639–650, 2016.
- [131] D.-K. Yao, K. Maslov, K. K. Shung, Q. Zhou, and L. V. Wang, "In vivo label-free photoacoustic microscopy of cell nuclei by excitation of DNA and RNA," *Optics Letters*, vol. 35, no. 24, pp. 4139–4141, 2010.
- [132] H. W. Wang, N. Chai, P. Wang, S. Hu, W. Dou, D. Umulis, L. V. Wang, M. Sturek, R. Lucht, and J. X. Cheng, "Label-free bond-selective imaging by listening to vibrationally excited molecules," *Physical Review Letters*, vol. 106, no. 23, pp. 1–4, 2011.
- [133] E. M. Strohm, M. J. Moore, and M. C. Kolios, "Single Cell Photoacoustic Microscopy: A Review," *IEEE Journal of Selected Topics in Quantum Electronics*, vol. 22, no. 3, pp. 1–15, 2016.
- [134] G. Ku, K. Maslov, L. Li, and L. V. Wang, "Photoacoustic microscopy with 2-microm transverse resolution." *Journal of Biomedical Optics*, vol. 15, no. 2, p. 021302, 2010.

- [135] S. Ye, R. Yang, J. Xiong, K. K. Shung, Q. Zhou, C. Li, and Q. Ren, "In vivo imaging of small animal models by PAM," in *Proc. of SPIE, Photons Plus Ultrasound: Imaging and Sensing*, vol. 8223, 2012, pp. 82 230X–82 230X–5.
- [136] J. Yao, L. Wang, J.-m. Yang, K. I. Maslov, T. T. W. Wong, L. Li, C.-h. Huang, J. Zou, and L. V. Wang, "High-speed label-free fPAM of mouse brain in action," *Nature Methods*, vol. 12, no. 5, pp. 407–410, 2015.
- [137] S. Hu, B. Rao, K. Maslov, and L. V. Wang, "Label-free photoacoustic ophthalmic angiography," *Optics Letters*, vol. 35, no. 1, pp. 1–3, 2010.
- [138] H. Li, B. Dong, Z. Zhang, H. F. Zhang, and C. Sun, "A transparent broadband ultrasonic detector based on an optical micro-ring resonator for photoacoustic microscopy." *Scientific Reports*, vol. 4, p. 4496, 2014.
- [139] D. Soliman, G. J. Tserevelakis, M. Omar, and V. Ntziachristos, "Combining microscopy with mesoscopy using optical and optoacoustic label-free modes," *Scientific Reports*, vol. 5, 2015.
- [140] J. C. Whitaker, *The electronics handbook*. Crc Press, 1996.
- [141] K. Wang, S. A. Ermilov, R. Su, H.-P. Brecht, A. A. Oraevsky, and M. A. Anastasio, "Imaging Model Incorporating Ultrasonic Transducer Properties," *IEEE Transactions on Medical Imaging*, vol. 30, no. 2, pp. 203–214, 2011.
- [142] A. Rosenthal, V. Ntziachristos, and D. Razansky, "Optoacoustic methods for frequency calibration of ultrasonic sensors," *IEEE Transactions on Ultrasonics, Ferroelectrics, and Frequency Control*, vol. 58, no. 2, pp. 316–326, 2011.
- [143] M. A. A. Caballero, A. Rosenthal, A. Buehler, D. Razansky, and V. Ntziachristos, "Optoacoustic determination of spatio-temporal responses of ultrasound sensors," *IEEE Transactions on Ultrasonics, Ferroelectrics, and Frequency Control*, vol. 60, no. 6, pp. 1234–1244, 2013.
- [144] E. M. Strohm, E. S. Berndl, and M. C. Kolios, "High frequency label-free photoacoustic microscopy of single cells," *Photoacoustics*, vol. 1, no. 3-4, pp. 49–53, 2013.
- [145] M. N. Polyanskiy, "Refractive index database," <http://refractiveindex.info>, accessed May 07 2016.
- [146] J. H. Barker, D. Kjolseth, M. Kim, J. Frank, I. Bondar, E. Uhl, M. Kamler, K. Messmer, G. R. Tobin, and L. J. Weiner, "The hairless mouse ear: an in vivo model for studying wound neovascularization," *Wound Repair and Regeneration*, vol. 2, no. 2, pp. 138–143, 1994.
- [147] P. Avci, M. Sadasivam, A. Gupta, W. De Melo, Y.-Y. Huang, R. Yin, R. Chandran, R. Kumar, A. Otufowora, T. Nyame, and M. R. Hamblin, "Animal models of skin disease for drug discovery," *Expert Opinion on Drug Discovery*, vol. 8, no. 3, pp. 331–355, 2013.
- [148] R. C. Gonzales, R. E. Woods, and S. L. Eddins, *Digital image processing using MATLAB*. Pearson Prentice Hall, 2004.
- [149] G. Wissmeyer, D. Soliman, R. Shnaiderman, A. Rosenthal, and V. Ntziachristos, "All-optical optoacoustic microscope based on wideband pulse interferometry," *Optics Letters*, vol. 41, no. 9, pp. 1953–1956, 2016.

- [150] E. Zhang, J. Laufer, and P. Beard, "Backward-mode multiwavelength photoacoustic scanner using a planar Fabry-Perot polymer film ultrasound sensor for high-resolution three-dimensional imaging of biological tissues." *Applied Optics*, vol. 47, no. 4, pp. 561–77, 2008.
- [151] C. M. Chow, Y. Zhou, Y. Guo, T. B. Norris, X. Wang, C. X. Deng, and J. Y. Ye, "Broadband optical ultrasound sensor with a unique open-cavity structure." *Journal of Biomedical Optics*, vol. 16, no. 1, p. 017001, 2011.
- [152] S. L. Chen, Z. Xie, L. J. Guo, and X. Wang, "A fiber-optic system for dual-modality photoacoustic microscopy and confocal fluorescence microscopy using miniature components," *Photoacoustics*, vol. 1, no. 2, pp. 30–35, 2013.
- [153] A. Rosenthal, S. Kellnberger, D. Bozhko, A. Chekkoury, M. Omar, D. Razansky, and V. Ntziachristos, "Sensitive interferometric detection of ultrasound for minimally invasive clinical imaging applications," *Laser and Photonics Reviews*, vol. 8, no. 3, pp. 450–457, 2014.
- [154] W. Song, W. Zheng, R. Liu, R. Lin, H. Huang, X. Gong, S. Yang, R. Zhang, and L. Song, "Reflection-mode in vivo photoacoustic microscopy with subwavelength lateral resolution," *Biomedical Optics Express*, vol. 5, no. 12, pp. 4235–4241, 2014.
- [155] A. Rosenthal, D. Razansky, and V. Ntziachristos, "High-sensitivity compact ultrasonic detector based on a pi-phase-shifted fiber Bragg grating." *Optics Letters*, vol. 36, no. 10, pp. 1833–1835, 2011.
- [156] S. Hu, K. Maslov, and L. V. Wang, "Second-generation optical-resolution photoacoustic microscopy with improved sensitivity and speed." *Optics Letters*, vol. 36, no. 7, pp. 1134–1136, 2011.
- [157] H. Estrada, E. Sobol, O. Baum, and D. Razansky, "Hybrid optoacoustic and ultrasound biomicroscopy monitors' laser-induced tissue modifications and magnetite nanoparticle impregnation," *Laser Physics Letters*, vol. 11, no. 12, p. 125601, 2014.
- [158] H. Wang, X. Yang, Y. Liu, B. Jiang, and Q. Luo, "Reflection-mode optical-resolution photoacoustic microscopy based on a reflective objective," *Optics Express*, vol. 21, no. 20, pp. 659–661, 2013.
- [159] A. Rosenthal, M. A. A. Caballero, S. Kellnberger, D. Razansky, and V. Ntziachristos, "Spatial characterization of the response of a silica optical fiber to wideband ultrasound," *Optics Letters*, vol. 37, no. 15, pp. 3174–3176, 2012.
- [160] G. Wild and S. Hinckley, "Acousto-Ultrasonic Optical Fiber Sensors : Overview and State-of-the-Art Acousto-Ultrasonic Optical Fiber Sensors : Overview and State-of-the-Art," vol. 8, no. 2008, pp. 1184–1193, 2011.
- [161] A. Rosenthal, D. Razansky, and V. Ntziachristos, "Wideband optical sensing using pulse interferometry," *Optics Express*, vol. 20, no. 17, pp. 19 016–19 029, 2012.
- [162] A. Rosenthal, S. Kellnberger, G. Sergiadis, and V. Ntziachristos, "Wideband fiber-interferometer stabilization with variable phase," *IEEE Photonics Technology Letters*, vol. 24, no. 17, pp. 1499–1501, 2012.
- [163] D. Soliman, G. J. Tservelakis, M. Omar, and V. Ntziachristos, "Combined label-free optical and optoacoustic imaging of model organisms at mesoscopy and microscopy resolutions," in *Proc. SPIE 9708, Photons Plus Ultrasound: Imaging and Sensing 2016*, 2016, p. 97083B.

- [164] S. Jiao, Z. Xie, H. F. Zhang, and C. a. Puliafito, “Simultaneous multimodal imaging with integrated photoacoustic microscopy and optical coherence tomography.” *Optics Letters*, vol. 34, no. 19, pp. 2961–2963, 2009.
- [165] Y. Wang, K. Maslov, C. Kim, S. Hu, and L. V. Wang, “Integrated photoacoustic and fluorescence confocal microscopy,” *IEEE Transactions on Biomedical Engineering*, vol. 57, no. 10, pp. 2576–2578, 2010.
- [166] B. Rao, F. Soto, D. Kerschensteiner, and L. V. Wang, “Integrated photoacoustic, confocal, and two-photon microscope,” *Journal of Biomedical Optics*, vol. 19, no. 3, p. 036002, 2014.
- [167] W. Song, Q. Xu, Y. Zhang, Y. Zhan, W. Zheng, and L. Song, “Fully integrated reflection-mode photoacoustic, two-photon, and second harmonic generation microscopy in vivo,” *Scientific Reports*, vol. 6, 2016.
- [168] A. Sheinfeld, W. J. Eldridge, and A. Wax, “Quantitative phase imaging with molecular sensitivity using photoacoustic microscopy with a miniature ring transducer,” *Journal of Biomedical Optics*, vol. 20, no. 8, p. 086002, 2015.
- [169] D. Razansky, M. Distel, C. Vinegoni, R. Ma, N. Perrimon, R. W. Köster, and V. Ntziachristos, “Multispectral opto-acoustic tomography of deep-seated fluorescent proteins in vivo,” *Nature Photonics*, vol. 3, no. 7, pp. 412–417, 2009.
- [170] H. F. Zhang, Z. Xie, S. Jiao, and C. a. Puliafito, “Laser-scanning optical-resolution photoacoustic microscopy,” in *Proc. SPIE 7177, Photons Plus Ultrasound: Imaging and Sensing 2009*, no. 414, 2009, p. 71770L.
- [171] L. Wang, K. Maslov, J. Yao, B. Rao, and L. V. Wang, “Fast voice-coil scanning optical-resolution photoacoustic microscopy,” *Optics Letters*, vol. 36, no. 2, pp. 139–141, 2011.
- [172] R. Nuster, P. Slezak, and G. Paltauf, “Light-sheet photoacoustic microscopy (LIS-PAM) with optical ultrasound detection,” in *Proc. SPIE 9708, Photons Plus Ultrasound: Imaging and Sensing 2016*, 2016, p. 97082E.
- [173] R. W. Boyd, *Nonlinear Optics*. Chapter 2, Academic Press, 2008.
- [174] A. A. Ghazaryan, P.-S. Hu, S.-J. Chen, H.-Y. Tan, and C.-Y. Dong, “Spatial and temporal analysis of skin glycation by the use of multiphoton microscopy and spectroscopy,” *Journal of Dermatological Science*, vol. 65, no. 3, pp. 189–195, 2012.
- [175] S. Roth and I. Freund, “Second harmonic generation in collagen,” *The Journal of Chemical Physics*, vol. 70, no. 4, pp. 1637–1643, 1979.
- [176] L. Mecklenburg, M. Nakamura, J. P. Sundberg, and R. Paus, “The nude mouse skin phenotype: the role of Foxn1 in hair follicle development and cycling,” *Experimental and molecular pathology*, vol. 71, no. 2, pp. 171–178, 2001.
- [177] J. G. Lyubovitsky, T. B. Krasieva, X. Xu, B. Andersen, and B. J. Tromberg, “In situ multiphoton optical tomography of hair follicles in mice,” *Journal of Biomedical Optics*, vol. 12, no. 4, p. 044003, 2007.
- [178] S. V. Plotnikov, A. C. Millard, P. J. Campagnola, and W. a. Mohler, “Characterization of the myosin-based source for second-harmonic generation from muscle sarcomeres.” *Biophysical Journal*, vol. 90, no. 2, pp. 693–703, 2006.
- [179] M. Seeger, A. Karlas, D. Soliman, J. Pelisek, and V. Ntziachristos, “Multimodal optoacoustic and multiphoton microscopy of human carotid atheroma,” *Photoacoustics*, vol. 4, no. 3, pp. 102–111, 2016.

- [180] R. B. Singh, S. a. Mengi, Y. J. Xu, A. S. Arneja, and N. S. Dhalla, "Pathogenesis of atherosclerosis: A multifactorial process," *Experimental and Clinical Cardiology*, vol. 7, no. 1, pp. 40–53, 2002.
- [181] W. Insull, "The Pathology of Atherosclerosis: Plaque Development and Plaque Responses to Medical Treatment," *American Journal of Medicine*, vol. 122, no. 1, pp. S3–S14, 2009.
- [182] T. T. Le, I. M. Langohr, M. J. Locker, M. Sturek, and J.-X. Cheng, "Label-free molecular imaging of atherosclerotic lesions using multimodal nonlinear optical microscopy." *Journal of Biomedical Optics*, vol. 12, no. 5, p. 054007, 2007.
- [183] M. B. Lilledahl, O. A. Haugen, C. de Lange Davies, and L. O. Svaasand, "Characterization of vulnerable plaques by multiphoton microscopy." *Journal of Biomedical Optics*, vol. 12, no. 4, p. 044005, 2007.
- [184] R. Y. Ball, E. C. Stowers, J. H. Burton, N. R. B. Cary, J. N. Skepper, and M. J. Mitchinson, "Evidence that the death of macrophage foam cells contributes to the lipid core of atheroma," *Atherosclerosis*, vol. 114, no. 1, pp. 45–54, 1995.
- [185] M. Schwarz, J. Aguirre, D. Soliman, A. Buehler, and V. Ntziachristos, "Unmixing chromophores in human skin with a 3D multispectral optoacoustic mesoscopy system," in *Proc. SPIE 9708, Photons Plus Ultrasound: Imaging and Sensing 2016*, 2016, p. 970855.
- [186] G. J. Tservelakis, S. Kellnberger, D. Soliman, M. Seeger, H. Yang, A. Karlas, L. Prade, and V. Ntziachristos, "Frequency domain optoacoustic microscope," *in preparation*.
- [187] A. M. Winkler, K. Maslov, and L. V. Wang, "Noise-equivalent sensitivity of photoacoustics," *Journal of Biomedical Optics*, vol. 18, no. 9, p. 97003, 2013.
- [188] G. Langer, B. Buchegger, J. Jacak, T. a. Klar, and T. Berer, "Frequency domain photoacoustic and fluorescence microscopy," *Biomedical Optics Express*, vol. 7, no. 7, p. 2692, 2016.
- [189] Y. Fan, A. Mandelis, G. Spirou, I. A. Vitkin, and W. M. Whelan, "Laser photothermoacoustic heterodyned lock-in depth profilometry in turbid tissue phantoms," *Physical Review E - Statistical, Nonlinear, and Soft Matter Physics*, vol. 72, no. 5, pp. 1–11, 2005.
- [190] S. Telenkov and A. Mandelis, "Fourier-domain biophotoacoustic subsurface depth selective amplitude and phase imaging of turbid phantoms and biological tissue." *Journal of Biomedical Optics*, vol. 11, no. 4, p. 044006, 2006.
- [191] S. Telenkov, A. Mandelis, B. Lashkari, and M. Forcht, "Frequency-domain photothermoacoustics: Alternative imaging modality of biological tissues," *Journal of Applied Physics*, vol. 105, no. 10, pp. 1–8, 2009.
- [192] S. Kellnberger, N. C. Deliolanis, D. Queirós, G. Sergiadis, and V. Ntziachristos, "In vivo frequency domain optoacoustic tomography," *Optics Letters*, vol. 37, no. 16, p. 3423, 2012.
- [193] T. W. Murray and O. Balogun, "High-sensitivity laser-based acoustic microscopy using a modulated excitation source," *Applied Physics Letters*, vol. 85, no. 14, pp. 2974–2976, 2004.

- [194] P. Mohajerani, S. Kellnberger, and V. Ntziachristos, "Frequency domain optoacoustic tomography using amplitude and phase," *Photoacoustics*, vol. 2, no. 3, pp. 111–118, 2014.
- [195] National Institutes of Health (US), *Guide for the care and use of laboratory animals*. National Academies, 1985.
- [196] P. Horowitz, W. Hill, and T. C. Hayes, *The art of electronics*, 2nd ed. Cambridge: Cambridge university press, 1989.
- [197] P. Mohajerani, S. Kellnberger, and V. Ntziachristos, "Fast Fourier backprojection for frequency-domain optoacoustic tomography," *Optics Letters*, vol. 39, no. 18, pp. 5455–5458, 2014.
- [198] Y. F. Leung, P. Ma, and J. E. Dowling, "Gene expression profiling of zebrafish embryonic retinal pigment epithelium in vivo," *Investigative Ophthalmology and Visual Science*, vol. 48, no. 2, pp. 881–890, 2007.
- [199] M. Takamiya, F. Xu, H. Suhonen, V. Gourain, L. Yang, N. Y. Ho, L. Helfen, A. Schröck, C. Etard, C. Grabher, S. Rastegar, G. Schlunck, T. Reinhard, T. Baumbach, and U. Strähle, "Melanosomes in pigmented epithelia maintain eye lens transparency during zebrafish embryonic development," *Scientific Reports*, vol. 6, no. October 2015, p. 25046, 2016.
- [200] T. M. S. Greiling and J. I. Clark, "Early lens development in the zebrafish: A three-dimensional time-lapse analysis," *Developmental Dynamics*, vol. 238, no. 9, pp. 2254–2265, 2009.
- [201] J. Enfield, E. Jonathan, and M. Leahy, "In vivo imaging of the microcirculation of the volar forearm using correlation mapping optical coherence tomography (cmOCT)," *Biomedical Optics Express*, vol. 2, no. 5, pp. 1184–1193, 2011.
- [202] C. Ince, "The microcirculation is the motor of sepsis." *Critical Care*, vol. 9, no. Suppl 4, pp. 13–19, 2005.
- [203] S. M. Daly and M. J. Leahy, "'Go with the flow ': A review of methods and advancements in blood flow imaging," *Journal of Biophotonics*, vol. 6, no. 3, pp. 217–255, 2013.
- [204] M. J. Leahy, *Microcirculation Imaging*. John Wiley & Sons, 2012.
- [205] P. Vennemann, R. Lindken, and J. Westerweel, "In vivo whole-field blood velocity measurement techniques," *Experiments in Fluids*, vol. 42, no. 4, pp. 495–511, 2007.
- [206] W. Groner, J. W. Winkelman, a. G. Harris, C. Ince, G. J. Bouma, K. Messmer, and R. G. Nadeau, "Orthogonal polarization spectral imaging: a new method for study of the microcirculation." *Nature Medicine*, vol. 5, no. 10, pp. 1209–1212, 1999.
- [207] J. O'Doherty, J. Henricson, C. Anderson, M. J. Leahy, G. E. Nilsson, and F. Sjöberg, "Sub-epidermal imaging using polarized light spectroscopy for assessment of skin microcirculation," *Skin Research and Technology*, vol. 13, no. 4, pp. 472–484, 2007.
- [208] S. Monstrey, H. Hoeksema, J. Verbelen, A. Pirayesh, and P. Blondeel, "Assessment of burn depth and burn wound healing potential," *Burns*, vol. 34, no. 6, pp. 761–769, 2008.
- [209] I. Wang, S. Andersson-Engels, G. E. Nilsson, K. Wärde, and K. Svanberg, "Superficial blood flow following photodynamic therapy of malignant non-melanoma

- skin tumours measured by laser Doppler perfusion imaging," *The British Journal of Dermatology*, vol. 136, no. 2, pp. 184–189, 1997.
- [210] W. R. Ferrell, P. V. Balint, and R. D. Sturrock, "Novel use of laser Doppler imaging for investigating epicondylitis," *Rheumatology (Oxford, England)*, vol. 39, no. 11, pp. 1214–1217, 2000.
- [211] K. R. Mathura, K. C. Vollebregt, K. Boer, J. C. De Graaff, D. T. Ubbink, and C. Ince, "Comparison of OPS imaging and conventional capillary microscopy to study the human microcirculation," *Journal of Applied Physiology*, vol. 91, no. 1, pp. 74–78, 2001.
- [212] S. M. Milner, S. Bhat, S. Gulati, G. Gherardini, C. E. Smith, and R. J. Bick, "Observations on the microcirculation of the human burn wound using orthogonal polarization spectral imaging," *Burns*, vol. 31, no. 3, pp. 316–319, 2005.
- [213] S.-L. Chen, Z. Xie, P. L. Carson, X. Wang, and L. J. Guo, "In vivo flow speed measurement of capillaries by photoacoustic correlation spectroscopy," *Optics Letters*, vol. 36, no. 20, p. 4017, 2011.
- [214] J. Wierwille, P. Andrews, M. Onozato, J. Jiang, A. Cable, and Y. Chen, "In vivo imaging of kidney microcirculation using Doppler optical coherence tomography," *Laboratory Investigation*, vol. 91, no. 11, pp. 1596–1604, 2011.
- [215] P. Li, A. Liu, L. Shi, X. Yin, S. Rugonyi, and R. K. Wang, "Assessment of strain and strain rate in embryonic chick heart in vivo using tissue Doppler optical coherence tomography," *Physics in Medicine and Biology*, vol. 56, no. 22, pp. 7081–7092, 2011.
- [216] R. A. Leitgeb, R. M. Werkmeister, C. Blatter, and L. Schmetterer, "Doppler optical coherence tomography." *Progress in retinal and eye research*, vol. 41, pp. 26–43, 2014.
- [217] R. K. Wang and L. An, "Doppler optical micro-angiography for volumetric imaging of vascular perfusion in vivo," *Optics Express*, vol. 17, no. 11, pp. 8926–8940, 2009.
- [218] P. J. van den Berg, K. Daoudi, and W. Steenbergen, "Review of photoacoustic flow imaging: Its current state and its promises," *Photoacoustics*, vol. 3, no. 3, pp. 89–99, 2015.
- [219] H. Fang and L. V. Wang, "M-mode photoacoustic particle flow imaging," *Optics Letters*, vol. 34, no. 5, pp. 671–673, 2009.
- [220] J. Brunner and P. Beard, "Pulsed photoacoustic Doppler flowmetry using time-domain cross-correlation: Accuracy, resolution and scalability," *The Journal of the Acoustical Society of America*, vol. 132, no. 3, p. 1780, 2012.
- [221] B. Ning, M. J. Kennedy, A. J. Dixon, N. Sun, R. Cao, B. T. Soetikno, R. Chen, Q. Zhou, K. K. Shung, J. a. Hossack, and S. Hu, "Simultaneous photoacoustic microscopy of microvascular anatomy, oxygen saturation, and blood flow," *Optics Letters*, vol. 40, no. 6, pp. 910–913, 2015.
- [222] J. Yao, K. I. Maslov, Y. Shi, L. a. Taber, and L. V. Wang, "In vivo photoacoustic imaging of transverse blood flow by using Doppler broadening of bandwidth," *Optics Letters*, vol. 35, no. 9, pp. 1419–1421, 2010.
- [223] H. Fang, K. Maslov, and L. V. Wang, "Photoacoustic doppler effect from flowing small light-absorbing particles," *Physical Review Letters*, vol. 99, no. 18, pp. 2–5, 2007.

- [224] H. Fang, K. Maslov, and L. V. Wang, "Photoacoustic Doppler flow measurement in optically scattering media," *Applied Physics Letters*, vol. 91, no. 26, pp. 2–4, 2007.
- [225] A. Sheinfeld, S. Gilead, and A. Eyal, "Photoacoustic Doppler measurement of flow using tone burst excitation," *Optics Express*, vol. 18, no. 5, pp. 4212–4221, 2010.
- [226] Y. Tong, H. Zhao, H. Fang, Y. Zhao, and X. Yuan, "Flow angle dependent photoacoustic Doppler power spectra under intensity-modulated continuous wave laser excitation," *AIP Advances*, vol. 6, no. 2, p. 025109, 2016.
- [227] Y. Zhao, Z. Chen, C. Saxer, S. Xiang, J. F. D. Boer, and J. S. Nelson, "Phase-resolved optical coherence tomography and optical Doppler tomography for imaging blood flow in human skin with fast scanning speed and high velocity sensitivity," *Optics Letters*, vol. 25, no. 2, pp. 114–116, 2000.
- [228] M. Omar, D. Soliman, and V. Ntziachristos, "Multimodal Optoacoustic Imaging," in *Image Fusion in Pre-Clinical Imaging*, C. Kuntner and Y. Hämişch, Eds. Springer, in preparation.

List of Figures

2.1	Basic interactions between light and matter	7
2.2	Absorption coefficient of water at different regions of the electromagnetic spectrum	8
2.3	Light-matter interaction processes at high photon energies ($E_\gamma > 1$ eV)	9
2.4	Jablonski diagram of electronic excitation and the most common de-excitation processes	10
2.5	Absorption spectra of the most abundant tissue chromophores	11
2.6	Jablonski diagram of the most common photon scattering processes	12
2.7	Shape and geometry of Gaussian beams	14
2.8	Optical path of a Keplerian beam expander	15
2.9	Spatial filtering of a Gaussian beam with a pinhole	16
2.10	Point spread function and spatial resolution	17
2.11	Schematic depiction of a typical confocal microscope	22
2.12	Jablonski diagram of the most common non-linear optical processes used in multiphoton microscopy	24
2.13	Comparison of the excitation volumes in single-photon and two-photon excitation fluorescence	25
2.14	SHG and THG microscopy of starch granules	28
2.15	Schematic depiction of a typical LSFM implementation	29
3.1	Principle of optoacoustic imaging	32
3.2	Simulation of optoacoustic signals for different source diameters	36
3.3	Simulation of optoacoustic signals from solid absorbers made of different materials	37
3.4	Simulation of optoacoustic signal attenuation in tissue and water.	39
3.5	Components of spherically focused ultrasound transducers based on glass lenses	40
3.6	Detection geometry of spherically focused transducers	42
3.7	Scanning in optoacoustic mesoscopy	43
3.8	Principle of the backprojection reconstruction method	45
3.9	Schematic illustration of the two RSOM configurations	47
3.10	Spatial and bandpass filtering of optoacoustic signals	49
3.11	Reconstruction geometry in RSOM	50
3.12	Reconstruction in RSOM using a weighted hyperbolic sensitivity field model	51
3.13	RSOM imaging of a 30 μm suture cross phantom	52
3.14	RSOM imaging of a mouse ear <i>ex vivo</i> using different reconstruction methods	53
3.15	RSOM imaging of a mouse ear <i>ex vivo</i> comparing the full bandwidth and multi-frequency reconstructions	54
4.1	Pigment translocation in melanophores	59
4.2	Brightfield observation of MCH-mediated melanosome aggregation in zebrafish larvae <i>in vivo</i>	60

4.3	Simulation of optoacoustic frequency shifts generated by spherical absorbers with changing size	61
4.4	Optoacoustic imaging of MCH-mediated melanosome aggregation in cultured <i>Xenopus laevis</i> melanophores	62
4.5	Optoacoustic imaging and frequency analysis of a 6 dpf zebrafish larva <i>in vivo</i> before and after MCH treatment	63
4.6	Optoacoustic imaging and frequency analysis of light background-induced melanosome aggregation in 5 dpf zebrafish larvae <i>in vivo</i>	65
4.7	3D optoacoustic imaging of light background-induced melanosome aggregation in a 5 dpf wildtype zebrafish larva <i>in vivo</i>	66
4.8	2D mapping of melanophore aggregation via optoacoustic frequency shifts during background adaption in zebrafish larvae <i>in vivo</i>	67
4.9	Optoacoustic monitoring of melatonin triggered melanosome aggregation in xenotransplanted wildtype <i>Xenopus</i> melanophores <i>in vivo</i>	68
5.1	Illumination and detection geometry in transmission-mode OM	72
5.2	Scheme of the OM setup	73
5.3	Hilbert transform of optoacoustic signals	75
5.4	Characterization of the 515 nm laser	76
5.5	Simulation of optoacoustic frequencies reaching the 80 MHz transducer as a function of the source diameter	77
5.6	Measurement of the transducer detection bandwidth and electrical impulse response	79
5.7	Lateral resolution characterization	80
5.8	OM imaging of model organisms <i>ex vivo</i>	82
5.9	Electrical impulse response correction	83
5.10	Scheme of the fiber detector based all-optical optoacoustic microscope	85
5.11	Characterization of the π -FBG sensor	86
5.12	Imaging of model organisms with the all-optical optoacoustic microscope	87
6.1	Scheme of the IMMSOM setup	94
6.2	Spatial resolution characterization of the IMMSOM microscopy modalities	96
6.3	Offset characterization of the IMMSOM modalities	97
6.4	multiscale optoacoustic imaging of a wildtype zebrafish larva <i>ex vivo</i>	98
6.5	Hybrid label-free imaging of a mouse ear larva <i>ex vivo</i>	99
6.6	Hybrid label-free imaging of a wildtype zebrafish larva <i>ex vivo</i>	100
6.7	Hybrid imaging of a human carotid atheroma slice	102
7.1	Optoacoustic signal strength comparison between TD-OM and FD-OM	109
7.2	IQ-demodulation principle	110
7.3	I and Q signals in heterodyne detection	111
7.4	Scheme of the hybrid FD-OM and multiphoton microscopy setup	113
7.5	Comparison of signal generation in TD-OM and FD-OM	114
7.6	3D printed mouse ear holder for <i>in vivo</i> experiments	115
7.7	Characterization of the 488 nm CW laser	115
7.8	FOV and field distortion characterization	116
7.9	Simulation of the transducer sensitivity field for monofrequent excitation	117
7.10	FD-OM imaging of a 50 μm suture cross phantom	118
7.11	Comparison of the SNR achieved in FD and TD optoacoustic microscopy	119

7.12	FD-OM imaging of a wildtype zebrafish eyeball <i>ex vivo</i>	120
7.13	FD-OM imaging of the vascular network in a mouse ear <i>in vivo</i>	121
7.14	Hybrid FD-OM and multiphoton imaging of a mouse ear <i>in vivo</i>	122
8.1	FD-OM Doppler shift detection scheme	127
8.2	Doppler shift detection using black nail polish	128
8.3	Doppler shift detection using black carbon particles flowing in a tube	130
8.4	Doppler shift calibration	131
8.5	Blood flow monitoring of a single vessel in a mouse ear during a terminal experiment	132
8.6	Blood flow profile of a single vessel in a mouse ear <i>in vivo</i>	133
8.7	2D blood flow mapping in a mouse ear <i>in vivo</i>	134
B.1	Numerical axial resolution simulation	147
C.1	Photograph of the IMMSOM system	149
C.2	Photograph of the FD-OM system	150
C.3	Photograph of the FD-OM <i>in vivo</i> mouse ear holder during a blood flow scan	150

List of Tables

6.1	Comparison of the imaging modalities combined in IMMSOM	92
7.1	Comparison of TD and FD optoacoustic microscopy	106
B.1	Comparison of axial resolution values for the 80 MHz transducer estimated by different methods	148

Index

- A-scan, 31, 44, 48, 75, 126
- Absorption coefficient, 8, 11, 33
- Acoustic
 - attenuation, 2, 32, 38, 39, 61, 72, 77–79
 - impedance, 31, 37, 58
 - lens, 40, 41, 43, 117
- Actin, 58
- ANSI exposure limits, 108, 113, 120, 122
- Autofluorescence, 2, 20, 92, 99, 122
- Avalanche photodiode (APD), 21

- B-scan, 31, 48, 75
- Backprojection, 32, 45, 46
 - binary mask model, 49, 50, 53, 54
 - delay-and-sum, 46
 - filtered, 46, 49–51, 54
 - WHSF model, 50, 52–54, 93
- Beam expander, 14, 15, 73, 93
- Beer-Lambert law, 8
- Birefringence, 26, 27, 92, 99

- Coherence-restored pulse interferometry (CRPI), 85–87
- Collagen, 27, 92, 99, 102, 122
- Confocal microscopy, 1, 19, 22, 23, 25, 26, 29, 72, 91
 - spinning disk, 23, 26
- Correlation mapping OCT (cmOCT), 126
- Cross section, 8–10, 12, 13
- Cumulative power spectrum (CPS), 60, 61, 63–65, 68, 69
- Cyclic adenosine monophosphate (cAMP), 58, 59

- Degree of freedom, 12
- Delta function, 34, 35
- Doppler
 - angle, 127, 129, 131
 - broadening, 128, 129, 131
 - shift, 125–131, 134, 135
- Doppler optical coherence tomography (DOCT), 126
- Doppler optical micro-angiography (DOMAG), 126
- Doppler ultrasound imaging (DUS), 125, 126
- Dynein, 58, 59

- Elastin, 20, 92, 99, 102
- Electrical impulse response (EIR), 77–79, 82, 88, 148
 - correction, 82, 83
- Electrical susceptibility, 23–28
- Electron beam physical vapor deposition, 79
- Electronic excitation, 9, 10
- Extinction coefficient, 8

- Fabry-Pérot interferometer (FPI), 84, 86
- Fiber Bragg grating (FBG), 84–86, 88
 - transmission notch, 84–86
- Flavin, 20
- Fluorescence, 11, 20–23, 25, 26, 28, 29
- Franck-Condon principle, 10
- Frangi vesselness filter, 51, 53, 54
- Frequency-domain optoacoustic microscopy (FD-OM), 3, 106, 112, 117, 119, 120, 122, 123, 126, 135

- G-protein-coupled receptor (GPCR), 58, 70
- Gaussian laser beam, 13–15, 27, 28, 80, 93
 - confocal parameter, 14, 17, 29, 96, 118
 - divergence, 13–15
 - spatial filter, 15, 73, 76, 112, 115
 - waist, 13, 14, 29
- Gouy phase shift, 27
- Grüneisen coefficient, 33
- Green's function
 - frequency-domain, 107
 - time-domain, 34

- Heat conversion efficiency, 33
- Heating function
 - frequency-domain, 107
 - time-domain, 34, 35, 108
- Heavyside function, 35
- Hemoglobin, 3, 11, 12, 31, 37, 71, 92, 103
- Heterodyne detection, 111, 127, 128, 130
- Hilbert transform, 74, 81, 114, 147
- Homodyne detection, 112, 127
- Huygens' principle, 35

- Image distortion
 - barrel, 18
 - pincushion, 18, 116
- Internal conversion, 11
- Intersystem crossing, 11
- IQ-demodulation, 106, 110, 112, 113, 122, 123, 127, 128, 130, 135

- Johnson noise, 109
- Kinesin, 58

- Label-free imaging, 2, 3, 20, 28, 71, 92, 103, 106, 120, 123, 126
- Laser Doppler imaging (LDI), 125
- Laser microscopy, 1, 2, 7, 18, 22
- Laser speckle imaging (LSI), 125
- Laser-scanning, 18–21, 23
OM, 72, 88, 92, 103, 105, 106, 112, 113, 116, 122
- Lifetime
fluorescence, 11
phosphorescence, 11
virtual state, 13, 25
- Light sheet fluorescence microscopy (LSFM), 19, 28, 29
- Local oscillator (LO), 110–112
- Mach-Zehnder interferometer, 86
- Magnetic resonance imaging (MRI), 30
- Mean free path (MFP), 8, 18, 19
- Melanin, 3, 11, 12, 31, 37, 57, 60, 61, 63, 64, 69, 71, 88, 92, 100, 103
- Melanosome translocation, 57–59, 66, 67
- Mesoscopic imaging, 2, 29, 30, 32, 91, 92
- Microelectromechanical systems (MEMS), 92
- Microflow, 125–127, 135
- Microscope objective
achromat, 18
apochromat, 18
back aperture, 20, 23, 73
fluorite, 18
immersion, 21, 72
magnification, 19
plan, 18
working distance, 21, 72
- Microtubules, 58, 59
- Model-based reconstruction, 32, 44
- Modulation depth, 108, 115, 116
- Molecular energy level
rotational, 10, 12
vibrational, 10–13
- Multi-frequency reconstruction, 32, 51, 53, 54, 98
- Multi-orientation RSOM (MORSOM), 69, 70
- Multimodal imaging, 91, 93, 103
- Multiphoton microscopy, 1, 19, 23, 25, 27, 29, 72, 91, 92, 106, 123
- Myomeres, 101
- Myosepta, 101
- Myosin, 27, 58, 92, 101
- Nicotinamide adenine dinucleotide phosphate (NADP), 20
- Non-centrosymmetry, 27, 28, 99
- Numerical aperture, 16, 20, 21, 25, 29, 42, 72, 84, 88, 93
- Nyquist–Shannon sampling theorem, 19, 48
- Optical
aberrations, 18, 81, 95
absorption, 2, 3, 7–12, 18, 26, 30, 31, 33, 34, 57, 92, 106, 110, 120, 126
diffraction, 7, 8, 13–15, 18, 23, 28, 73, 77, 96, 115
diffusion limit, 19, 30, 32, 103
fluence, 33, 34, 55, 108
fluence rate, 34
reflection, 7, 8, 24
refraction, 8, 18, 24
window, 12, 26
- Optical projection tomography (OPT), 30
- Optical sectioning, 19, 22
confocal microscopy, 22
LSFM, 28
multiphoton microscopy, 23, 25
OM, 72
- Optoacoustic microscopy (OM), 2, 3, 19, 71, 73, 114, 119, 122, 126
axial resolution, 71, 78, 81, 83, 84, 95, 147, 148
contrast, 71
epi-illumination, 72, 73, 84, 88, 103
lateral resolution, 2, 71, 72, 75, 80, 81, 84, 88, 95
penetration depth, 2, 71, 92
- Optoacoustic wave equation
frequency-domain, 107
time-domain, 33
- Orthogonal polarization spectroscopy (OPS), 125
- Pair production, 9
- Phase matching, 26, 27
- Phosphorescence, 11
- Photoacoustic effect, 31, 78
- Photobleaching, 2, 21, 23, 26, 92
- Photoelectric effect, 9, 10, 21
- Photomultiplier tube (PMT), 21, 95
- Phototoxicity, 2, 26, 92
- Piezoelectric effect, 40
- Point spread function (PSF), 16, 80
axial, 17
transverse (Airy disk), 16, 23, 25, 81, 96
- Pulse-echo method (PE), 31, 78, 79
- Quadrature signals, 110, 111, 127
- Quantization, 10
- Quantum yield, 11, 12, 33
- Quartz-enhanced tuning fork (QTF), 109
- Radon transform, 35, 45
- Raster-scan optoacoustic mesoscopy (RSOM), 32, 46, 47, 49, 54, 58, 66, 92
axial resolution, 44, 48, 69, 147, 148
lateral resolution, 2, 43, 44, 48, 69, 71, 96, 97
penetration depth, 66, 71, 93, 96
- Rayleigh criterion, 16, 17
- Sarcomeres, 101
- Scattering
acoustic, 2, 19, 32, 58
anti-Stokes, 13

- Compton, 9, 10
- Mie, 13, 19
- optical, 2, 7, 8, 12, 13, 18, 19, 22, 23, 26, 29, 32, 58, 125
- Raman, 13
- Rayleigh, 12, 13, 26
- Stokes, 13
- Scattering coefficient, 8, 19
- Second-harmonic generation (SHG), 26–28, 92, 99, 101, 122
- Selection rules, 12
- Side lobe
 - frequency, 36
 - spatial, 40, 50
- Singlet state, 10, 11
- Skin depth, 79
- Spatial impulse response (SIR), 32, 41, 77, 80, 88, 89
- Speckle variance OCT (svOCT), 126
- Spin-orbit coupling, 11
- Stokes shift, 11
- Stratum corneum, 99
- Stress relaxation time, 33
- Synthetic aperture focusing technique (SAFT), 46

- Thermal relaxation time, 33
- Thermoelastic expansion, 31, 107
- Third-harmonic generation (THG), 27, 28, 92, 122
- Time-of-flight (TOF), 31, 44, 46, 105, 106
- Transport mean free path (TMFP), 19, 29
- Triplet state, 11
- Two-photon absorption (TPA), 24, 25
- Two-photon excitation fluorescence (TPEF), 24–27, 92, 102, 122

- Ultrasound imaging, 29, 31, 91
- Ultrasound transducers, 31, 33, 135
 - delay line, 41, 49, 117
 - numerical aperture, 43
 - optical, 84
 - piezoelectric, 40–42, 84, 116

- Virtual detector technique, 46, 49
- Virtual state, 13, 25

- Wiener deconvolution, 82
- Wildtype transplanted frog (WTF) melanophores, 68, 69

- X-ray computed tomography (X-ray CT), 30, 45